Investigation of Dual-Jet Air Curtains For a Landing Gear Noise Reduction Technology

KUN ZHAO

Supervisor: Dr. Gareth J. Bennett

Department of Mechanical & Manufacturing Engineering

Trinity College Dublin

Ireland

May 2017

A thesis submitted to the University of Dublin in partial fulfillment of the requirements for the degree of Ph.D

Declaration

I declare that this thesis has not been submitted as an exercise for a degree at this or any other university and it is entirely my own work.

I agree to deposit this thesis in the Universitys open access institutional repository or allow the library to do so on my behalf, subject to Irish Copyright Legislation and Trinity College Library conditions of use and acknowledgement.

Kun Zhao, January 2017

Abstract

As the popularity of air travel increases, noise that it causes to the communities around airports has become a major concern to the aeronautical industry. World leading economic entities, such as EU and US, have made aircraft noise reduction an important section in their blueprint for aviation development. Airframe noise, generated by unsteady flow over the landing gear and high lift devices is of the prime interest due to its large contribution to the overall aircraft noise output. Thus, landing gear noise, the main source of airframe noise during take-off and approach when the engine operates at a low thrust, has been widely investigated. Some technologies have been proposed to reduce its noise emission, e.g. fairings and wheel hub caps. The prevailing fundamental idea behind these technologies is to cover the non-aerodynamic elements, thereby reducing the turbulent interaction. However, even these rudimentary add-ons may impede the inspection, maintenance and brake cooling of the landing gear, in addition to adding to the structural complexity and weight. The above mentioned technologies suggest incremental improvements to the reduction of landing gear noise. However, similar to the step-change innovative technologies in aeroengine design that have significantly reduced overall aircraft noise, innovation in low noise landing gear design is now required to help meet future environmental noise targets.

The air curtain, also referred to as the planar jet, is proposed as a disruptive breakthrough technology to be installed upstream to the landing gear. It aims to deflect the incoming flow, shielding the bluff body so as to reduce the flow-induced noise. A preliminary study in 2009 validated its usefulness for aerodynamic noise reduction. However, it is also found that the emission of the air curtain self-noise introduced a limiting factor that impairs the performance of this technology, which can hinder the ultimate implementation. As such, this thesis investigates an alternative novel dual-jet configuration to

minimise the air curtain self-noise emission. More specifically, in addition to the primary jet, a second jet is situated upstream of it, at a lower velocity, which reduces the total noise by both allowing the primary jet to operate at a lower velocity for the same shielding height and also by reducing the slot edge-exit noise due to allowing the primary jet to issue at 90°.

A main objective of this study is to validate and improve the performance of dual air curtains on the flow-induced noise reduction. Using tandem rods as a generic bluff body, this work first involves an approach to optimize the configuration of the air curtain application. In this study, the approach was proposed and utilised based on CFD simulations and PIV experiments. With the optimized configuration, both single jet and dual jet geometries were able to achieve substantial noise reduction. In particular, due to increased shielding of the bluff body, the introduction of the extra jet improved the total noise reduction when compared to the single jet. However, the suppression of primary jet noise was found to be less obvious than expected as the sound pressure level at some high frequency ranges was found to increase compared to the single jet. Thus, an optimal configuration of the dual jet geometry was proposed and tested, which requires less velocity from both jets for the same shielding height to the bluff body. The configuration was validated to be able to maximise the noise reduction with much less production of the jet self-noise.

This study also discusses the flow regime of dual planar jets in the crossflow from the perspective of the fluid mechanics, which provides a good theoretical foundation for the implementation of the air curtain technology. Firstly, a novel approach to defining the jet leeward edge was developed based on a series of PIV experiments. Furthermore, based on CFD results, the recirculation structures of the flow regime and the development of the dual jets were characterised.

In addition, this study preliminarily discusses the possibility of the combined use of dual air curtains with other technologies, using perforated fairings as an example. This work experimentally compares the individual use of dual air curtains with the perforated fairing, after which the combined use was tested. As a conclusion a recommendation was made, which accounts for not only acoustic performance but also engineering implementation.

As a proof-of-concept, work in this study can contribute to the final realisation of the dual air curtains technology.

Acknowledgments

First and foremost, I would like to thank my supervisor, Prof. Gareth J. Bennett, for his guidance and knowledge about my Ph.D. Without his fatherly support, patience and assistance, not only to my research but also to my life in Dublin, never would there be this thesis. Furthermore, the profession and working style that I have learned from him will definitely benefit my future. Thank you again.

I would like also to thank Dr. John Kennedy. Thanks to his demonstration of PIV, how-wire etc., and the experimental experience that he shared with me, I could confidently handle my work in the Fluids Lab. In addition, I would like to thank other academic staff that I have worked with, particularly to Profs. Henry Rice and Ciaran Simms.

The administrative and technical staff in Parsons offered me enormous help. Thanks to Mrs. Judith Lee who helped me solve all of the problems that I met in the department. Also, thanks to Mick, Sean, JJ, Alex and Gabriel who turned my idea into the real product.

To other two members of Gar's Ph.D. team: Eleonora and Patrick. I will never forget those days we spent together in the office, lab, pav and Kennedy's. Even though we are from three different continents, the memory will definitely maintain the friendship and will link all of us forever.

To other colleagues in the most international office in Parsons building: Dan, Jason, Kavin, Alberto, Sara and Alesia. With them the office is much more enjoyable that I could have hoped for. Of course, there is Sajad, who needs to be highlighted. Thank you for keeping the office quiet.

Special thanks to my parents. As the only child of you, I am sorry for being so far for this long time. Without your love, nothing could I achieve never and ever. Also to Xiao, your presence in my life drives away all pains.

At last but not least, I would like to give my deepest gratitude to the country–Republic of Ireland. Thank you for being so generous to me in the four years period. Life here really makes me fall in love with this beautiful land. No matter where I go in the future, my memory stays and my heart stays. As my second motherland, you will be deeply missed in my life.

Publications and Awards

Journal Articles

1. **Kun Zhao**, Xixiang Yang, Patrick N. Okolo, Zeping Wu and Gareth J. Bennett. "Use of dual planar jets for the reduction of flow-induced noise." AIP Advances 7, No. 2, 2017: 025312.

   DOI: 10.1063/1.4976336

2. **Kun Zhao**, Xixiang Yang, Patrick N. Okolo, Weihua Zhang and Gareth J. Bennett,"Use of Plane Jet for Flow-Induced Noise Reduction of Tandem Rods". Chinese Physics B, 2016, 25(6): 64301064301.

   DOI: 10.1088/1674-1056/25/6/064301

3. **Kun Zhao**, Sajad Alimohammadi, Patrick N. Okolo, John Kennedy, and Gareth J Bennett, "Aerodynamic noise reduction using dual-jet planar air curtains". Journal of Sound and Vibration.

   (In Preparation)

4. **Kun Zhao**, Patrick N. Okolo, John Kennedy, and Gareth J. Bennett, "Interaction between Tandem Jets in a Crossflow". Experiments in Fluids.

   (In Preparation)

5. **Kun Zhao**, Patrick N. Okolo, John Kennedy, and Gareth J. Bennett, "A Study of Dual Air Curtains and Perforated Fairings for the Reduction of Landing Gear Noise Reduction". AIAA Journal.

   (In Preparation)

Conference Articles

1. **Kun Zhao**, Patrick N Okolo, John Kennedy and Gareth J Bennett, "A Study of Planar Jet Flow Control and Perforated Fairings for the Reduction of the Flow-induced Noise of Tandem Rods in a Crossflow (AIAA 2016-2772)". In the 22nd AIAA/CEAS Aeroacoustics Conference, Lyon, France, 30 May-1 June, 2016

   DOI:10.2514/6.2016-2772

2. Gareth J. Bennett, **Kun Zhao**, John Philo, Yaoyi Guan and Scott C Morris, 2016, "Cavity Noise Suppression Using Fluidic Spoilers (AIAA2016-2756)". In the 22nd AIAA/CEAS Aeroacoustics Conference, Lyon, France, 30 May-1 June, 2016

   DOI: 10.2514/6.2016-2756

3. Patrick N. Okolo, **Kun Zhao**, John Kennedy, Gareth J. Bennett, 2016, "Mesh Screen Application for Noise Reduction of Landing Gear Strut (AIAA2016-2845)". In the 22nd AIAA/CEAS Aeroacoustics Conference, Lyon, France, 30 May-1 June, 2016

   DOI: 10.2514/6.2016-2845

4. **Kun Zhao**, Elonora Neri, Patrick N Okolo, John Kennedy. and Gareth J. Bennett, 2015, "Landing Gear Noise Reduction by Double Jet Air Curtain Configuration". In the 22nd International Congress on Sound and Vibration, Florence, Italy, 12-16 July, 2015

   DOI: 10.13140/RG.2.1.2702.1203

5. Patrick N. Okolo, **Kun Zhao**, Elonora Neri, Patrick N Okolo, John Kennedy and Gareth J. Bennett, 2015, "CAA Noise Reduction Parametric Study of Mesh Screens Applied to Landing Gears". In the 22nd International Congress on Sound and Vibration, Florence, Italy, 12-16 July, 2015

   DOI: 10.13140/RG.2.1.4537.1287

Awards

1. Champion of the 18th Sir Bernard Crossland Symposium and Postgraduate Research Workshop

Contents

List of Symbols and Abbreviations

Symbols

c	Speed of sound
d	Internal distance between the near sides of the two jet outlets for the dual-jet geometry
D	Diameter of the tandem rods
l_p	Distance from the wind tunnel nozzle exit to the centre of the primary jet outlet
P	Pitch between the two tandem rods
U_∞	Velocity of the crossflow
U_{jp}	Velocity of the primary air curtain
U_{ju}	Velocity of the upstream air curtain
w_p	Width of the primary air curtain outlet
w_u	Width of the upstream air curtain outlet

Abbreviations

Chapter 4

F	Crossflow
F-R	Crossflow+Tandem rods
F-R-AC	Crossflow+Tandem rods+Primary air curtain
F-R-AC-ACu	Crossflow+Tandem rods+Primary air curtain+Upstream air curtain
F-R-AC-ACu-1	Crossflow+Tandem rods+Primary air curtain+Upstream air curtain (configuration 1)
F-R-AC-ACu-2	Crossflow+Tandem rods+Primary air curtain+Upstream air curtain (configuration 2)
F-AC	Crossflow+Primary air curtain
F-AC-ACu-1	Crossflow+Primary air curtain+Upstream air curtain (configuration 1)
F-AC-ACu-2	Crossflow+Primary air curtain+Upstream air curtain (configuration 2)

Chapter 5

R1	Upstream recirculation structure in the Delta zone
R2	Downstream recirculation structure in the Delta zone

Chapter 6

F	Crossflow
F-R	Crossflow+Tandem rods
F-R-AC	Crossflow+Tandem rods+Primary air curtain
F-R-AC-ACu	Crossflow+Tandem rods+Primary air curtain+Upstream air curtain
F-R-PF_u	Crossflow+Tandem rods+Perforated fairing
F-R-AC-ACu-PF_u	Crossflow+Tandem rods+Primary air curtain+Upstream air curtain +Perforated fairing (Configuration 1)
F-R-AC-ACu-PF_d	Crossflow+Tandem rods+Primary air curtain+Upstream air curtain +Perforated fairing (Configuration 2)
F-AC	Crossflow+Primary air curtain
F-AC-ACu	Crossflow+Primary air curtain+Upstream air curtain
F-PF_u	Crossflow+Perforated fairing

Chapter 1

Introduction

1.1 Context and Motivation

Noise pollution has become a very serious environmental problem due to the annoyance caused by noise that results in many problems, e.g. sleep disturbance and decreased work performance. It is extremely harmful to human health because there are serious health consequences of the elevated sound level, especially the unwanted noise. In particular, the elevated noise level in the workplace can lead to hearing impairment, mental illness, hypertension and heart disease. Although some hearing loss occurs naturally with age [1], in many developed nations the cumulative impact of noise is sufficient to impair the hearing of a large fraction of the population over the course of a lifetime [2], e.g. Noise Induced Hearing Loss (NIHL) [3]. As such, like other types of pollutions, the entire world is fighting with noise. For instance, Europe Union requires the member states to determine the exposure to environmental noise by strategic noise mapping, elaborate plans etc. [4].

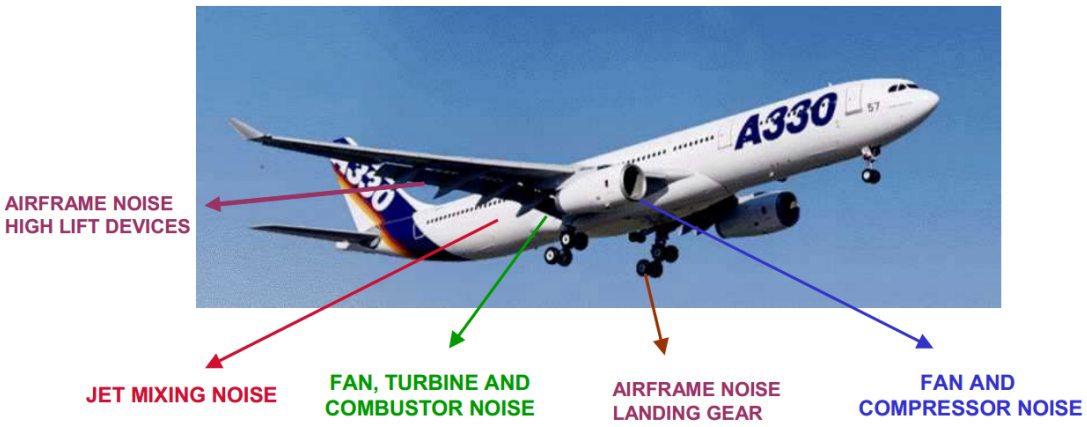

Figure 1.1: Aircraft noise sources [5]

Aircraft noise is emitted by the aircraft or its components (Figure 1.1 [5]), during a variety of flight phases, e.g. approach and take-off. It is only second to road traffic noise in the city in its unsociable levels, frequency and time of occurrence, and is often at the top of the list in rural areas [6]. Due to the dramatically increasing popularity of air travel and the rapid development of aeronautics in the past decades, aircraft noise has become not only an engineering problem but also a political and social issue [7]. Therefore, aircraft noise generation, especially at approach and take-off, is an essential consideration in the design of new commercial aircrafts [5, 8]. Most of the global leading economic

and political entities have set targets to solve this problem. For example, EU and US have put cleaner and quieter aircraft into their future aeronautical development vision. To be more specific, the ACARE (Advisory Council for Aeronautics Research) of EU manages a strategic research agenda which aims to achieve the goals fixed in the European Aeronautics [7]. In the agenda there is an ambitious and detailed goals for aircraft noise reduction. The main task is to reduce the perceived noise by 50% for 2020 compared to 2000 [7]. Figure 1.2 [5] illustrates the record of the aviation industry in reducing the aircraft noise entering service from the widespread introduction of commercial jet aircraft in the 1960s and to the year of 2020. It is observed that the aircraft noise has been continuously decreasing due to the technology development in the aviation industry. A much faster, safer, more comfortable and quieter air travel will be realised in the future.

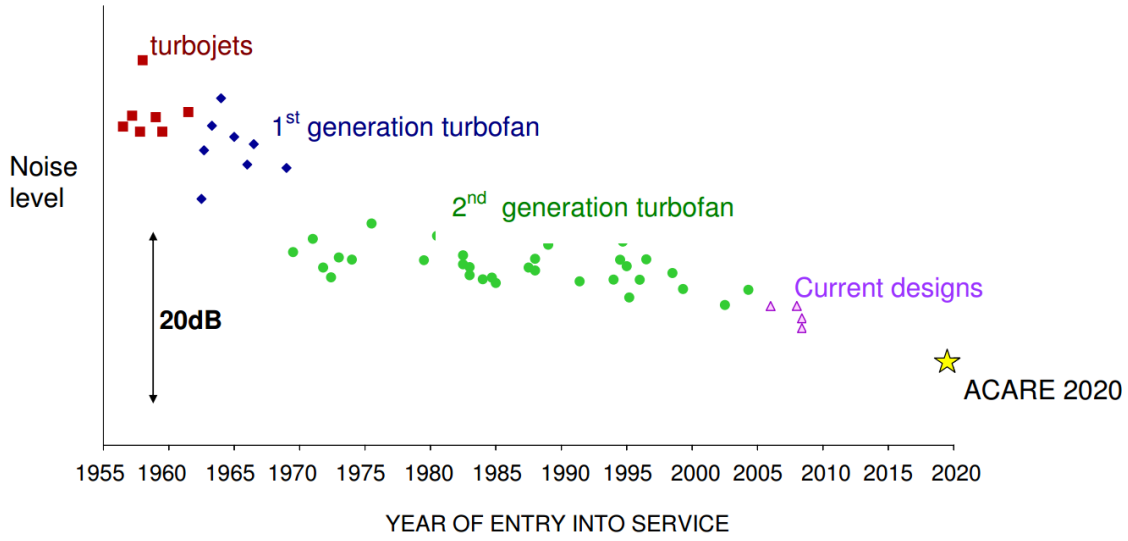

Figure 1.2: Noise level of the aircraft entering into service [5]

Generally speaking, aircraft noise sources (Figure 1.1 [5]) can be classified into two categories: engine noise and airframe noise. They both can induce negative effects on not only people inside the aircraft, such as flight crew and passengers, but also those on the ground. Due to the progress of noise isolation, confinement and reduction technologies, lower noise within the aircraft has been widely promoted. As such, impacts of the noise on those people on the ground, especially the communities near airports have become the primary concern.

Since the 1970s, the engine noise has been significantly reduced due to the application

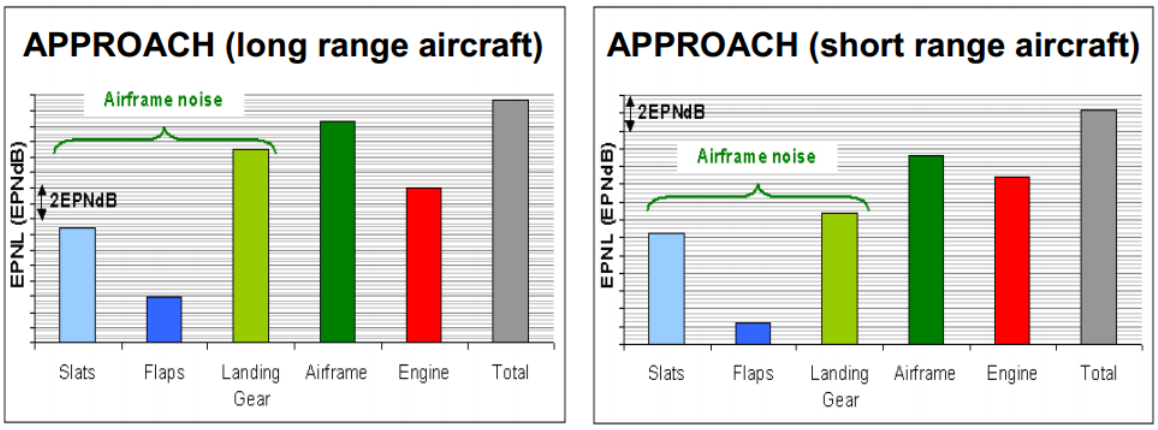

Figure 1.3: Relative approach noise source weight for short and long range Airbus aircraft (Source: airbus) [9]

of high bypass ratio configurations [10]. The bypass ratio of a turbofan engine is defined as the ratio between two mass flow rates. One is the air drawn through the fan disk that bypasses the engine core (un-combusted air); the other is the air passing through the engine core. It has been validated that the high bypass ratio turbofan can not only generate more thrust for the same amount of fuel used by the core, but is also much quieter. As such, the step change in the configuration of the engine makes airframe noise reduction increasingly pressing. Figure 1.3 [9] illustrates weight of noise sources for the long range aircraft and short range aircraft at approach. It is concluded that airframe noise is the dominant noise source compared to the engine noise.

Airframe noise is generated through the interaction of turbulent flows with solid bodies on the aircraft [11]. It was first identified as a lower "aircraft noise barrier" in the early 1970s and since 1990, airframe noise reduction has become a matter of prime interest in aeroacoustic research [9]. Fundamentally speaking, sources of the airframe noise include landing gears, slat, flap, spoilers, etc. As shown in Figure 1.3, the landing gear is found to be one of the dominant sources of airframe noise at approach.

The Landing gear has a complex structure and primarily designed to support the landing aircraft load. In order to facilitate inspection and maintenance, which are crucial to safety, aerodynamic design of the landing gear is not refined and thereby many potential noise sources are directly exposed to the airflow (Figure 1.4). Consequently, the landing gear noise is a thorny engineering issue. Difficulties in resolving landing gear noise are

summarised as follows:

- There are numerous structures and components which are not optimized in term of aeronautics and aerodynamics in the landing gear .
- Landing gear noise can contribute to approximately 30% of the overall noise emission of the aircraft at approach and take-off [12].
- The noise signature is broadband in nature covering frequencies from approximately $90Hz$ to $4kHz$ [12].
- The exposed communities suffer high annoyance associated with the noise frequency range.
- Components with non-aerodynamic shape can generate high level tonal noise as a direct noise source, which is extremely detrimental to human hearing.
- The wake can interact with other airframe components and become an indirect noise source [9].

(a) Airbus A380 nose landing gear **(b)** Boeing 747 main landing gear

Figure 1.4: Examples of nose and main landing gears

In order to reduce landing gear noise, technologies like fairings [13, 14] have been proposed, but mostly only have been tested at the laboratory level. The common fundamental idea is to cover the bluff body with other aerodynamically refined components.

Although a good noise reduction can be achieved, some other problems may be introduced, e.g. disturbance to the inspection and the maintenance. Hence, an air curtain, also referred to as a planar jet, was proposed to reduce the landing gear noise [15]. The air curtain has been applied in various engineering fields, e.g. area confinement [16], smoke confinement [17], biological safety [18], etc. Fundamentally, the concept of using the air curtain for landing gear noise reduction is to apply an upstream blowing jet to deflect the air flow that passes the landing gear and thereby the aerodynamic noise can be reduced. Figure 1.5 [15] is an example of the air curtain configuration. With shielding from the air curtain, a significant noise reduction can be expected.

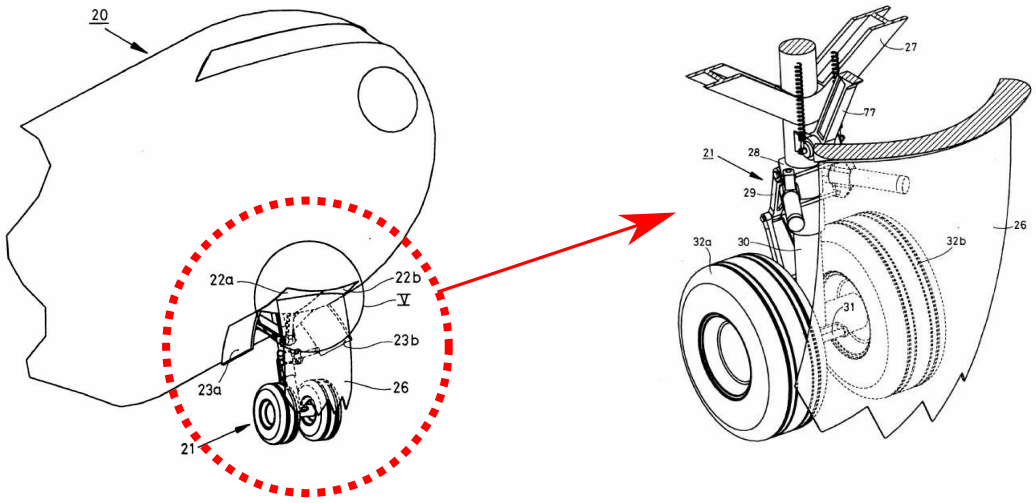

Figure 1.5: Example of the air curtain used for landing gear noise reduction [15]

Main advantages of the air curtain technology include the efficient noise reduction, facilitation of the landing gear maintenance and inspection, ease of controllability, etc. Therefore, this is a new technology with great potential but a low technology readiness level. Moreover, a very recent study [19] has found that despite substantial noise reduction, the use of air curtain can generate significant jet noise, which can impede the future implementation and must be dealt with. As such, improvements are required to minimise the jet noise emission and enhance the noise reduction achieved.

In this study, a novel dual-jet air curtain geometry is proposed and validated to attained further noise reduction for the landing gear. To be more specific, in addition to the primary jet, there is one more jet installed upstream, termed as the upstream jet. This configuration has the potential to substantially reduce landing gear noise. As such, valida-

tion of this technology was carried out in this study. Fundamental research related to the dual-jet air curtain geometry, especially in terms of fluid mechanics, has been conducted.

1.2 Scope and Objectives of the Thesis

An objective of this investigation is to provide a proof-of-concept study for dual air curtains, which is an alternative air curtain geometry to further reduce landing gear noise. In addition, this study aims to lay a good theoretical foundation for the optimization of this technology from the perspective of fluid mechanics, i.e. dual planar jets in crossflow. The possibility of combining the use of dual air curtains with other technologies is also discussed.

Firstly, the ability of the dual-jet geometry to reduce flow-induced noise is validated. In particular, the superiority of the dual-jet geometry over the single-jet geometry is confirmed. This has been conducted mainly through both aerodynamic and aeroacoustic measurements in the open-jet wind tunnel experiments.

Secondly, as a generic flow regime that dominates in the application of flow-induced noise reduction using air curtains, namely dual jets in crossflow, is studied based on PIV tests and CFD simulations.

Finally, the potential of a combined use of other technologies, e.g. the perforated fairing is discussed. The comparison between the combination and the sole use of air curtain application is performed.

1.3 Thesis Outline

Contents of this report are organized as follows:

Chapter 2 begins with the mechanisms of the landing gear noise generation. Then, technologies that can be found in the published work including journal articles and patents, which were proposed for landing gear noise reduction are reviewed. In particular, the work related to the single jet air curtain to date is described in detail. In addition, the literature on the fluid mechanics and aeroacoustics of turbulent jets is reported. The review includes the single turbulent jet and tandem jets in the quiescent flow. Moreover, effects on the jets from crossflow are also introduced through review of studies to date on

jet(s) in crossflow.

Chapter 3 describes the experimental facilities and measurement techniques utilised in the study, including the low speed open-jet wind tunnel system, the air curtain generator, the microphone array, PIV, hot-wire anemometry and flow visualization. Furthermore, summary of the algorithms used in the study of acoustics such as spectral analysis and beamforming are reported.

Chapter 4 is the core of this thesis, which mainly focuses on validation of the dual-jet geometry‘s improved performance. More specifically, a geometric optimization is carried out based on a CFD study. The test body is then situated in the optimised position. Then the acoustic performance of the dual-jet geometry is compared to the single-jet to confirm the improved performance. It is worth noting that two configurations of the dual-jet geometry were tested: the first installs an extra upstream jet without altering the primary jet; by contrast, the second reduces the primary jet speed to maintain the equivalence of the shielding height for the bluff body to the single jet.

Chapter 5 is on the flow regime of dual jets in crossflow. In this chapter, the regime is studied using both experimental and numerical approaches. Attentions are given especially on the leeward edge definition, recirculation structures and development of the dual jets in crossflow.

Chapter 6 investigates the possibility of combining the air curtain application with other landing gear technology, namely, perforated fairings. Different geometries are discussed, including the combined one with both dual air curtains and fairings. Based on the performance, the recommendation on the configuration is given.

Chapter 7 provides a summary of this thesis. In the meantime, it points out the future work that is worth pursuing.

Chapter 2

Literature Review

2.1 Landing Gear Noise Reduction Technologies

In this chapter, state of the art for landing gear noise reduction technology is reviewed. This review is based on open publications, e.g. journal articles, patents and technical reports. In particular, the study of landing gear noise reduction using an air curtain is introduced in detail.

2.1.1 Fundamentals

Landing gear is primarily designed to support the entire load of a landing aircraft. Due to requirements of safety, controllability and structure stability, the landing gear is not only mechanically complex but also geometrically intricate. As illustrated in Figure 2.1 [20], there are numerous components in the landing gear, which demonstrate the complexity of the device. Consequently, when directly exposed to a high speed flow, the landing gear can become a significant noise source in an aircraft.

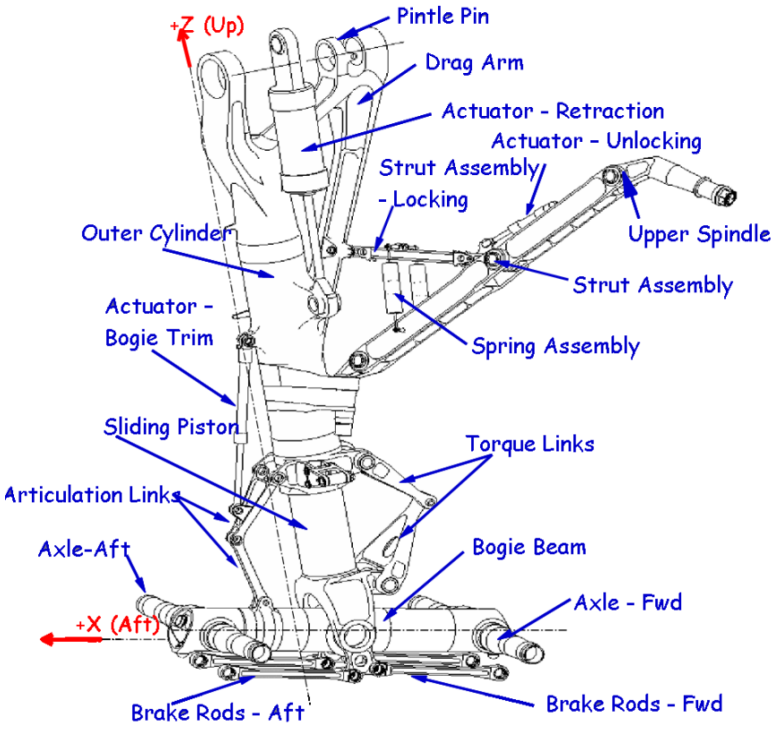

Figure 2.1: Description of landing gear components with wheels omitted (picture supplied by Airbus) [20]

Fundamentally speaking, several noise generation mechanisms coexist in the assembly.

The landing gear noise is generated by turbulence, vortex shedding, boundary layer, wake interaction with bluff bodies and resonance caused by air flow over cavities (Helmholtz resonator). Therefore, the main characters of the noise are broadband. Nevertheless, some tonal noise still exist. Being highly undesirable, tonal noise can result in serious annoyance and consequently impact the perceived noise. For example, cavity resonance is the most significant source of the tonal noise in landing gear. The vortex shedding of bluff bodies can generate tonal noise as well, which relates to the von Kármán vortex street. Note that sound generation occurs at the vortex shedding frequency, which scales on Strouhal number (St) that is given by:

$$St = \frac{fl}{v} \tag{2.1}$$

where f is the vortex shedding frequency, l is the characteristic length and v is the flow velocity. Since the Strouhal number is dependent on the Reynolds number, it is concluded that the larger the buff body is, the lower the frequency is. As such, the wheel mainly contributes to the low frequency noise and other smaller components provide the high frequency range. It is worth indicating that due to the complexity of the landing gear geometry, wake flow from upstream components in the landing gear can interact with downstream components, which may significantly contribute to the overall noise generation [21]. In terms of the overall sound level, it is found that landing gear noise generation follows a dipole behaviour, thereby the sound intensity scales with 6^{th} power of local flow velocity, which means that the overall noise can be reduced by substantially reducing the impinging flow velocity.

In addition, it is observed that directivity of the landing gear noise also introduces more complexity. With the landing gear model of Boeing 777 in the laboratory, it was found [22] that the noise generally directs forward of the aircraft and away from the door side of the gear. However, another lab test based on Airbus A340 model [23] reported that the directivity is almost omnidirectional. As such, the uncertainty of the directivity requires more considerations in the design of noise reduction technology.

In summary, due to characteristics of the landing gear noise, the noise reduction technology should be able to:

- reduce impinging flow velocity over the landing gear or component;

- suppress cavity resonance;
- shield small components;
- prevent turbulent boundary layer or wake interaction among the landing gear components.
- work for all directivity.

2.1.2 State of the Art in Landing Gear Noise Reduction

As mentioned earlier, landing gear, a main contributor to the aircraft noise emission at take-off and approach, consists of various bluff body noise emission from complex geometries. Overall level of the noise emission is dependent on specifics of the landing gear‘s actual design. In general, the landing gear noise is dominated by broadband noise, and the sound intensity increases with the 6^{th} power of the local flow speed. Prior to discussion of the technology, there are three main constraints that must be put forward [9]:

1. Operation. It is without a doubt that operation of the landing gear must not be impeded, which is the premise of all technologies. For example, gear locations, limitation of the landing gear loads, brake cooling, etc.

2. Safety. As the landing gear supports entire load of the aircraft, the safety is the top concern of the design.

3. Cost. Cost of the technology implementation can be, for example, more weight, more system complexity, increased time of maintenance and inspection.

Furthermore, some additional constraints need to be considered such as ease of implementation and effects of weather.

To date, a variety of technologies have been proposed, which are introduced in the following sections regardless of TRL (Technology Readiness Level).

2.1.2.1 Fairings

An aircraft fairing represents a noise-reducing element which has a smoother outline (solid fairings) with potentially a porous structure (perforated fairings). They are deployed to cover bluff bodies with complex geometries in the landing gear to reduce the noise.

Theoretically they can be applied to any part of the landing gear. Figure 2.2 [24, 25] shows examples of the fairing installation on the landing gear.

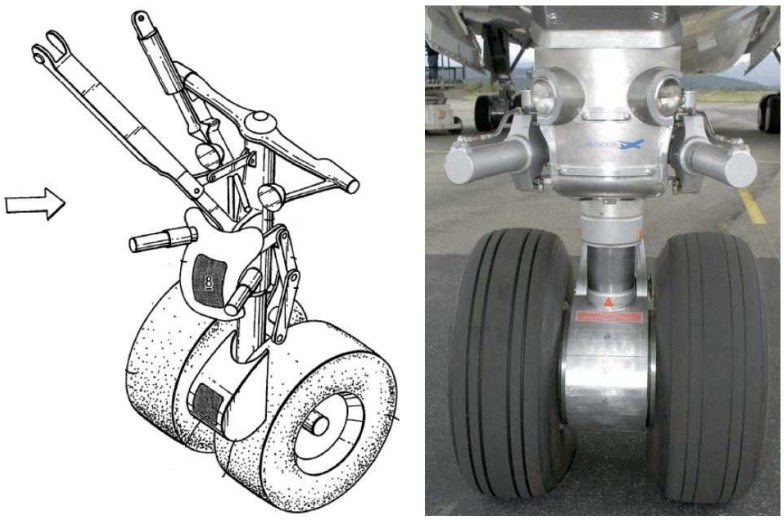

Figure 2.2: Examples of the solid landing gear fairings [24, 25]

Investigations into the use of fairings to reduce aircraft have been adopted by both independent academics and industry. The fairing has become one of the technologies with the highest TRL (technology readiness level) for the landing gear noise reduction, which is foreseen to be implemented in the near future. For example, RAIN (Reduction of Airframe and Installation Noise) is an EU project running from 1998-2002, which tested solid fairing to reduce landing gear noise. This project was carried out on a non-operable representative model with complete fairings. The results of RAIN saw a noise reduction of more than $10dB$ over a wide range of frequencies [10]. RAIN was followed by further projects in a higher TRL in EU research programme, e.g. SILENCER (Significantly Lower Community Exposure to Aircraft Noise) [10]. However, individually customized fairings covering different gear components should be adopted accounting for practical design needs [26]. For example, Dobrzynski et al.[27] achieved significant improvement by installing individual fairings on the component of the landing gear. The tests were carried out with a full scale Airbus A-340 model and results indicated that a potential noise reduction of $2dB$ to $3.5dB$ in terms of overall sound pressure level (OASPL) could be attained. Similar noise reduction achievement using such add-on fairings was also successfully obtained for Boeing 777 aircraft in both wind tunnel and flight tests [28, 29].

Nonetheless, despite significant noise reduction, two disadvantages of the solid fairings were identified [26]. One is that the solid fairings can deflect the high speed flow onto adjacent uncovered gear components. As a consequence, the noise reduction could be lost due to an undesired noise increase from other uncovered components. The other is attributed to the vortex shedding from the relatively large size of the fairing, which can generate low frequency noise.

In response to advantages of the solid fairing, the perforated fairings were proposed and expected to reduce the deflected flow speed and eliminate the vortex shedding mentioned above. As such, extensive work has been carried out on the fairing with different porosity (40-60%), and most of the studies concluded that benefits can be achieved using perforated fairings in comparison with the solid version [30, 31]. For example, Li et al. [30] investigated four different types of fairings; solid, perforated, perforated with edge brushes and slotted with cloth on a four wheel main landing gear model, shown in Figure 2.3 [30]. They found that the slotted undertray&cloth was the most effective configuration for the noise reduction because it functioned in all low, mid and high frequency ranges. The second best was perforated undertray. However, the perforation geometry requires investigation and optimisation in order to attain further reductions in the low frequency range. Moreover, the self-noise in the high frequency range that is generated from the edges may offset the benefits, which also needs suppression. Though the edge brushes covering brakes of the landing gear were shown to reduce the self-noise, this solution might cause brake cooling problems.

Boorsma et al. [31] also found that the perforation can contribute to reducing the increased low frequency noise introduced by the solid fairings in comparison with the plain landing gear configuration. Additionally, they studied the effectiveness of perforation location by covering various parts of the fairing surface respectively. It was found that the stagnation area perforations are responsible for most of the noise decrease.

However, though conclusions have been made that more noise reduction can be achieved through optimization of the peroration, little information can be found on the methodology.

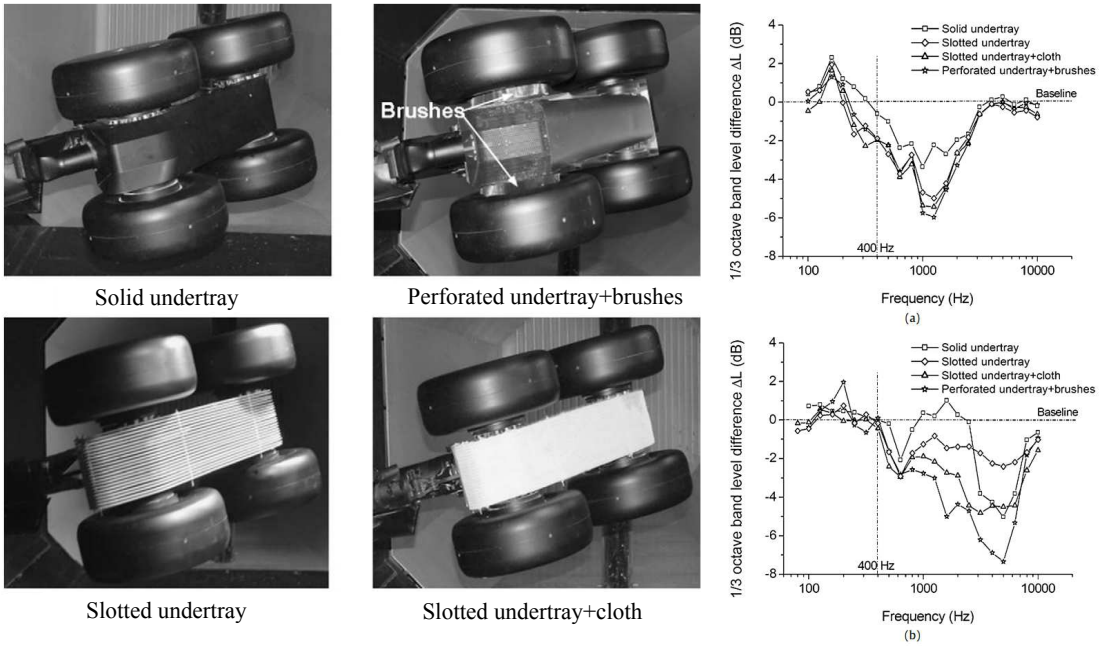

Figure 2.3: Test set-up of the add-on undertray fairings and their noise reduction performance: (a) side view; (b) ground view [30]

2.1.2.2 Wheel Hub Caps

A wheel hub cap is simply utilised to cover the wheel hub void, thereby reducing the noise caused by interaction of the air and the wheel during take-off and approach. To some extent, it can be regarded as a type of fairing. Firstly proposed in 2003 [32], the wheel hub cap can be easily implemented and has little impact on the landing gear operation. The main concern is that the design must accommodate wheel serviceability. For example, the cap should be removable to facilitate inspection and maintenance of the wheel. In addition, in some cases there is a gap between the wheel rim and tyre, which may induce cavity noise. As a solution, some sealing element can be applied, which thereby presents an intact smooth surface to the air blowing over the wheel. However, easy removal must be taken into account to avoid impeding inspection and maintenance. Figure 2.4 [33] is a schematic of the wheel hub cap.

2.1.2.3 Hole covering

Similar to the cavity noise, flow over a small hole in the landing gear can excite a resonance, shown in Figure 2.5 [9]. As mentioned earlier, landing gear structures consist of various

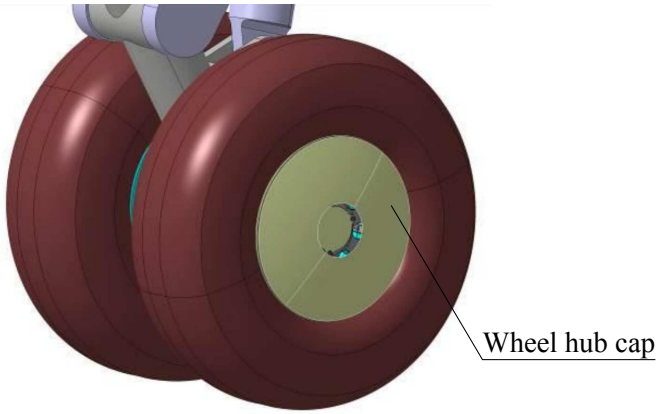

Figure 2.4: Conceptual design of the wheel hub cap of the landing gear [33]

struts and components. Consequently, there are numerous joints with hollow pins for the connection. When the flow passes these pins, resonances can be induced. Such excited resonances are characterized by distinctive tones, which are extremely annoying. Obviously, those tones can be avoided by coverings. However, it is indicated that pin-hole covers are not easy due to corrosion problems [9]. For example, water from the ambient air may be condensed in the covered pins, which can result in rust and thereby cause damage on the structure of the landing gear. It is expected that the condensation can be limited by the use of porous materials.

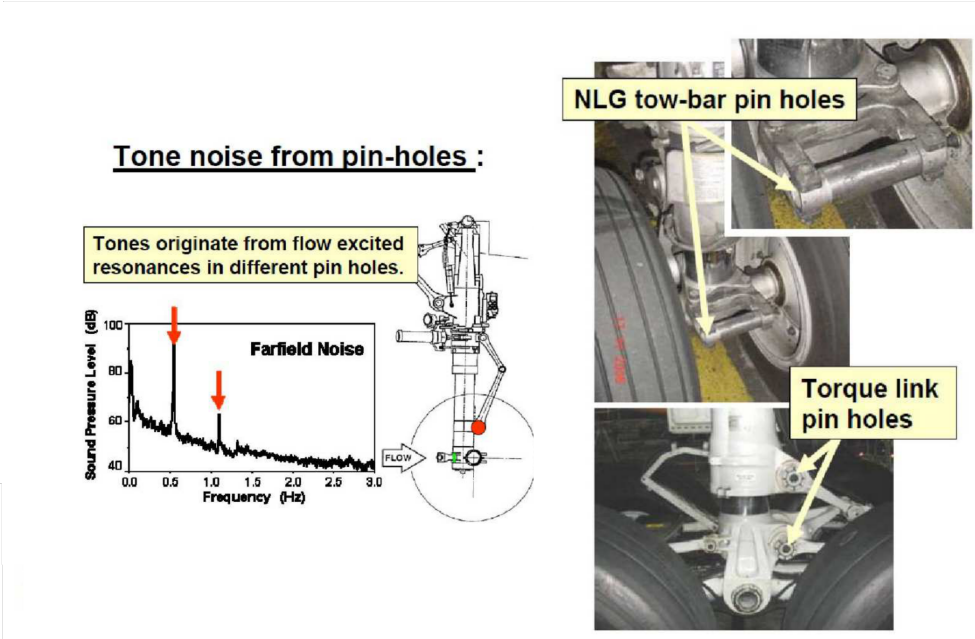

Figure 2.5: Tone noise generated from pin holes of the landing gear [9]

2.1.2.4 Mesh

In recent study, meshes have been proposed as low noise treatments of the landing gear, as it was observed that they have potential for improvement over the perforated fairings. Meshes have been tested on generic bluff bodies, where a single and combined H strut were used to represent a simplified landing gear strut [34]. A variety of mesh porosities and shapes were tested and these meshes produced significant broadband noise reduction. Figure 2.6 [34] describes the test section and various mesh shapes tested in previous studies, where noise reduction was achieved for all tested meshes and angles of attack. In particular, cylindrical meshes, which were wrapped around the struts in the tests, could provide significant noise reduction (5-10dB) in the low and intermediate frequency ranges. It was also found that this noise reduction occurred for all tested mesh porosities, and appeared to increase with the porosity. Besides, the noise reduction was also dependent on the mesh hole shape, and it was found that the lateral elliptical shape could provide best results. However, no systematic theory has been established on how to make a selection of porosity, hole shape, etc. to achieve the maximum noise reduction. As such, recently Okolo et al. [35] have developed a numerical model to predict the performance of the mesh for noise reduction of the landing gear strut, which has the potential to provide an evaluation on the mesh design. This model, as a hybrid, coupled Improved Delayed-Detached Eddy Simulation (ID-DES) with fowcs Williams-Hawkings (FWH) acoustic analogy. The model is expected to be further improved and eventually applied to the performance evaluation and porosity optimization.

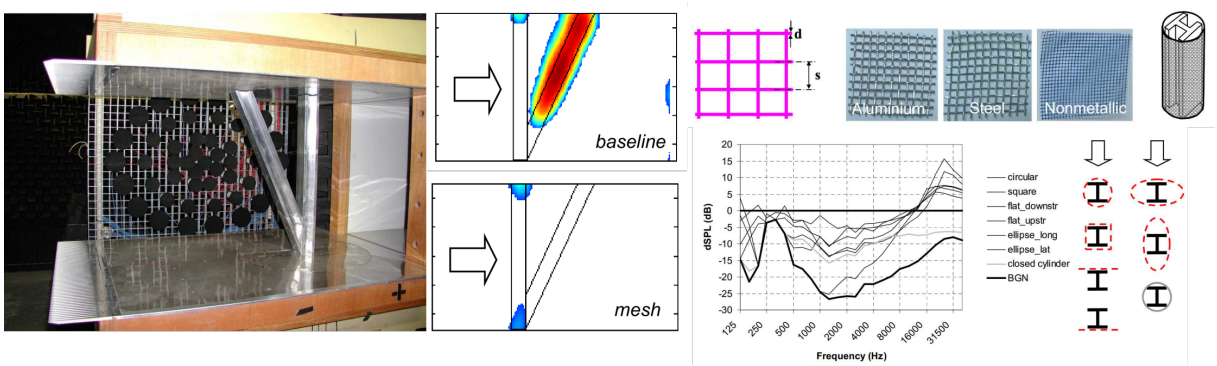

Figure 2.6: Bluff body noise reduction using mesh [34]

The reason why mesh can significantly reduce the bluff noise can possibly be: 1. mesh

can reduce the local impinging flow velocity; 2. mesh may break up the incoming flow into small vortices so that the spanwise coherent vortex shedding from the strut can be affected; 3. mesh may move the vortex shedding away from the solid strut surface, thus reducing the acoustic radiation efficiency. However, mechanisms of the noise reduction of meshes still need to be further investigated.

2.1.2.5 Plasma Actuator

A plasma actuator is a novel technology that was recently proposed for landing gear noise reduction. It operates in the atmospheric pressure air condition and holds the potential to reduce flow-induced noise through modifying the local flow field by introducing extra momentum [36]. As shown in Figure 2.7 [37], a DBD plasma actuator generally comprises two electrodes which are flush mounted on both sides of a dielectric plate [26]: one is directly exposed to the ambient air, the other is insulated by a dielectric material. A high AC voltage of a particular waveform, applied to the exposed electrode, weakly ionises the atmospheric air adjacent to the exposed electrode. The ionised air (plasma) in the presence of the electric field gradient produced by the electrodes results in a body force that acts on the external air to induce airflow (synthetic jet) along the actuator surface [26].

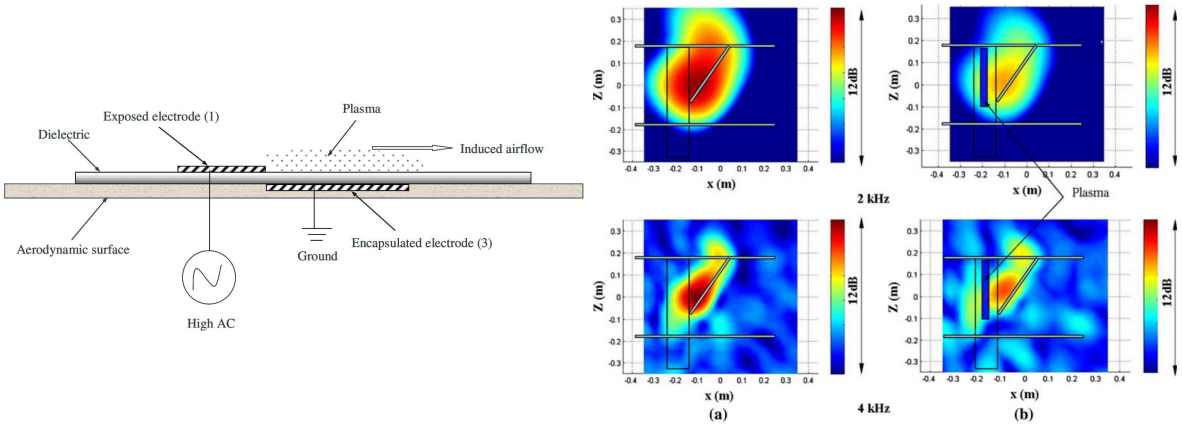

Figure 2.7: Schematic side view of the SD plasma actuators (not in scale) and the flow-induced noise reduction using SD plasma on the noise map [37]

Some studies [37, 38, 39] have demonstrated the benefit of using the dielectric barrier discharge (DBD) plasma actuators to attenuate the tonal noise of a cavity and the overall broadband noise. For example, Thomas et al. [39] used a circular cylinder to represent

the generic model of the landing gear. They found that at a Reynolds number of 3.3×10^4, using the plasma actuator, the vortex shedding was completely eliminated and the turbulence level in the wake was substantially reduced. In terms of the sound pressure level, a $13.3dB$ reduction was achieved in the near field. However, the physical principles of the plasma are still not understood adequately, not to mention the complexity of the add-ons for the plasma generation. As such, though appearing to be promising, landing gear noise reduction using plasma actuator still requires more investigations.

2.1.2.6 Blowing Flow Control

Blowing flow control was recently proposed [40, 41] to reduce interaction noise among components of the landing gear. As mentioned earlier, in the landing gear wake of the upstream components can interact with the downstream components, which can be a significant indirect noise source. In the study of Angland et al. [40], two generic bluff bodies, i.e. a cylinder and an H-beam, were utilised to represent the upstream and downstream components of the landing gear. In the meantime, distributed blowing jets through the surface of a cylinder were tested to reduce the interaction noise. More specifically, there are two configurations that were investigated, shown in Figure 2.8. One is with the cylinder upstream (OH configuration) and the other is downstream (HO configuration). The blowing flow was ejected from the inside of the cylinder to the 12 plenum chambers, which were covered by a permeable plate. The plate allows the air to pass through. Two pore diameters of the plate were taken to carry out the tests, with porosity constant at 30%. Structure of the cylinder is illustrated in Figure 2.8 [40].

In their investigations, it was observed that [40] without the use of the blowing jets the OH configuration was the noisiest. Flow measurement revealed that in OH configuration the velocity peak was generated in the shear layers at the extremity of the cylinder wake, which impinged the H-beam and produced interaction noise. When the blowing was applied, it was found that the streamwise growth of the shear layer thickness was successfully suppressed. As a consequence, a broadband noise reduction was achieved. In HO configuration, the mean flow field was characterised by the recirculation region between the two objects and the shear layer of the H-beam that is reattached on the cylinder, both of which cause interaction noise. Test results showed that the blowing flow

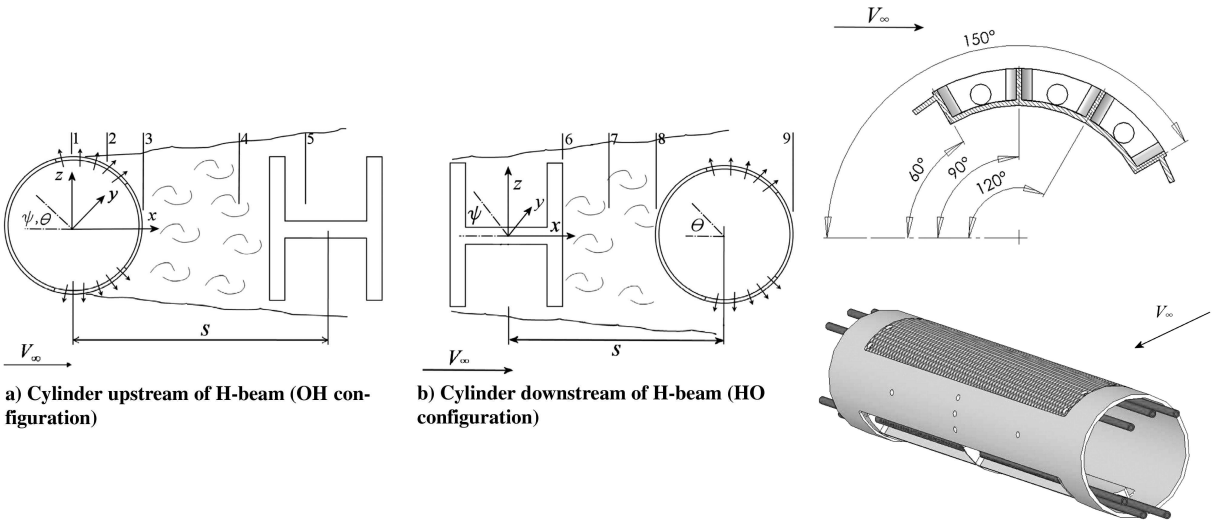

Figure 2.8: Test configurations and blowing system of the cylinder [40]

from the downstream cylinder can move the reattachment of the shear layer downstream, which widened the recirculation region between the cylinder and the H-beam and reduced the crossflow fluctuations between the two bluff bodies. Thereby the interaction noise also dropped.

Aubert et al. [41] numerically further investigate the same technology for landing gear noise reduction based on the open-source CFD sover OpenFOAM. More specifically, two geometries using cylinders were investigated, shown in Figure 2.9 [40]. The first one was only with one cylinder as the main strut, which aims at discussing the noise reduction obtained from the blowing on an isolated bluff body as well as the characteristics of the flow field. In the other geometry, one more inclined cylinder was added upstream as a drag-stay. The blowing was applied at different locations of the main strut in each geometry, i.e. $\theta = \pm 30^o, 180^o$. In addition, some other cases, with blowing only applied in the drag-stay instead but at same locations, were attempted in the dual cylinders geometry. It was observed that only blowing from the upstream drag-stay could effectively reduce both the self-noise of each cylinder and the interaction noise. By contrast, other configurations could reduce either the self-noise or the interaction noise but were found to increase the other. The mechanism of the best reduction can be explained by a stabilization of the shear layers and a reduction of the velocity fluctuations in the wake of the drag-stay [41]. However, the authors indicated that there was a limit in the study, which is that there are only a few specific values that were tested. They expected their future work to examine

a larger set of blowing parameters.

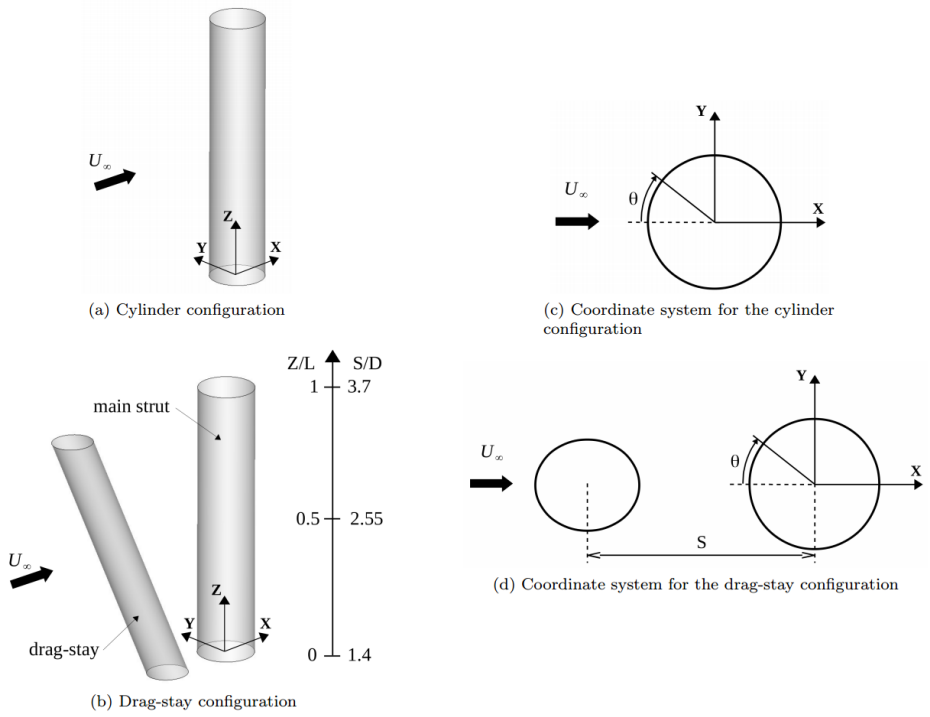

Figure 2.9: Interaction noise configurations tested and blowing system of the cylinder [40]

2.1.2.7 Discussions and Evaluations on the Landing Gear Noise Reduction Technologies

There are six technologies in total discussed above proposed for landing gear noise reduction: fairing, wheel hub caps, hole covering, mesh, plasma actuator and blowing flow control. Additionally, there are some novel conceptual proposals, e.g. boundary layer suction and vortex generator. However, since no open publications can be found, they are not introduced in details in this thesis. All technologies mentioned above have been validated to be able to effectively reduce flow-induced bluff body (or landing gear noise) to a different extent. Nonetheless, it cannot be denied that each of them does have its own drawbacks. For example: 1. impedes visual inspection and the maintenance of the landing gear (faring, wheel hub caps, mesh); 2. impedes brake cooling (faring); 3. added weight and complexity to the landing gear (fairing, wheel hub caps, hole covering, mesh, plasma actuator, blowing flow control); 4. lack of understanding of the physics (plasma actuator); 5. low technology readiness level (mesh, plasma actuator, blowing flow con-

trol). Consequently, there are two solutions to these negative effects. One is that more investigations need to be conducted to continue the existing technology improvement. The other is to develop more technologies to offer more options and comparisons for the aeronautical engineers. This study adopts the second solution and aims to develop a novel one, i.e. dual air curtains.

2.1.3 Single Air Curtain

The air curtain was proposed for landing gear noise reduction in 2004 [15] in a patent. The idea of this concept is to apply an upstream (planar) jet to deflect the incoming flow around the landing gear (component), thereby reducing the local flow speeds and the aerodynamic noise. As one alternative blowing control technology, it is, however, distinct from the one discussed in Section 2.1.2.6, which aims to use a number of small round jets ejected from one component of the landing gear to disturb interaction between the components and therefore reduce the interaction noise. The air curtain technology is installed to completely shelter the landing gear from impinging of the incoming flow, which is expected to fundamentally remove the mechanism of the noise generation. In this section research on the air curtain technology to date is reviewed and comments are also given.

2.1.3.1 Research to date

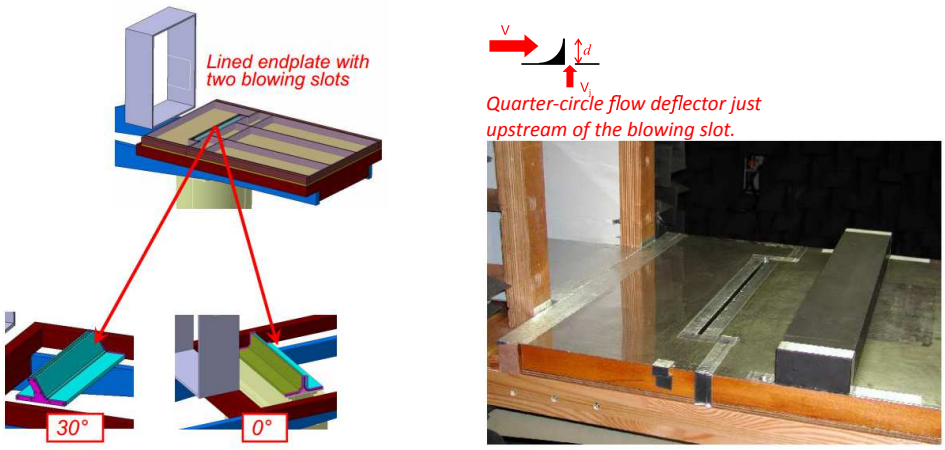

Figure 2.10: Set-up for the air curtain and bluff body in the test section of the open-jet wind tunnel [19]

To date, significant work has been carried out on landing gear noise reduction using an air curtain by Oerlemans and Bruin [19]. To be more specific, a series of experimental tests were performed in an open-jet wind tunnel in the NLR. A generic bluff body was chosen to imitate the landing gear noise source, which was mounted on an endplate attached with outlet of the wind tunnel. The position of the bluff body was optimised based on the model derived by Ramaprian and Haniu [42], which will be introduced in Section 2.2.2.1. As shown in Figure 2.10 [19], an upstream planer jet slot was situated upstream to the bluff body, which has different blowing angles. Also, one microphone array was mounted on top of the test section to perform acoustic measurement, mainly beamforming. In addition, several farfield microphones were also installed, shown in Figure 2.11 [19]. In their study blowing with different angles were tested as mentioned above, so were different blowing speeds and blowing widths. Moreover, a quarter-circle flow deflector upstream to the blowing outlet was attempted.

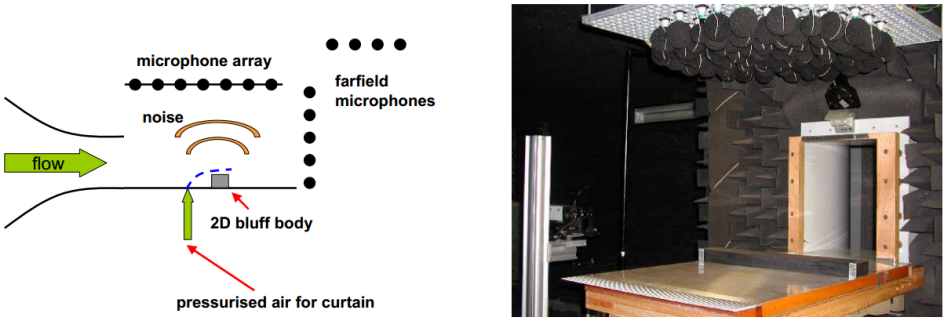

Figure 2.11: Test set-up for the study of landing gear noise reduction using singe air curtain [19]

As test results showed, for the normal blowing, when the air curtain turned on, the bluff body noise could be significantly reduced. However, the air curtain, as a planar jet, became the subsequent main noise source instead due to its self noise, namely jet noise. Meanwhile, it was also found that the jet noise increased with its speed (Figure 2.12 [19]). When the oblique blowing was applied, to achieve same shielding height a lower blowing velocity was needed. As such, slight self noise reduction could be achieved. Likewise, when the quarter-circle deflector was mounted, same shielding height could be attained by reducing the jet velocity and correspondingly more self noise reduction was acquired compared with the normal blowing. However, the jet self noise can still impede

implementation of the air curtain for landing gear noise reduction.

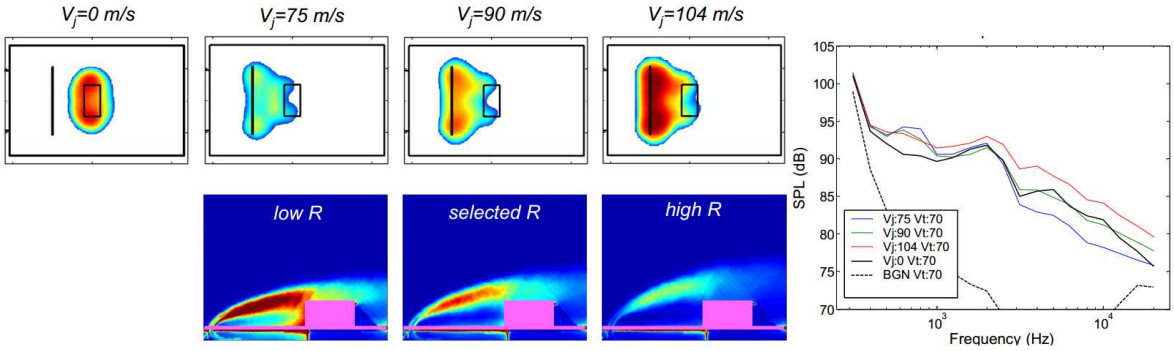

Figure 2.12: Measurement results of the noise reduction using air curtain including flow visualization, noise localization and noise spectrum [19]

Oerlemans and Bruin [19] also discussed mechanism of the air curtain noise generation based on test results for the isolated planar jet that is without crossflow. They found that for the jet with high speed, the noise level scaled with the 8^{th} power of the jet speed. This is in agreement with the literature, thereby the jet mixture is the dominated factor on the noise generation. By contrast, for those jets with a low velocity that were used for the bluff noise reduction, the noise level scaled with the 5^{th} power of the jet speed. This suggested that rather than jet mixing noise, jet nozzle edge blowing is the dominant mechanism of air curtain noise generation. Later on, this will be also discussed in the review of jet acoustics in the following section.

2.1.3.2 Discussions on the Air Curtain Technology

The air curtain has many an advantage towards other technologies. To begin with, it can be turned off before landing gear retracts on take-off with little impact on the kinematics of stowage and would also be turned off upon landing to allow for inspection and maintenance. Secondly, it could not impede free fall safety requirements and could be a very low weight solution. What is more, on approach to landing, safety regulations require aero-engines to operate at 40% thrust rather than idle as a contingency for the need of an emergency take-off. The air curtain solution would allow a much desired flow bleed for the jet outlets and in turn, it is this re-routed flow that would provide the mass flow required for the air curtain.

However, the air curtain noise from itself, i.e. the jet noise, maybe impede the final

implementation of this technology. This problem can be to some extent alleviated by modifying blowing angle of the jet or adding and deflector. Note that both approaches require simultaneously reducing the jet speed. However, an oblique blowing angle may lead to instability of the jet and what is worse, there are more risk that jet may directly blow the landing gear if the angle and speed are not carefully manipulated. As for the deflector, which is a bulging part directly exposed to the incoming flow, it may become a new bluff body to induce noise.

Discussion above necessitates new solutions to the air curtain self noise. As such, this work proposes a dual jets geometry, i.e. with an extra upstream jet that mainly possess lower velocity. More specifically, an upstream jet shelters the primary jet from the incoming flow and consequently, its interaction noise can be reduced. Also, with lower velocity, the upstream jet will generate much less noise than the primary jet. Here a hypothesis is made that total noise emission is reduced compared to the single jet configuration. Meanwhile, another configuration of the dual jets geometry is also to be validated, which has reduced velocities in both jets but the same shielding with the corresponding single jet geometry. Because the velocities of both jets are reduced, the noise emission is expected to be dramatically lower than not only the single jet application but also the original dual jets.

Because air curtains act essentially as planar jet, it is categorised as the turbulent jet. Research to date on the turbulent jet, especially when they are in a crossflow, are reviewed in the next section.

2.2 Turbulent Jet

This chapter is concerned with the incompressible turbulent jets and their characteristics in the crossflow. In particular, the focus is primarily fixed on the performance of the planar jet, referred to as the air curtain.

2.2.1 Turbulent Jet in the Quiescent Flow

In many cases of a liquid or gas, the intrusion of one fluid to another is quite common. Therefore, it is quite helpful to categorise the various type of intrusion based on momen-

tum, buoyancy, etc. (Table 2.1).

Table 2.1: Types of intrusions of a fluid into another and the corresponding terminology [43]

	Continuous Injection	Intermittent Injection
Momentum Only	Jet	Puff
Buoyancy Only	Plume	Thermal
Both Momentum and Buoyancy	Buoyant Jet or Forced Plume	Buoyant Puff

Whenever a jet enters a quiescent flow, the jet mixes violently with the ambient fluid, creating turbulence and the jet itself grows thicker. In the meantime, a shear layer is formed between the jet and ambient fluid, which is highly turbulent, and eventually merges into a complete turbulent flow. This jet is accordingly termed as the turbulent jet. In terms of exit shape, the turbulent jet can be categorised as the round jet, the planar jet, etc. In this section, the incompressible turbulent jets are discussed.

2.2.1.1 Fundamental Concepts

1. **Development of the Turbulent Jet**

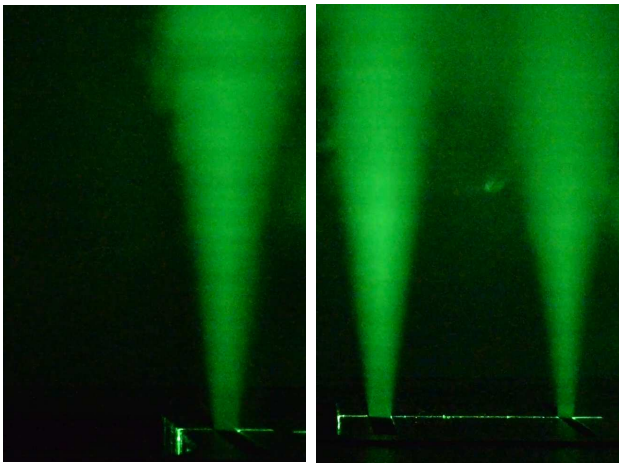

(a) Single jet **(b)** Dual jets

Figure 2.13: Flow visualization of the planar jet

Figure 2.13 is the flow visualization results of both a single planar jet and dual planar jets, attained by the author of this thesis. The acquisition of these results will be discussed later in Chapter 3. For the turbulent jet, due to the differences in velocity, outlet shape, configuration, etc., development of the jet can be substantially distinct from each other.

However, similarities have been found in the turbulent jet. More specifically, Figure 2.14 [44] illustrates a schematic of the mean flow field of a turbulent jet. Experimental observations on the mean velocity field indicate that a turbulent jet can be divided into two distinct regions, termed as the flow development region and the fully developed region. Inside the flow development region, there exists a wedge-like zone, which is termed as the potential core. In the potential core, the jet velocity remains to be constant. Note that length of the development region is as long as the potential core in the axial direction. In the fully developed region, the turbulence has penetrated to the axis. Consequently, centreline velocity has decayed and the potential core has disappeared. For instance, Figure 2.15 [45] reports a measurement of the centreline velocity decay of a round jet in the axial direction, in which those regions can be easily distinguished.

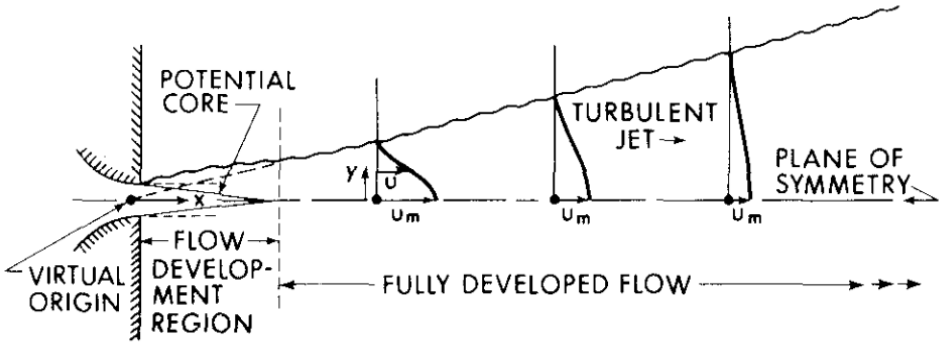

Figure 2.14: Definition sketch of plane turbulent free jets [44]

2. **Jet Half Width**

In the fully developed region, it is found that the transverse distribution (in y direction) of the mean velocity in the axial direction, is characterised with a same geometrical shape like a top hat as shown in Figure 2.16. u_m denotes the mean axial velocity, which has the maximum magnitude in a traverse distribution. As illustrated in Figure 2.16, u decreases continuously from u_m to zero, theoretically at an infinity distance to the centreline. For a round jet, velocity of the transverse distribution in the range of $x/d > 40$ can be well described by a Gaussian profile, which is written as:

$$u = u_m e^{-\frac{r^2}{b^2}} \tag{2.2}$$

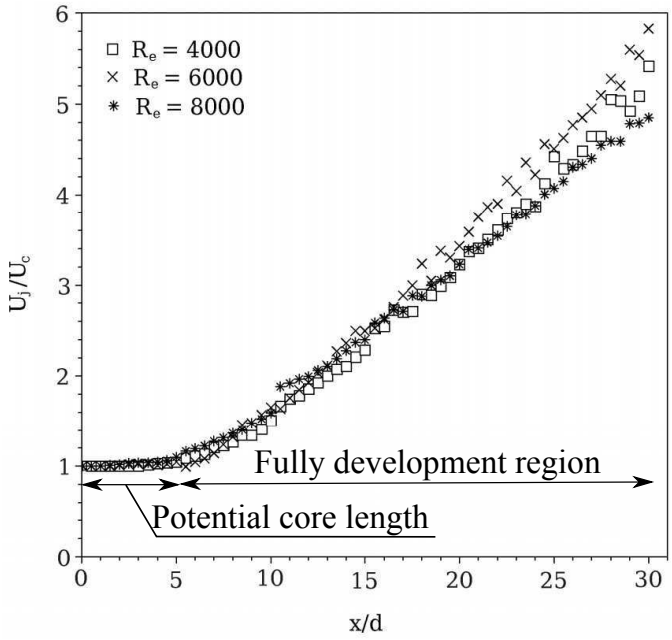

Figure 2.15: Decay of the centreline mean velocity (measured from the round jet with different Reynolds number) [45]

where r is the axial distance to the centreline and b is local jet width. Note that this width denotes the distance from the jet centreline to the edge. Therefore, it is necessary to define a length that can be used to represent the typical width of the jet. In general, the half jet width is widely used in the turbulent jet study. To be more specific, $b_{1/2}$ represents a typical length where u is equal to a half of u_m. As such, $b_{1/2}$ is termed as the half jet width and the locus of $b_{1/2}$ is defined as the half width edge of the jet.

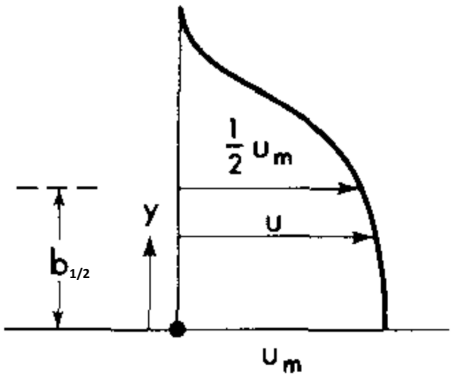

Figure 2.16: Example of the traverse distribution of the mean velocity in the fully developed region of a jet

3. **Self-Similarity**

It has been found that there exists similarity in the traverse velocity distribution at different streamwise positions, termed as self-similarity. For example, Figure 2.17 [46] shows results of the traverse velocity measurements. Raw data in Figure 2.17 (a) further describe centreline velocity decay and axisymmetry in the traverse velocity distribution. Meanwhile, if the raw data are normalised to a dimensionless form by dividing $b_{1/2}$ in X and u_m in Y, it is shown in Figure 2.17 (b) that the velocity distribution at different x almost falls on one common curve. This similarity has been observed in a large number of turbulent jet investigations.

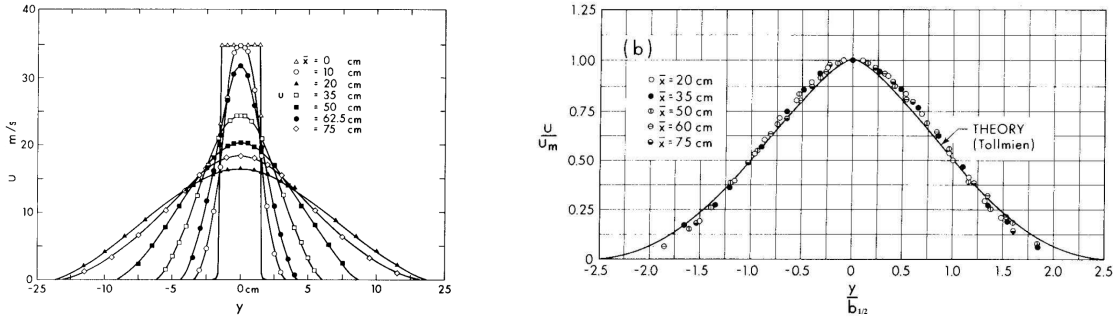

(a) Raw data **(b)** Normalization

Figure 2.17: Measurements of traverse velocity distribution for a plane turbulent free jet at different streamwise positions [46]

4. **Governing Equations**

Governing equations of the mean flow of the steady turbulent jet, e.g. the planar jet in a 2D coordinate system, are the continuity equation:

$$\frac{\partial u}{\partial x} + \frac{\partial v}{\partial y} = 0 \tag{2.3}$$

and the momentum equation:

$$\rho u\frac{\partial u}{\partial x} + \rho v\frac{\partial u}{\partial y} = -\frac{\partial p}{\partial x} - \frac{\partial \rho\overline{u'^2}}{\partial x} - \frac{\partial \rho\overline{u'v'}}{\partial y} \tag{2.4}$$

$$\rho u\frac{\partial v}{\partial x} + \rho v\frac{\partial v}{\partial y} = -\frac{\partial p}{\partial y} - \frac{\partial \rho\overline{v'^2}}{\partial y} - \frac{\partial \rho\overline{u'v'}}{\partial x} \tag{2.5}$$

5. **Entrainment**

Entrainment is the transport of fluid across an interface between two bodies of fluid by a shear induced turbulent flux [47]. Due to the shear layer, entrainment exists in the turbulent jet, which specifically means the inclusion of ambient fluid into the main jet

stream. It has been demonstrated that the entrainment greatly affects the development of a jet. For instance, a direct consequence of the entrainment is that mass flux increases with the distance from the jet exit [48].

The mechanism of the turbulent jet entrainment is very complex and it has not been completely understood. However, it has been known that the process of the entrainment occurs in three phases [49, 50, 51]. The first phase, termed as the induction phase, involves the engulfment of the ambient fluid driven by the BiotSavart-induced velocity of large vortices residing at the edge of a jet. The inducted fluid, although still irrotational, forms a part of the moving turbulent fluid [51]. In the following phase, due to the turbulent straining, the spatial scale of the inducted fluid reduces to a smaller value at which viscous diffusion dominates. At last, the inducted fluid mixes at the molecular level with the turbulent flow because of viscous diffusion.

Half a century ago, Morton et al. [52] proposed the most successful hypothesis for the entrainment, which assumes that the mean inflow velocity across a turbulent interface is proportional to some characteristic velocity at the boundary of an inflow. More superficially, if a coefficient is assumed (α), the relationship between the magnitude of the entrainment velocity (u_e) and centreline velocity can be written as [53, 54]:

$$u_e = \alpha u_m \tag{2.6}$$

Therefore, variation of the mass flux (Q) along the streamwise direction can be written as:

$$\frac{dQ}{dx} \propto u_e \tag{2.7}$$

6. **Jet Spreading**

Spreading is one of the main characteristics of a turbulent jet, which is also referred as growth of the jet. Spreading is affected by various factors such as inlet velocity profile, nozzle geometry, jet Reynolds number, fluid temperature, etc. Due to the wedge-like shape of the spreading, a virtual origin is assumed to appear behind nozzle of the jet, shown in Figure 2.18 [55].

For the 2D planar jet, it is found that half width of the jet can be written as:

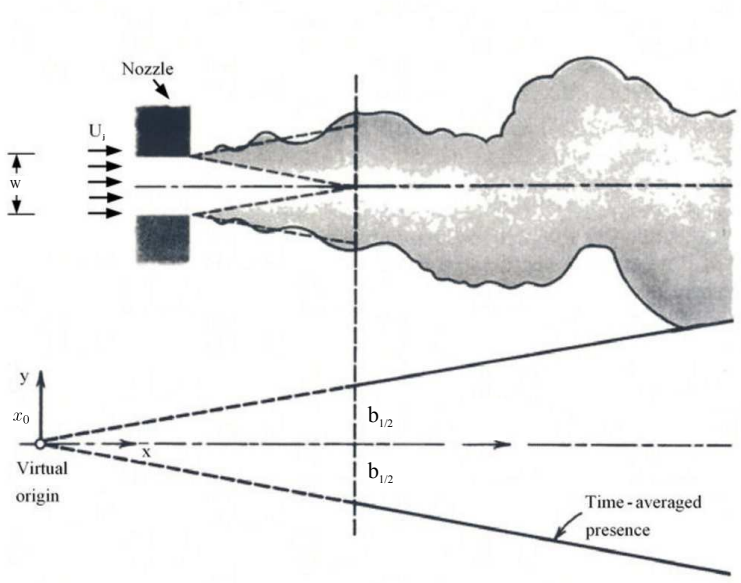

Figure 2.18: Virtual origin of the jet [55]

$$b_{1/2}(x)/w = C_1(x/w + C_2) \tag{2.8}$$

The coefficient C_1 is a measurement of the jet spreading rate [56]. C_2 is related to the virtual origin of the jet. More specifically,

$$x_0 = -C_2 w \tag{2.9}$$

On the values of C_1 and C_2, Kotsovinos reviewed investigations on the planar jet carried out in 1976, which are reported in Table 2.2. It is found that C_1 varies between 0.09 and 0.12 [56]. Moreover, the virtual origin can be either upstream to the jet exit or downstream.

2.2.1.2 Tandem Jets

Tandem jets play an important role in the engineering applications, e.g. air-conditioning vents and diffusers at waste water treatment plants. Also, as an interesting flow regime, tandem jets have been widely investigated through experiments and CFD simulations. Early studies [66, 67, 68, 69] have demonstrated that the flow field is quite different from a single jet due to the interaction between two jets. In particular, jets are injected separately from orifices and their trajectory will deviate from straight lines on account of

Table 2.2: Jet spreading coefficients measured by the year of 1976

Experiments	AR	x_{min}/w	x_{max}/w	Re ($\times 10^{-3}$)	C_1	C_2
Albertson et al. [57] (1950)	720-5760	24	2300	10	0.128	/
Flora&Goldschmidt [58] (1969)	50	/	90	20	0.11	/
Förthmann [46] (1934)	21	0	25	70	0.096	0.6
Goldschmidt & Eskinazi [59] (1966)	16	15	67	16	0.099	-0.066
Heskestad [60] (1965)	120	47	155	35	0.11	-4.2
Jenkins & Goldschmidt [61] (1973)	24	30	60	14	0.088	4.5
Kotsovinos	54	20	94	2	0.109	-2.5
[62] (1975)	13	14	37	2	0.087	6.5
Mih & Hoopes [63] (1972)	59	/	300	20	0.117	/
Miller & Comings [64] (1957)	40	0	40	20	0.096	1.6
Nakaguchi [65] (1961)	133	/	100	10	0.106	0.3

Note: AR is the aspect ratio, i.e. spanwise length divided by w. x_{min} and x_{max} are the closest and farthest distance of the measurement to the jet exit

mutual entrainment of the ambient fluid. As a result, two jets will merge and eventually combine if the initial space between those two jet orifices is close. For example, Figure 2.13.(b) shows the flow pattern of dual planar jets through flow visualization.

Likewise, along the streamwise direction, the flow field of tandem jets can be subdivided into three regions [67]: the converging region, the merging region and the combined region. Figure 2.19 [70] illustrates the flow field of two parallel planar jets ejected into a quiescent environment. The converging region extends from the nozzle exit to the point where the inside shear layers of the jets merges, denoted as point *mp*. The merging of the jets is due to the asymmetric nature of the entrainment rates, which results in a region of sub-atmospheric pressure between the jets [70]. In the converging region, strong circulation can be induced between the two jets. Therefore, this zone is termed as the recirculation zone. If the spanwise velocity profile is extracted, reverse flow may be detected in the converging region due to the recirculation [71]. By contrast, no reverse flow can be

found in the merging region and the combined region, which are bounded by the combined point *cp*. The combined point is defined as the point with the maximum velocity along the symmetry plane. In the combined region, the velocity profile resembles a single jet. In other word, there exists self-similarity in the traversed jet profiles.

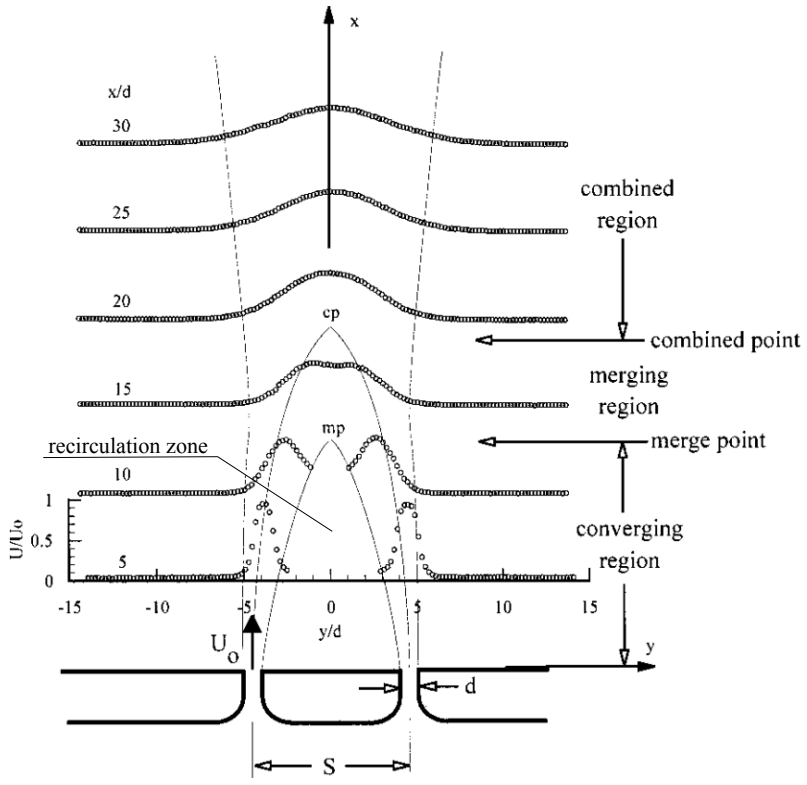

Figure 2.19: Development of dual identical jets in a quiescent flow [70]

Fujisawa et al.[71] utilised PIV to study the flow characteristics of the two parallel plane jets of different velocities. Then found that when the jet velocity ratio decreases, both trajectories move to the high velocity side and the width of the combined jet is reduced. Also, the height of the converging region decreases. Therefore, the jet velocity ratio is a key factor that affects the development of the dual jets. Investigations of Yin et al.[72] using twin circular jets mainly focus on the effects from Reynolds number on the interference between two jets, which is reflected through Reynolds shear stress and turbulent energy. Their test results concluded that the larger the Reynolds number is, the stronger the inference is. Karimpour et al.[73] numerically extended the investigation to the effects on the merging from different jet slot widths and momentum fluxes. In their

study, the concept of nozzle-separation-to-nozzle-width (ζ) was proposed, written as:

$$\zeta = \frac{Z}{\sqrt{w_1/w_2}} \tag{2.10}$$

where Z, w_1, w_2 represent the spacing of the jet axes and the width of two jets. If the merging distance (X_m) is defined as the streamwise distance from the beginning of the combined region i.e. *cp* to the jet exist. It is found that for equal jets ($w_1 = w_2$), the scaled merging distance (χ_m), which is the ratio of X_m and Z, is independent of the nozzle width provided that ζ is large enough($\zeta > 18$). This finding was also experimentally validated by Baratian et al.[74]. Moreover, Karimpour et al.[73] also observed that for unequal jets ($w_1 \neq w_2$), χ_m is relatively independent of the momentum flux ratio under the condition of $0.2 < M_1/M_2 < 0.9$. However, the role of ζ in the dual jets still needs to be confirmed.

2.2.1.3 Acoustics of the Low Speed Turbulent Jet

The noise of the turbulent jet is a very broad research topic, which involves noise generation, propagation, reduction, etc. As such, the research area can be subdivided into, in terms of the jet velocity, subsonic jet noise, transonic jet noise, supersonic jet noise and hypersonic jet noise. Also, in terms of the jet exit shape, there are subdivisions such as the round jet noise, planar jet noise with high aspect ratio or low aspect ratio, etc. There are distinctions in the mechanism of the noise generation among those subdivisions.

Research on the jet noise commenced in the year of 1952 because it was this year when the first one of the two epoch-making papers by Sir James Lighthill was published [75, 76]. Generally, these two papers have been regarded as marking not only the beginning of jet noise research but also the birth of the discipline "Aeroacoustics" [77]. In those papers, Lighthill established the renowned Acoustic Analogy Theory, which helps to identify sources of the aeroacoustic noise. The fundamental idea of the theory is to transform the compressible equation of motion into a form that can represent acoustic wave propagation. Therefore, the equation is given as:

$$\frac{\partial^2 \rho}{\partial t^2} - c^2 \bigtriangledown^2 \rho = \frac{\partial^2 T_{ij}}{\partial x_i \partial x_j} \tag{2.11}$$

where T_{ij} is the Lighthill stress tensor and it can be written as:

$$T_{ij} = \rho v_i v_j + (p - \rho c^2)\delta_{ij} \tag{2.12}$$

p and τ_{ij} are the fluctuating pressure and viscous stresses. δ_{ij} is the Kronecker delta. Within the framework of the Acoustic Analogy Theory, the left side of Equation 2.11 is regarded as the acoustic wave propagation and the right side is the sources that generate the sound field. In addition, the source terms involve second spatial derivatives and they are referred as quadrupoles [77]. Also, he suggested that the quadrupoles are related to particular eddies that are inside turbulence. One important result that is from the Acoustic Analogy Theory is the 8^{th} Power Law [78] for the jet noise. More specifically, Lighthill established that the sound intensity radiated by a jet (I_j) scales with 8^{th} power of the jet velocity, i.e. $I_j \sim U_j^8$.

Later on, effects of other factors on the jet noise were extensively investigated, e.g. temperature and enthalpy fluctuations. For example, it is found that the turbulent velocity fluctuations are correlated to the temperature fluctuations [79]. As such, an assumption was made that the dipole source is dominant instead of the quadrupole in a heated jet, which is in effect related to the enthalpy ratio. Experimental data [80, 81, 82] supported this view and a source term U_j^6 was added. Furthermore, Fisher et al. [83] assumed that the Reynolds stress term and the entropy are independent and uncorrelated. As a result, the term U_j^4 appears as a monopole. Therefore, a general form of the sound jet intensity can be written as:

$$I_j \sim AU_j^8 + BU_j^6 + CU_j^4 \tag{2.13}$$

where A, B and C are complex functions depending on the flow conditions. In particular, on the planar jet, Munro and Ahuja [84, 85] tested the jets with an aspect ratio between 100 and 3,000 (12 cases). Measurements were conducted at different observation angles θ with an equal distance r. They found that the sound intensity scaling can be expressed as:

$$I_j \sim \frac{\rho_m^2 U_j^8 L_{eq}^2}{\rho_0 c^5 r^2}(1 - M_c cos\theta)^{-5} \tag{2.14}$$

where ρ_m is the density of the mixing region and ρ_0 is the ambient mean density. L_{eq} is an equivalent length scale, M_c is the convective Mach number. The equivalent length scale is written as:

$$L_{eq} = w^{\frac{3}{4}} l_{span}^{\frac{1}{4}} \tag{2.15}$$

w and l_{span} are the streamwise width and spanwise length of the jet outlet.

To identify noise sources is a core research area related to a turbulent jet noise. However, there is no clear answer to this apparently simple question, despite fifty years of research [86]. Obviously, the mechanisms of the jet noise generation are highly correlated to the turbulence structure. It is observed [87, 88] that turbulence inside the jet and the free shear layer consists of both large turbulence structures and fine-scale structures. The large turbulence structures are somewhat more deterministic than the fine-scale turbulence motion. They dominate dynamics and overall mixing processes of the jet and free shear layers [77]. Besides, it is found that the turbulent structures are not completely random but more coherent and orderly [89, 90]. More importantly, those coherent structures were recognised as being involved in the jet noise generation since the early 1970s [86]. After a few years, it became clear that the large turbulence structures are an important direct noise source of the supersonic jet [77]. By contrast, they are not as same important as in the subsonic jets [77]. To be more specific, early measurements on the low speed data implied that there is an additional important noise source because the noise emission does not follow the U_j^8 law [91]. Several investigations suggested that the additional noise source, also the main noise source, may be the turbulent air stream passing the exit lip of the jet nozzle (classic lip noise) [91, 92, 93], i.e., more general, the noise of the jet nozzle edge blowing. Moreover, it has been indicated that the classic lip noise follows a U_j^5 law [93]. It is worth noting that in the air curtain validation carried out by Oerlemans and Bruin [19], it was found that the noise emission of the air curtains also followed U_j^5 law. Therefore, they concluded that jet nozzle edge blowing was the main mechanism for the air curtain self-noise generation.

2.2.2 Turbulent Jet in the Crossflow

The turbulent jet injected into a crossflow, compared to the jet in a quiescent flow, is inherently a more complex regime. Due to its various engineering applications, it has been

widely investigated. In this section, characteristics of this flow regime are introduced.

2.2.2.1 Single Jet in Crossflow

1. **Overview**

In terms of one jet in the crossflow, the turbulent jet emerges from an orifice or slot in a steady stream. Shortly, the jet bends over downstream after some distance for the entrainment of ambient fluid with crossflow momentum. More specifically, Figure 2.20 is a flow visualization image of a turbulent planar jet issuing into a steady crossflow, which blows from the left side. It is clearly shown that the jet bends towards downstream and continuously spreads. The incoming crossflow decelerates and changes its direction when it approaches the windward boundary of the jet as if it was blocked by a rigid body. However, the jet and incoming crossflow interact with each other. For example, the jet entrains fluid from the crossflow and consequently gets defected. Generally, for the non-buoyant jet, the development of the jet can be subdivided into Momentum-Dominated Near Field (MDNF) and Momentum-Dominated Far3D Field (MDFF) [94]. Prior to the

Figure 2.20: Flow visualisation of a planar jet in the crossflow

discussion of these two regimes, an important concept has to be introduced, which is the momentum length scale (l_m) [44, 95, 96]. The general expression for all 3D jets is written as:

$$l_m = \frac{\sqrt{M_0}}{U_\infty} \tag{2.16}$$

where M_0 is the jet momentum flux. For a round jet, $M_0 = \pi d^2 U_j/4$. d is diameter of the jet orifice. In addition, for 2D planar jet, Haniu and Ramaprian proposed a specific expression of the momentum length scale, in which $M_0 = wU_j^2$. The expression is written as [42]:

$$l_m = \frac{M_0}{U_\infty^2} = wK^2 \tag{2.17}$$

where K is the velocity ratio that is equal to U_j/U_∞. To describe these two fields, a 2D Cartesian coordinate system is established and will be used in the remainder of this thesis. As schematically shown in Figure 2.21, the crossflow blows from the left to the right. The origin of the system coincides with the centre of the primary jet outlet, regardless of the single jet or the dual jets geometries. The X axis is streamwise, pointing downstream, and the Y axis is vertical and points to the top. Therefore, in Figure 2.21 when $y << l_m$, the jet-induced momentum is significantly larger than the crossflow, therefore the jet is only slightly affected by the ambient and accordingly the jet entrainment is similar to a jet in the stagnant fluid with a slight deflection. When $y >> l_m$, the jet is significantly bent over, and the jet behaviour is analogous to an advected line puff [97]. These two regimes are respectively termed as MDNF and MDFF. As shown in Figure 2.20, MDNF is obvious because the deflection near the jet slot is slight until MDFF is approached.

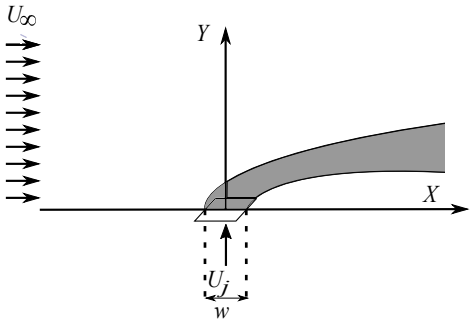

Figure 2.21: 2D Cartesian coordinate system established for the jet in crossflow

2. **Jet Trajectory and Edges**

The mean jet trajectory describes the extent to which the jet penetrates into the crossflow [98]. To date, there are different ways of jet trajectory definition. Prior to the introduction of these definitions, the natural system that is conventionally used is established. As shown in Figure 2.22 (a), this natural system is for a round jet, which possess 3 axes, i.e. α, β and γ. α is the trajectory of the jet, also termed as the centreline.

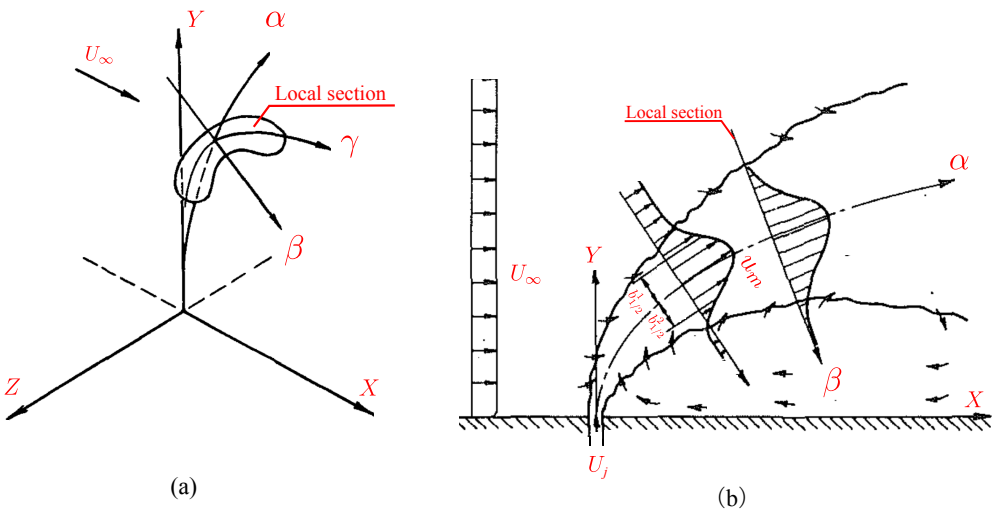

Figure 2.22: Natural system for the jet: (a) 3D round jet (b) 2D planar jet

When α is found, in an arbitrary normal plane of α, termed as local section hereinafter, β is the locus of those points with maximum velocity in their own planes that are parallel to the plane $X-Y$. γ axis is perpendicular to α and β. In 2D system, the natural system is also established without γ, shown in Figure 2.22 (b).

Therefore, it is concluded that α is the core of the natural system because the other two axises are based on α. In general, the jet trajectory (α) can be defined as the locus of the velocity maxima, scalar concentration maxima or vorticity maxima in local sections. Otherwise, the time-averaged streamline that originates from the centre of the jet exit can be used as the trajectory [98]. As such, different definitions can yield different trajectories. For example, the trajectory based on the maximum local velocity penetrates 5-10% deeper ($+Y$) into the crossflow than the corresponding scalar concentration trajectory [42, 99, 100]. Despite distinctions in these definitions, the round jet trajectory is found to scale with K and d, i.e.[98]:

$$\frac{y}{Kd} = A(\frac{x}{Kd})^B \tag{2.18}$$

where A and B are two constants. In terms of the planar jet, normally treated as a 2D jet, the study by Ramaprian and Haniu [42] provides the best model to predict the trajectory of such flows to be found in the literature to date. Applications foreseen by these authors were cooling tower plumes, smoke stack exhausts and thermal discharges into rivers,

etc. In their study, they examined two-dimensional buoyant (heated) jets issuing into a hydraulic flume perpendicular to the direction of flow. To be more specific, in the absence of significant buoyancy effects, an assumption was made that the behaviour of the jet only depends on its initial (kinematic) momentum flux and the crossflow velocity. Therefore, a dimensionless analysis of the relevant variables can be conducted, which yields:

$$\frac{y}{l_m} \propto (\frac{x}{l_m})^{1/2} \tag{2.19}$$

where l_m is the momentum length scale for the 2D jet mentioned above. Based on the experiment data, Equation 2.19 was corrected and the model is written as:

$$\frac{y}{l_m} = 1.2(\frac{x}{l_m})^{0.54} \tag{2.20}$$

As discussed earlier, the jet continuously spreads with the deflection. In order to be applied for flow-induced noise reduction, it is necessary to discuss the edge of the jet. Unlike the turbulent jet in a quiescent flow, there is no axisymmetry in the presence of crossflow momentum. In particular, for a 2D jet, the windward and the leeward edges develop separately with the spreading. Therefore, the definition of the jet edge in crossflow is distinct from the quiescent ambient. For example, in the round jet study, the edge of the jet can be defined as a curved surface. In the surface, the velocity excess that is above the undisturbed crossflow is 10% of the maximum excess in the local section. This definition was first introduced by Squire[101]. Moreover, due to the 3D characteristics of the round jet, the edge of the round jet can be subdivided into leading edge, trailing edge, etc., illustrated in Figure 2.23 [102].

For the planar jet, Ramaprian and Haniu [42] used the half jet width $b_{1/2}$ to define the edges. More specifically, as shown in Figure 2.22 (b), the edges are the locus of those points in the local sections with a velocity that is equal to half of the maximum. Here α coincides with the trajectory defined by the local velocity maxima. $b^1_{1/2}$ and $b^2_{1/2}$ represent the windward and the leeward half widths of the jet respectively. In addition, some factors that affect spreading of the jet are worth noting. In particular, the curvature of the jet trajectory produces stronger mixing in the windward edge and reduces mixing in the leeward edge, which can result in a larger growth rate in the jet windward part and a smaller one in the lower part for spreading [42]. However, the presence of the finite edge

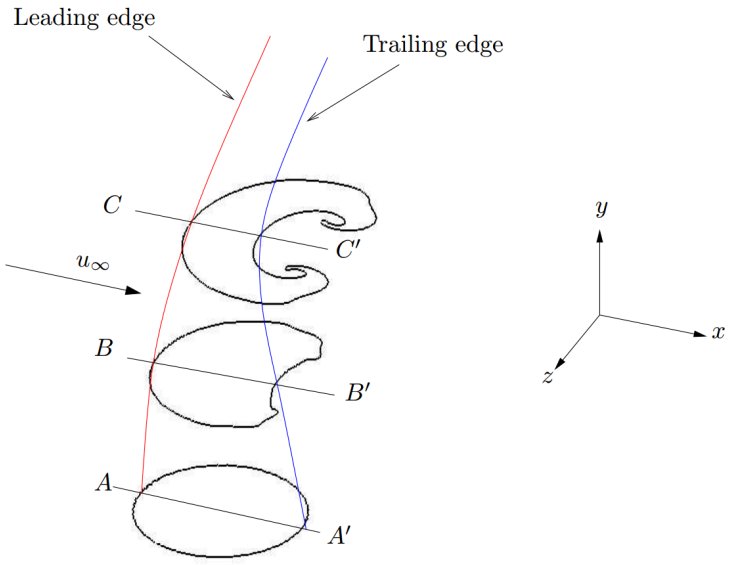

Figure 2.23: Leading edge and trailing edge of the round jet (A-A', B-B', C-C' are different local sections) [102]

velocity may counteract these trends [42]. More precisely, there is coflow on the windward part and contraflow on the leeward part. Obviously, the coflow is from the crossflow, but the contraflow is induced by the strongest recirculation below the jet, illustrated in Figure 2.22 (b).

The measurement data on the planar jet edges are described in Figure 2.24 [42] and experimental conditions are reported in Table 2.3. In addition, a straight line with a slope of 0.11, which corresponds to the same planar jet in a quiescent flow is plotted [103]. It is found that the overall spreading is slightly larger than the jet in the absence of the crossflow.

Studies discussed above have made significant achievements in the research of the jet trajectory as well as the edge. Especially the work by Ramaprian and Haniu [42], which, as mentioned earlier, obtained the best model to date for the planar jet. Furthermore, significant conclusions on the planar jet edge were drawn, which was referred to by Oerlemans and Bruin [19] to find the optimised position for the bluff body to reduce noise using an air curtain (Section 2.1.3).

3. **Entrainment and Recirculation**

As mentioned earlier, the entrainment of the ambient fluid with crossflow momentum

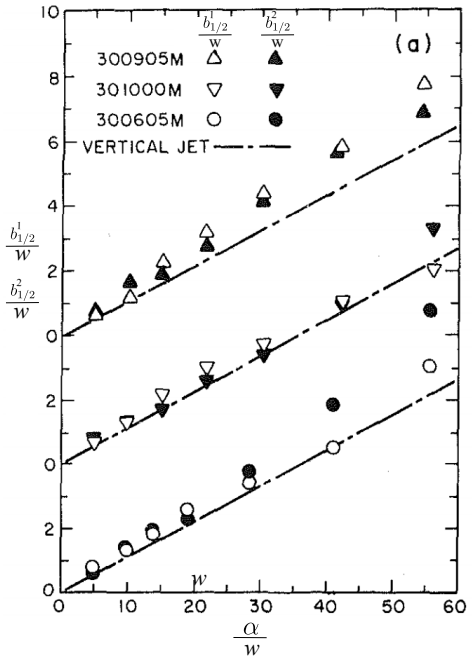

Figure 2.24: Spreading of the planar jet half width [42]

Table 2.3: Experimental conditions in the study of Ramaprian and Haniu [42]

Test No.	U_j(m/s)	U_∞(m/s)	K	w(mm)
301000M	0.3	0.03	10	5
300905M	0.3	0.03	9	5
300605M	0.3	0.05	6	5

underlies the deflection of a jet in crossflow. It has been observed that similarity exists in the entrainment mechanism with that of the vertical turbulent jet. However, when the crossflow is introduced, some unique characteristics are worth noting. To begin with, the entrainment rate can be enhanced. However, it is extremely complicated to directly measure the entrainment rate of the jet in a crossflow. This inference was achieved from the concentration decay over the jet trajectory [99].

Secondly, the intrusion of external momentum from the entrainment has been found to be the explanation to the complicated inherent structures in the jet, as schematically shown in Figure 2.25, [104]. Camussi and Stella [104] have made the best summary to date on these structures, which classify these structures into two groups. More specifically, the group one refer to those structures which are induced by the interaction among the jet, crossflow and wall. This group include Counter-Rotating Vortex Pair (CRVP), Horseshoe Vortices (HSV), Wall Vortices (WV) and Upright Vortices (UV). The group two consist

of those structures that exist in the free jet as well, but whose vorticity evolution and destabilization are influenced by the crossflow, e.g. Ring-Lie Vortices (RLV).

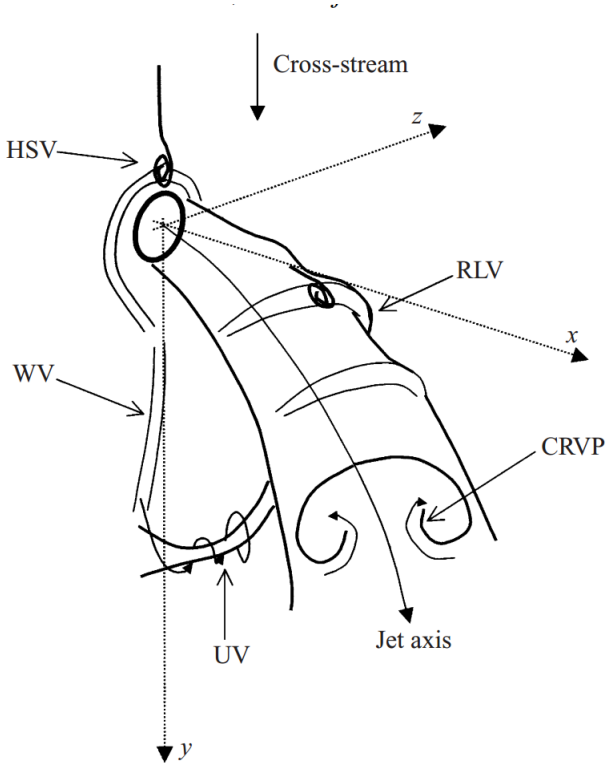

Figure 2.25: Main vortical sturctures formed in a jet in the crossflow-stream (crossflow) [104]

Moreover, the main recirculation zone below the jet is the characteristic induced by the entrainment that has a direct influence on the noise reduction. In particular, due to the shielding from the jet, ambient fluid below the jet loses its crossflow momentum. As such, it tends to be entrained into the jet more than other regions. The strong entrainment transports fluid in the upper part of the zone below the jet, which results in the pressure difference between the upper and the lower parts. As a consequence, fluid will return from the upstream to the zone in the lower part. The entire process explains the existence of the main recirculation, which can be observed in the streaklines in Figure 2.26 [105].

Discussions on the recirculation zone can be found in many studies [42, 105, 106, 107]. For example, work by Ahmed et al.[107] has performed measurements on the recirculation zone using PIV. More specifically, two tests with different momentum ratios were measured. The time-averaged results are presented in Figure 2.27 [105]. Note that the one on the top of each sub-figure is the result from the test with a smaller momentum ratio.

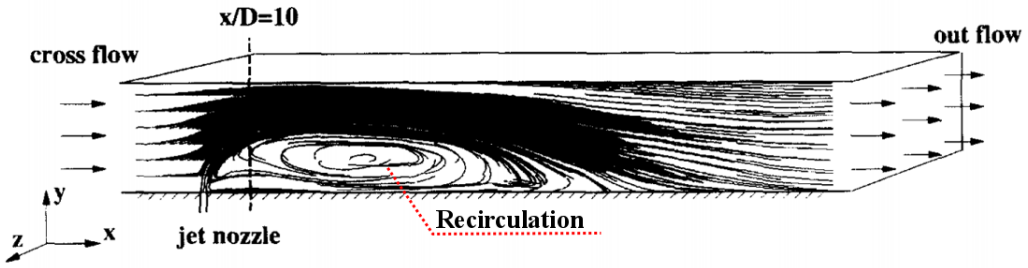

Figure 2.26: Streakline plot of the single plane jet in a crossflow [105]

Figure 2.27 (a) shows the streamlines of those cases. The streamline pattern provides an approach to defining the dimension of the recirculation zone [105]. More specifically, the height and length of the recirculation zone can be determined by the streamline that originates from the downstream edge of the jet slot. It is also worth noting that bifurcating characteristic can be found due to the presence of the flow three-dimensionality [108]. As obviously shown in Figure 2.27 (a), a higher momentum ratio can result in a larger recirculation zone. Figure 2.27 (b) is the normalized mean streamwise velocity contour. It can be observed that the jet can accelerate the streamwise motion of the crossflow over the jet for both cases and the acceleration increases with the momentum ratio. In addition, the low velocity region appears to be in the centre of the recirculation zone. Figure 2.27 (c) shows the turbulence intensity. In the case with a lower momentum ratio, the highly turbulent flow created by the jet is closer to the wall when compared to the case with higher momentum ratio. However, in the top part of the crossflow, the case with lower momentum ratio spans the turbulence much less than the case with higher momentum ratio. In terms of distribution, the normalised Reynolds stress contour in Figure 2.27 (d) is in agreement with the turbulence intensity. In particular, the high Reynolds stress region is also close to the wall in the case with lower momentum ratio. As for the magnitude, it is found that the Reynolds stress dramatically increases with the momentum ratio. In summary, the momentum ratio has a significant impact on the development of the jet in a crossflow, including the recirculation zone.

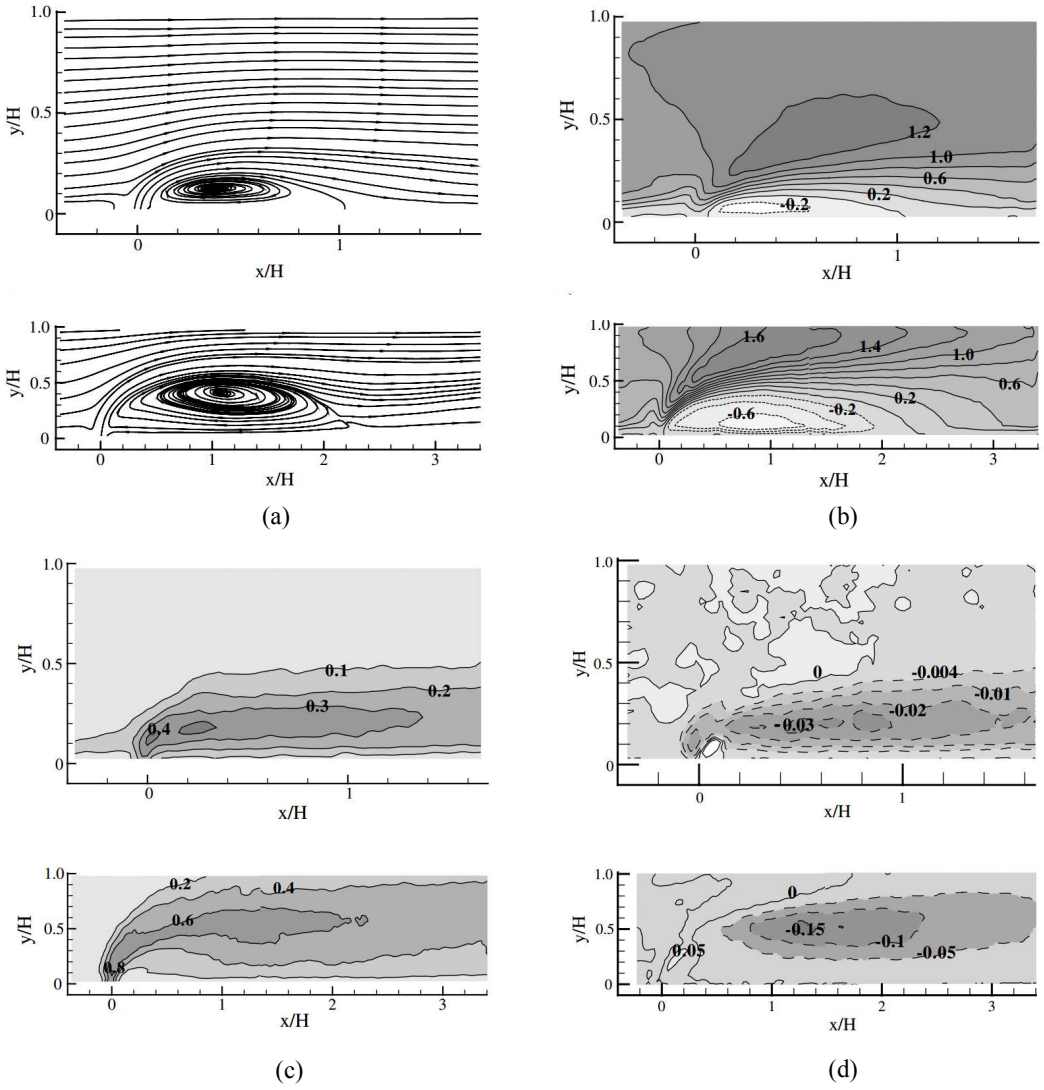

Figure 2.27: Mean patterns of the recirculation induced by the jet in a crossflow with different momentum ratios: (a). Streamlines; (b). Normalized streamwise velocity; (c). Turbulence intensity; (d). Normalised Reynolds stress [105]

2.2.2.2 Tandem Jets in Crossflow

Tandem jets in crossflow can be frequently observed in engineering applications. For example, waste water discharge and cooling jets on the turbine blades. This thesis aims to validate a proposal for the landing gear noise reduction using dual jets. Therefore, studies on the tandem jets in crossflow to date that were found in the literature are reviewed.

Tandem jets in a quiescent flow has been discussed in Section 2.2.1.2. When an ambient crossflow is introduced, the flow field of tandem jets will become more complicated. In

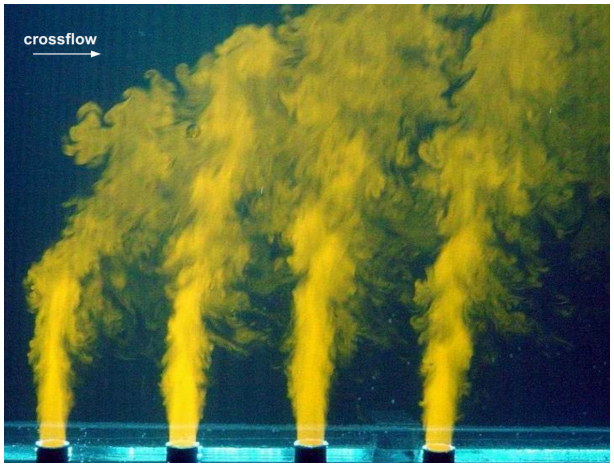

Figure 2.28: Tandem jets in crossflow [109]

particular, the merging and combination of these two jets still occur like in a quiescent flow. Furthermore, unique characteristics also exist as a result of the interaction with the crossflow. For example, jet defection. More specifically, the leading jet, also referred to as the upstream jet, is deflected more than the downstream jets (or rear jets) [97, 109, 110], shown in Figure 2.28 [109]. This is because the leading jet shelters the rear jets so that the rear jets are discharged into an ambient with less crossflow momentum.

In the 1970s, many significant studies were carried out on tandem jets in crossflow. One of the earliest was by Schwendemann [111]. This work measured trajectories of the tandem jets with normal and inclined injections. Then the measurement was referred to by Ziegler and Wooler [112] to compare their analytical models. In their models, the leading jet is assumed to be not influenced by the presence of the rear jets until intersection occurs. By contrast, the rear jet is modified by the leading jet and behaves as an equivalent single jet injected into the crossflow with less dynamic pressure. One more study that is worth mentioning in the same decade is by Kamotani and Greber [110], who conducted investigations on twin jets with a close spacing in the crossflow. They found that the downstream jet almost remains vertical until it meets the wake of the upstream one. As introduced earlier, for the single jet in a crossflow, in the MDNF where $y/l_m << 1$, the jet almost keeps to be vertical. This concept can be also extended to the tandem jets. For example, the work by Kamotani and Greber [110] revealed that MDNF of the rear jets can be increased due to the existence of the front jet. In other word, the ambient fluid sheltered by the upstream jet possesses much less crossflow momentum.

In the following decades, more progress was achieved. Isaac and Schetz [113] conducted simulation on the tandem jets in crossflow. More specifically, their work extended the momentum integral approach that had been developed for the single jet [114] to the prediction of jet trajectories. The core of the approach is a set of coupled nonlinear ordinary differential equations, which were solved numerically based on the fourth order Runge-Kutta method. Their models also take the interaction between the two jets into account, by modifying the drag coefficient sensed by each jet. The simulation was compared with the measurements by Ziegler and Wooler [112] and the results showed good agreement with the experiment. Here it is worth noting that their simulation was only applied to predict the trajectories before the two jets intersect. In order to explain this, the subdivided regions from the dual jets in quiescent flow are brought in the study with a crossflow. More specifically, the flow field of the tandem jets can be subdivided into the converging region, merging region and combined region like in a quiescent flow, which are illustrated in Figure 2.29. I and II represent the trajectories of the front jet and the rear jet before the merging point, III is the combined trajectory. As such, the simulation by Isaac and Schetz [113] only worked on the trajectories I and II. A more careful measurement on the velocity and surface pressure was performed by Schetz et al. [115] on the dual jets in a crossflow, which concentrates on the converging region and merging region. Furthermore, a comparison between the measurement and the simulation by Isaac and Schetz [113] was also conducted in this work, which confirmed the validation of the simulation. Later on, the work by Issaac and Jakubowski [116] extended the measurement on the turbulence intensity and Reynolds shear stress.

Subsequently, due to the development of the fluid measurement technology, more and more significant studies were carried out, Ali [109] in his master project did a systematic study on the tandem jets in a crossflow. In his work, Laser-Induced Fluorescence technique (LIF) and Acoustic Doppler Velocimetry (ADV) were used to measure the flow field of interest with dyed water jets. In the dual jets geometry, he found from the LIF tests that the jet merging phenomena is mainly dependent on the spacing between the two jets as well as the length scale (l_m). Therefore, the regime can be summarised as three subdivisions: closely spaced jets, moderately spaced jets and widely spaced jets. In the closely spaced jets, 2D and 3D spacing in their tests, both jets merge inside MDNF. Then

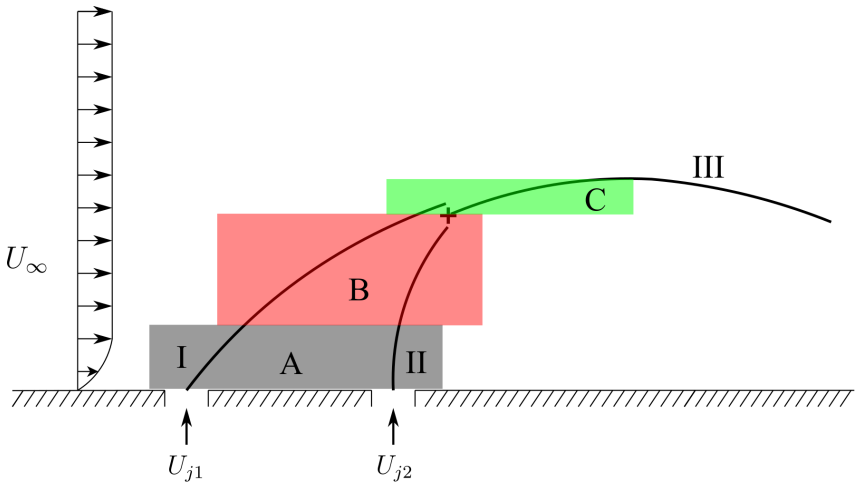

Figure 2.29: Schematic of the subdivisions in tandem jets in crossflow: A. Converging region; B. Merging region C. Combined region

the jets entrain each other with concentration gradient reducing. It has been observed that the merging in the closely spaced jets, i.e. the converging region and merging region can be compared to the jets in a quiescent flow, and the combined jet resembles a single jet with a larger width. The LIF concentration contour of the closely spaced jets is shown in Figure 2.30.(a). In the moderately spaced jets, for example, with 10D spacing shown in Figure 2.30.(b), when the merging occurs, the front jet has bent over but the rear jet still stays in the MDNF. In the widely spaced jets, when merging, both jets have gone beyond MDNF, depicted in Figure 2.30.(c). Moreover, measurements on the post-merging, i.e. combined region, were also conducted in his study. It is concluded that the LIF concentration distribution is similar to a single jet. One more interesting experimental approach in the work of Ali [109] that is worth mentioning is the individual jet isolation measurement in the tandem jets set-up, which only dyed one water jet instead of both in the LIF. This approach can respectively show the trajectory of each jet in the tandem jets set-up with a clearer view. Ali [109] compared these trajectories in the multiple jets geometries and confirmed the less deflection in the rear jets.

PIV, as a more informative fluid measurement technique, was also applied in the tandem jets in a crossflow. For example, Gutmark et al. [117] experimentally compared the dynamics of the single round jet and dual round jets in a crossflow. In the study, the single jet geometry was obtained by shutting off the orifice of the front jet in the dual jets configuration. As such, the single jet possesses same conditions with the rear

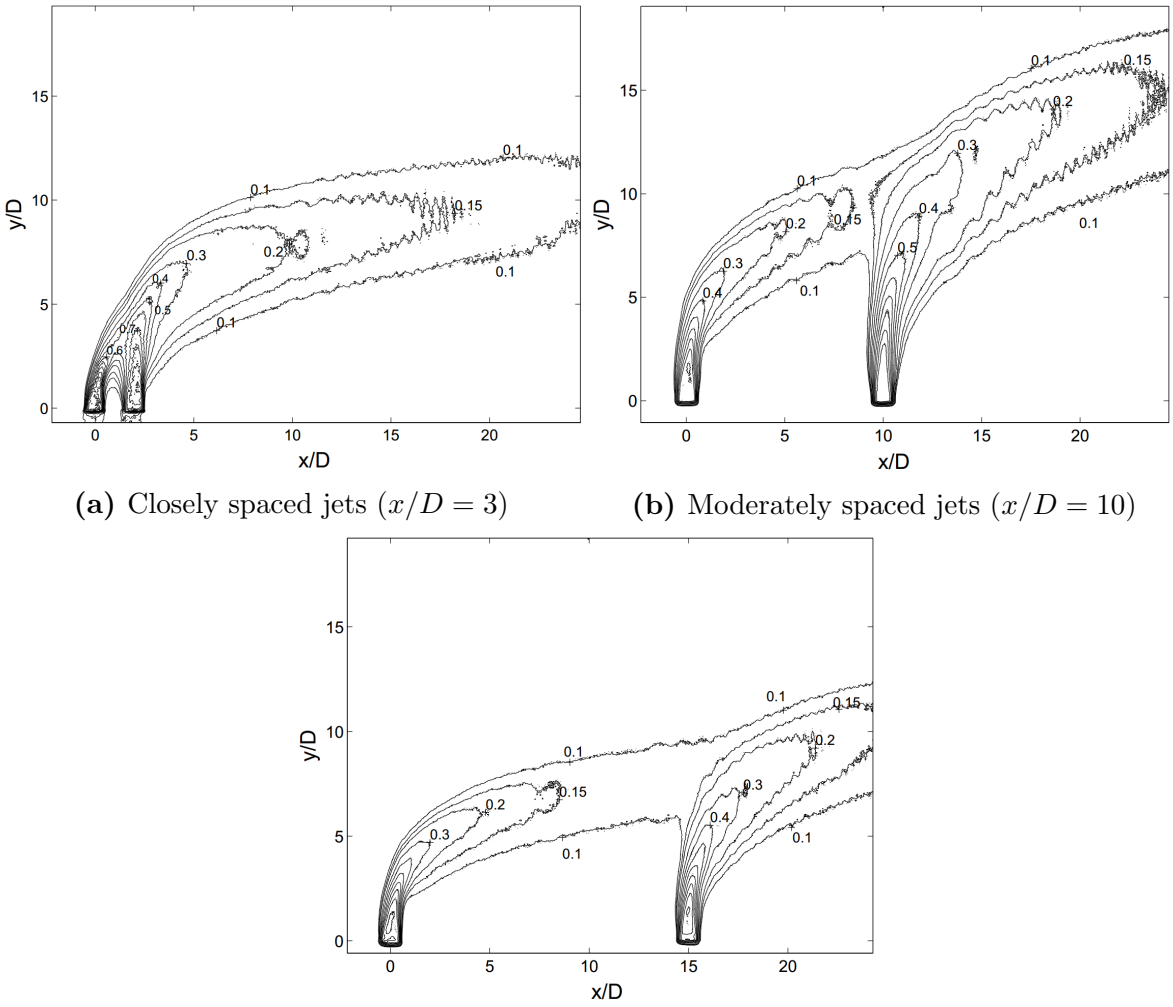

(a) Closely spaced jets ($x/D = 3$)

(b) Moderately spaced jets ($x/D = 10$)

(c) widely spaced jets ($x/D = 15$)

Figure 2.30: LIF concentration of the dual jets in the crossflow [109]

jet in the dual jets configuration. This approach helps clearly reveal the influence from the front jet on the rear one. Moreover, the streamwise velocity profile was used to locate the merging point of the two jets. To be more specific, Figure 2.31[117] illustrates the streamwise velocity profiles at different y after normalization. It is observed that there are two peaks in the orifice proximity ($y = 0.33rd, y = 0.67rd$). Obviously, they are on the trajectory of each jet. However, those two peaks decrease with y, especially the front one ($y = rd, y = 1.33rd$). This can be explained by the merging process of the two jets. When y goes higher ($y = 1.67rd, y = 2rd$), the front peak disappears and only one peak, with a much reduced height, can be observed. It is suggested that the two jets have combined into one in this area. In addition, the comparison of the turbulence kinetic energy between

the single jet and dual jets was carried out, shown in Figure 2.32[117]. It is found that the interaction between the jets affects the shear layer on both leeward and windward sides of the jets. Also, a quantitative comparison can be made through streamwise profiles, shown in Figure 2.33 [117]. More examples can be given on the studies of the tandem jets in a crossflow using PIV, e.g. work by New and Zang [118] investigated trajectory scaling of the tandem twin jets in crossflow based on PIV data. Therefore, it has been validated that PIV can be of great use for the investigation of this flow regime.

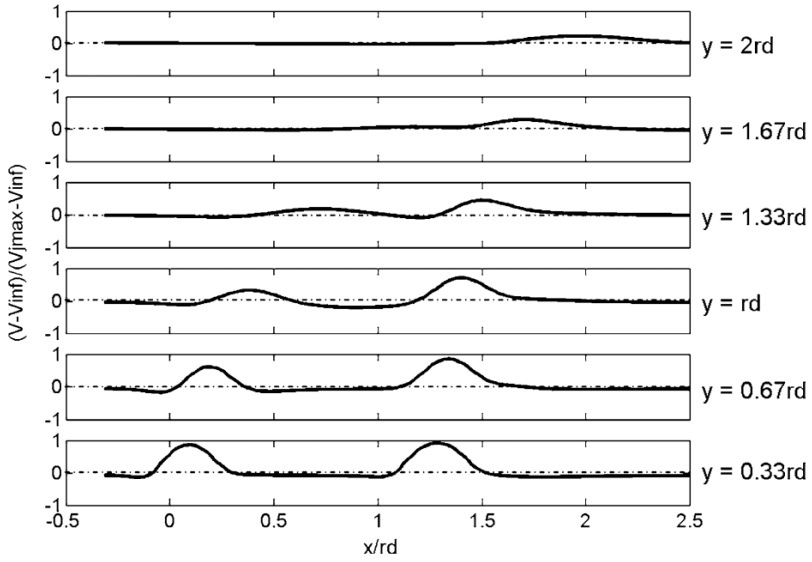

Figure 2.31: Normalised streamwise velocity profile of the dual jets at different y [117]

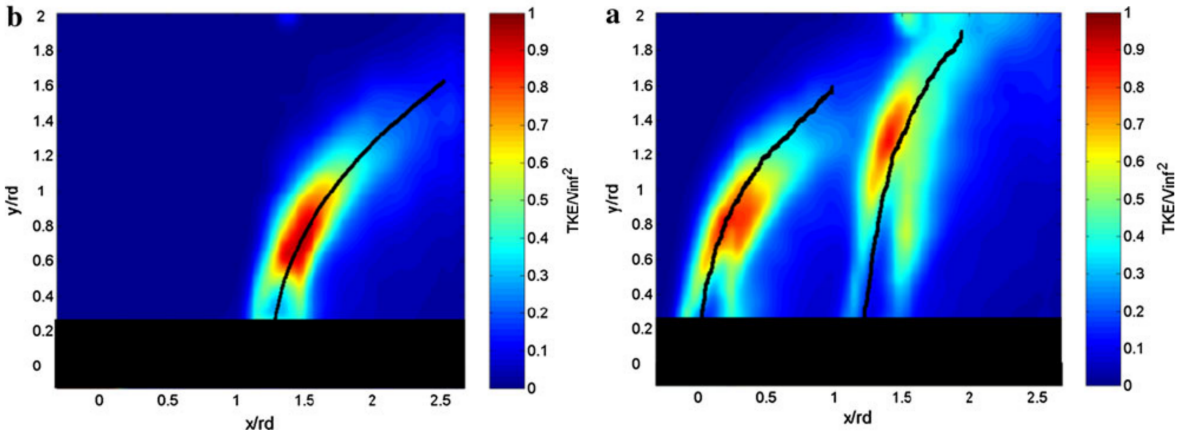

(a) Single jet **(b)** Dual jets

Figure 2.32: Turbulent kinetic energy acquired from PIV [117]

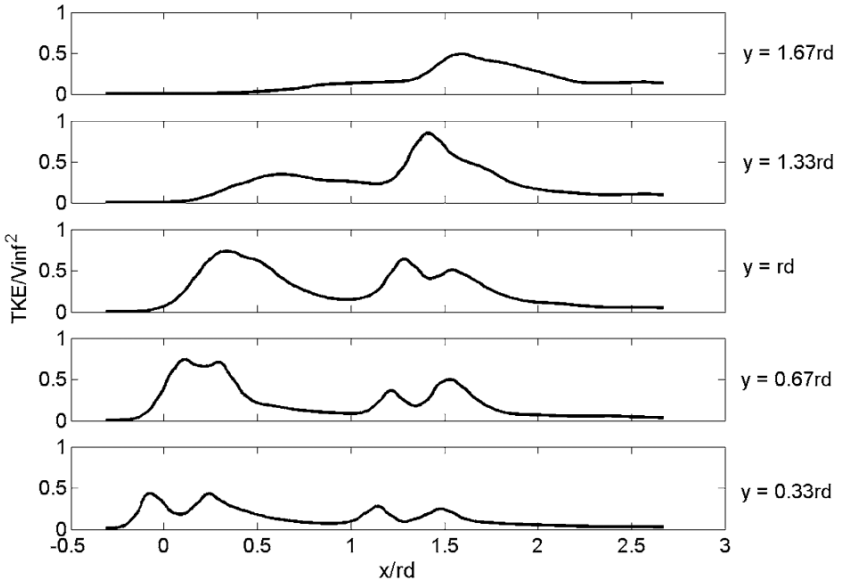

Figure 2.33: Streamwise turbulence kinetic energy of the dual jets at different y [117]

2.2.2.3 Acoustics of the Jet in Crossflow

When the jet is ejected into the crossflow, the interaction with the ambient will cause substantial effects on the jet noise. However, few investigations have been carried out on the acoustics of the jet in a crossflow. The only relating work that can be found in the literature was conducted by Oerlemans and Bruin [19] as an acoustic consideration for the air curtain used for landing gear noise reduction. To be more specific, they found that for a single jet with different speed and slot width, the noise emission increases when the crossflow is introduced and the scale of the increase is dependent on the frequency. Also, when the jet speed is fixed, an acceleration of the crossflow speed will result in more noise as well. They found that the noise increase may be partially explained by the increased slot corner noise, shown in Figure 2.34 [19]. The slot corner noise is more obvious in the low speed jet than the high speed jet, which suggests that it is related to the curvature of the deflected crossflow around the planar jet. This is because, with a larger momentum flux, the high speed jet has a less curvature than the low speed jet.

As discussed earlier, jet noise may impede implementation of the air curtain application. Therefore, the dual-jet air curtain is proposed, which will be described in detail and validated in the following chapter.

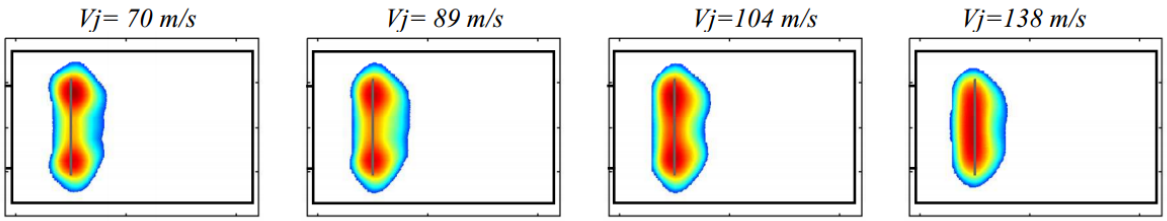

Figure 2.34: Noise map (4kHz) for the 8-mm jet in a 70m/s crossflow with different jet speeds [19]

2.2.3 Summary

In this chapter, research on the turbulent jet related to this study is reviewed, which involves both fluid mechanics and aeroacoustics. The review begins with a single jet in the quiescent flow by inducing its development, half width, self-similarity etc. Because dual jets are used in this study to reduce landing gear noise, research on the tandem jets are also summarised as well as the jet noise. Moreover, the performance of the turbulent jet in a crossflow is discussed in the second section. Likewise, the review in this section first focuses on the single jet in crossflow. Due to the interaction with the crossflow, the development of the jet is significantly different from the quiescent flow, which is reflected on the trajectory, edges, entrainment, etc. Further, when more jets are situated in the crossflow, more complexity will follow on. As such, the characteristics of the tandem jets in a crossflow are described in this section. In addition, information on the acoustics of the jet in the crossflow is also reported.

The research review in this chapter lays a theoretical foundation for the investigation in the following chapter.

2.3 Contributions of the Thesis

This thesis advances the study of an interesting flow regime in the aspect of fluid mechanics and aeroacoustics: dual planar jets in a crossflow. Also, the corresponding application applied as a technology to reduce landing gear noise is discussed. The contributions of the thesis include the following:

- Proposal and validation of the use of dual planar jets in the crossflow as a noise

reduction technology for the landing gear

- Proposal of an approach to optimise the configuration of air curtains to improve the shielding provided to a bluff body, thereby improving flow-induced noise reduction.
- Investigation into the combined use of dual air curtains and perforated fairings for the reduction of flow-induced noise.
- Proposal of a novel approach to defining the leeward edge of a planar jet in crossflow.
- Characterization of the recirculation structures for dual planar jets in the crossflow.
- Characterization of the development of dual planar jets in the crossflow.

In the following chapters, these contributions will be discussed in detail.

Chapter 3

Experimental Rig and Instrumentation

In this chapter, the experiment rig, measurement instrumentation and data process algorithms are introduced in details.

3.1 Experimental Rig

All experimental investigations in this study were carried out in the rig within Fluids, Acoustics and Vibration Lab in Trinity College Dublin. As illustrated in Figure 3.1, the experimental rig consists of a low-speed open-jet wind tunnel, a planar jet generator and a test platform. In addition, a microphone array is attached on top of the platform. More specifics will be also depicted in this section.

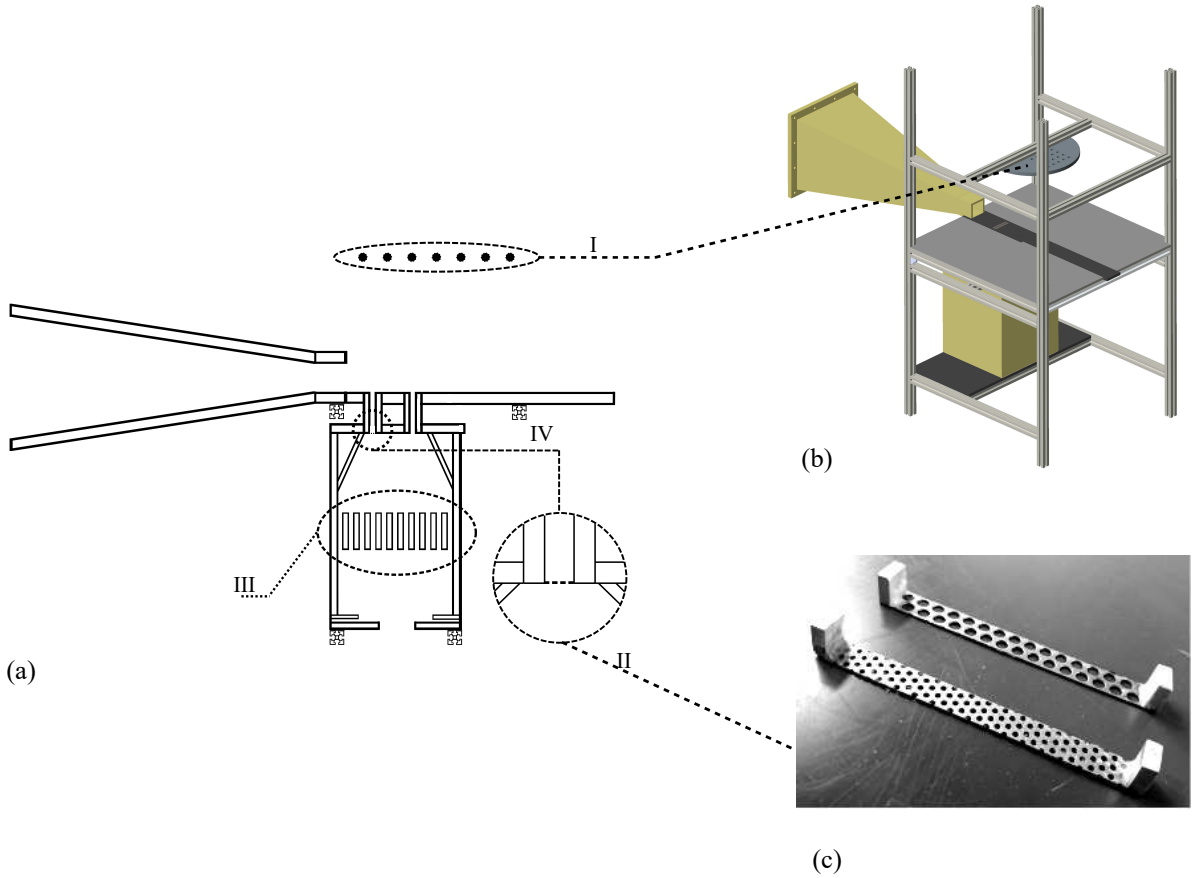

Figure 3.1: Schematic of the experimental rig (not in scale): (a) 2D View (b) 3D View (c) meshes for controlling jet speed (I. microphone array; II. jet outlet and its mesh for reducing speed; III. honeycomb structure IV. aluminium extrusion bar)

3.1.1 Low Speed Open-Jet Wind Tunnel

The open-jet wind tunnel was powered by a $5.5kW$ centrifugal blower. As illustrated in Figure 3.1, the length of the nozzle is $1000mm$ and the outlet size is $75mm \times 75mm$. Between the blower and the nozzle, a plenum is connected as shown in Figure 3.2 (a). The dimension and internal structure of the plenum are reported in Figure 3.2 (b). In order to ensure a low turbulence intensity in the crossflow and to uncouple the flow from the centrifugal blower, two layers of honeycomb screen are installed inside the plenum. The flow speed of the wind tunnel can be up to $70m/s$, and the speed can be controlled by adjusting intake area of the centrifugal blower.

(a) Cut-off

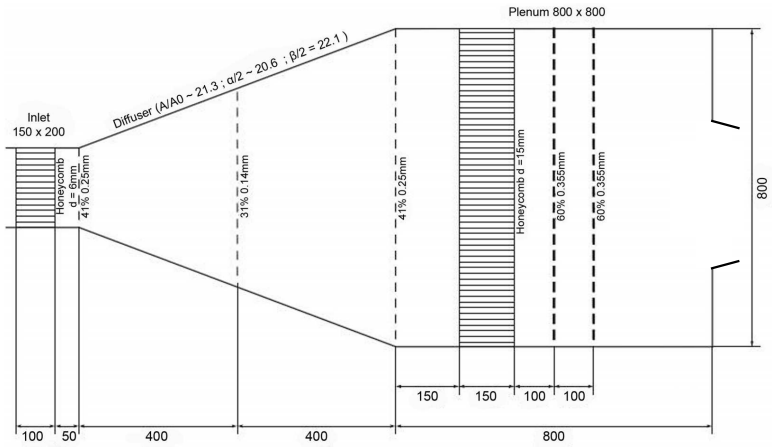

(b) Schematic

Figure 3.2: Cut away view of the plenum of the low speed wind tunnel

3.1.2 Planar Jet Generator

The planar jet generator is operated by a 2.2kW centrifugal blower, a cubic plenum and a few jet nozzles. Both 2D and 3D section views of the generator are respectively illustrated

in Figure 3.1(a) and Figure 3.3. A hole is drilled in the bottom of the plenum as the flow inlet, which is linked to the blower through a hose. The height of the plenum is $540mm$ and the size of the horizontal section is $424mm \times 424mm$. Likewise, one layer of the hexagonal grid honeycomb with $6mm$ edge length is installed inside the plenum to uncouple the flow and the blower. Moreover, baffles are added inside the plenum to reduce the recirculation. These devices can reduce the turbulence intensity of the planar jet ejected.

Since the main focus of this study is the multiple planar jets in crossflow, the required jet generator should be able to produce more than one jet with controllable speed. As such, the number of the jet nozzles in this generator is designed to be changeable for specific tests. In particular, the outlet of the jet nozzles is rectangular with a constant spanwise length of $100mm$. However, the width of the outlet can be modified as required. When there are tandem planar jets, the nozzles are managed to be parallel with each other. Furthermore, the speed of the planar jet can be manipulated mainly by adjusting the inlet area of the blower. Moreover, in the multiple jets configuration, jet speed difference can be attained by placing a mesh between the plenum and the jet nozzles as the mesh has different porosity. Examples of the mesh utilised in this study are shown in Figure 3.1 (c). As such, the required speed for each jet can be achieved after calibration.

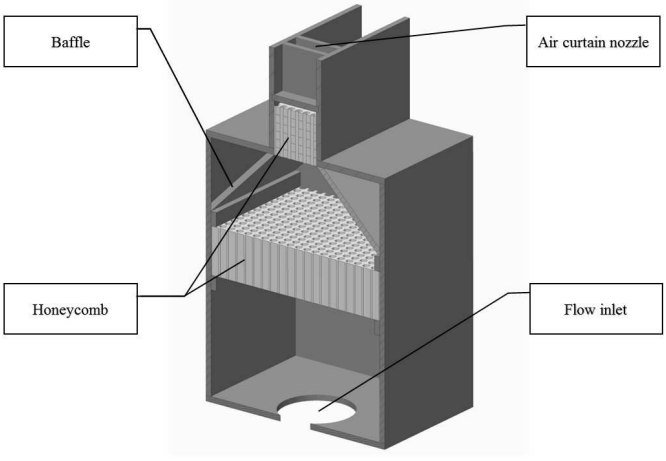

Figure 3.3: Plenum of the planar jet generator

3.1.3 Test Platform

As shown in Figure 3.1, an endplate, referred as the test platform, is attached to the wind tunnel nozzle and flush with the nozzle outlet. The test platform is assembled with three

main plates and some minor pieces, which allow the planar jet nozzle to be flush with the platform as well. Additionally, it is symmetric with respect to the centreline with a size of $1000mm \times 1000mm$. The platform enables a 3/4 open test section, on which the test object can be installed. In addition, the entire system is supported by aluminum extrusion frame.

3.2 Micromanometer

Micromanometer is a microprocessor-based precision measuring instrument for flow velocity, mass flow and pressure measurement. Due to the ease of set-up and the rapidness of measurement, it was utilised to preliminarily measure the flow velocity.

In this study, the instrument is the FCO510 Micromanometer supplied by the Furness Controls, which is shown in Figure 3.4. The specification of this instrument can be found in the manual [119]. This micromanometer is equipped with a sensitive ultra low-range differential pressure transducer, which has a resolution down to 0.001 Pa. In addition, as an instrument based on the principles of Pitot tube, this micromanometer is supplied with some necessary accessories including twin core silicon tubing and a 200mm long Pitot static probe. In the measurement of this study, the probe was installed to preliminarily measure the crossflow flow and the jet velocity.

Figure 3.4: Measurement chain of the Dantec Dynamics Hotwire System and 55P11 probe

3.3 Hot-wire Anemometry

Hot-wire Anemometry operated in the constant temperature mode was utilised to measure flow speed and turbulence level in this study. The anemometry uses a very fine alloy wire, usually tungsten alloy on the order of several micrometers, electrically heated up to some temperature above the ambient. When air flow passes the wire, it has a cooling effect due to forced convection. As the electrical resistance of most metals is dependent upon the temperature of the metal, a relationship can be established between the resistance of the wire and flow speed. In brief, the essence of this technique is the principle of forced convection and its effects on the electrical resistance of the metal wire. The advantage of the hot-wire anemometry can be summarized as high accuracy, high frequency response, high signal-to-noise ratio, flexible data process, etc [120]. Also, the hot-wire probe can be used over a very wide range of velocity measurements provided an accurate calibration is conducted.

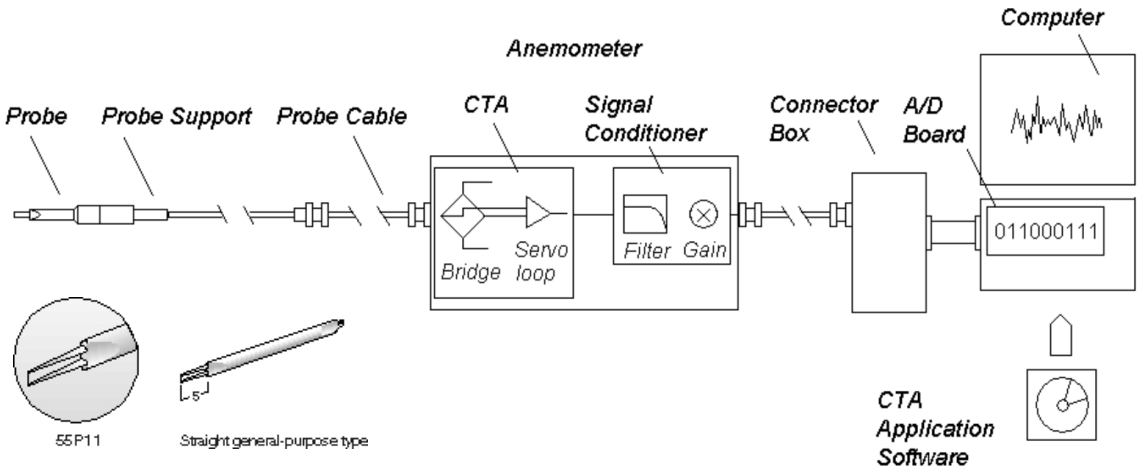

Figure 3.5: Measurement chain of the Dantec Dynamics Hotwire System and 55P11 problem [121]

In the experiment, the Dantec CTA system was utilised to do the data acquisition and the probe was Dantec 55P11. A schematic of the measurement chain and the probe is shown in Figure 3.5 [121]. The hot-wire system can work with a sampling rate up to $120kHz$. The probe allows measuring one velocity component in the 3D system. .

The accuracy of the measurement is dependent on the quality of the calibration.

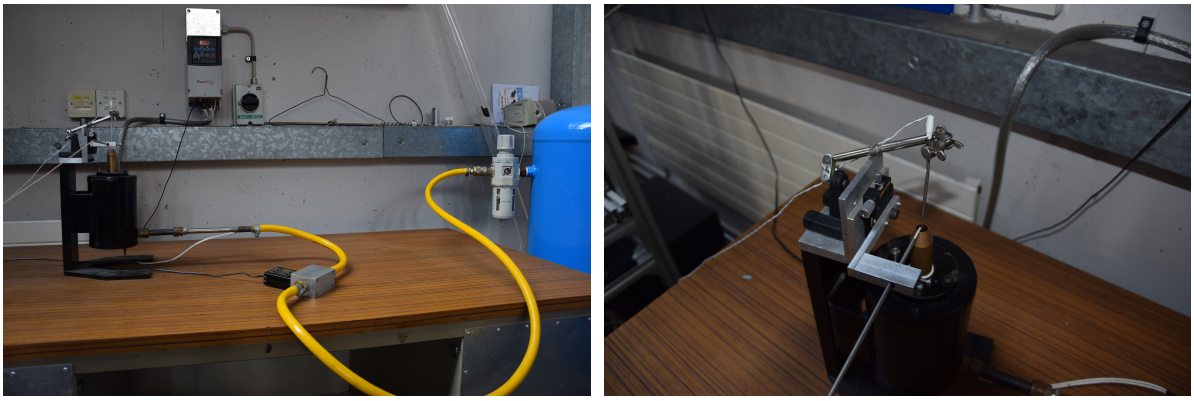

(a) Calibration facilities **(b)** Probe set-up

Figure 3.6: Hot-wire probe calibration

Therefore, a self-contained calibration unit was built in the lab, shown in Figure 3.6 (a). The unit consists of a compressed air supply, a settling tank, an Alicat mass flow meter, a probe mount and a few jet nozzles for different velocity ranges. The flow meter has a reading range of $0 - 400$ SLPM (Standard Litre Per Minute), which is equivalent to a velocity range of $0 - 70m/s$ with the selected nozzle. Prior to the calibration, the probe was mounted outside the nozzle outlet but inside the core region of the jet flow so as to calibrate the probe with the same flow speed read from the flow meter, depicted in Figure 3.6 (b). In addition, a thermal couple was attached downstream to the probe. On one hand, it could measure the ambient temperature of the reference flow, which was used for correction further discussed later; on the other hand, the downstream measurement did not interfere the flow passing the wire. After the calibration, a fifth-order polynomial curve was fitted, with the voltage signal from the wire resistance and velocity as the variables. As drawn in Figure 3.7, the polynomial is the hot-wire test basis.

Since the ambient temperature of the calibration and the tests is different and the heat transfer is dependent on the temperature difference between the wire and the ambient flow, an inherent measurement error exists in the hot-wire anemometry, especially for the constant temperature mode, i.e. the effects of ambient temperature drift. Therefore, it is necessary to carry out a correction. The equation used in this study is proposed by Bearman[122], which is written as:

$$E_{corr} = \sqrt{\frac{T_w - T_0}{T_w - T_a}}.E_a \tag{3.1}$$

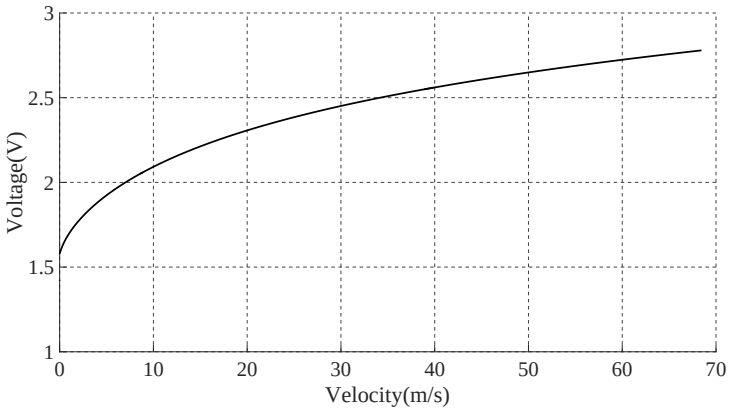

Figure 3.7: Calibration curve

where E_a is the acquired voltage. T_w, T_0 and T_a are the sensor temperature, the ambient reference temperature in the calibration and the ambient temperature in the data acquisition respectively.

Figure 3.8: Set-up of the hot-wire measurement

In the how-wire measurement, in addition to the instrument introduced above, a traverse was configured to control the measurement location in the flow, shown in Figure 3.8. The traverse was installed on top of the extrusion frame or beside the platform. It involved taking hot-wire measurements at set intervals in the vertical or horizontal directions perpendicular to the flow. The displacement of the traverse was achieved through a servo-motor mounted on a slider-type support, which was controlled by Matlab

code. It is worth noting that the measurements of different instruments including hot-wire, PIV, microphone array etc. were not simultaneously conducted, thereby they would not interfere with each other. More information on the hot-wire measurement location will be reported in the corresponding results section.

3.4 PIV

Particle Image Velocimetry, abbreviated as PIV, is an optical method for quantitative flow measurement, which allows obtaining both instantaneous and time-mean (after being processed) fluid properties. In this section its principles and the set-up are introduced.

3.4.1 Fundamentals of PIV

PIV requires of seeding the fluid with tracer particles, which is assumed to faithfully follow the flow motion. With the help of high power laser, the fluid with entrained particles is illuminated and visualised. Consequently, the motion of the seeding particles is used to calculate speed and direction (the velocity field) of the flow so that it can be investigated. Main advantages of PIV can be summarised as non-intrusive technique, good resolution and accuracy, velocity field reconstruction, etc.

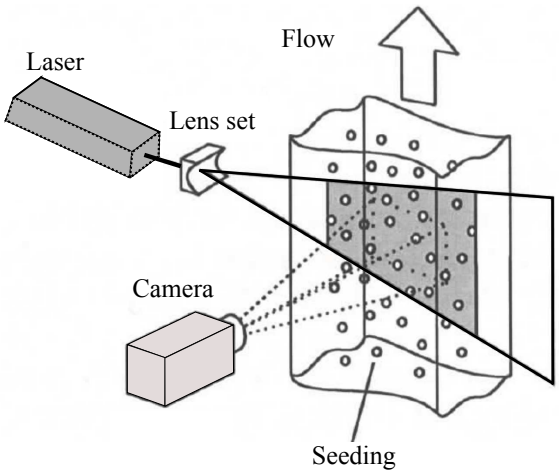

Figure 3.9: Typical PIV set-up

As Figure 3.9 shows, a typical 2D PIV system is generally equipped with a high power laser, a set of lenses, a digital image recording camera and seeding devices. To be more specific, the most commonly used laser is pulsed Neodyme-YAG (Nd:YAG) laser, doubled

in frequency (532 nm). The pulse duration and the repetition rate are dependent on the flow regime of interest and the hardware configuration. The lens set, in which there are concave and convex lenses, is to generate the laser plane on which the camera is focused. As for the camera, digital images recording is generally conducted via a CCD sensor (Charge-Coupled Device) which converts photons to an electric charge based on the photoelectric effect [123]. In the PIV test, when the flow field is visualised using the laser plane and particles, the camera captures numbers of image pairs simultaneously with the pulse of the laser. Those images are subsequently processed through the cross-correlation function to obtain the velocity vector field.

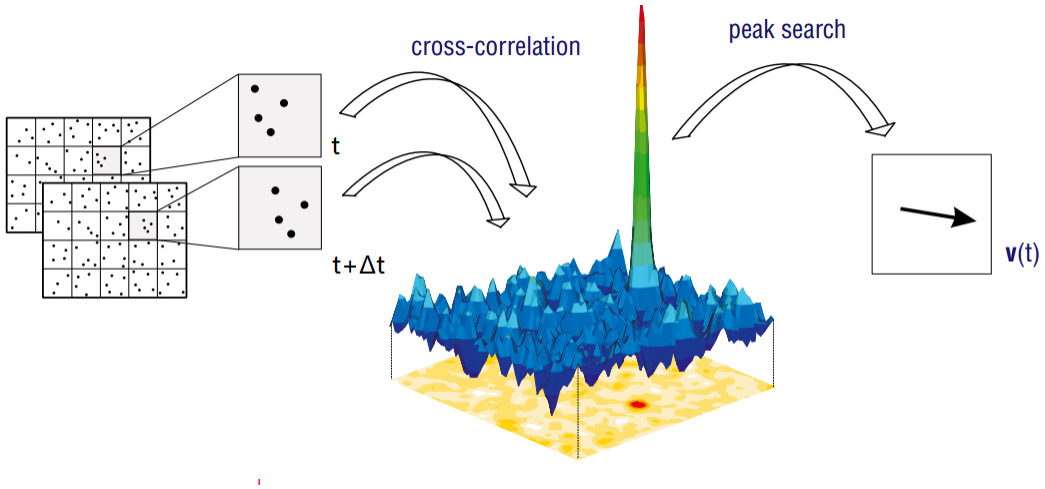

Figure 3.10: PIV Cross-correlation process [124]

Figure 3.10 [124] illustrates general process of the cross-correlation, which can be summarised as four core steps [125, 126, 127]:

1. Divide the images into a rectangular grid of much smaller regions, defined as interrogation windows.

2. Correlate each interrogation windows in the first image with the corresponding one in the second image.

3. Locate the displacement peak and compute the velocity vector.

4. Assemble the flow velocity field.

The interrogation window size must be properly chosen. On one hand, it should be large enough to achieve statistically a significant number of homogeneous particles

contained within it; on the other hand, it needs to be adequately small so that the second order effects, i.e. displacement gradient can be neglected. For instance, an image with a resolution of 1280×1280 pixels can be divided into 20×16 interrogation windows if the window size is 64×64 pixels and therefore a total of 320 velocity vectors can be attained. Additionally, in order to achieve more vectors, an overlap of the interrogation windows can be adopted instead of using smaller window size. For the same case above if a 50% overlap is used, 1209 vectors can be obtained. Furthermore, in practical terms, the multi-pass correlation is often conducted. To be more specific, the first iteration is used to find an estimate of the corresponding velocity vector. Subsequent iterations use this information to shift the interrogation windows accordingly. In this way, a more precise cross-correlation can be obtained as the number of related flow particles between interrogation windows is maximized. The standard cross-correlation expression to calculate the vector fields is written as:

$$C(\Delta x, \Delta y) = \sum_{x=0,y=0}^{x<p,y<p} I_1(x,y) I_2(x+\Delta x, y+\Delta y), -\frac{p}{2} < \Delta x, \Delta y < \frac{p}{2} \tag{3.2}$$

where C is the 2 dimensional correlation coefficients for the displacements Δx and Δy; p is the number of pixels along on dimension of the interrogation window; I_1 and I_2 denote the image intensities of two corresponding interrogation windows. More information on the fundamentals of 2-D PIV, e.g. data quality evaluation and effects of the seeding particles, can be found in the monograph [128].

3.4.2 PIV Set-up

Figure 3.11 illustrates the test set-up in this study. To be more specific, the DaVis low-speed PIV system was utilized. The system consists of a $15MJ$ New Wave Solo PIV Double Pulse Laser– the Nd:YAG laser, a DaVis Flowmaster 3 CCD camera, a lens set and a seeding system. As shown in Figure 3.11, the laser source was installed on top of the extrusion frame. The laser beam was reflected, focused and ultimately diverged into a sheet through an optical laser set. The laser set utilised in the study is similar to the example shown in Figure 3.12. This example includes 3 lenses: two concave for diverging and one convex for converging. The first lens is a diverging lens and the second

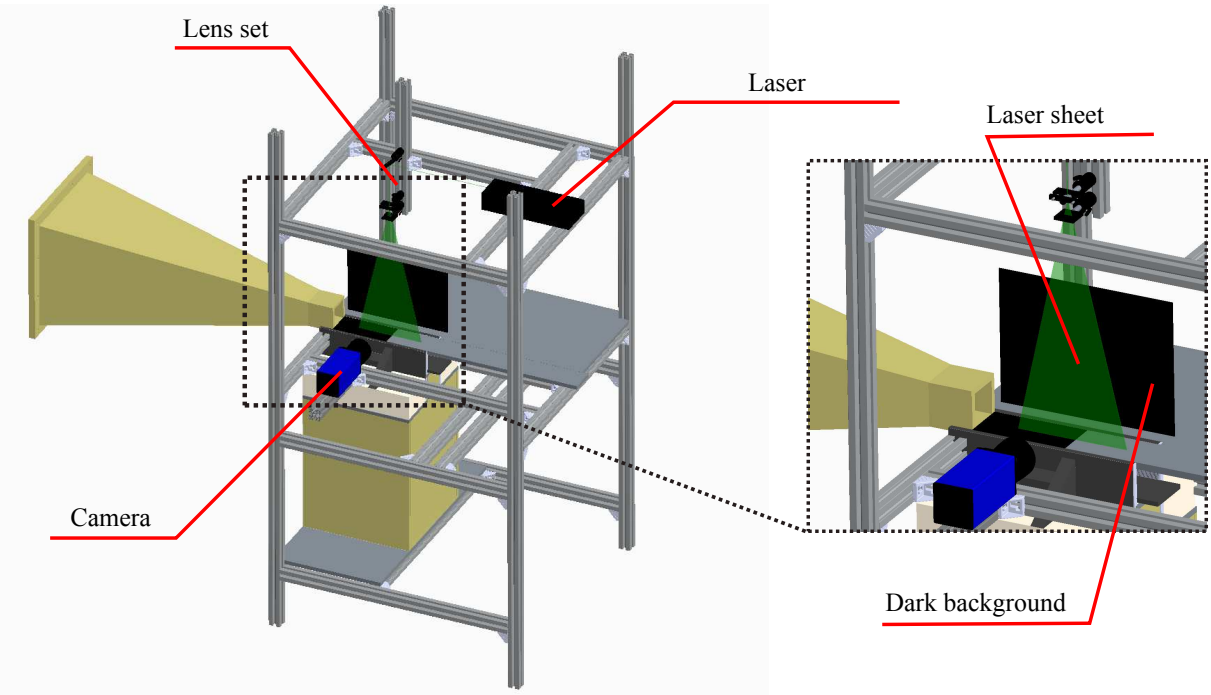

Figure 3.11: PIV test set-up

one is a converging lens. These two lenses are mainly used to focus the beam on the height of interest. Also, they can compress the circular beam into an ellipse. The third lens is responsible for widening the beam waist. As described in Figure 3.12 [129], the eccentricity of the ellipse is enlarged through the third lens so that the required width and sharpness of the laser sheet for the measurement plane can be achieved. In addition, the location adjustment of the beam waist can be managed by varying the distance between the second and the third lenses.

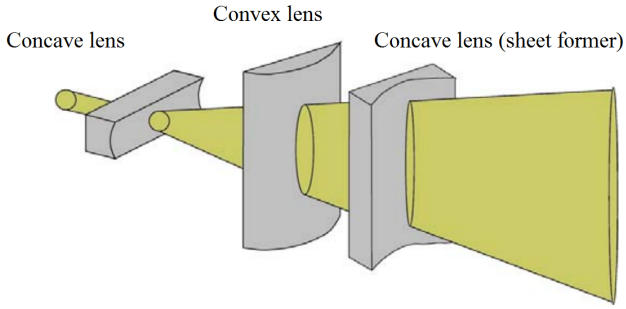

Figure 3.12: Example of a typical optical lens set in PIV

Moreover, a DaVis Flowmaster 3 CCD camera was attached parallel to the laser sheet. The distance from its lens to the sheet could be manipulated for different measurement purpose, which will be further reported in the corresponding sections. However, the lens was always adjusted to focus on the measurement plane. The camera can capture image pairs with the pulsing laser, and a resolution of 1280×1280 pixels can be achieved. For each test case, a number of coupled images were captured at 4Hz and the time between two paired images, i.e. Δt was 10 μs.

The seeding process was carried out through Phantom 135 smoke system, which has a particle diameter size of $0.2\mu m$. Because the test section was an open environment, in order to obtain a flow with steady particle intensity, the entire room of the lab was seeded by the smoke system. The seeding process was conducted by injecting particles into the wind tunnel blower, which can dramatically accelerate the process. Additionally, a black cardboard was placed $10cm$ away behind the measurement plane as the dark background, which could help improve the quality of the process.

3.5 Flow Visualization

Flow visualization is the technology in fluid dynamics applied to make the flow patterns visible so as to obtain qualitative or quantitative information on the flow regime of interest. To date, a variety of approaches have been developed to cater for different research needs, e.g. surface flow visualization, particle tracer methods, optical methods etc. In this study, the laser based flow visualization is utilised. To be more specific, particles are initially added into the flow and a laser sheet is generated to illuminate the flow field. As such, with the help of the camera, jet spreading can be captured and visualised.

In the test, the laser source used is a laser pointer with a wavelength of $532nm \pm 10nm$ at $5mW$. Likewise, an optical lens set was set to generate the laser sheet as required, in which there are two lenses. The first one is a convex lens with a long focal length, which can focus the laser on the area of interest; the second one is a concave lens that is used to diverge the beam and generate the laser sheet. The entire set-up is shown in Figure 3.13 (a). Moreover, a Nikon D3300 CCD camera was utilised to take photos of the jet pattern. In order to acquire a time-mean visualization, for each case, 50 pictures were captured

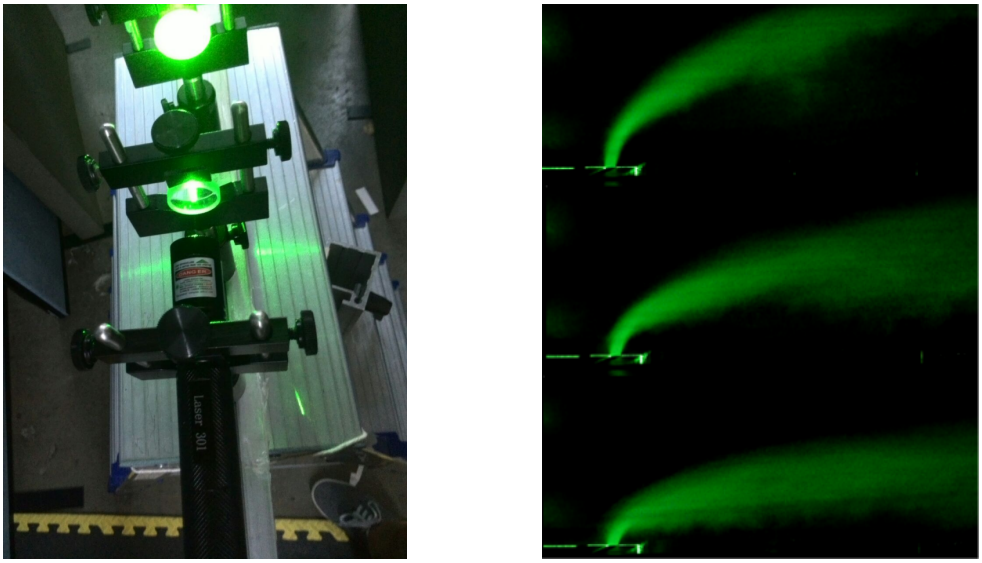

(a) Laser source and the optical set-up **(b)** Examples of the flow visualization

Figure 3.13: Flow visualization used in the study

and averaged. Examples of the flow visualization results are reported in Figure 3.13 (b).

In addition, in order to quantitatively measure the pattern of the jet, a photo calibration was carried out prior to the tests. Firstly, the camera was fixed on the tripod horizontally. After being focused on the laser sheet, the camera took a calibration photo as shown in Figure 3.14. More specifically, there is a cube in the photo, the real dimension of which is $200mm \times 10mm$. The top edge of the cube is as long as $200mm$ with a total pixel number of 3,490 and the height of the cube is $100mm$ with a total pixel number of 1,470. Therefore, an average can be achieved for the resolution of the photo, which is equal to $16.5p/mm$ (pixel per millimetre). With this resolution, a 2-D Cartesian coordinate system can be established, with the centre of the primary jet outlet to be the origin. This system is as same as the one introduced earlier. As such, every point can be localised in the system.

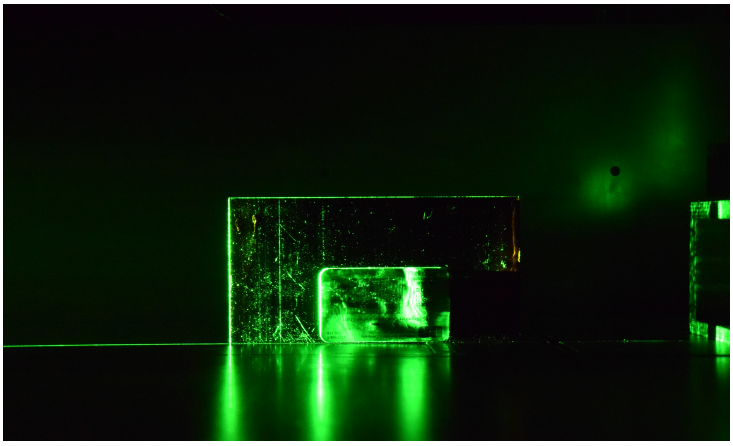

Figure 3.14: Flow visualisation calibration photo

3.6 Acoustic Measurement

In this section, acoustic measurements conducted by the microphone array are introduced.

3.6.1 Microphone Array

As discussed earlier, a microphone array was mounted on top of the extrusion frame to carry out acoustic measurements. As illustrated in Figure 3.1.I, the array has a planar semi-circle shape with a diameter of $600mm$. It is kept parallel to the test platform and equipped with 25 KE 4 Sennheiser electret microphones. Sensitivities of these microphones were checked using a microphone calibrator. In addition, a camera was attached to the centre of the array, which allows noise localisation to be based on real cut-out background. The array has an irregular pattern, shown in Figure 3.15(a). This irregular pattern can reduce the typical spatial aliasing of the regular array. In the experiment, the array was placed $620mm$ higher than the end-plate. This relatively short distance was chosen so as to achieve a maximum signal-to-noise ratio (SNR). The auxiliary data acquisition system was National Instrument DAQ system NI PXI-1033 together with signal amplifiers. The specification of the data acquisition system can be found in the user manual [130]. The sampling frequency was set to be $100kHz$ in the experiment because the audible range of human hearing is $20Hz - 20kHz$ and the Nyquist-Shannon sampling criterion requires that the sampling rate is at least twice of the maximum component frequency needed to be measured. Additionally, the sampling duration was made to be $6s$. A front view of the array is shown in Figure 3.15 (b).

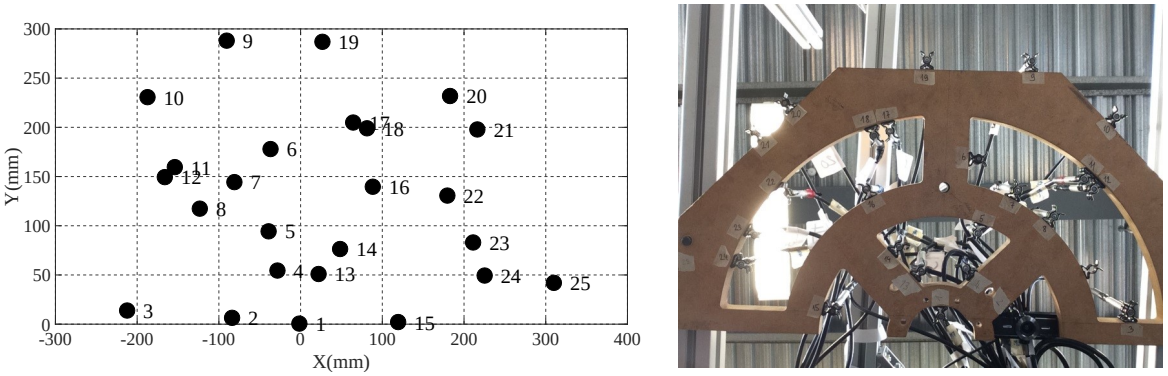

(a) Microphone pattern **(b)** Front view

Figure 3.15: Microphone array

3.6.2 Noise Spectral Analysis

Noise spectrum analysis was carried out using two approaches: auto-spectrum from one microphone in the array and 1/3 octave band spectrum as an average of all microphones. Principles of these two methods are introduced in the following.

3.6.2.1 Auto-Spectrum

The auto-spectrum is calculated based on Fast Fourier Transform (FFT) and Power Spectrum Density (PSD) [131, 132] described in the following.

Fourier integral, which is required by the random signal in the determination of its continuous frequency spectrum, is written as:

$$x(t) = \int_{-\infty}^{\infty} X(f) e^{j2\pi ft} df \tag{3.3}$$

where f is the frequency and $x(t)$ can be regarded as a summation of all continuous sinusoid spectra. Note that $X(f)$ is a complex quantity as a function of f from $-\infty$ to ∞, termed as Fourier Transform of $x(t)$ and expressed as:

$$X(f) = \int_{-\infty}^{\infty} x(t) e^{-j2\pi ft} dt \tag{3.4}$$

In practical applications, infinite limits do not exist when a signal is sampled for analysis. As such, the expression of the Fourier Transform in a finite range $(0, T)$ is written as:

$$X(f, T) = \int_{0}^{T} x(t) e^{-j2\pi ft} dt \tag{3.5}$$

Also, the signal is sampled discretely. For discrete data $x(t)$, which has N sampling points with an equal time interval of Δt, the Fourier Transform can be calculated as:

$$X(f_k) = \sum_{n=1}^{N} x_n e^{(-j\frac{2\pi kn}{N})}\Delta t \qquad k = 1, 2, ..., N \tag{3.6}$$

where f_k is the discrete frequency values for the computation of $X(f, T)$ and it is usually calculated as $f_k = k/T$. x_n is the signal value at time $n\Delta t$. This is the Discrete Fourier Transform (DFT). The results of the DFT is a $N \times 1$ complex matrix. Additionally, Fast Fourier Transform (FFT), which is described as "the most important numerical algorithm of our lifetime" [133], is a collection of algorithms for the fast computation of DFT.

Prior to the discussion of PSD, the mean square value ψ^2 is introduced, which measures the combined tendency and dispersion of a signal. It is written as:

$$\psi^2 = E[(x)^2] = \lim_{N\to\infty} \frac{1}{N} \sum_{n=1}^{N} (x_n)^2 \tag{3.7}$$

For a random signal $x(t)$, it is demonstrated that its mean square value, ψ_x^2 equals to the sum of the individual ψ^2 of the harmonic components (c_n). Thus,

$$\psi_x^2 = \sum_{n=-\infty}^{\infty} E[(c_n)^2] \tag{3.8}$$

Therefore, ψ_x^2 consists of discrete contributions in each frequency interval Δf. Here the Power Spectrum, $P_{xx}(f_x)$ is defined as the contribution to ψ_x^2 in Δf. As such,

$$P_{xx}(f_k) = E[(c_n)^2] \tag{3.9}$$

Thus,

$$\psi_x^2 = \sum_{n=-\infty}^{\infty} P_{xx}(f_k) \tag{3.10}$$

The discrete Power Spectra Density (PSD), $S_{xx}(f_k)$ is defined as:

$$S_{xx}(f_k) = \frac{P_{xx}(f_k)}{\Delta f} \tag{3.11}$$

which is the power spectrum divided by the frequency interval. Hence, if the signal is, for example, pressure fluctuation with the unit of Pa, then the unit of PSD is Pa/Hz.

As mentioned earlier, the sampled signal is always discrete with finite length in practice. Additionally, data are averaged in the frequency domain so as to reduce its random error. For instance, there is a real signal $x(t)$ which has a total length of N_t (number of the elements). It is divided into n_s equal segments that have a length of N_s. Each segment is denoted as $x_i(t)$ and $i = 1, 2, ..., N_s$. Note that $n_s = N_t/N_s$. Therefore, the PSD for the discrete data, two sided, can be calculated as:

$$\hat{S}_{xx}(f_k) = \frac{1}{N_t \Delta t} \sum_{i=1}^{n_s} |X_i(f_k)|^2 \qquad k = 1, ..., N_s \tag{3.12}$$

which is related to the DFT. In acoustics, it is customary to use one sided PSD, meaning that it is obtained by integrating over the positive frequency range. The one sided PSD is written as:

$$\hat{G}_{xx}(f_k) = \frac{2}{N_t \Delta t} \sum_{i=1}^{n_s} |X_i(f_k)|^2 \qquad k = 1, ..., \frac{N_s}{2} \tag{3.13}$$

Generally for noise study the auto-spectrum in dB is preferable. The corresponding dB spectrum is achieved from one sided PSD by:

$$dB = 20 log_{10} \frac{\sqrt{\hat{G}_{xx}(f_k)\Delta f}}{P_{ref}} \tag{3.14}$$

where P_{ref} is the reference pressure, conventionally $P_{ref} = 2 \times 10^{-5} Pa$. In the test, the auto-spectrum from one specified microphone was used to perform analysis.

3.6.2.2 One Third Octave Band Spectrum

The human audible range has been separated into eleven unequal segments, where the highest frequency is twice of the lowest frequency. These segments are termed octave bands. Furthermore, one octave band can be separated into three ranges, referred as the one third octave bands. Details of the octave bands and one third octave bands can be found in Appendix A.

In spectral analysis, the mean square pressure is determined in each of contiguous frequency bands, and it is plotted as a function of the band centre frequency [134]. Prior to calculating the one third octave band spectrum, the mean square sound pressure density on the average of each band, i.e. PSD of each band, needs determining. The algorithm of PSD calculation has been introduced earlier. If p_i is the mean square sound pressure

density on the average in the ith band, P_i is the band mean square sound pressure level, then,

$$P_i^2 = p_i^2 \Delta f_1 \tag{3.15}$$

where Δf_1 is the corresponding bandwidth. Conventionally, the one third octave band spectrum is expressed in dB as well. Therefore, the Sound Pressure Level (SPL) of each band in dB is written as:

$$dB_i = 20log\frac{P_i}{P_{ref}} \tag{3.16}$$

Moreover, in order to evaluate the overall acoustic performance of an experimental test, the one third octave band spectrum as an average of all microphones in the array was utilised. To calculate the averaged spectrum, dB level in each band of each microphone requires determining. For example, if dB_{ij} denotes the dB level of the jth microphone in the ith band, then the average of all microphones in that band is written as:

$$d\bar{B}_i = 10log(\frac{\sum_{j=1}^{M} 10^{\frac{dB_{ij}}{10}}}{M}) \tag{3.17}$$

Therefore, the averaged spectrum of all microphones in the one third octave bands can be achieved. Moreover, one more formula is introduced to subtract one noise source from the one third octave band spectrum. In particular, if dB_{all} is the overall SPL measured in one band, including noise source S. When all noise sources are shut off except S, another SPL can be attained, which is in effect the SPL of S and denoted as dB_s. Therefore, the noise that is generated by S is isolated, i.e. dB_s. Supposing S is an unwanted noise source, it can be eliminated from dB_{all} by:

$$dB_e = 10log(10^{\frac{dB_{all}}{10}} - 10^{\frac{dB_s}{10}}) \tag{3.18}$$

where dB_e is the SPL with the elimination of noise source S. This method was used to perform SNR correction, which will be discussed in the subsequent corresponding section. Note that all one third octave band spectra presented in the following of this thesis are the average of all microphones.

3.6.3 Beamforming

Beamforming is a microphone-array-based measurement technique for sound source localization from medium to long measurement distances. It has become a standard method for the spatial noise mapping and has been compared to the acoustic camera [135].

The core of the beamforming algorithm can be described as Delay-And-Sum (DAS) of the microphone array signals. More specifically, the array is virtually focused on each point of the measurement plane as shown in Figure 3.16 [136]. After one microphone is picked up as the reference, the relative time delays of other microphones will be calculated and summed. In addition, beamforming can be carried out in either frequency domain or time domain.

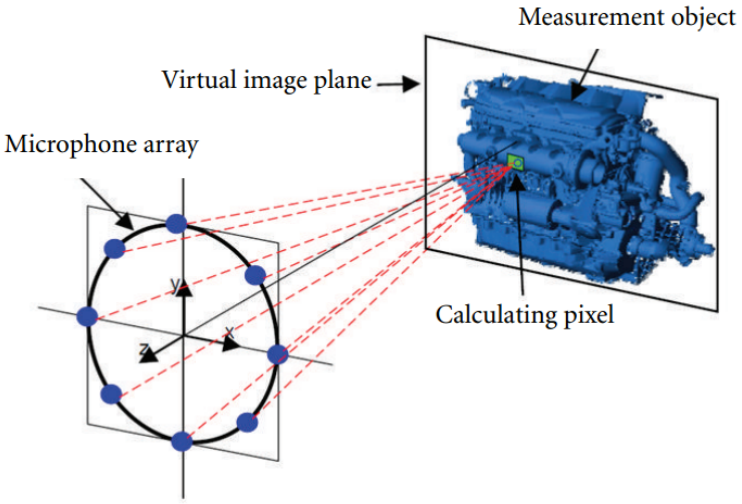

Figure 3.16: Principle of beamforming [136]

3.6.3.1 Beamforming Algorithm

In order to explain beamforming algorithm, a point sound source, radiating a sound signal at an arbitrary location $\boldsymbol{X}$ in a Cartesian coordinate system is assumed, denoted by S_o. Meanwhile, there are a number of microphones located in the same Cartesian coordinate system, whose positions are described by $\boldsymbol{\xi}_i = (x_i, y_i, z_i)$. Here the subscript refers to the microphone number from 1 to M. Therefore, the directional vector of each microphone referred to S_o is calculated as:

$$\boldsymbol{r}_i = \boldsymbol{\xi}_i - \boldsymbol{X} \tag{3.19}$$

As such, the acoustic pressure induced by S_o in the position of each microphone, i.e. $\boldsymbol{\xi}_i$ is expressed as:

$$f_i(\boldsymbol{\xi}_i, t) = \frac{\sigma(t - \tau_i)}{4\pi|\boldsymbol{r}_i|} \tag{3.20}$$

where σ is the emitted source and τ_i is the time delay between the emission from S_o and the acquisition by ith microphone. Thus, τ_i can be calculated as:

$$\tau_i = \frac{|\boldsymbol{r}_i|}{c} \tag{3.21}$$

c is the speed of sound. In the following, beamforming algorithms in frequency domain and in time domain will be respectively introduced.

1. Frequency domain beamforming

Beamforming in the frequency domain, also referred as the conventional beamforming, is the original method for noise localization using beamforming. However, it is limited to processing narrowband frequency. Although several broadband approaches have been developed, conventional beamforming is still widely used mainly due to its considerably shorter process time and concentration on the particular frequency.

Prior to the beamforming process, DFT is conducted to the time pressure signals $f_i(t)$ recorded by each microphone as:

$$F(f) = \sum_{i=1}^{\frac{T_s}{F_s}} f_i e^{(-j\frac{2\pi k i F_s}{T_s})} \Delta t \qquad k = 1, 2, ..., \frac{T_s}{F_s} \tag{3.22}$$

where T_s and F_s are the sampling time and sampling frequency, Δt is the time interval between each sampling and $\Delta t = 1/F_s$. The core of beamforming in frequency domain (DAS) can be fundamentally expressed in Equation 3.23. To be more specific, G is a point in the grid of the virtual image plane, whose location is denoted as $\boldsymbol{X}_G$. The complex beamformer output power from G is denoted by BF_{FD}, then BF_{FD} of the frequency of interest (f_{oi}) is calculated as:

$$BF_{FD}(\boldsymbol{X}_G, f_{oi}) = \frac{1}{M^2} \boldsymbol{h}(\boldsymbol{X}_G)^H \boldsymbol{G} \boldsymbol{h}(\boldsymbol{X}_G) \tag{3.23}$$

where $\boldsymbol{h}$ is the steering vector with a size of $M \times 1$. $\boldsymbol{h}^H$ is the Hermitian matrix of $\boldsymbol{h}$. Each element of $\boldsymbol{h}$ is written as:

$$h_i = e^{-j2\pi f_{oi}\tau_i} \tag{3.24}$$

$\boldsymbol{G}$ in Equation 3.23 represents the Cross Spectral Matrix (CSM) of the microphone signals. It is a $M \times M$ matrix. If g_{ij} denotes the element in ith row and jth column, i.e. the ith jth microphone, it is a result of convolution expressed as:

$$g_{ij} = \langle F_i(f_{oi}) F_j^*(f_{oi}) \rangle \tag{3.25}$$

BF_{FD} is a complex number. In order to make it referable using SPL expressed in dB, it is transformed by:

$$dB_S = 20log\frac{|BF_{FD}(\boldsymbol{X}_G, f_{oi})|}{P_{ref}} \tag{3.26}$$

2. Time domain beamforming

A systematic algorithm of beamforming in time domain is first introduced by Dougherty [137], which brought in several benefits to the noise source localization. The main advantage of this approach is the ability to deal with short pulses, transients, and broadband signals directly. Moreover, it can depict an averaged sound pressure level distribution within the sampling time.

Figure 3.17 [138] illustrates the key procedures of the beamforming in time domain. As mentioned earlier, τ_i is the time duration of the sound prorogation from the source to each microphone. Likewise, if one microphone is chosen as the baseline, for example, the one with minimum τ_i, then the time delay of other microphones can be expressed as:

$$\Delta_i = \tau_i - min(\tau_i) \tag{3.27}$$

As such, if the pressure signals simultaneously acquired by each microphone are written as $p_i(t - \Delta_i)$, the beamforming output from G can be attained by:

$$BF_{TD}(\boldsymbol{X}_G) = \sqrt{\frac{1}{T_s}\int_0^{T_s}\left[\frac{1}{M}\sum_{i=1}^{M} p_i(t-\Delta_i)\right]^2 dt} \tag{3.28}$$

Likewise, the beamformer is refereed to the sound pressure level in dB, expressed as:

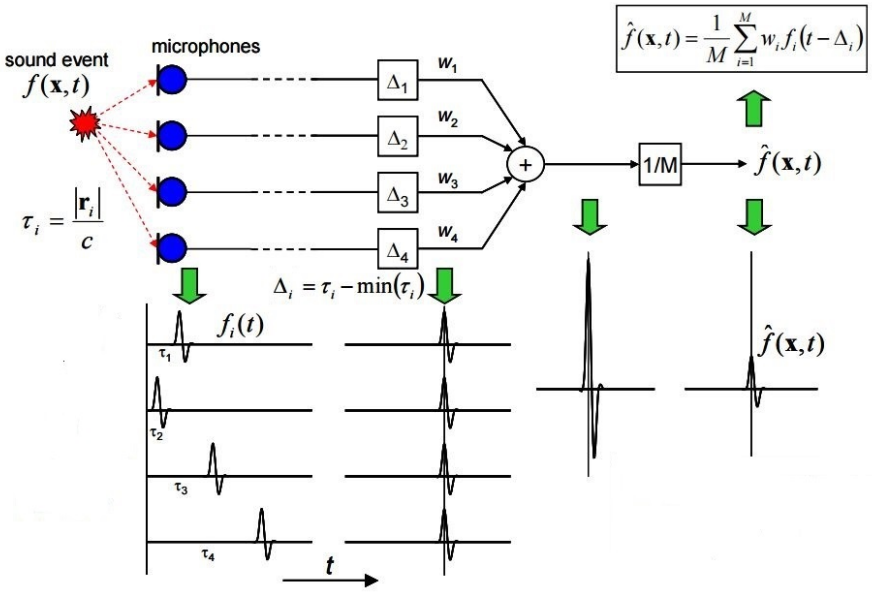

Figure 3.17: Procedures of time domain beamforming [138]

$$dB_{TD} = 20log\frac{|BF_{TD}(\boldsymbol{X}_G)|}{P_{ref}} \tag{3.29}$$

As mentioned earlier, beamforming in time domain is a time-average analysis for the broadband signal. However, it may not be as informative as the beamforming in the frequency domain in terms of particular frequencies or bands. Thus, a filter is usually coupled with the time domain beamforming. For example, one third octave bandpass filter, which is also adopted in this study. More specifically, prior to the beamforming, raw data were pre-processed with the one third octave bandpass filter. Therefore, the noise localization will concentrate on the frequency range of the band as required.

3. Diagonal deletion

When the microphone array works, the auto-power that does not contain usable source localization information is occasionally higher than the useful cross-power between microphones. As a consequence, the contrast can be limited in the final beamforming output. Sijtsma [139] indicated two examples: 1. microphones are affected by aerodynamic disturbances when tests are conducted inside a close wind tunnel section; 2. coherence between microphones can be lost as a result of sound propagating through a turbulent medium, e.g. shear layer. Therefore, diagonal deletion is widely utilised to reduce the microphone self-noise by subtracting the auto-power.

For beamforming in the frequency domain, the diagonal deletion can be simply carried out by zeroing the diagonal elements of $\boldsymbol{G}$. Therefore, the new beamforming output is written as:

$$BF_{FDdd}(\boldsymbol{X}_G, f_{oi}) = \frac{1}{M^2}\boldsymbol{h}(\boldsymbol{X}_G)^H \hat{\boldsymbol{G}}\boldsymbol{h}(\boldsymbol{X}_G) \tag{3.30}$$

$\hat{g}_{ij}$ is the element of $\hat{\boldsymbol{G}}$, which is calculated as:

$$\hat{g}_{ij} = \begin{cases} g_{ij} & i \neq j \\ 0 & i = j \end{cases} \tag{3.31}$$

The expression of the beamforming in the time-domain is written as:

$$BF_{TDdd}(\boldsymbol{X}_G) = \sqrt{\frac{1}{T_s}\int_0^{T_s}\left\{\left[\frac{1}{M}\sum_{i=1}^{M} p_i(t-\Delta_i)\right]^2 - \frac{1}{M^2}\sum_{i=1}^{M} p_i^2(t-\Delta_i)\right\}dt} \tag{3.32}$$

4. Shear layer correction

When the sound propagates through the shear layer between an open-jet flow and a quiescent air, it will be refracted and the refraction depends on the flow Mach number and propagation angles, which will affect the accuracy of the beamforming noise localization to some extent. Therefore, it is necessary to apply a correction for the refraction effects. In recent literature, not much theory has been established on how these effects work on the sound propagation, but some early studies [140, 141] have laid good research foundation. Amiet[142] extended the research to including the wave spreading effects of refraction and developed a simplified method to perform the correction, experimentally verified by Ahuja et al [143]. Procedures of using Amiet method expressed in the Cartesian coordinate system are described in the following [142, 144, 145].

Figure 3.18 [144] depicts the modelling of the shear layer correction, in which the shear layer is assumed to be with a zero thickness. A Cartesian coordinate system is established, whose origin coincides with a point sound source (S). Height from the shear layer to the point source is h. One microphone is placed outside the flow, whose position is described by (x_i, y_i, z_i). I denotes the intersection point between the wave ray SI and the shear layer. Due to the refraction, an equivalent microphone position is assumed, termed as the corrected observer (C). r_m, r_1 and r_2 are the length of SM, SI and IM respectively. In

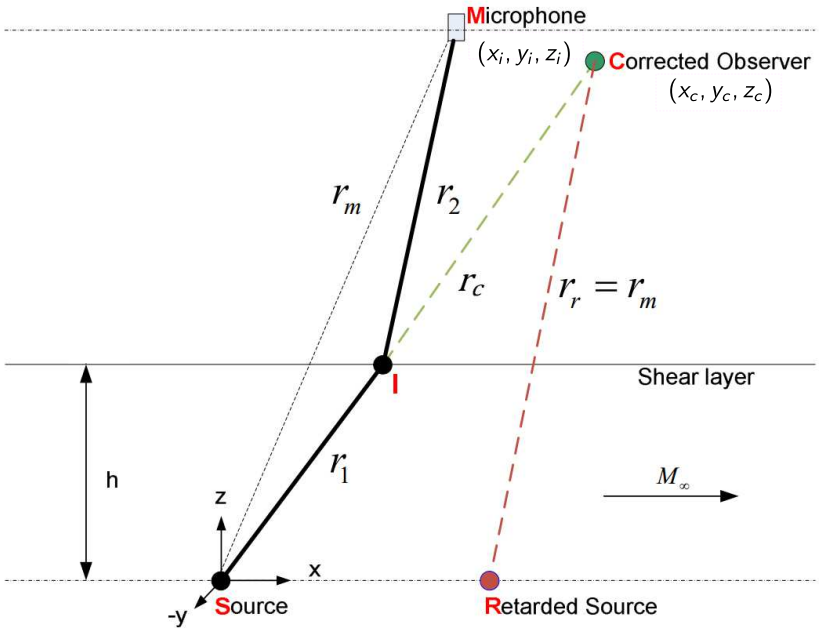

Figure 3.18: Ray geometry in the shear layer correction method [144]

addition, the acoustic wave arriving at C appears to be from a retarded source R and the retarded distance is r_r with the nominal sound speed c_0 (sound speed in quiescent air). In this study, r_r is assumed to be equal to r_m.

The nominal wave propagation time from the source to the microphone is written as:

$$t_0 = \frac{r_m}{c_0} \tag{3.33}$$

However, the actual propagation duration is expressed as:

$$t_a = \frac{r_1}{c_1} + \frac{r_2}{c_0} \tag{3.34}$$

Since S is the origin, expressions of r_1 and r_2 are written as:

$$r_1 = \sqrt{x_I^2 + y_I^2 + z_I^2} \tag{3.35}$$

$$r_2 = \sqrt{(x_i - x_I)^2 + (y_i - y_I)^2 + (z_i - z_I)^2} \tag{3.36}$$

where (x_I, y_I, z_I) represents location of I, which can be obtained by assuming that C coincides with I in Equation (A23) from reference [142]. Therefore, an equation set to

calculate (x_I, y_I, z_I) can be derived as:

$$\begin{cases} \frac{x_I}{\sqrt{x_I^2+(1-M_\infty^2)(x_I^2+z_I^2)}} - (1-M_\infty^2)\frac{x_i-x_I}{\sqrt{(x_i-x_I)^2+(y_i-y_I)^2+(z_i-z_I)^2}} \\ \frac{y_I}{\sqrt{x_I^2+(1-M_\infty^2)(x_I^2+z_I^2)}} - \frac{y_i-y_I}{\sqrt{(x_i-x_I)^2+(y_i-y_I)^2+(z_i-z_I)^2}} \\ z_I = h \end{cases} \tag{3.37}$$

where M_∞ is the Mach number of the crossflow. With Equation 3.37 postilion of I can be localised. As Equation 3.34 shows, the effect of convection on the acoustic wave propagating speed within the test section is taken into account, and incorporated into a model for source-to-microphone propagation [144]. As such, the actual speed of sound within the test section is written as:

$$c_1 = \frac{x_I}{\sqrt{(x_I^2+y_I^2+z_I^2)}} M_\infty c_0 + \sqrt{(\frac{x_I}{\sqrt{x_I^2+y_I^2+z_I^2}} M_\infty c_0)^2 + c_0^2 - (M_\infty c_0)^2} \tag{3.38}$$

Variables calculated above are used to correct the shear layer effect by modifying the time delay. For example, in the frequency domain, instead of Equation 3.24, element of the steer vector is written as:

$$\hat{h}_i = e^{-j2\pi f_{oi}\hat{\tau}_i} \tag{3.39}$$

where $\hat{\tau}_i$ is the time delay in terms of the actual propagation time.

3.6.3.2 Array Calibration

As mentioned above, the microphone array pattern has substantial effects on the beamforming noise localization. In order to validate the effectiveness of the microphone array pattern in the noise localization, a response test to the simulated monopole was carried out. More specifically, a monopole point source, as shown in Figure 3.19 is assumed to be in the origin of a spatial Cartesian system, i.e. (0, 0, 0). In the meanwhile, a virtual semi-circular microphone array with the same pattern as the real array is placed inside, parallel to the X-Y plane. The distance between the array and the X-Y plane is $620mm$, thereby the configuration matches up with the experimental set-up. The calculation of the sound pressure signal acquired by each microphone can be referred to Equations 3.19–3.21.

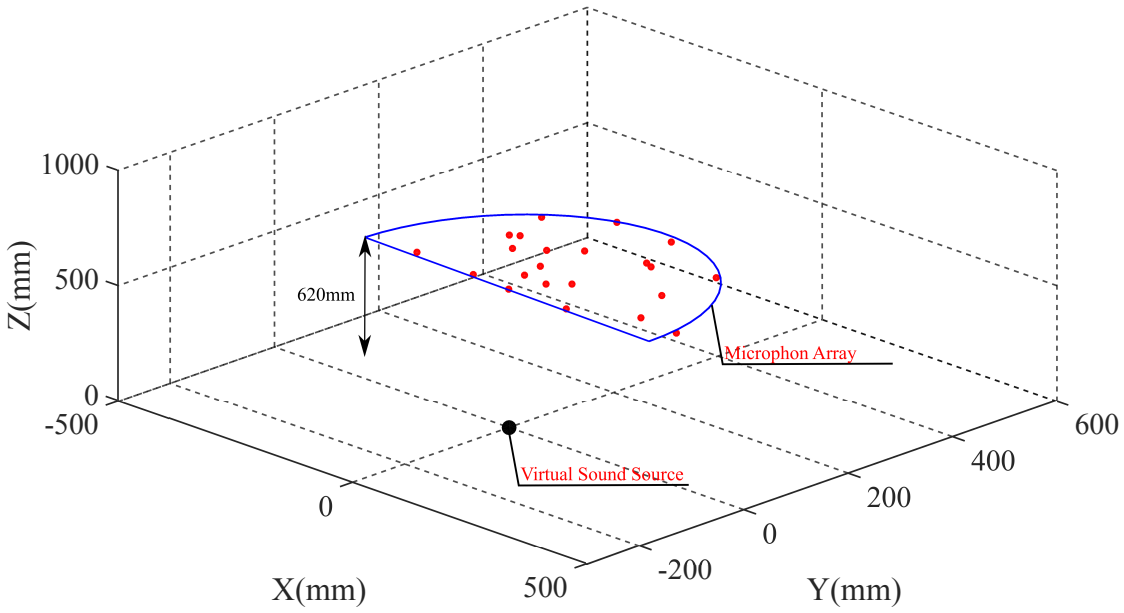

Figure 3.19: Configuration of the beamforming simulation

The validation was carried out for the beamforming in both time domain and frequency domain. The dynamic range, which is the level of the sidelobes relative to the main lobe, was calculated. In the frequency domain, beamforming was performed with different frequencies of interest (frequency of monopole source was set to be equal to the frequency of interest), the dynamic range of the frequency domain beamforming at different frequencies of interest are reported in Table 3.1. Moreover, the corresponding noise localization is illustrated in Figure 3.20.

Table 3.1: Dynamic range of the frequency domain beamforming simulation at different frequencies of interest

Frequency of Interest	$1kHz$	$2kHz$	$4kHz$	$5kHz$	$6kHz$	$15kHz$
Dynamic Range	\	$20.3dB$	$28.8dB$	$28.3dB$	$22.3dB$	$27.7dB$

As is depicted in Table 3.1, the dynamic range is dependent on the frequency of interest. For $1kHz$, the dynamic range is very small and the sidelope can not be recognised. Also, the total colorbar range is only $7.8dB$. Therefore, the main noise sources cannot be distinguished in this frequency. When it equals to $2kHz$ or higher, the dynamic range can be over $20dB$, which is adequately large. In terms of the noise localization in Figure 3.20, the contour describes the SPL distribution on the virtual plane of interest. To begin with,

it is found that the peak of the contour at all frequencies coincides with the monopole source. However, side lobe level at low frequencies is so high that the resolution of the low frequency is not satisfying. This is in agreement with previous conclusions that the resolution of the array (ROA) is dependent on the array size and frequency of interest f_{oi} (or wavelength λ) when the microphone number is fixed. i.e.

$$ROA \propto \frac{\lambda}{d} = \frac{c}{f_{oi}D} \tag{3.40}$$

In other word, the higher the frequency of interest is, the better the resolution can be. Hence, considering the unsatisfying resolution and dynamic range at low frequencies, in this study, the beamforming in frequency domain was only carried out for $f_{oi} \geq 5kHz$.

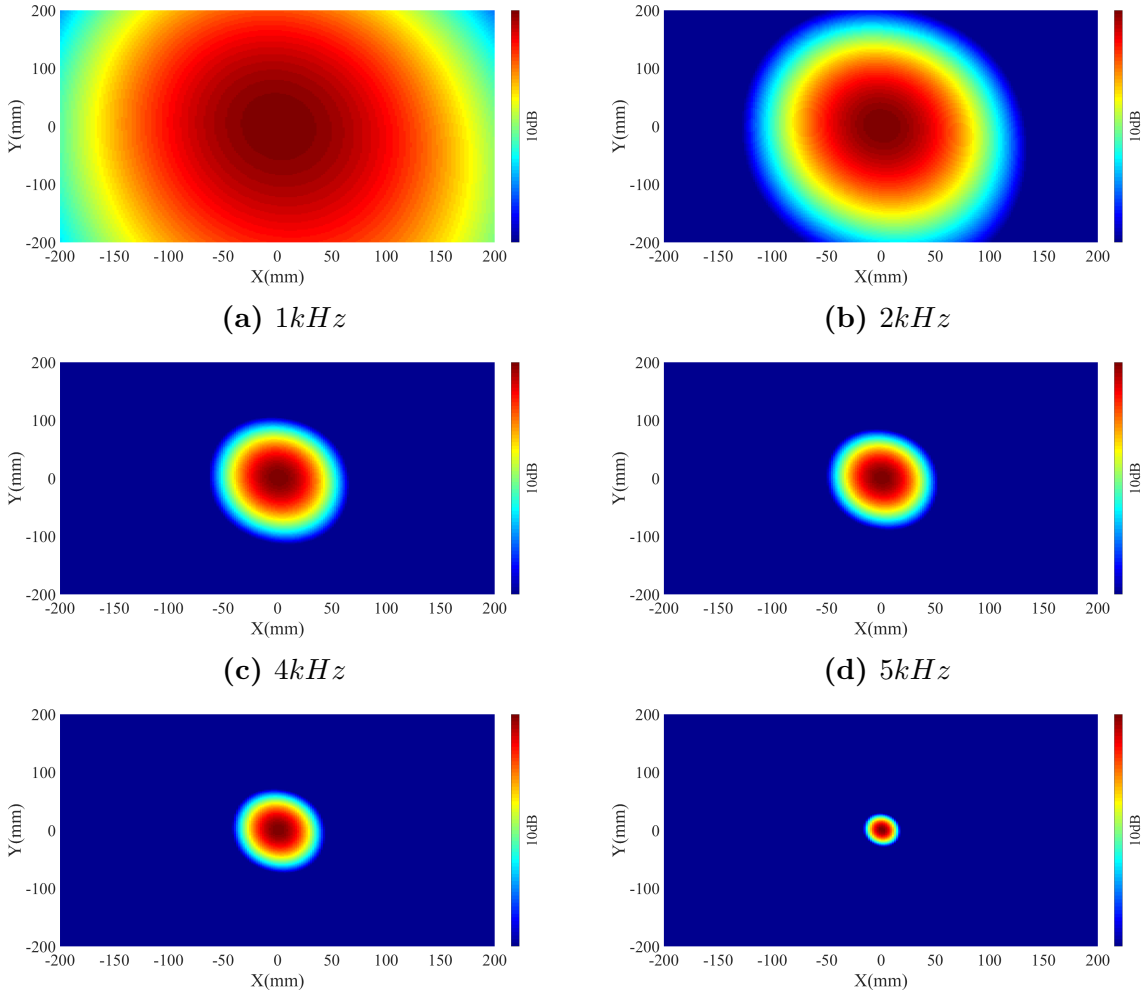

(a) $1kHz$ **(b)** $2kHz$

(c) $4kHz$ **(d)** $5kHz$

(e) $6kHz$ **(f)** $15kHz$

Figure 3.20: Beamforming noise localization with simulated monopole source (frequency domain)

Table 3.2: Dynamic range of the time domain beamforming simulation with a monopole source at different frequencies

Monopole Frequency	$1kHz$	$2kHz$	$4kHz$	$5kHz$	$6kHz$	$15kHz$
Dynamic Range	\	$17.6dB$	$19.5dB$	$16.8dB$	$17.1dB$	$8.3dB$

Likewise, similar conclusions can be also found in the time domain beamforming. In particular, time-domain beamforming using the array pattern was also validated. As a broadband algorithm, time-domain beamforming can process data in a broadband frequency range within a time interval, and it does not require a frequency of interest. However, the resolution is dependent on the signal frequency. Therefore, the monopole source was still used to distinguish the variation of the resolution, processed as a broadband signal. The dynamic range is reported in Table 3.2 and the corresponding noise localization is shown in Figure 3.21. Note that due to the dramatically longer process time compared to the frequency domain beamforming, a more coarse virtual grid was adopted for the time domain. Thus, there is less refined contour in Figure 3.21 compared to Figure 3.20.

Table 3.2 reports the dynamic range in time-domain noise localization, the adequate dynamic range can be attained only when the monopole frequency is high enough. Likewise, in $1kHz$ the main the dynamic range is very narrow. It is found that the resolution of the beamforming increases with the monopole frequency, despite that the monopole is well localised by the peak of the contour. Therefore, the time domain beamforming was only conducted for those one third octave bands whose lower limit is higher than $5kHz$. Besides, it is worth noting that obvious ghost sources arise in Figure 3.21.(f), whose monopole is at $15kHz$. Considering the dynamic range is over 3dB, those high frequency range results are still adopted.

As introduced earlier, beamforming was superimposed on the cut-out captured by the camera attached to the array. As such, the corresponding calibration requires to be performed ahead of the beamforming, termed as image calibration. The calibration is aimed to establish a Cartesian coordinate system in the background cut-out. More specifically, the platform was attached with orthogonal axises, i.e. the white cross shown in Figure 3.22. Note that in Figure 3.22 the nozzle of the wind tunnel is in the centre of the right side. A few grid lines were marked on the axises with equal intervals, with

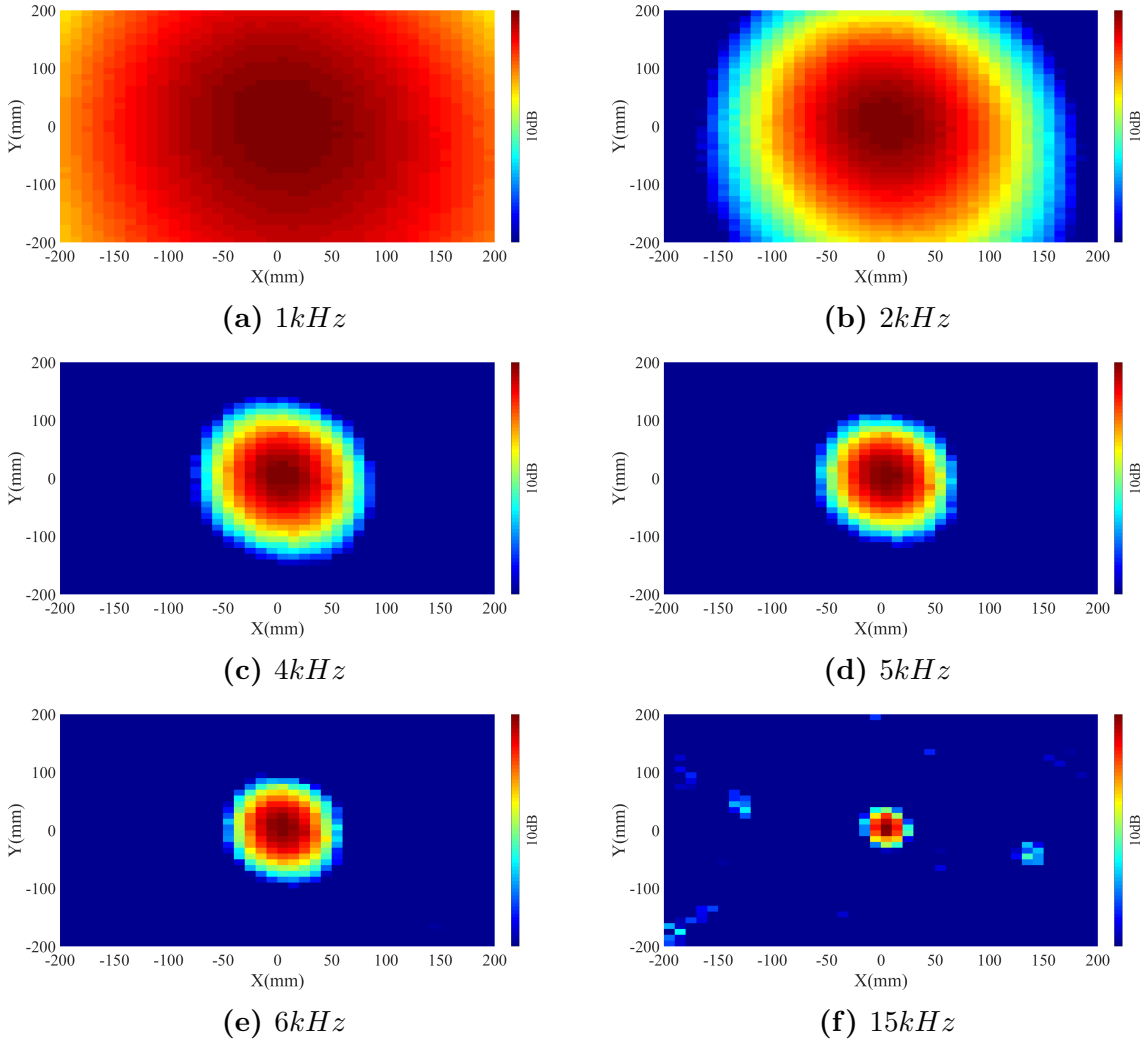

(a) $1kHz$ **(b)** $2kHz$

(c) $4kHz$ **(d)** $5kHz$

(e) $6kHz$ **(f)** $15kHz$

Figure 3.21: Beamforming noise localization with simulated monopole source at different frequencies (time domain)

which the cut-out resolution could be calculated ($603Pixels/m$). Then two indices of the origin in the image matrix were then picked up, which essentially represent the relative location of the origin in the image matrix. With the resolution of the cut-out and indices of the origin, noise sources could be localised on the cut-out.

To validate the accuracy of the noise localization, a calibration technique using one small speaker was conducted. In particular, the speaker was placed on the test platform with different positions as illustrated in Figure 3.23. This speaker generated a tonal signal or broadband signal. Beamforming in the frequency domain and in the time domain was carried out respectively to localise the speaker. For example, the results of the time domain are reported in Figure 3.24.

Figure 3.22: Calibration photo

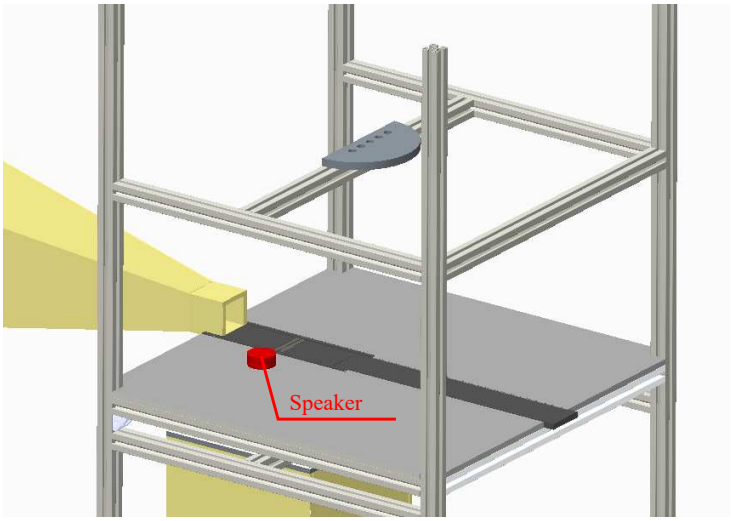

Figure 3.23: Microphone array calibration using one speaker

In Figure 3.24, the speaker emitted broadband noise at different positions and beamforming was carried out. Note that to facilitate reading, the background photo was transformed compared to the calibration photo in Figure 3.22, thereby the wind tunnel is in the centre of the bottom side. This view will be used in the following of the study. In this view, the crossflow blows from the bottom to the top. As such, X axis is streamwise and the Y axis is spanwise. The localization results show that the peak of the SPL contour correctly localises the position of the speaker, which validates the accuracy of beamforming in the time domain. Likewise, same tests were conducted for the frequency domain beamforming. However, the speaker emitted tonal signal instead of the broadband. The

tonal signal was set to be at different frequencies and in different positions. Results also confirmed the accuracy of noise localization. Due to a large number of pictures, results are not displayed in this thesis.

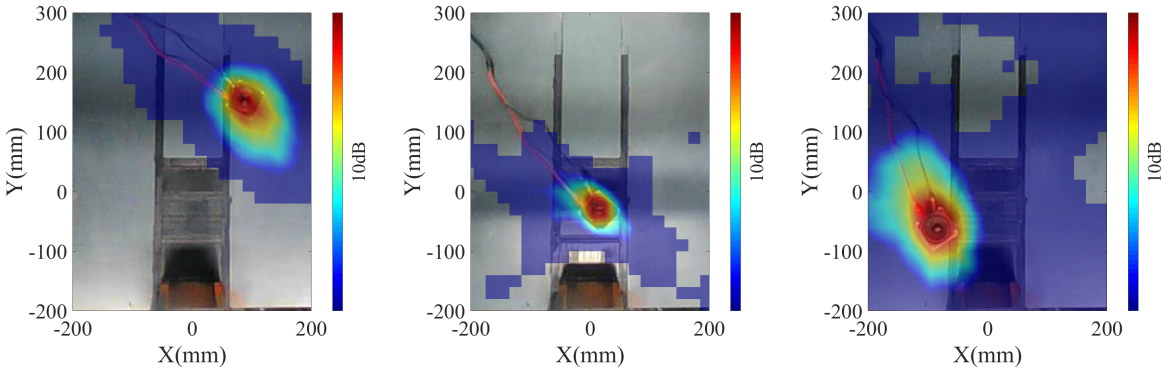

(a) Position I **(b)** Position II **(c)** Position III

Figure 3.24: Speaker source localization (time domain)

3.7 Test Conditions

In this section, the test conditions of the experimental rig are introduced, including the crossflow conditions and background noise conditions.

3.7.1 Crossflow

As mentioned in Section 3.1.1, the crossflow velocity can be manually controlled by adjusting the inlet area of the blower, which allows the crossflow speed to vary within the range in $0-70m/s$. Besides, prior to each measurement, the blower had run enough long time to obtain stable flow conditions, e.g. temperature, which particularly affects the hot-wire measurement. The hot-wire measurement was initially carried out to characterise the crossflow. A spanwise section of the crossflow was measured using the hot-wire, which is $100mm$ downstream from the outlet of the wind tunnel. In the measurement plane, a grid was schemed to perform the measurement and the traverse mentioned above was used to control the sampling position in the grid. The grid spans from the centre of the nozzle to the right side of the flow with a $60mm$ offset, and its height is $40mm$. There are 13 columns of sampling positions inside the grid, the spacing between the columns is 5mm. In each column, the vertical spacing between two sampling points begins from

$1mm$ at the bottom and then alters to $2mm$ when the height exceeds $30mm$. Note that this measurement grid will also be used for how-wire tests in the remainder of this thesis. In the calibration case, U_∞ was controlled to be $50m/s$

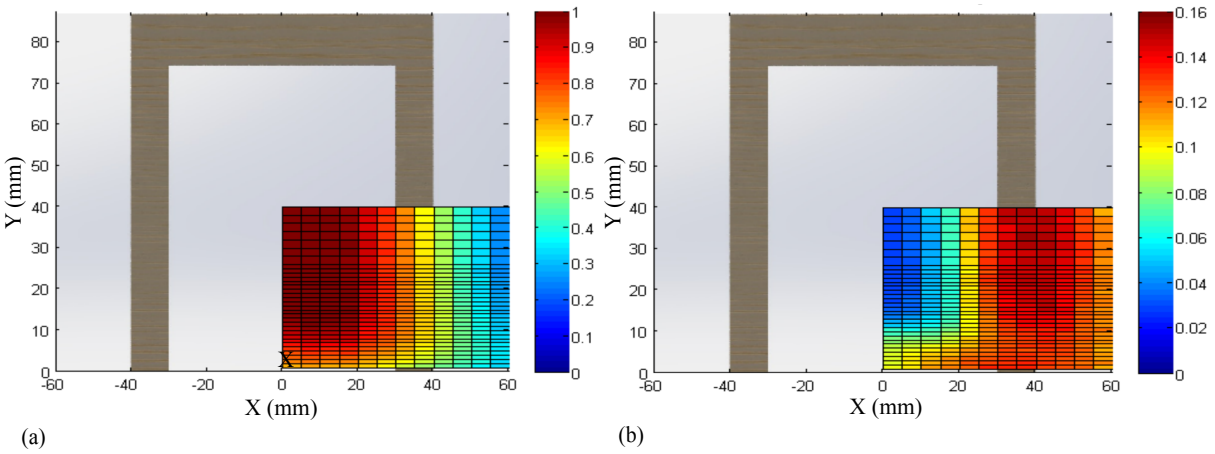

Figure 3.25: Characteristics of the crossflow spanwise section: (a). normalised mean flow velocity; (b). turbulence intensity

Figure 3.25 provides a comprehensive display of the hot-wire results used to determine the normalised mean flow velocity and turbulence intensity of the measurement plane. In Figure 3.25, the relative position of the nozzle outlet is illustrated in scale. From the normalised mean flow velocity contour, it is found that the boundary layer has an influence on the flow less than 10 mm high from the test platform. In the horizontal direction, the velocity begins to decrease when close to the right edge proximity of the nozzle outlet. From the contour in Figure 3.25 (b), it is observed that the central region of the nozzle outlet possesses a turbulence intensity within 2%. The high turbulence level is found in the shear layer on the side and boundary layer in the bottom.

3.7.2 Background Noise

The background noise of the rig can be attributed to a variety of noise sources, e.g. the blower. It was characterised so that pressure fluctuations induced by the sources of interest that will be discussed later can be distinguished.

Figure 3.26 illustrates the spectral of the background noise in the human audible range $(20Hz - 20kHz)$. (a) is the auto-spectrum achieved from Microphone No.1 and (b) is the one third octave band spectrum averaged through all microphones. Both are in the

logarithm scale. In Figure 3.26 (a) it is found that the background noise fluctuates when the frequency is less than 1kHz and would dramatically decline when the frequency is greater than 1kHz. As such, it is suggested that the background noise mainly concentrates in the low frequency range that is less than 1kHz. Additionally, the peak of the spectrum is found to be around $320Hz$. It is unclear where this peak is from, but a possible explanation can be the blade passing frequency of the blower. In Figure 3.26 (b), the background noise likewise begins to dramatically decline after $1kHz$. Therefore, the frequency range of interest will be over $1kHz$.

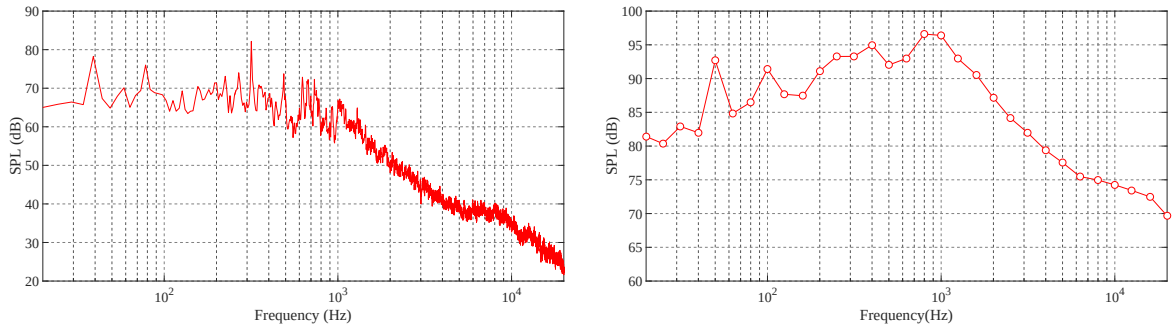

(a) Auto-spectrum achieved from Microphone No.1

(b) One third octave band spectrum averaged through all microphones

Figure 3.26: Noise spectra of the background noise

Chapter 4

Noise Reduction using Dual Planar Jets

In this Chapter, investigations on the use of dual planar jets geometry for the flow-induced noise reduction are introduced.

4.1 Test object and Set-up

As a proof-of-concept study, a generic landing gear assembly was selected to be the test object, which is represented by tandem rods, shown in Figure 4.1 (a). The choice was made based on the mechanisms of the landing gear noise generation, which were summarised in Section 2.1.1. First of all, the flow impinging to the rods can generate turbulence, vortex shedding, boundary layer etc., which are a direct noise source that also exists in the landing gear. Secondly, the turbulent wake of the upstream rod can interact with the downstream rod, which can result in more noise emission. In the landing gear, the interaction between bluff bodies can be found as well. Thirdly, tandem rods can be simplified as a 2D system in a side view, which can facilitate the test set-up and data analysis.

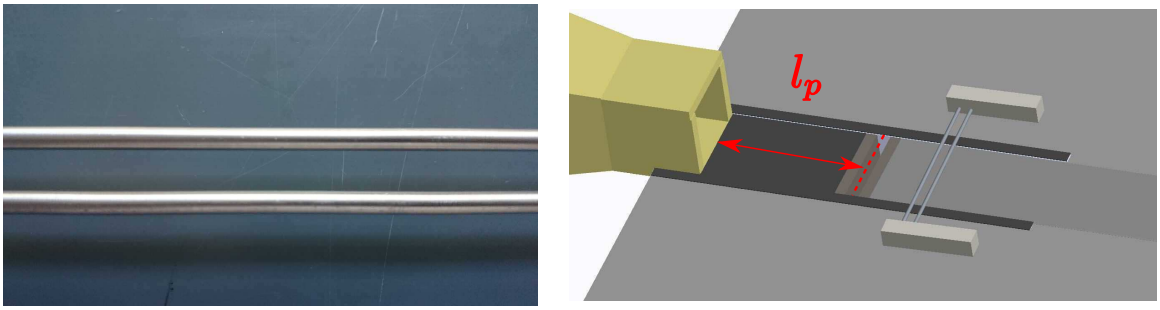

(a) **(b)**

Figure 4.1: (a) Tandem rods used in the experiment; (b) Schematic of test set-up for the single-jet

In experimental tests, the diameter of the tandem rods (D) is 4mm. The pitch between two rods is denoted as P. Previous studies[146, 147] concluded that the specific values of P/D can lead to different flow regimes. For instance, when $2.5 < P/D < 3.2$ intermittent shedding can be detected in the region between two cylinders and the vortex shedding occurs on the rear cylinder. In other word, the vortex shedding mainly takes place and is well established behind the downstream rod. Meanwhile, the interaction exists between the wake of the upstream rod and the downstream rod. The flow features are similar to

the landing gear. As such, it was adopted and P/D was made to be 3 in this study. The rods were supported by two blocks and the span of the rods was much longer than the crossflow width so that those two blocks would not be blown to generate extra noise. For example, the set-up of the single jet geometry is schematically shown in Figure 4.1(b). In addition, the distance from the wind tunnel nozzle to the centre of the primary jet outlet, denoted as l_p, was configured to be $185mm$. Note that the dimension of l_p was fixed in this study, regardless of the variation of the slot width and the jet number.

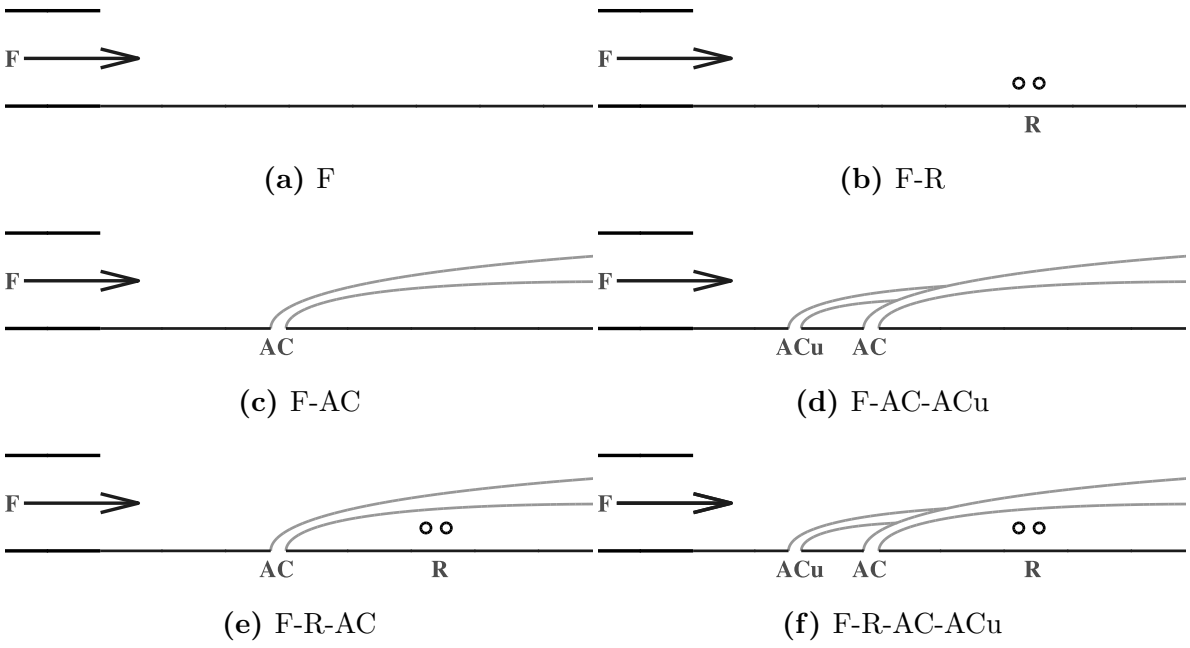

(a) F **(b)** F-R

(c) F-AC **(d)** F-AC-ACu

(e) F-R-AC **(f)** F-R-AC-ACu

Figure 4.2: Geometries of the test campaign

In this study, there are six geometries that were tested. If F, R, AC and ACu are used to denote the crossflow, rods, primary air curtain and upstream air curtain respectively, these six geometries can be abbreviated as F, F-R, F-AC, F-AC-ACu, F-R-AC and F-R-AC-ACu (Figure 4.2). In particular, F is the geometry only with the crossflow. This one was tested as the noise baseline or background noise. Note that when the test was performed, the outlets of the air curtains were sealed to avoid additional cavity noise. In F-R, the rods were installed in the optimised position found in the following section. This position was kept unchanged in all tests with the rods for comparison. Likewise, all outlets of the air curtains were sealed. F-AC and F-AC-ACu are configurations with the air curtains, but the rods are not placed inside. These two geometries were adopted

to characterise the air curtain noise. At last, the rods were replaced to discuss the noise reduction in F-R-AC and F-R-AC-ACu. In addition, in the geometry with dual air curtains, i.e. F-AC-ACu and F-R-AC-ACu, two configurations with different air curtain speed pairs were tested, which will be further discussed in the subsequent section.

Herein, it is worth mentioning again that the sole air curtain in the single-jet geometries and the downstream air curtain in the dual-jet geometries are termed as the primary air curtain (or primary jet). The second air curtain in the dual-jet geometry is termed as the upstream air curtain (or upstream jet). The slot widths of the primary jet and the downstream jet are donated as w_p and w_u. The dimensions of w_p and w_u in this Chapter are 10mm and 8mm. In the experimental set-up, the space between the near sides of two jets, d was 50mm in the dual-jet geometries.

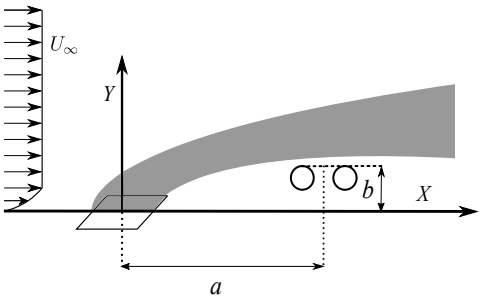

Figure 4.3: Schematic of the rods position

Moreover, the relative position of the rods to the primary jet is illustrated in Figure 4.3, which is depicted in the same Cartesian ordinate system used throughout this thesis. In Figure 4.3, a is the distance between the origin and the centre of the primary jet outlet, b is the top height of the rods. Values of a and b will be optimised and determined in the flowing section. Hereinafter, the optimised values of a and b are termed as the shielding position and the shielding height of the planar jet regardless of the jet number, which are denoted as a_0 and b_0.

4.2 Shielding Optimization

As mentioned in Section 2.1.3, the air curtain can deflect the incoming flow (crossflow), thereby reducing the local flow speed around the bluff body. In other word, the shielding to the bluff body plays a crucial role in the noise reduction using the air curtain. The

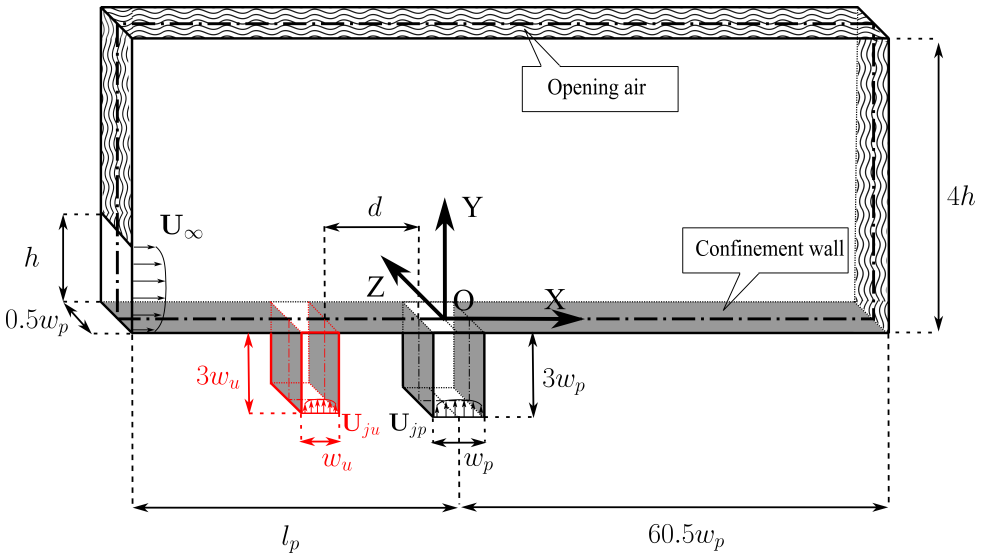

Figure 4.4: Computational domain of the flow simulation

flow structure in the shielding area of an air curtain is described in detail in Section 2.2.2.1, e.g. the recirculation zone. The complexity of the shielding area necessitates optimization in the use of the air curtain for noise reduction. To be more specific, how to find the shielding position and the shielding height for a particular jet. Therefore, the optimization was conducted in this chapter using CFD simulations.

4.2.1 Numerical Approach

In order to optimise the use of the air curtain for noise reduction, including both the single-jet and the dual-jet geometries, it is of great importance to investigate the flow regime, which can be simplified as the planar jet in crossflow. As such, the steady CFD simulation is employed to predict the flow features.

4.2.1.1 Computational Domain and Boundary Conditions

The entire computational domain for this study is illustrated in Figure 4.4, which reproduces the exact configurations used in the accompanying experiment introduced above. For the planar jet in crossflow, symmetry exists related to the centre plane of the regime. In this study, a 3D simulation was adopted to approximate the flow and the side boundaries were set to be translational periodic.

In Figure 4.4, the same Cartesian coordinate system is established, with the parameters

of this domain represented using different symbols. In particular, h denotes the height of the crossflow inlet, which can eject the crossflow with a speed of U_∞. From the crossflow inlet to the origin, the horizontal distance of the confinement, likewise, denoted as l_p. In order to capture potential flow features at the exit region of the nozzle, the nozzle depth is set to be $3w_p$. The jet is ejected with a speed of U_{jp} from the bottom of the nozzle so that it can fully develop before being deflected. The distance from the origin to the right side limit of the domain, including a half width of the primary jet outlet and the confinement downstream to the primary jet, is controlled to be $60.5w_p$, which is long enough to capture the flow characteristics. Moreover, when the dual-jet geometry is simulated, one more jet nozzle, i.e. the upstream jet with a speed of U_{ju}, is added inside the rig. The nozzle is highlighted in the red color in Figure 4.4 and the depth is $3w_u$. As mentioned above, the distance between near-side edges (d) is used rather than between centres. In terms of the entire domain, the height (Y direction) is set to be $4h$ excluding the jet nozzle depth, and the length (X direction) is $60.5w_p + l_p$. Besides, as mentioned earlier the translational periodic boundary condition is adopted for the front side and the back side of the domain in Figure 4.4. As such, the width (Z direction) of the domain is set to be $0.5w_p$ to reduce the computational cost. Because dimensions of the domain were controlled to reproduce the accompanying experiment, h, l_p, w_u and w_p designed to be 75mm, 185mm, 8mm and 10mm respectively.

On the boundary conditions of the air curtain inlet, previous numerical studies[148, 149, 150, 151] with the major focus on the planar jet (in crossflow or coflow) generally utilised a parabolic velocity profile for the jet inflow condition. Likewise, in this study the primary jet outflow velocity profile is adopted and expressed as [148]:

$$\frac{u_{jp}}{U_{jp}} = 1 - (\frac{x_p}{0.5w_p})^8 \tag{4.1}$$

where x_p is the local spanwise coordinate (X direction) whose origin is in the centre of the inlet. U_{jp} is the amplitude of the planar jet velocity (maximum velocity at the centre of the nozzle). In this study, it is also used to denote the primary jet speed. The turbulence level is defined through the turbulent kinetic energy k and the turbulent dissipation ϵ[152].

More specifically,

$$k = I_j(u_j)^2 \tag{4.2}$$

$$\epsilon = C_\mu \frac{k^{\frac{3}{2}}}{0.03e} \tag{4.3}$$

The turbulence intensity I_j is made to be 5%. Additionally, the boundary condition of the crossflow is managed to be similar with the jet except that the turbulence intensity is higher (6%). Additionally, all confinement is non-slip walls and other boundaries are opening air, allowing the flow to leave and re-enter the domain freely. Velocities of each simulation case are listed in Section 4.2.3.

4.2.1.2 Turbulence Model

The correct turbulence model should be used in order to resolve the major flow features in the computational domain. Turbulence strongly affects the important global features of the flow, so an accurate and reliable prediction of turbulent flow phenomena is essential. Based on the flow physics and computational requirements, depending on the generated grid and accuracy, a decision on the suitable turbulence model can be made [153, 154]. In this case, the conservation laws for incompressible flow, namely continuity, and momentum equations are used together with an appropriate turbulence model for CFD simulations. The primary factor in achieving accurate results is the choice of turbulence model, rather than the other investigated parameters. The RANS turbulence models are broadly used in practical modelling for suitable accuracy and efficiency. Through a comprehensive investigation, the effect of the different turbulence models on the results is investigated in this study, trying to make the final decision on the appreciate model. As a common problem in $k-\omega$ turbulence model, the model is extremely sensitive to the inlet free stream turbulence properties. The specific formulation of the Shear Stress Transport (SST) turbulence model allows switching between $k-\epsilon$ and $k-\omega$ behaviours depending on the level turbulence in the flow fields, in an attempt to use the best of both and also avoid the common problems in each of them. SST model is found to suit best in order to achieve most accurate results, as a compromise between well modelling the major turbulent features in the computational domain and keeping the computational costs as low as possible.

4.2.1.3 Meshing and Calculation

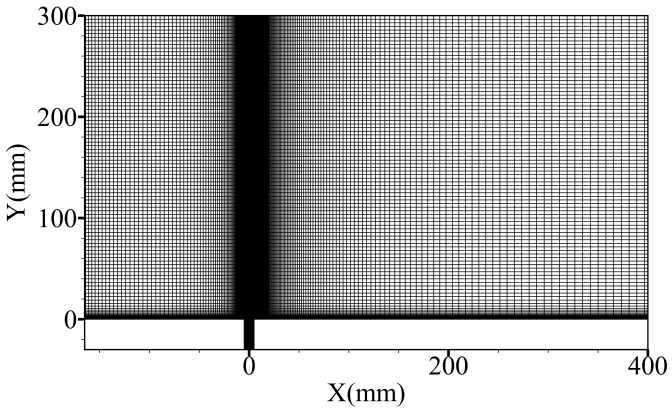

(a) single-jet configuration

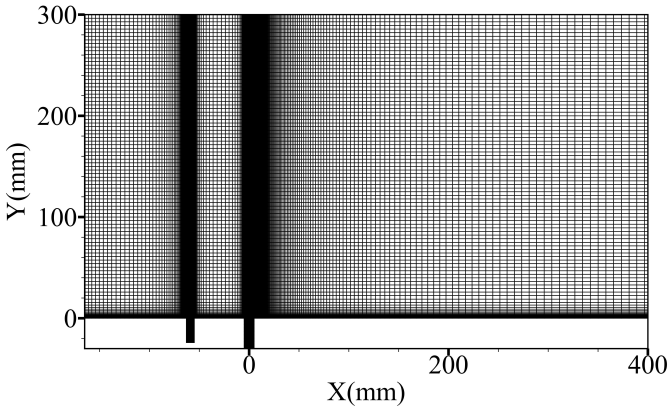

(b) dual-jet configuration

Figure 4.5: Front view of the meshes used for the numerical study

Meshing is a crucial part of the entire CFD process and it has a great influence on the solver convergence and accuracy. In this study, a few factors were considered for the mesh generation. To be more specific, in order to capture the laminar and transitional boundary layers correctly, the location of the nearest grid cell to the wall should approximate $y^+ = 1$. In the meantime, since the interaction region of the planar jet and crossflow is relatively more complicated, a refined grid should be adopted in this region. The ICEM CFD was employed to create the mesh in this study. As is illustrated in Figure 4.5, mesh examples of both the single-jet and the dual-jet configurations are illustrated in a front view. Furthermore, the section of $x = 0$ from a side view of the mesh is shown in Figure 4.6. As discussed earlier, the translational periodic boundary condition is applied to the

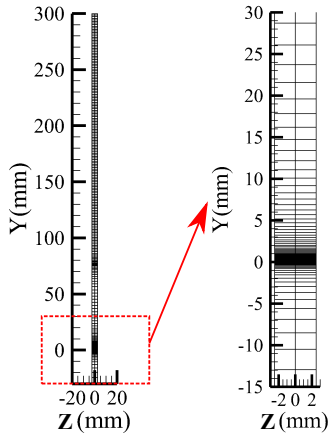

Figure 4.6: Side view of the mesh used for the numerical study (x=0)

front side and back sides of the mesh, which means the 3D simulation is in effect equivalent to a 2D flow. Therefore, the thickness of the mesh has little impact on the simulation result, and the number of the mesh layers on the side view can be managed to be very a few to reduce computational cost. Thus, as illustrated in Figure 4.6, there are only 2 layers on the side view of the mesh in this study.

In CFD simulation, the refinement level of mesh can lead to variation in the simulation results to a different extent, which necessitates the analysis of the mesh resolution independence, which is termed as the mesh sensitivity analysis. In this study, the sensitivity of the mesh was carefully investigated. For instance, five meshes with the different refinement of the single-jet, whose sizes are reported in Table 4.1, were used to assess the impact of grid resolution on results of velocity profiles at different locations. The process for the mesh sensitivity study is described in the following in detail. Figure 4.7 gives the flow speed contour of the test case acquired by PIV experiment (both U_∞ and U_{jp} were designed to be $40m/s$, from the measurement $U_\infty = 40.23m/s$, $U_{jp} = 40.15m/s$). Both X and Y are normalised and non-dimensionalised by w_p. the acquisition of this PIV data will be discussed in the flowing section. Then four vertical speed probes were extracted at X/w_p =-3, 3, 6 and 9 respectively, termed as P1, P2, P3 and P4 in Figure 4.7. Profiles of these four probes have been used for numerical model validation as well, which will be also described in the subsequent section.

Figure 4.8 is the corresponding speed profiles of the four probes acquired by simulations, which displays Y/w_p against u/U_∞. Note that in order to highlight the difference

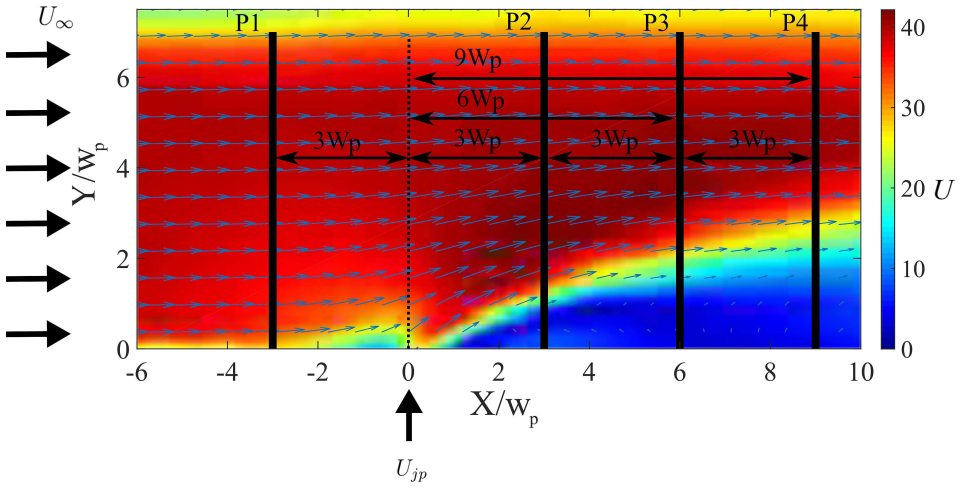

Figure 4.7: Speed probes for the numerical mesh independence study as well as model accuracy validation (The PIV velocity contour of the flow field with $U_\infty = 40.23m/s$ and $U_{jp} = 40.15m/s$, i.e. Case 6 in Table 4.2)

Table 4.1: Meshes with different refinement used for sensitivity study (Single-jet)

Mesh No.	1	2	3	4	5
Nodes	270,744	303,648	367,860	404,775	496,044

clearly, a limited range of Y/w_p is shown. It is found that the simulation is less independent of the mesh downstream (P4) than the upstream (P1). As such, P4 can be used to conduct the mesh independence evaluation. In Figure 4.8.(d), Mesh 3 is only at most 1% (percentage offset against Mesh 5) away from Mesh 5, i.e. the finest one. With a good order of approximation, we can proceed with Mesh 3 as it is acceptable that the final selection causes only 1% difference from the finest one while having much less computational cost. Therefore, Mesh 3 is sufficient enough to obtain a numerical solution, which is independent of the grid resolution and was used for the simulations in this study. Likewise, the mesh independence analysis was also performed for the dual-jet configuration and the final mesh possesses 500,688 nodes. In addition, it is advisable to use 2nd order upwind discretization scheme for mean flow, turbulence and transition equations. All calculations were carried out using ANSYS CFX 14.5 as the solver.

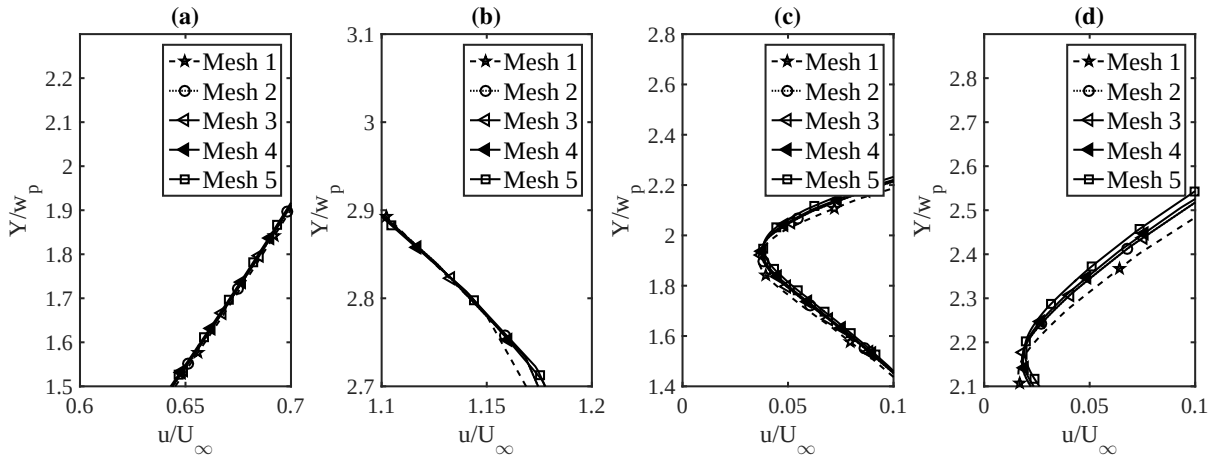

Figure 4.8: Mesh sensitivity analysis over speed profiles at different locations: (a) P1(X/w_p =-3); (b) P2(X/w_p =3); (a) P3(X/w_p =6); (a) P4(X/w_p =9)

4.2.2 PIV frame assembly and set-up

As mentioned earlier, the model was validated through 2-D PIV experiment. The experiment was carried out with the rig described in Section 3.1 and Section 3.4. However, due to the limitation of PIV frame size, the conventional 2-D PIV measurement cannot capture the entire development of the jet in a crossflow. Therefore, a frame assembly approach was conducted in this study, which is introduced in this section.

Since the proposal of PIV was put forward, this technology has been applied to a wide range of flow research [104, 155] to provide a quantitative measurement of the flow field. In the meantime, the improvement in both data process algorithm and hardware installation has been progressing. So far in addition to the normal 2-D PIV, there are 3-D stereoscopic PIV, micro-PIV, tomographic PIV, etc., which have been developed for various applications. Most of these new types are equipped with more than one camera or special cameras. However, it is not rare that there is only one normal 2-D PIV system in the lab with a single camera. When the analysis is conducted, due to the limitation of the camera view range, it is difficult to fully capture the flow field of interest. In addition to adding one more camera, one solution is to enlarge the window size by moving the camera farther from the focus plane. However, the resolution can be drastically reduced is this way is utilised. As such, an approach to assembling frames is adopted for the time mean analysis in this study, which is able to achieve a complete flow structure of interest. In particular, when a large number of PIV image pairs at different positions are processed

and averaged to acquire time-mean flow field, the algorithm can assemble these frames into a continuous one. Note that these frames continuously distribute in the streamwise direction with partial overlap. This approach was used to investigate the flow regime of the jet in a crossflow. The method will be depicted in detail in the remainder of this section and the algorithm is introduced through an example of dual jets in the crossflow. The data are processed with Davis software and an open-access Matlab toolbox–PIVMat. Davis was used to carry out data acquisition and process the raw image pairs to achieve vector flow field. The vector flow field then was post-processed with PIVMat [156].

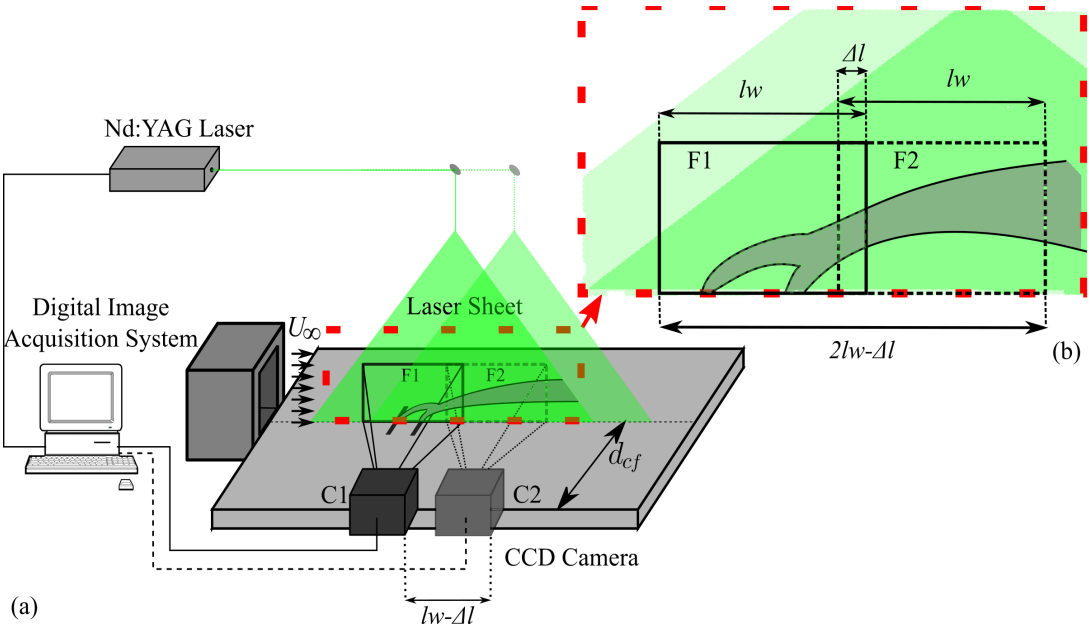

Figure 4.9: Schematic of the PIV test set-up

1.Algorithm

The entire PIV set-up is schematically shown in Figure 4.9 (a), in which two planar jet outlets are inside the crossflow. As introduced earlier, the centrelines of the wind tunnel, endplate and jet outlets aligned with each other. The LaVision Flowmaster 3 CCD camera was attached beside the endplate so that the lens was parallel to the laser sheet. The distance from the laser sheet to the lens, d_{cf} was controlled to be 500mm. As a consequence, the size of camera view range was 125.31mm×83.92mm, 125.94mm was the dimension of l_w in Figure 4.9 (b). Note that the X coordinate of the frame left limit is -71.09mm, and the right limit is $38.22mm$. In addition, the camera could be horizontally traversed to a different position beside the endplate to attain another view range of the

flow. In the meantime, the laser sheet could move as well along with the camera.

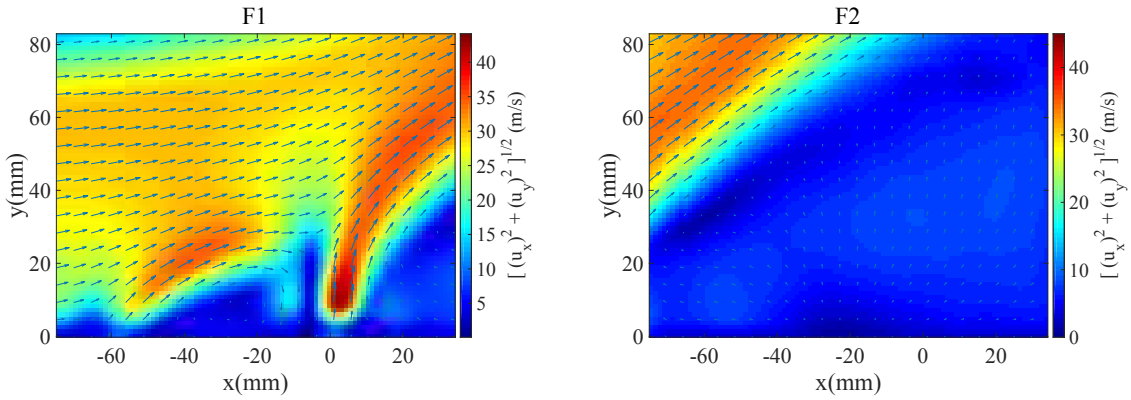

(a) F1 **(b)** F2

Figure 4.10: Mean flow fields of F1 and F2

The PIV assembly begins with paired image acquisition. In particular, there are two sampling positions, i.e. C1 and C2 in Figure 4.9 (a). The camera was traversed and successively situated at C1 and C2. It is worth noting that calibration was conducted only at C1. Then the translation between C1 and C2 is denoted as $l_w - \Delta l$, which must be smaller than l_w. In this experiment $l_w - \Delta l$ was controlled to be $100mm$. 500 paired images were acquired at each position respectively. Those images were processed with multi-pass correlation of 32×32 (50% overlap) and 16×16 (25% overlap) in Davis. The file extension of the result data that Davis saved is ".vc7", which can be directly loaded and processed in Matlab using the toolbox for the post-process. There are a few PIV process toolboxes that can be downloaded online with free access such as PIVlab, Openpiv, PIVMat. In this study PIVMat was utilised to perform the analysis. The data were loaded for each frame in Matlab, as a structure array. The array includes two matrices and two vectors, which are the core data in the entire array. These two matrices, with a size of 85 × 107 in this study, contain the velocity components in X and Y respectively at each pixel. As such, the results were averaged so that a time-mean flow field can be achieved at different positions, shown in Figure 4.10 (a) and (b). As the two matrices possess same structure but different element values, they can be respectively denoted by one capital letter. In other word, one capital letter can be used to denote both matrices, **A** for F1 and **B** for F2. As such, the mean of **A** and **B** can be expressed as:

$$\bar{\mathbf{A}} = \{\mathbf{a}_1, \mathbf{a}_2, ..., \mathbf{a}_{\beta-1}, \mathbf{a}_\beta\}_{\alpha\times\beta} \tag{4.4}$$

$$\bar{\mathbf{B}} = \{\mathbf{b}_1, \mathbf{b}_2, ..., \mathbf{b}_{\beta-1}, \mathbf{b}_\beta\}_{\alpha\times\beta} \tag{4.5}$$

where $\alpha = 85$ and $\beta = 107$. In the meantime, their corresponding coordinates are provided in the two vectors mentioned above, termed as the coordinate vectors. These two vectors contain the position information in two orthogonal directions, i.e. X and Y. More specifically, 107 elements in X direction and 85 elements in Y direction. It is worth noting that when the camera is traversed, the coordinate vectors will not vary with the camera position because the calibration is referred to its own frame. Thus, these two vectors in both F1 and F2 are denoted as $\mathbf{X}_\beta$ and $\mathbf{Y}_\alpha$ for X and Y respectively. Elements inside these vectors are the real X and Y coordinates of each pixel rather than the pixel indices, and the vectors hereinafter are expressed as:

$$\mathbf{X}_\beta = [x_1, x_2, ..., x_\beta - 1, x_\beta] \tag{4.6}$$

$$\mathbf{Y}_\alpha = [x_1, x_2, ..., x_\alpha - 1, x_\alpha] \tag{4.7}$$

As such, the number of the elements in stream-wise dimension inside Δl can be written as:

$$n = [\beta \times \frac{\Delta l}{l_w}] \tag{4.8}$$

where"[ ]" gives the round integer of the inside value.

The new assembled frame is a combination of F1 and F2 with removing the superposition in F2. Therefore, the length of the new frame is as long as $2l_w - \Delta l$ and the matrix size for the new assembled frame should be as long as $2\beta - n$. In addition, a coefficient is added inside for the correction, denoted as *co*. The value of *co* is dependent on continuity, which can be any of 0, 1, 2, etc. As such, the new assembly is as long as $2\beta - n + co$. If denoted as $\bar{\mathbf{M}}$, the assembled mean velocity matrix can be written as:

$$\bar{\mathbf{M}} = \{\mathbf{a}_1, \mathbf{a}_2, ...\mathbf{a}_{\beta-1}, \mathbf{a}_\beta, \mathbf{b}_{n+c}, \mathbf{b}_{n+c+1}, ...\mathbf{b}_{\beta-1}, \mathbf{b}_\beta\}_{\alpha\times(2\beta-n+co)} \tag{4.9}$$

Furthermore, the assembled coordinate vectors for X axis can be expressed as:

$$\mathbf{X'} = \{x_1, x_2, ...x_{\beta-1}, x_\beta, x_\beta+\delta, x_\beta+2\delta, ...x_\beta+(n-c-1)\delta, x_\beta+(n-c)\delta\}_{1\times(2\beta-n+co)} \quad (4.10)$$

where δ is the real position interval between two adjacent values in $\mathbf{X}_\beta$. Note that δ is a constant regardless of in $\mathbf{X}_\beta$ and $\mathbf{X}_\beta$, and the value is only dependent on the calibration. Obviously, the assembled coordinate vectors for Y remains to be same, i.e.

$$\mathbf{Y'} = \mathbf{Y}_\alpha \quad (4.11)$$

Then the new array including $\bar{\mathbf{M}}, \mathbf{X'}$ and $\mathbf{Y'}$ can be achieved and shown using PIVMat (Figure 4.11). The assembled PIV frame was used to validate CFD model in this Chapter. Moreover, the investigations on the leeward edge of the jet in a crossflow in Chapter 5 is based on the assembled frame as well.

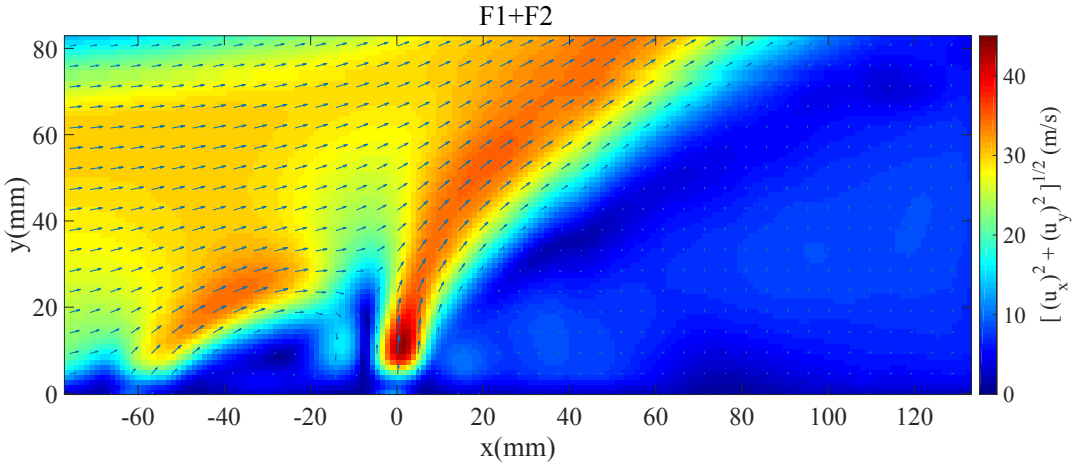

Figure 4.11: Assembled frame of F1 and F2

2. Selection of *co*

This approach can be of good use when there is a limited field of view for the PIV camera. Therefore, it is necessary to discuss the quality of this assembled frame. As an assembly of multiple frames, continuity plays an important role. As mention earlier, continuity has a direct influence on the choice of *co*. Therefore, the variation of the continuity with *co* can be criteria for the selection between the choices of *co*.

For the continuity analysis in this study, horizontal velocity profiles are used. More specifically, Figure 4.12 is the same assembled frame depicted above. It has been known that the joint is somewhere around $X = 38.22(mm)$, whose uncertainty due to the round

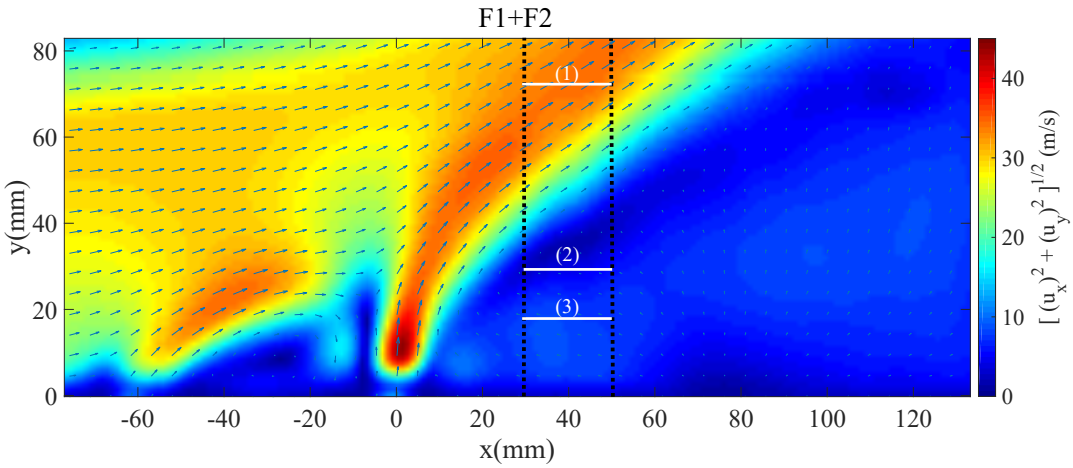

Figure 4.12: Example of the continuity analysis probes

calculation mentioned above as well as the value of *co*. Therefore, three random horizontal probes were extracted to evaluate the continuity, starting from $30mm$ and ending at $40mm$. However, those probes should be averted from being inside the area with high velocity gradient. This is because the velocity profile from the high gradient area may be mistaken as incontinuous. For example, those in Figure 4.12, they are $y = 18.61mm$, $y = 28.11mm$ and $y = 70.88mm$. These probes, their corresponding velocity profiles are shown in Figure 4.13 with different *co*. In the meantime, the junction inside each sub-figure and its adjacent positions are highlighted with a rectangle. From the comparison between different *co*, it is clear shown that the continuity of the speed profile is affected by the value of *co*. The best continuity occurs when $co = 1$. Therefore, in this study *co* was set to be equal to one.

The performance of this assembly method is obviously affected by other factors as well, e.g. the dimension of l_w, Δl and d_{cf}, set-up of the multi-pass correlation, etc. In this study, they are not discussed.

4.2.3 Simulation Campaign and Numerical Model Validation

In this study, a serious of systematic and parametric simulations were conducted. Table 4.2 reports the initial conditions of all cases. In particular, Cases 1-10 are for the single-jet geometries corresponding to F-AC and Cases 11-17 are for the dual-jet geometries corresponding to F-AC-ACu. Meanwhile, in order to validate the numerical modelling, both single-jet and dual-jet models were compared with the experimental cases that have

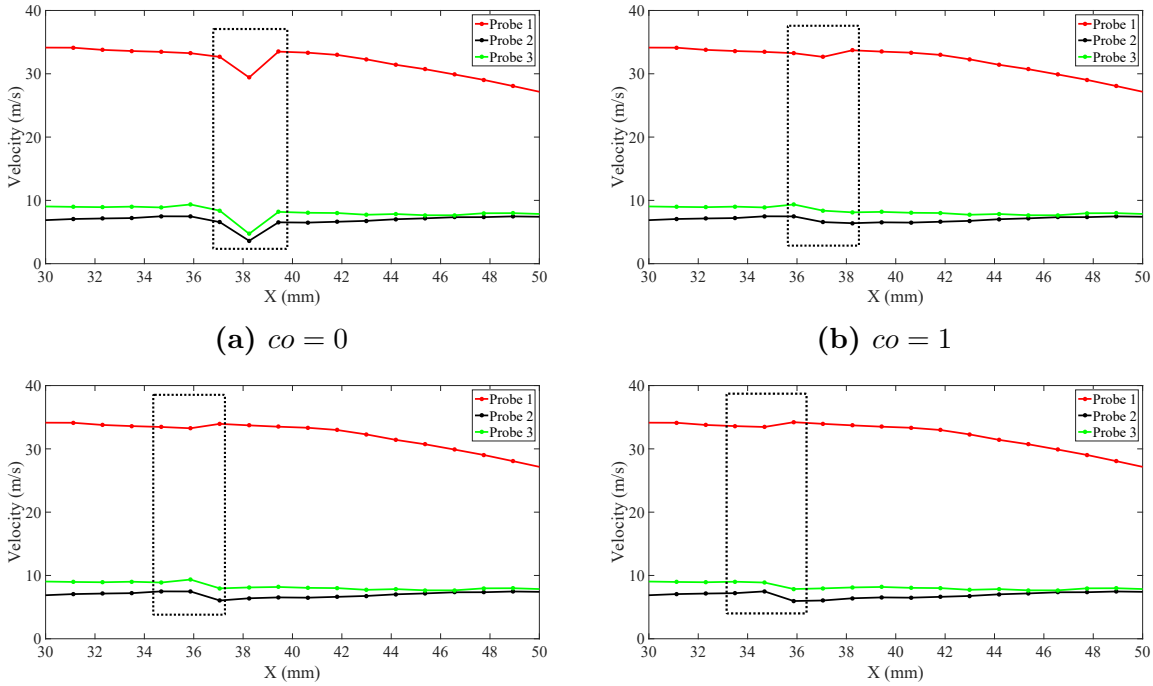

(a) $co = 0$ **(b)** $co = 1$

(c) $co = 2$ **(d)** $co = 3$

Figure 4.13: Continuity analysis of the frame assembly

same flow initial conditions, i.e. Cases 6 and Case 17. The validation of the single-jet modelling is described in the following as an example.

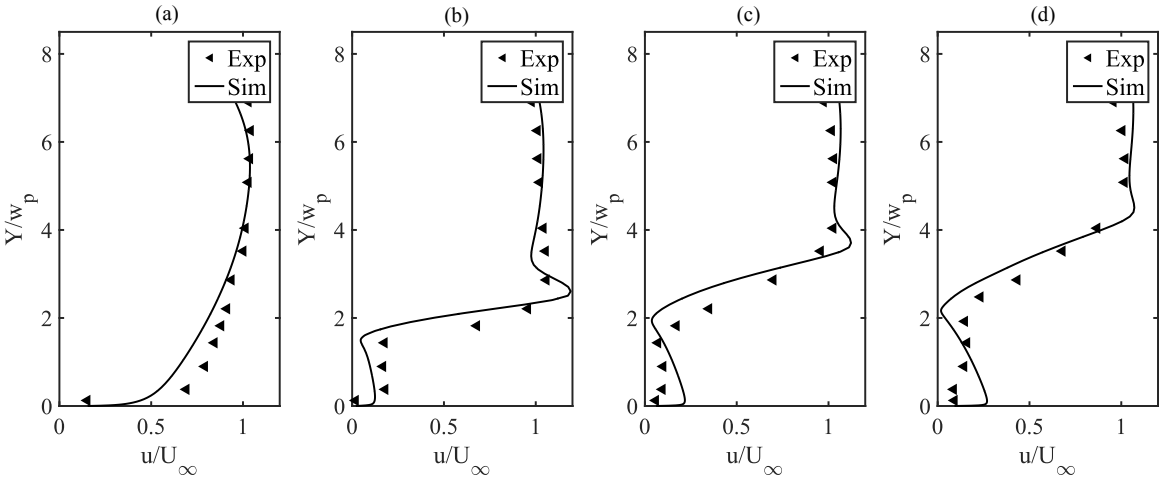

Figure 4.14: Comparison between experiment and simulation in terms of the normalised speed profile of the validation sections: (a)P1 (b)P2 (c)P3 (d)P4

As mentioned earlier, the numerical model for F-AC was validated with experimental data acquired by PIV. To be more specific, Case 6 in Table 4.2 was checked based on the

Table 4.2: Simulation matrix

Run No.	U_∞	U_{jp}	U_{ju}	w_p	w_u
1	60 m/s	60 m/s	/	10mm	/
2	50 m/s	60 m/s	/	10mm	/
3	50 m/s	50 m/s	/	10mm	/
4	50 m/s	40 m/s	/	10mm	/
5	50 m/s	30 m/s	/	10mm	/
6	40 m/s	40 m/s	/	10mm	/
7	30 m/s	30 m/s	/	10mm	/
8	50 m/s	50 m/s	/	8mm	/
9	50 m/s	50 m/s	/	12mm	/
10	50 m/s	50 m/s	/	14mm	/
11	50 m/s	50 m/s	40m/s	10mm	8mm
12	50 m/s	50 m/s	30m/s	10mm	8mm
13	50 m/s	50 m/s	20m/s	10mm	8mm
14	50 m/s	40 m/s	30m/s	10mm	8mm
15	50 m/s	40 m/s	20m/s	10mm	8mm
16	50 m/s	30 m/s	20m/s	10mm	8mm
17	40 m/s	40 m/s	30m/s	10mm	8mm

experimental data from PIV with identical test set-up and initial conditions. Since the key to reducing the noise is to reduce the impinging speed, the flow speed is the most important factor that needs to be taken into account and therefore, it was chosen to be the validation criterion. In other word, speed profiles of the sampling sections as same as those used for sensitivity study (Figure 4.7) were compared. Figure 4.14 shows the velocity profiles of both experimental and numerical results. All graphs were plotted with Y/w_p against u/U_∞. As illustrated in Figure 4.14, the trend of the profiles from the simulation is in good agreement with experimental data. However, in terms of the value for each sampling point, the difference between simulation and experimental results still exists. If the difference is quantitatively defined as $(r_{sim} - r_{exp})/r_{exp}$, where r is u/U_∞, it is found that for each sampling point the difference is within 10%. Therefore, it is reasonable to conclude that this model is sound enough to be applied for the flow prediction. Likewise, same validation process was conducted for the simulation model with dual jets by Case 17. Within the error range, it can be applied for the prediction as well.

4.2.4 Optimization

4.2.4.1 Theoretical Model

Unlike the circular jet which has far more engineering applications, the planar jet has attracted less research interest. For the single planar jet in crossflow, the study by Ramaprian and Haniu[42] provides the best model to date to predict the trajectory of the air curtain in the flow regime, which has been introduced in Section 2.2.2.1. In the model, the centreline of the jet is written as:

$$\frac{y}{l_m} = 1.2(\frac{x}{l_m})^{0.54} \tag{4.12}$$

As mentioned in Section 2.2.1, one linear jet issuing into a quiescent air spreads with a half width can be expressed by Equation 2.8. If the virtual origin is ignored, i.e. making $C_2 = 0$. Equation 2.8 can be simplified as:

$$b_{1/2}(x) = C_1 x \tag{4.13}$$

with x being the distance along the centreline of the jet from the exit slot. C_1 a coefficient varying between 0.09 and 0.12 (Table 2.2[56]). However, the planar jet in a crossflow possesses significantly different flow conditions due to the co-flowing ambient velocity along the windward edge, the strong curvature along the edge trajectories and the consequence of a recirculation zone which can develop under the leeward side of the jet. These three factors influence the stability and entrainment of the outer and inner shear layers. Ramaprian and Haniu[42] found that the planar jet in a crossflow tends to have a larger spreading rate. If the width of the jet is estimated to be:

$$b_{1/2}(s) = C_b s \tag{4.14}$$

where s is the curved centreline trajectory in the natural system (Figure 2.22 in Section 2.2.2.1) and C_b is the proportionality constant, which was found to be between 0.12 and 0.15 in their studies.

Validation of the theoretical model was conducted through flow visualization. Figure 4.15 shows the results for the single-jet (U_∞ =50.45 m/s, U_{jp} = 50.23 m/s) and the dual-jet (U_∞ = 50.45 m/s, U_{jp} = 49.86 m/s, U_{ju} = 40.96 m/s) geometries. Each of them

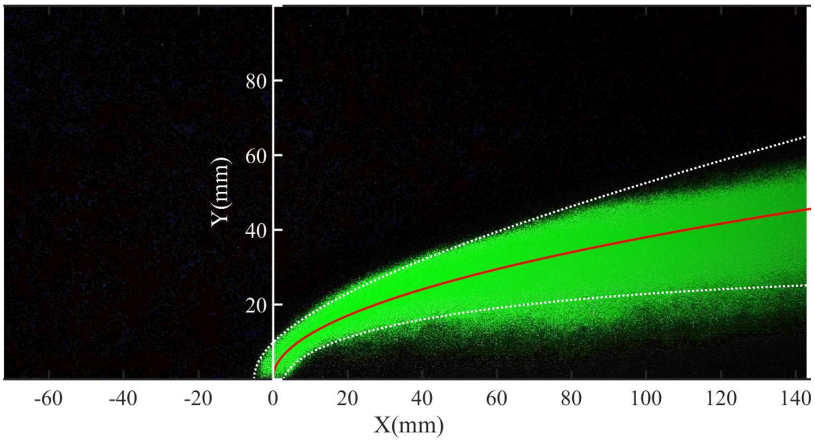

(a) Single air curtain

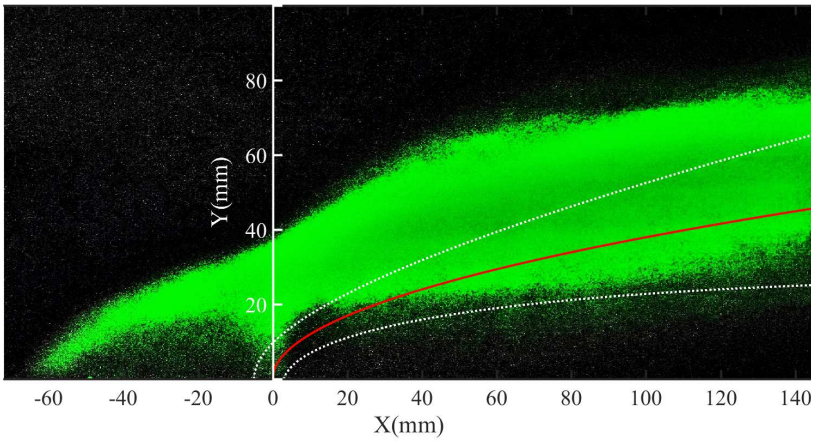

(b) Dual air curtains

Figure 4.15: Results of the flow visualization

is an average of 50 images. The contrast ratio and brightness of them were enhanced and adjusted to highlight the flow pattern. More importantly, as discussed earlier, those pictures were calibrated and accordingly the same 2-D Cartesian coordinate system used throughout this study was established, which enables the jet centreline trajectory as well as the edges to be superimposed. From Figure 4.15.(a), it is found that the model can well capture the curvature of the jet in the outlet proximity. But being a quadratic curve, the model cannot well predict the jet pattern further downstream. This downstream inaccuracy may be explained by the recirculation induced by the air curtain. Therefore, an improved model, which can better describe the flow pattern, especially further downstream

is required. Moreover, the same curves were superimposed on the dual jets geometry as well, which will be discussed later on.

4.2.4.2 Numerical Analysis

Figure 4.16.(a) is an example of the speed contour acquired with CFD simulation for Case 3. In addition, the streamline that passes the centre of outlet is illustrated, which is defined as the centreline trajectory of the primary jet for both single-jet and dual-jet geometries. As seen in Figure 4.16.(a), a low speed area is induced behind the air curtain due to the shielding from the crossflow. However, inside the low speed area, there is a relatively high speed flow in the endplate proximity, but the speed of this part is still much lower than the region beyond the shielding. As shown in the corresponding streamline graph in Figure 4.16.(b), this part can be attributed to the recirculation that is induced by the air curtain itself. As a consequence, this low speed area, as well as the recirculation inside, should be taken into account in order to find the best relative position.

As introduced earlier, the shielding position and shielding height are determined based on the simulation. When an air curtain is applied to flow-induced noise reduction, its shielding height must be adequate to fully shelter the bluff body so that noise can be maximally reduced. However, the high jet speed required by a high shielding height can lead to an increase in the jet noise emission, not to mention the accompanying extra energy consumption. As such, taking all factors discussed above into account, it is reasonable to make the shielding position, a_0 align with the centreline peak, where in effect the maximum shielding stays when a jet is given.

For the single jet, a parametric analysis was performed with the model in order to determine the dependence of the centreline trajectory on U_∞, U_{jp}, R and w_p. Results are shown in Figure 4.17. Because the cases in Figure 4.17(b) and (c) have same w_p, both of them are normalised by w_p. Figure 4.17(a) shows how the peak of the centreline increases with slot width when the velocities are kept constant (Cases 3, 8, 9 and 10). This is a result of the increase in the momentum of fluid and the peak also occurs further downstream. Figure 4.17(b) shows the response of an air curtain to a change in velocity ratio, R for a fixed w_p of 10mm (Cases 2-5). This is in effect a study of the increase in jet velocity when all other parameters are kept constant. As expected, the maximum height

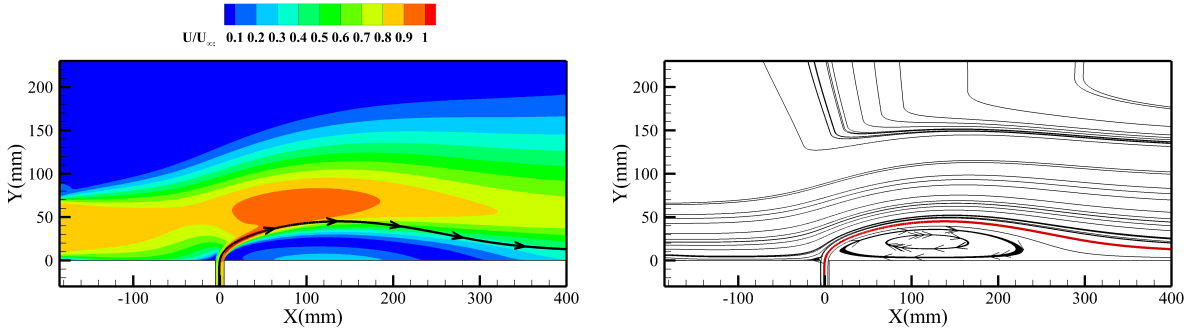

(a) Speed contour **(b)** Streamline

Figure 4.16: Example of the flow pattern acquired with CFD simulation

increases with R. Figure 4.17(c) confirms how the trajectory depends on the velocity ratio (Cases 1, 3, 6 and 7). It is observed that when R is kept constant, the change of the speed pair will not affect the jet trajectory.

As discussed earlier, the shielding position is set to align with the centreline peak, shown in Figure 4.18.(a). For acoustic tests, both U_∞ and U_{pj} are controlled to be 50m/s, i.e. Case 3. From Figure 4.17(c) it is concluded that a_0 is $14.2w_p$, which is 142mm. In order to determine the value of b_0, the vertical speed profile of Case 3 at $X = 14.2w_p$ is extracted and shown in Figure 4.18.(b), along with Cases 11 and 14. As depicted in Figure 4.18.(b), the speed initially increases from zero. This increase can be explained by the recirculation induced by the air curtain itself, which is in agreement with the conclusion made from the speed contour and streamline. When the local extreme value is passed and the speed begins decreasing, it means that the profile has penetrated into the recirculation. Once the increasing trend begins again, the speed will shortly approach to the main stream level. In another word the profile has gone beyond the air curtain shielding area.

b_0 is determined based on the characteristics of the velocity profile at a_0. As discussed earlier, the noise emission of the rods is positively correlated to the impinging flow speed, that is to say, the key to reducing noise is to reduce the local flow speed. As such, the easiest idea is to define and use a speed threshold to find the shielding height in the speed profile at the shielding position. Then the rods can be placed below so that the impinging

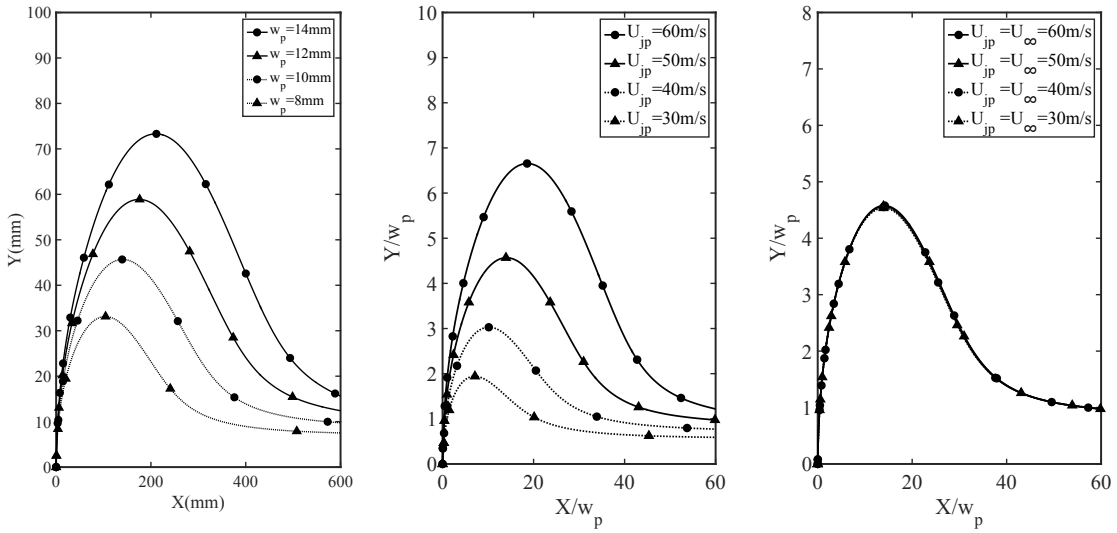

(a) **(b)** **(c)**

Figure 4.17: Centrelines of the primary air curtain in a crossflow in the single-jet geometries: (a) $U_\infty = 50m/s$, $U_{jp} = 50m/s$. Independent variable is w_p (b) $U_\infty = 50m/s$, $w_p = 10mm$. Independent variable is U_{jp} (b) $U_\infty = 50m/s$. Independent variables are U_∞ and U_{jp} ($U_\infty = U_{jp}$)

speed will be lower than the threshold speed. There are some considerations that must be clearly noted. On one hand, the threshold should be low enough to ensure reduced impinging speed; on the other hand, the threshold must ensure a sufficient shielding height to fully shelter the rods. Therefore, a compromise has to be agreed and the threshold was accordingly set to be a quarter of the maximum speed in the profile in this study. In Figure 4.18.(b), the limit found with the threshold is marked in each profile. For Case 3, the limit is (0.25, 3), which means that the shielding height of Case 3, b_0 is $3w_p$. As such, the top of the rods should be lowered than $3w_p$, i.e. $b < b_0$. In order to avoid blowing due to the leeward edge curvature, the height was made to be 28mm. In summary, a and b were controlled to be 142mm and 28mm. In this chapter, they were kept to be constant in all geometries and configurations with the rods to facilitate comparison. Figure 4.19 displays the velocity contour of Case 3, 11 and 14 in the range of interest. Moreover, the rods were illustrated with two white circles in scale at the optimised position. The dual jets geometry will be discussed later on. As shown in Figure 4.19 (a), rods are obviously inside the low speed region below the air curtain and higher than the relatively high speed endplate proximity. This confirms that the optimised position attained with the threshold

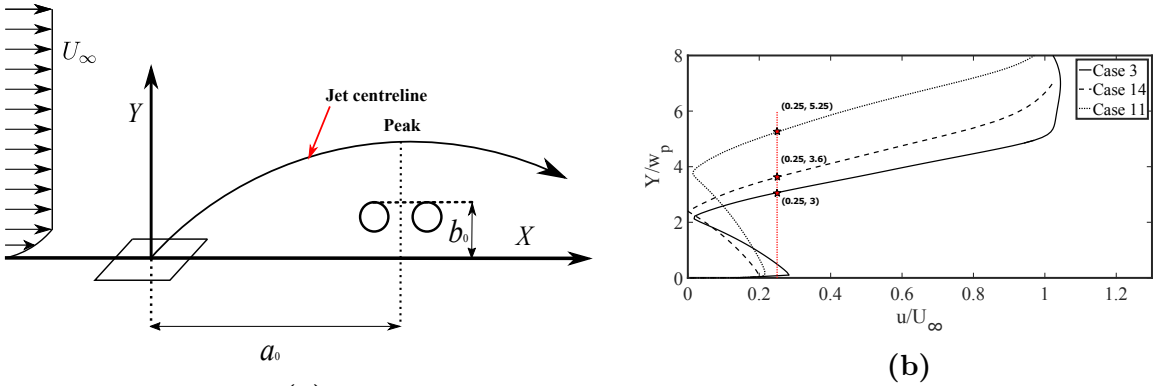

(a) (b)

Figure 4.18: (a) Schematic of the rods position (b) Speed profiles at $X = 14.2w_p$

can achieve a low local flow speed for the rods.

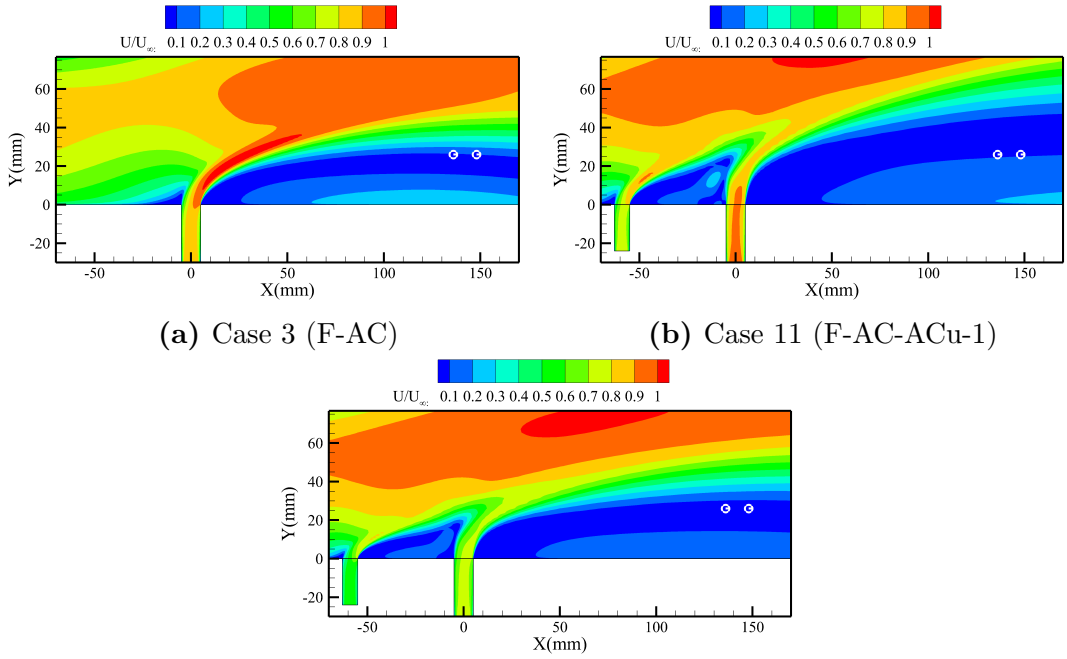

(a) Case 3 (F-AC)

(b) Case 11 (F-AC-ACu-1)

(c) Case 14 (F-AC-ACu-2)

Figure 4.19: Velocity contour of the flow field and relative position of the tandem rods (in scale)

4.3 Single-Jet Configuration

In this section, the acoustic performance of the single jet air curtain is tested. The explanation on the noise reduction is given based on aerodynamic measurements.

4.3.1 Acoustic Measurement

The acoustic performance was evaluated through measurements from the microphone array. To begin with, the overall performance was assessed through the averaged one third octave band spectra of all microphones. The measured SPL was corrected based on the SNR, which is based on the algorithm introduced in Section 3.6.2.2. To be more specific, the spectrum of F is shown in Figure 4.20, used as the background noise (baseline noise). If the SNR of other case compared to the background noise was smaller than 3dB, the sound level was set to be equal to the level of F, which in effect is an upper limit for the actual level. If the SNR was higher than 3dB, the sound levels were corrected on a pressure basis. For example, both original and corrected spectra of F-R are shown in Figure 4.20. The difference is more obvious in the high frequency range. Hereinafter, all one third octave band spectra shown were corrected based on the background noise.

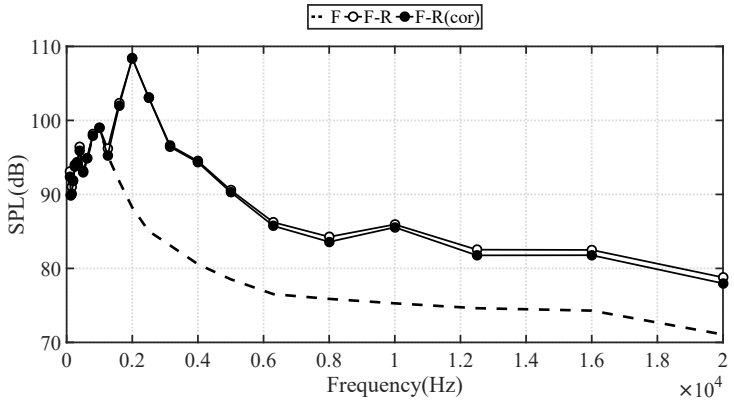

Figure 4.20: SNR correction

Figure 4.21, illustrates the noise characteristics of F, F-R, F-R-AC and F-AC. First of all, it is clearly shown that all spectra, including those in the subsequent figures, overlap with each other in the frequency range lower than 1,250Hz. As such, it can be concluded that noise in this range is mainly attributed to the background noise despite the SNR correction. Therefore, the discussion in the following will exclude this range. As shown in Figure 4.21(a), in F-R there is the main tone which is as noisy as 108.8dB in the band of 2,000Hz. In the meantime, the SPL of F-R is much higher than that of other spectra at different frequencies. In order to confirm the location of the main noise sources, noise maps acquired by time domain beamforming with one third octave band filter are shown.

Figure 4.22 and Figure 4.23 are typical examples of the noise map for each case at the frequency of 4,000Hz and 10,000Hz respectively. The noise map in Figure 4.22 (a) and Figure 4.23 (a) for F-R confirm that rods are a strong noise source. In addition, note that the colour bar range of the contour was set to be large enough (21dB for Figure 4.22 and 22dB for Figure 4.23) to clearly show the SPL comparison with different cases. Therefore aliasing problem can deteriorate to some extent, especially for the low frequency range. However, it is validated that the localization still works fine for the main noise source in each map.

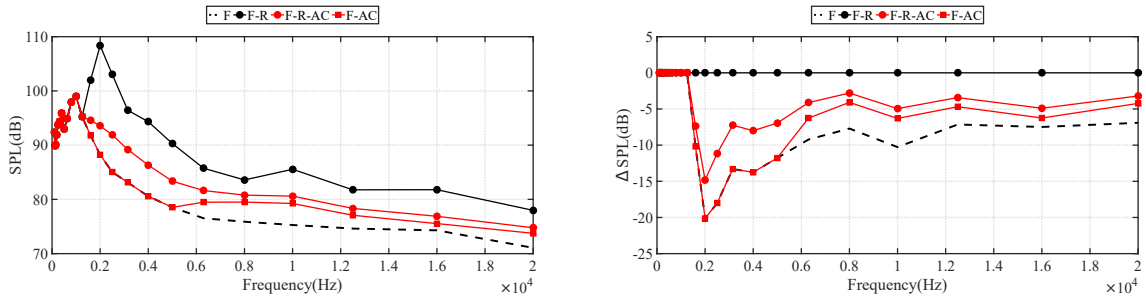

(a) SPL **(b)** ΔSPL referred to F-R

Figure 4.21: One third octave band spectra related to the single-jet air curtain configuration

By contract, SPL level of F-R-AC is much lower than F-R. In order to improve the description of the noise reduction, the relative SPL level, i.e. ΔSPL [34] is presented in Figure 4.21(b), in which all are referred to F-R. Note that for diagrams of Δ SPL in this thesis, the reference can be different. Therefore, the reference will be clearly indicated in the caption. As Figure 4.21(b) shows, the noise reduction using an air curtain can be 3-15dB for different frequencies. For example, the tone at 2,000Hz can be well removed and reduced by 15dB. Moreover, due to the SNR correction, it is, in effect, an upper limit of the actual noise level that is determined here. Therefore, the actual noise reduction can be slightly more. Thus, it is confirmed that with an air curtain a substantial noise reduction can be achieved.

Furthermore, in F-AC, i.e. the case that rods were removed, an SPL reduction can be found when compared to F-AC-R. In the low frequency range (≤5,000Hz) ΔSPL is higher than the high frequency range (>5,000Hz). The only explanation is that the rods still produce noise when the air curtain is turned on and can be a main noise source.

Particularly, in the low frequency range, after removal of the rods in F-AC, the SPL is equal to the background noise. Therefore, the rods are the only noise source in this frequency range in F-R-AC. In the high frequency range, SPL of F-AC is still higher than the background level even though the rods were no longer there. The only difference in the set-up here is the introduction of the air curtain. Thus, it is concluded that air curtain itself can be another main contributor to the total noise emission. These conclusions can be further confirmed by the noise map. As seen in Figure 4.22(b) and Figure 4.23(b), apart from substantial SPL reduction compared to F-R, the main noise source is the rods at 4,000Hz and air curtain outlet at 10,000Hz respectively.

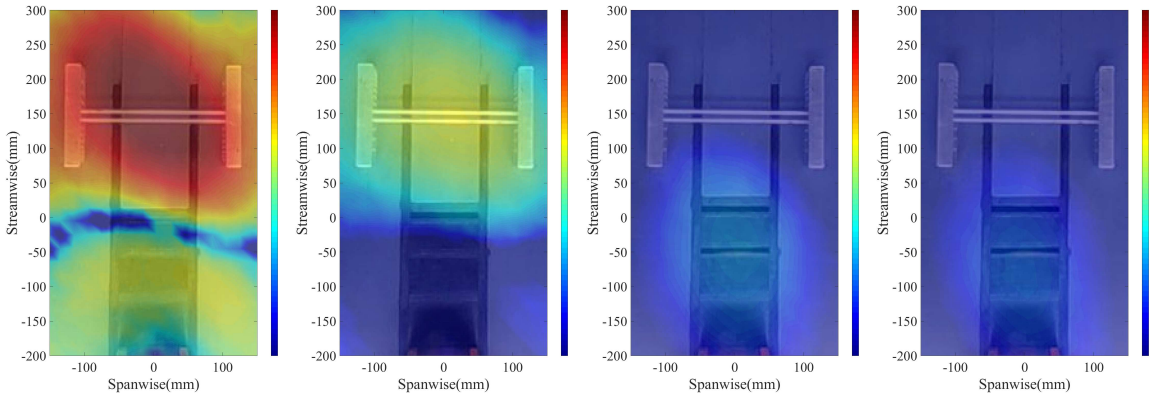

(a) F-R **(b)** F-R-AC **(c)** F-R-ACu-AC1 **(d)** F-R-ACu-AC2

Figure 4.22: Noise source map with one-third octave band filter centred at 4,000Hz

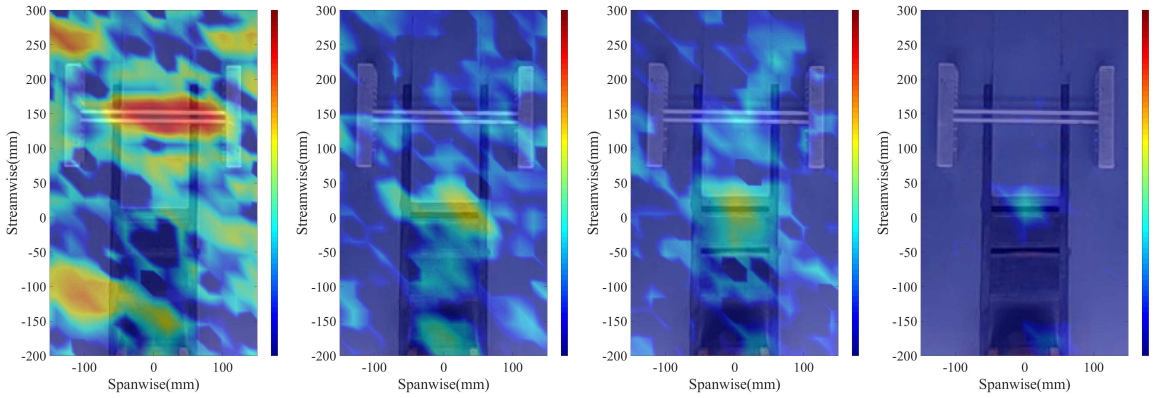

(a) F-R **(b)** F-R-AC **(c)** F-R-AC-AC1 **(d)** F-R-AC-AC2

Figure 4.23: Noise source map with one-third octave band filter centred at 10,000Hz

In addition to the one third octave band spectrum, the auto-spectrum from one microphone, though not from an overall perspective like the one third octave band spectrum,

can reflect more characteristics of the sound signal with directivity. However, in terms of directivity measurement, those microphones were not installed as a directional array, and the measurements were not conducted in an anechoic chamber. However, the spatial distribution of those microphones can to some extent reflect the directivity of the noise emission. Microphones No. 1 and No. 19 were nicely situated upstream and downstream to the rods in the centreline, illustrated in Figure 4.24. As such, the auto-spectra from these two microphones were analysed to characterise the acoustic performance of each test in the downstream direction and upstream direction.

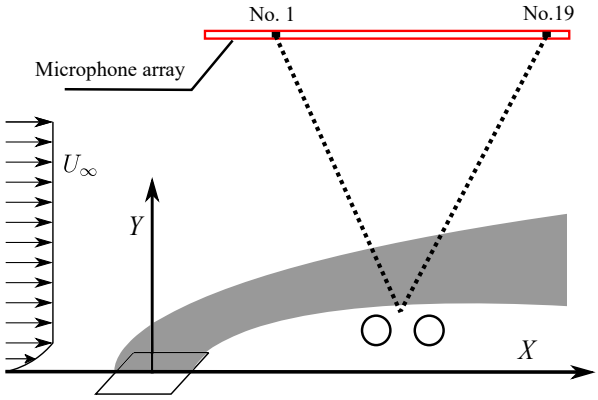

Figure 4.24: Directivity Schematic of the Microphone No. 1 and No. 19 in the array (not in scale)

Figure 4.25 shows the auto-spectra from microphone No. 1 and No. 19 respectively. Overall, those measurements from these individual microphones are in agreement with the averaged one third octave band. For example, the highest peak of F-R in both No. 1 and No. 19 stays in the frequency of $2,000$Hz, inside the same band that the peak stays in the one third octave band spectra. Furthermore, it is observed that there are two main peaks in the spectrum of F-R regardless of the microphone number, which stays around $2,000$Hz. The strongest main tone, i.e. the one with higher frequency, should correspond to the vortex shedding of the downstream rod. By contrast, the second main tone is from the vortex shedding of the upstream rod. As introduced above, intermittent shedding can be detected in the region between two cylinders, not as strong as the main vortex shedding behind the downstream rod, which also explains why the sound pressure level of the strongest main tone is dominant.

In terms of the directivity, SPL from microphone No. 1 and No. 19 at the same

frequency is not comparable because the distances from rods to these two microphones are not equal. However, trend of the SPL variation in a same frequency range can be compared to observe sound pressure distribution at different frequencies related to the directivity.

In the F-R spectra of Figure 4.25(a) and (b), two obvious tones can be both detected, which is independent on the microphone location. However, the relative SPL varies with the directivity. For the upstream microphone No. 1 , the SPL of two tones is nearly equal. However, for the downstream microphone No. 19 the second highest tone is over 3dB lower than the maximum. As such, it is concluded that intermittent shedding from the upstream rod can have a stronger influence to the upstream acoustic field than the downstream. Furthermore, it is found that some peaks exist in the frequency range $9,000Hz < f < 10,000Hz$ for microphone No. 19, but they can be hardly detected in No. 1. A possible explanation is that these peaks may be mainly from the interaction noise between two rods. To be more specific, the wake of the upstream rod can interact with the downstream one and generate interaction noise, the propagation of which may depend on the direction. One proof is that when there is the air curtain (F-R-AC), these peaks are suppressed. As for those spectra belonging to other geometries, no obvious difference can be observed

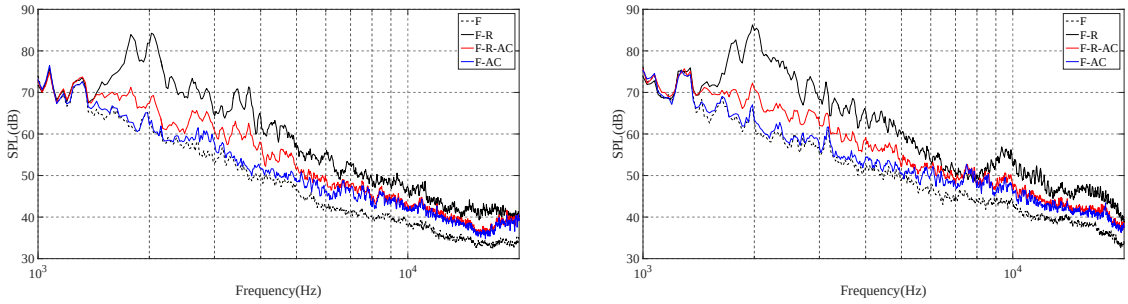

(a) No. 1 **(b)** No. 19

Figure 4.25: Auto-spectra related to the single jet geometry from Microphone No. 1 and No. 19 in the array

4.3.2 Flow Measurement

To further investigate the mechanism of the noise generation and reduction, flow measurements using hot-wire anemometry were conducted, introduced in Section 3.3. To be more

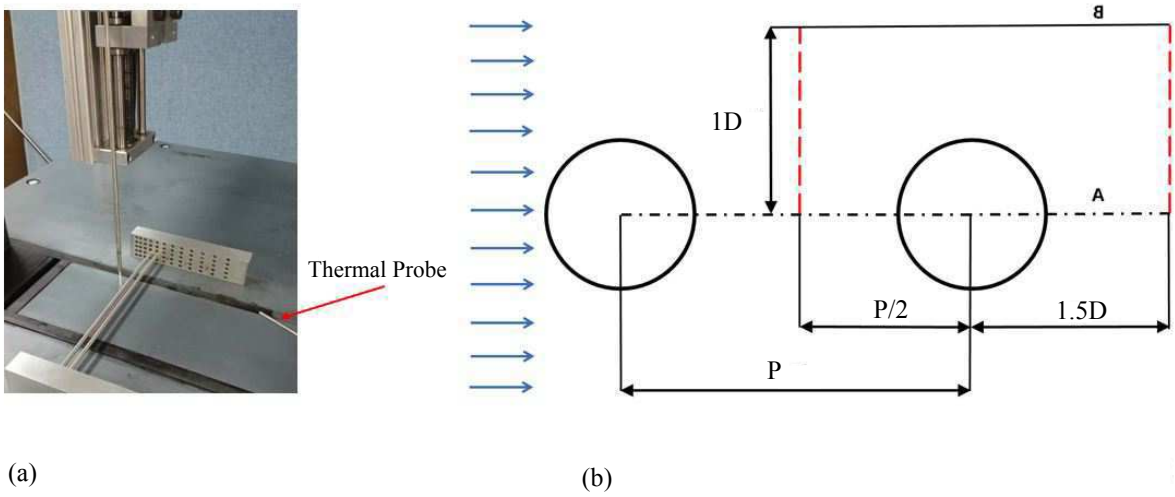

Figure 4.26: Hot-wire measurement: (a). measurement set-up (b). schematic of the test section (not in scale)

specific, the hot-wire, at a sampling rate of 100kHz, was used to measure the velocity and Reynolds stress as well as to calculate fluctuation spectra. Due to the limitation of the experimental instrumentation, it is impossible to measure the real impinging speed and Reynolds stress on the test body surfaces. Thus, some typical test sections were chosen, which can reflect the flow variation among different configurations. Since the test body position was chosen based on CFD simulations, the impinging speed to the entire tandem rods, as a whole entity, can be decreased by the air curtain, thereby reducing the overall noise emission. This reduction has been validated above. In terms of the interaction noise, the key to the reduction is to diminish convection velocity and turbulent stress from the upstream rod. As such, measurements with a hot-wire were undertaken in two planes.

Figure4.26(b) schematically illustrates the measurement sections (dotted red lines), which started from Line A and ended to Line B. Line A was the centreline of the rod section and parallel to the endplate. Line B was $1D$ higher than line A. The entire measurement was conducted inside the centre plane of the open-jet tunnel. The first section was in the middle of the gap between two rods, which approximately measured the impinging speed and Reynolds stress to the downstream rod. The second section was $1.5D$ behind the downstream rod, which enabled the measurement of the wake behind the downstream rod. As introduced earlier, the hot-wire support tube with the probe was mounted on a vertical traverse connected to a servo motor. The samples were taken every

$0.125D$ in each section. As for the Reynolds stress, since the single-wire hot-wire (Dantec 55P11) could only measure the velocity in one dimension, the streamwise component was chosen, i.e. $\overline{u'u'}$. This is also dominant over the other stress term. The real test set-up is shown in Figure 4.26(a), and the thermal probe set inside the downstream flow field was used to perform the thermal correction.

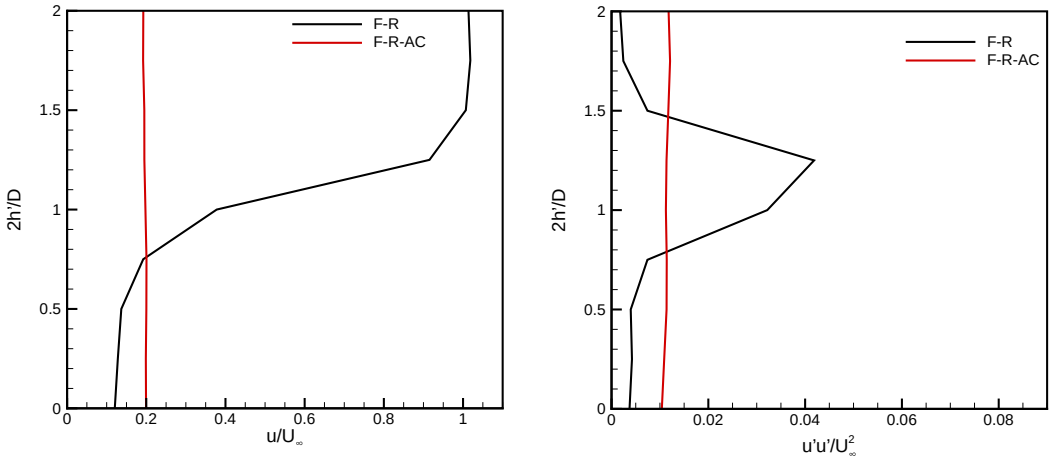

(a) Velocity **(b)** Reynold stress

Figure 4.27: Profiles of the test section in the middle of two rods

Figure 4.27 and Figure 4.28 show the profiles from the two test sections. Y axis is the altitude referred to the centre of the rods, denoted as h', non-dimensionalised by the radius of rods $D/2$. Also, the fluctuation velocity and Reynolds stress have been non-dimensionalised by U_∞ and ${U_\infty}^2$ respectively as the X axis. As illustrated in Figure 4.27.(a), F-R unexpectedly begins with lower velocity than the F-R-AC at a low height. More precisely, in the range of $0 < 2h'/D < 0.7$. CFD simulations have demonstrated that flow speed in the area behind the air curtain could be significantly reduced. Therefore, the mechanism of the slight increase in the flow speed between the rods is ambiguous, but it can be possibly attributed to the recirculation induced by the air curtain. Although velocity in the F-R profile is lower than F-R-AC in the low height range, it increases from $2h'/D = 0.7$ and shortly reaches the crossflow velocity level. By contrast, F-R-AC keeps to be with low velocity and does not increase. A characteristic height must be indicated, which is $2h'/D = 1$. The height corresponds to where the top edge of the rods is. At this characteristic height $u/U_\infty = 0.18$ for F-R-AC and $u/U_\infty = 0.5$ for F-R. Acoustic

tests have already shown that interaction noise reduction can be achieved using the air curtain. It is suggested that in term of the interaction noise, flow velocity in the region that is close to top edge of the rods plays more important role than the centre.

Apart from velocity, turbulence level also influences the noise emission. Figure 4.27.(b) depicts the Reynolds stress term, which is the sign of the turbulence level. Obviously, $u'u'$ peaks around $0.9 < 2h'/D < 1.3$ in F-R as a result of the vortex shedding from the upstream rod. In contrast, the peak can be eliminated through the introduction of the air curtain. Likewise, in the regions with low height ($2h'/D < 0.75$) and high height ($1.5 < 2h'/D$), Reynolds stress in F-R-AC is higher than F-R due to the low turbulence level of the crossflow. Therefore, a similar conclusion can be made that the impinging turbulence level at the characteristic height is dominant over others in terms of interaction noise generation; the air curtain is able to reduce the impinging velocity as well as the turbulence level to the downstream rod at the characteristic height.

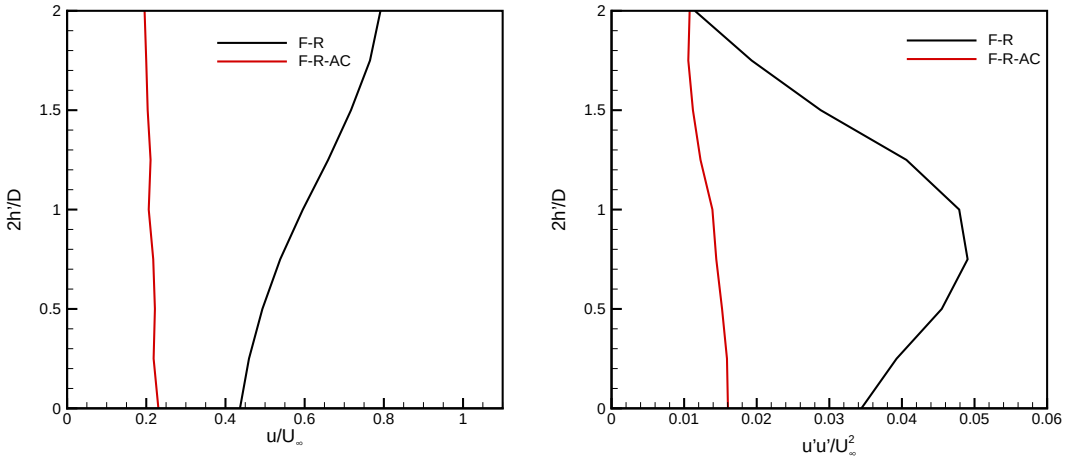

(a) Velocity **(b)** Reynold stress

Figure 4.28: Profiles of the test section behind the downstream rod

Figure 4.28 is the measurement results of the downstream section, in which both u and $u'u'$ can be significantly reduced when the air curtain is on. More specifically, u of F-R is much lower than F-R-AC at all sampling points. As for Reynolds stress shown in Figure4.28(b), firstly it is found that $u'u'$ peaks at $2h'/D = 1$. Undoubtedly, at this height, the peak is a direct result of the vortex shedding. However, the Reynolds stress is reduced in F-R-AC.

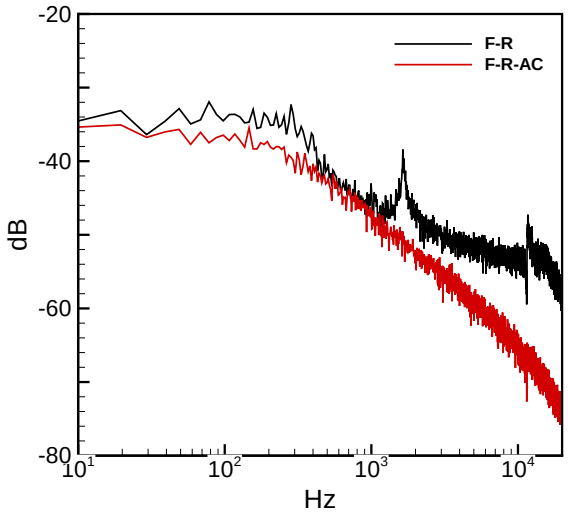

Figure 4.29: Velocity fluctuation spectral at h'/r=1

In order to further validate the elimination of the vortex shedding using the air curtain, the spectra of velocity fluctuation in F-R and F-R-AC were analysed. Since the characteristic height behind the downstream rod is the main region where vortex shedding occurs, data acquired from this height in the downstream section were chosen to calculate the spectra. Data of the velocity fluctuation were averaged over 110 blocks, using a block size of 4,096. The calculation algorithm is as same as the one used for the auto-spectrum, which has been introduced in Section 3.6.2.1 . The fluctuation spectra are also referred to U_∞ and expressed in dB by:

$$dB = 20log\frac{u'}{U_\infty} \tag{4.15}$$

Figure 4.29 is the results. It is observed that the fluctuation level stays high in the low frequency range that is below around 400Hz in the spectrum of F-R. Then it declines with an increase of the frequency. An important characteristic here is that there exists two fluctuation peaks. It is observed that appearance of the first peak is to some extent similar to those peaks in the acoustic auto-spectrum because they all possess continuity with the adjacent frequencies. It suggests that this one is mainly from the vortex shedding. However, the second peak shows a sudden increase, which does not correspond to the fluctuation of the flow. A possible explanation is that this peak may come from the flow-induced vibration of the hot-wire support. More specifically, the flow speed was high

when there was no air curtain. As a consequence, the flow may have induced vibration of the hot-wire probe holder, which also can be recorded by the wire. Because this vibration is from the flow fluctuation, there is no continuity shown in the spectrum. In F-R-AC, overall speaking the fluctuation significantly decreases for all frequencies. In particular, those two peaks have been well removed by the air curtain. Removal of the first peak can fundamentally explain the tone reduction in the noise spectra in Figures 4.21 and 4.25, i.e. removal of the vortex shedding. The removal of the second peak is because the flow-induced vibration has been weakened with less local speed around the hot-wire holder.

4.3.3 Summary

This section discussed the noise reduction using one air curtain. Explanations to the entire scenario are discussed in the following. When the crossflow blows the rods, in addition to the main vortex shedding established behind the downstream rod, which in effect is the cause of the main noise tone, intermittent shedding also form behind the upstream rod. On one hand it can directly induce noise production; on the other hand, the wake of the upstream rod will interact with the downstream rod and consequently generate extra noise. When the air curtain is turned on, the recirculation induced by the air curtain mentioned above can result in complex local flow around the rods. As such, despite significant noise reduction, the rods can be one of the main noise sources in addition to the air curtain. On the air curtain self-noise, Oerlemans and Bruin[19] have conducted the most significant investigations to date. They concluded that for the subsonic planar jet without cross-flow, the dominant mechanism for jet noise generation is the jet mixing and the slot edge blowing. Since no information can be found on the effect of crossflow on the noise emission of the planar jet, it is reasonable to make such inference that when the crossflow is introduced, more jet mixing noise will be generated than in a quiescent flow. Furthermore, since the jet bends over downstream, shown in Figure 4.15 (a), more edge blowing noise can be generated. Therefore, the air curtain itself can be another main noise source after it turns on.

4.4 Dual-Jet Configuration

In this section the dual-jet air curtain geometry is proposed and investigated to further reduce landing gear noise.

4.4.1 Dual Jets Hypothesis

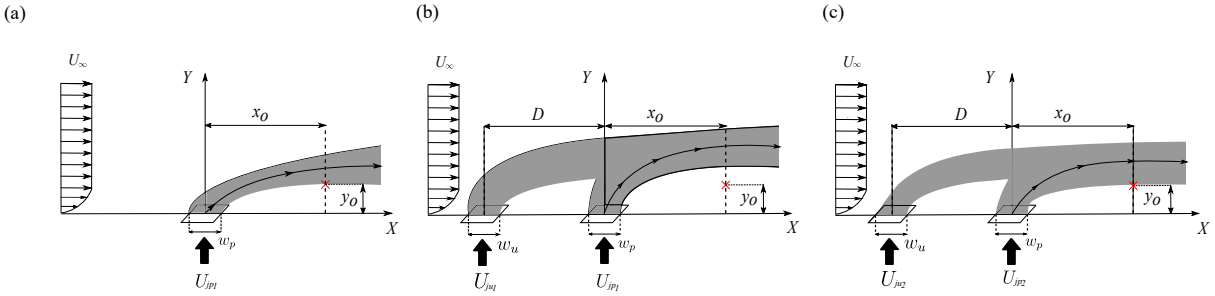

Figure 4.30: Planar jets in the crossflow:(a). F-AC (b). F-AC-ACu-1 (c). F-AC-ACu-2

The proposal to use a dual planar jets geometry in order to reduce flow-induced noise is developed according to the characteristics of tandem jets in crossflow. As mentioned earlier, tandem jets in crossflow have been found to be much different from the single jet [97, 110, 117]. More specifically, when the upstream jet is introduced within the primary jet set-up, these jets merge along the deflection region as a result of interaction with the crossflow. The trajectory and edge of the primary jet become higher. Figure 4.30 illustrates the related dual jets and single jet in a crossflow, with the 2D Cartesian coordinate system. The primary jet trajectory is also marked within each schematic, defined as the streamline passing through the origin. As shown in Figure 4.30(a), x_0 is an arbitrary horizontal position, while the corresponding height of the jet leeward edge, which determines the maximum shelter given to a bluff body located downstream, is y_0. In Figure 4.30(b), the upstream jet deflects the crossflow, thereby protecting the primary jet. As such, the primary jet leeward edge is increased as shown in Figure 4.30(b). Note that the primary jet speed in Figure 4.30(a) and (b) are equal, and given as U_{jp1}. The speed of the upstream jet is U_{ju1} and $U_{ju1} < U_{jp1}$ Therefore, an initial hypothesis can be drawn that the tandem jets geometry could potentially lead to a lesser noise emission from a bluff body located downstream of the set-up when compared to the single jet geometry set-up. Potentially, a higher leeward edge provides an improved shelter for the bluff body, thereby causing

more noise reduction. Also, the interaction noise between the crossflow and primary jet is much lower due to further protection by the upstream jet. Finally, since the upstream jet has a lower speed, its self-noise is less than the primary jet, and as such, less overall noise emission is produced.

A second and more important hypothesis can be also made based on a new configuration of the dual jets geometry. The idea is to maintain the shelter height used for the single jet geometry as the same shielding height for the dual jets configuration by subsequently reducing the speed of both primary and upstream jets, which would obviously result in jet self-noise suppression. The second configuration is as illustrated in Figure 4.30(c), with U_{ju2} and U_{jp2} speed of the two jets. Note that $U_{ju2} < U_{ju1}$ and $U_{jp2} < U_{jp1}$.

These two configurations of the dual-jet geometry were tested with flow-induced noise reduction effects as the core objective. These are denoted as F-R-AC-ACu-1 and F-R-AC-ACu-2 herein (F-AC-ACu-1 and F-AC-ACu-2 are for the cases without rods).

4.4.2 Shielding Height Increase

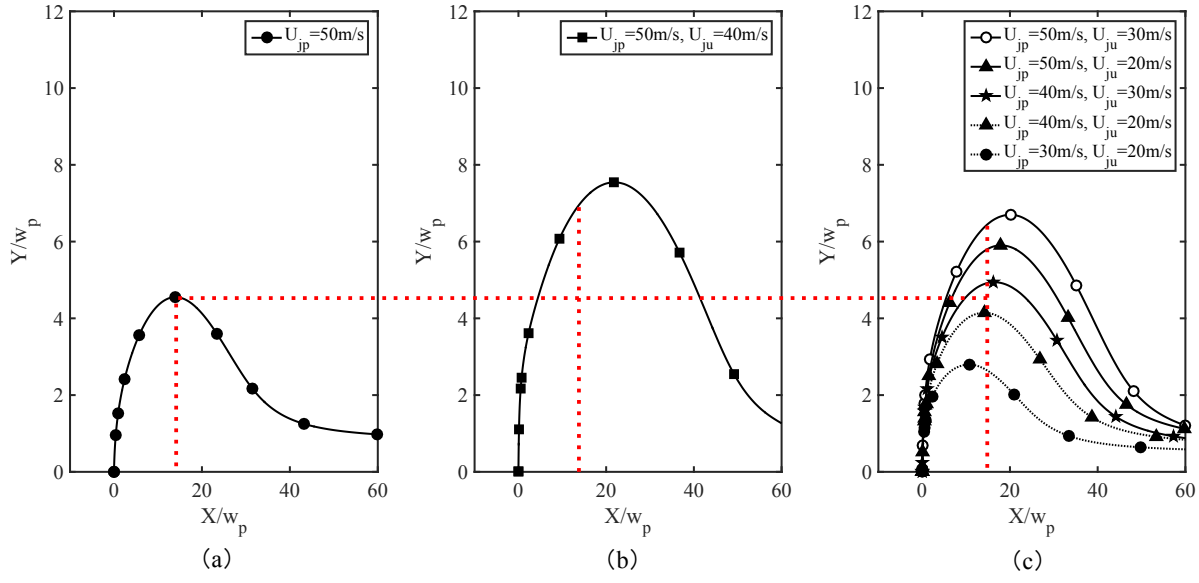

Figure 4.31: Centreline comparison of the primary air curtain in crossflow between the single-jet and the dual-jet air curtain configurations

Prior to validation of the hypothesis, CFD simulation for dual jets in crossflow were conducted and analysed. Firstly, a parametric analysis was performed of the effect on the primary jet centreline from the upstream jet. Centrelines of the primary air curtain

in each case are illustrated in Figure 4.31. More specifically, the crossflow speed is 50 m/s in all cases. The same single-jet case used for the acoustic test above is shown in Figure 4.31.(a). Meanwhile, centrelines of the primary jet with an upstream air curtain speed of 40 m/s is shown in Figure 4.31.(b) and more cases with different pairs of U_{jp} and U_{ju} are shown in Figure 4.31.(c), which are referred to as jet pair speed in the remainder of the thesis. In addition, a horizontal dash line is made, starting from the peak of the centreline in the single jet configuration, i.e. the shielding position. This dash line links to the point in Figure 4.31.(c) that is located at same shielding position of the single jet, penetrating Figure 4.31.(b). Apart from the horizontal dash line, three more vertical lines are respectively drawn in each figure at the x of the single jet shielding position, where $x = 142mm$. Note again that it is the shielding position (optimised X position) for the single-jet configuration, which is used in all figures to clearly show the comparison. With these dash lines, it is confirmed that due to shelter of the upstream air curtain, the centreline trajectory of the primary jet can be elevated. It is suggested that shielding of the primary jet can be also increased, which can be confirmed by the flow visualization. Figure 4.15 (b) depicts flow pattern of the dual jets. Those curves that have been acquired from the theoretical model of the single-jet case including the centreline, leeward and windward edges, are also superimposed. It is clearly shown that the leeward edge, which is the edge most related to the shielding, is obviously elevated. So is the shielding height. In addition, it is observed from Figure 4.15 (b) that instead of being directly averted, the primary jet is almost vertically ejected. To be more precise, the height of the primary jet MDNF (Momentum-Dominated Near Field), which has been introduced in detail in Section 2.2.2.1, can be increased. This may reduce the edge blowing of the primary jet and contributes to the self-noise suppression. There are more features that worth discussing such as the jet width expansion and the interference between two jets. Since they are less related to the shielding, no investigation is carried out in this study.

The second hypothesis, i.e. to keep the shielding height of the dual-jet configuration as same as the single-jet configuration by reducing the speed of both jets, is believed to be able to further contribute to the noise reduction. The height of the landing gear is a fixed parameter from a perspective of practical implementation. Likewise, the position

of the rods is fixed in this study, i.e. the optimised position. Therefore, in the dual jet geometry, the speed of the primary air curtain can be reduced to some extent in order to maintain equivalent shielding. As a consequence, a further noise reduction can be possibly achieved as a benefit, not to mention less energy consumption. To date no research has been performed to quantify the shielding height increase. Thus, it is difficult to find the jet pair speed that can give an exact same shielding height as the single-jet. However, compared to the leeward edge, the jet centreline is easier to localise. Previous studies have concluded that the performance of the combined jet is similar to an elevated single jet[97, 109, 110]. Therefore, it makes sense to use the centreline to find the equivalent shielding. To be more specific, the height of the new centreline in the second dual jet configuration is expected to be as same as the single jet. As mentioned earlier, the position of the rods was kept same in all configurations for comparison. Therefore, the height of the new centreline is expected to be as same as the single jet at $x = 142mm$. Among these simulation cases, it is observed that the one with $U_{jp} = 40$ m/s and $U_{ju} = 30$ m/s has the closest height at $x = 142mm$. Therefore, this case together with the one in Figure 4.31(b) were used for the acoustic measurements. In summary, tests for F-AC-ACu-1 and F-AC-ACu-2 were made to be as same as Case 11 and Case 14.

Figure 4.17 (b) and (c) display the flow speed contour of Case 11 and Case 14 from simulations. Likewise, the rods were illustrated inside in scale. In Case 11, the low speed area has been extended and become larger than the single-jet. The rods are still inside but more close to the relatively high-speed part of the endplate proximity. In Case 14, it is observed that the shielding given to the rods is approximately as high as the single jet, and the rods are surrounded by the lowest speed flow in the contour. Therefore, it is confirmed that Case 14 can be used for the validation of the second hypothesis.

In the experimental tests, $U_{jp1} = 49.86$ m/s and $U_{ju1} = 49.96$ m/s in F-R-AC-ACu-1 and $U_{jp2} = 41.15$ m/s and $U_{ju2} = 29.96$ m/s. These tests were used for the acoustic measurements.

4.4.3 Acoustic Performance of the Dual-Jet Air Curtains

Likewise, acoustic measurements were conducted for both F-R-AC-ACu-1 and F-R-AC-ACu-2. Their noise reduction compared to F-R is shown in Figure 4.32. It is apparent

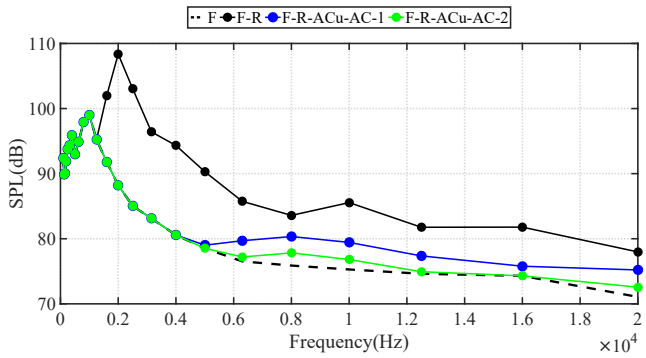

Figure 4.32: One third octave band spectra related to the dual-jet air curtain configurations

that both F-R-AC-ACu-1 and F-R-AC-ACu-2 perform well in terms of noise reduction. In the frequency range that is lower than 5,000Hz, both of these two configurations can lower the broadband noise level. In particular, the main tone can be well removed and the new SPL is equal to the background noise. It means that the rods almost no longer made noise in this frequency range with the use of dual-jet geometries.

In the range higher than 5,000Hz, when compared to F-R, the SPL becomes much lower as well using the dual-jet. More importantly, the advantages of using F-R-AC-ACu-2 is clearly shown here. It is observed from the subsequent SPL that F-R-AC-ACu-2 is quieter than F-R-AC-ACu-1. In particular, the SPL of F-R-AC-ACu-2 is as same as the background noise in a couple of frequencies, but F-R-AC-ACu-1 always has higher SPL than the background.

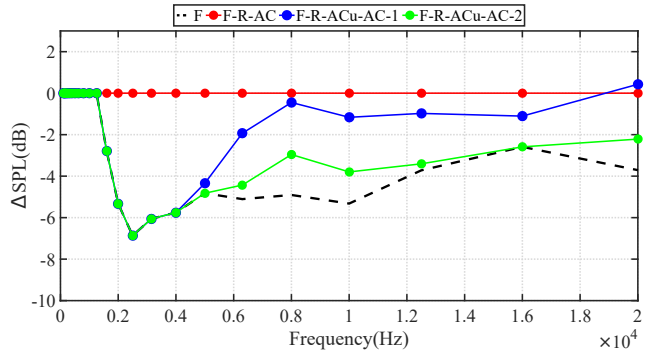

Figure 4.33: One third octave band reference spectra related to the comparison between the single-jet and the dual-jet configurations (ΔSPL referred to F-R-AC)

The comparison of noise reduction between the single air curtain and dual air curtains

geometries is clearly illustrated by the ΔSPL in Figure 4.33. Note that all spectra in Figure 4.33 are refered to F-R. Overall, the total noise emission of the dual-jet cases is much less than the single jet. The magnitude of the reduction is highly dependent on the frequency. For example, in both dual-jet configurations, the maximum reduction appears at 2,500Hz by 7dB. However, in F-R-AC-ACu-1 there is an increase compared to F-R-AC at 20,000Hz, which is discussed later on. In terms of the comparison within the dual-jet geometries, apart from being quieter than F-R-AC-ACu-1, F-R-AC-ACu-2 does not have any increase than F-R-AC.

The noise maps are in good agreement with the spectra. More specifically, the noise maps centered at 4,000Hz and 10,000Hz of the dual-jet geometries were also compared in Figure 4.22 and Figure 4.23, mentioned earlier. It is observed that the rods in both F-R-AC-ACu-1 and F-R-AC-ACu-2 are much quieter than the F-R-AC at 4,000Hz, and a slight reduction achieved by F-R-AC-ACu2 compared to F-R-AC-ACu1 can be found. At 10,000Hz, the F-R-AC-ACu-1 doesn't show any superiority over F-R-AC, but F-R-AC-AC-2 is much quieter around the nozzle. As such, it is concluded that the dual-jet geometry is superior over the single jet geometry. Compared with the single jet air curtain, it can achieve more reduction of the rods noise. Furthermore, the jet self-noise can be suppressed using the improved dual jet configuration, which keeps the shielding height by reducing the jet pair speed.

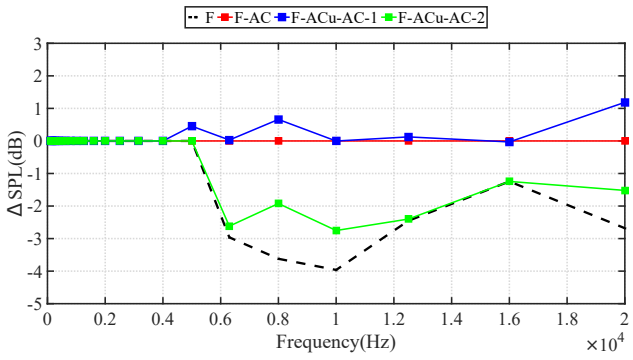

Figure 4.34: One third octave band reference spectra related to the air curtains (ΔSPL referred to F-AC)

Further discussion on the jet noise suppression was made based on those configurations without rods, i.e. F-AC, F-AC-ACu-1 and F-AC-ACu-2. Figure 4.34 is the ΔSPL refereed

to F-AC. It is found that the introduction of the upstream air curtain in F-AC-ACu1 can cause more noise production than F-AC, even though it can reduce the rods noise. This suggests that the first hypothesis is partially incorrect for the landing gear noise reduction. To be more specific, only by the introduction of an extra jet cannot suppress the total jet self-noise as anticipated. However, it can improve the shelter to the landing gear and achieve further noise reductions. One obvious reason is that the upstream jet noise including jet mixing (with crossflow) noise and edge blowing noise can contribute to the total emission. The other is that, as shown in Figure 4.15(b), the upstream jet bends over downstream and interacts with the primary jet. This jet mixture can be another contributor to the noise increase. With shielding of the upstream air curtain, the primary air curtain may generate less noise. However, this reduction cannot offset the extra emission caused by the introduction of the upstream jet, especially at 5,000Hz, 8,000Hz and 20,0000Hz. By contrast, the acoustic performance of F-AC-ACu-2 validates the second hypothesis. To be more specific, $\Delta SPL \leq 0$ in F-AC-ACu-2 and the SPL reduction compared to F-AC can be up to 2.9dB. In particular, F-AC-ACu-2 is almost as quiet as the background noise at 5,000Hz, 6,300Hz 12,500Hz and 16,000Hz. Therefore, the dual-jet air curtain configuration based on the second hypothesis can be of great use for the jet self-noise suppression. Likewise, the auto-spectra acquired from Microphone 1 and No. 19 are also reported to show the directivity. No obvious difference can be found between two microphones, therefore, further discussion is not given here. Note again that

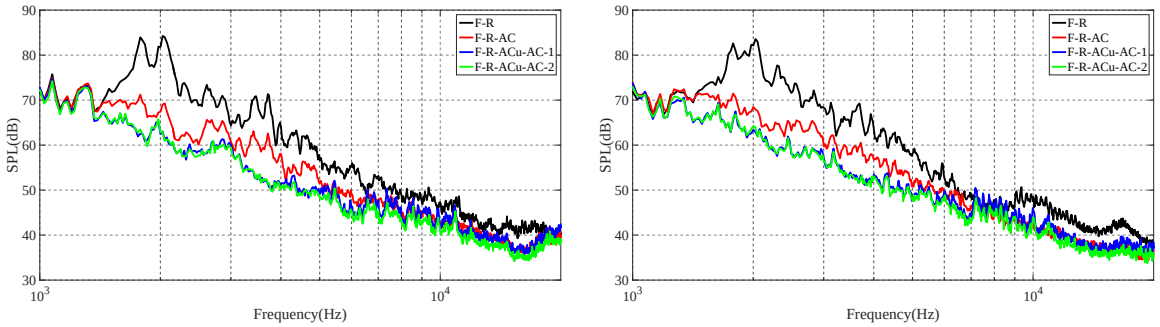

(a) No. 1 **(b)** No. 19

Figure 4.35: Auto-spectra related to the dual-jet geometries from Microphone No. 1 and No. 19 in the array

all tests of the dual geometry were carried out with the optimised position of the single

jet configuration to facilitate comparison. Therefore, it means that some more potential noise reduction is possible.

4.5 Conclusions

The main objectives of this Chapter is to validate the hypotheses of the dual air curtains geometry for improved landing gear noise reduction. Herein, the tandem rods were chosen to be the test body and the single-jet configuration was first investigated with the optimised position found by CFD simulation. Despite significant noise reduction, the rods and the air curtain itself were respectively identified to be the subsequent main noise sources in different frequency ranges. In response, the dual-jet geometry, including two configurations based on two hypothesis, was proposed to further reduce the noise emission. More specifically, one possesses the same primary jet speed and the other possesses approximately the same shielding by reducing jet pair speed. Acoustic tests revealed that the dual-jet configurations are superior to the single-jet by achieving more noise reduction. Especially the dual-jet configuration with reduced jet pair speed can maximise the noise reduction through decreasing the jet-self noise.

On the planar jet in crossflow, the flow visualization concluded that the existing model for predicting the jet trajectory as well as the boundaries can well predict the jet in the outlet proximity, but the prediction does not show a good performance in the downstream region. Therefore, a more accurate theoretical or semi-empirical model is needed. In addition, the flow visualization as well as the CFD simulations also revealed that the introduction of the upstream jet can lead to a trajectory elevation, a width expansion of the primary jet, and more importantly, shielding height increase, which contributes to the superiority of the dual air curtains geometry.

Chapter 5

Fluid Mechanics of the Dual Planar Jets in Crossflow

Dual jets in the crossflow is the flow regime that underlies the application of the dual air curtain geometry for the landing gear noise reduction. As such, the aerodynamic performance of the dual jets in crossflow is discussed based on PIV experiment and CFD simulations in this Chapter.

5.1 Leeward Edge

This section proposes and describes a novel approach for the leeward edge definition of the planar jet in crossflow.

5.1.1 Motivation of the Approach

In Session 2.2.2.1, research on the definition of the jet centreline as well as the edges has been introduced. To be more specific, a natural coordinate system is frequently established, with the jet centreline to be the α axis. Within the natural coordinate system, the jet half width is used to define the edges of the jet. This approach to defining the jet width was used by Oerlemans and Bruin [19] to fine the optimised shielding position for the bluff body.

However, it is found that the optimised position using this approach is questionable. First of all, on the definition. To be more specific, the jet edges are defined based on the local section,shown in Figure 5.1. The local section is achieved as the normal plane to the jet trajectory. In the meantime, one of the jet trajectory definitions is the locus of the maxima in different local sections. Therefore, there is a suspect of the circular definition. As mentioned above, there are different definitions of the jet trajectory. When the trajectory is defined as the time-averaged streamline that originates from centre of the jet outlet, the circular definition can be broken up because streamlines are calculated as the curves that are tangent to the flow velocity field. Even so, it is still time-consuming to find a series of cross-sections that are normal to the trajectory.

Second, on the model. Experimental work conducted by Ramaprian and Haniu [42] utilised a water jet in a water flume, which possesses extremely low velocity, reported in Table 2.3. As such, it is questionable if the model can be applied for the case with much higher jet velocity, not to mention the difference between the water jet and the gas jet.

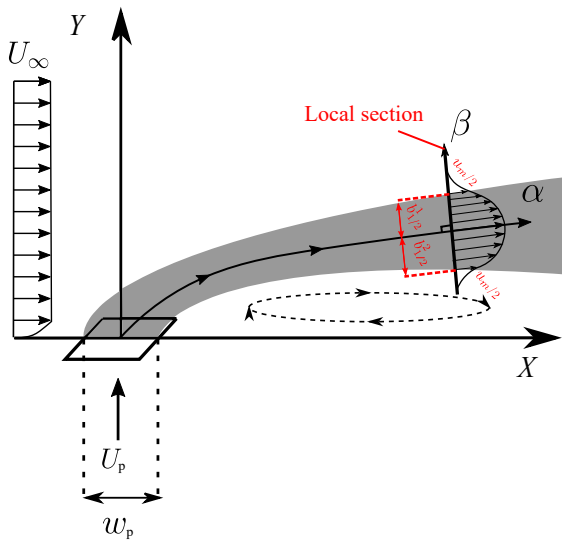

Figure 5.1: 2D Natural system established for the jet in crossflow

Thirdly, the half jet width. As mentioned above, the model was applied for bluff body noise reduction. More specifically, the bluff body was situated below the leeward edge of the half width, which means that an impinging flow velocity to the bluff body can be up to half of the local maximum. As discussed earlier, the reduction of the impinging velocity is crucial to the air curtain technology. Half of the local maximum, to some extent, is still high. Therefore, a new definition for the jet leeward edge definition, is expected . Because the leeward edge is the edge that is most related to the optimised shielding position,. In this section, a novel leeward edge definition approach is proposed and validated, which can bypass the complexity of the natural system as well as the jet trajectory. This approach aims to improve the proposal of the new jet pattern model.

5.1.2 Test Campaign

Work in this section is experimental using PIV. The rig has been introduced in detail in Section 3.4. Likewise, PIV frame assembly approach was also carried out to extend the view range, and the the set-up has been shown in Section 4.2.2. In this section w_u and w_p were set to be 10mm&10mm and 10mm&14mm. Apart from this, the flow conditions are reported in Table 5.1. The PIV tests covered both single-jet and dual-jet geometries with different initial conditions. Likewise to the simulation cases, each of them was given a run Number as shown in Table 5.1.

Table 5.1: PIV Test matrix of the planar jet in crossflow

No.	U_∞(m/s)	w_p(mm)	U_{jp}(m/s)	w_u(mm)	U_{ju}(m/s)
S010101	40.12	10	50.15	/	/
S010102	40.32	10	40.32	/	/
S010103	40.24	10	30.10	/	/
S010201	30.15	10	49.52	/	/
S010202	29.18	10	40.13	/	/
S010203	30.15	10	30.11	/	/
S020101	40.13	14	50.04	/	/
S020102	39.24	14	40.35	/	/
S020103	40.22	14	30.15	/	/
S020201	30.43	14	50.23	/	/
S020202	29.89	14	40.15	/	/
S020203	30.02	14	30.23	/	/
D0101010101	40.34	10	49.89	10	49.54
D0101010102	40.10	10	50.02	10	30.18
D0101010103	39.68	10	49.15	10	19.98
D0201010101	40.05	14	50.01	10	50.25
D0201010102	40.11	14	43.24	10	30.14
D0201010103	40.43	14	50.35	10	20.35

5.1.3 Leeward Edge Definition

The method utilised is based on PIV test results. Figure 5.2 shows the velocity contour of Case No. S010102. The velocity profiles were extracted from a number of probes, which are parallel to the Y axis. For example, three of these probes, P1, P2 and P3 are illustrated in Figure 5.2 and their velocity profiles are depicted in Figure 5.3. It is observed in Figure 5.3 that there exists a similar trend between P1 and P2. To be more specific, those two profiles begin with low magnitude at $y/w_p = 0$ and increase to the local maxima, which is 17.2m/s for P1 ($y/w_p = 0.3$) and 8.5m/s for P2 ($y/w_p = 1.2$). With the height continuously increasing and accordingly passing the local maxima, the magnitude declines to the local minimum and then accelerates again until it reaches the global maximum velocity. By contrast, P3 does not display the same trend. It begins with an increase from $y/w_p = 0$ and fluctuates around 10m/s until $y/w_p = 3$. Then it increases to the global maximum. These characteristics can be also reflected in the velocity contour. As depicted in Figure 5.2, both P1 and P2 penetrate a relative high speed region below the planar jet while P3 is outside.

Proceeding further, a velocity threshold is utilised to define the leeward edge of the

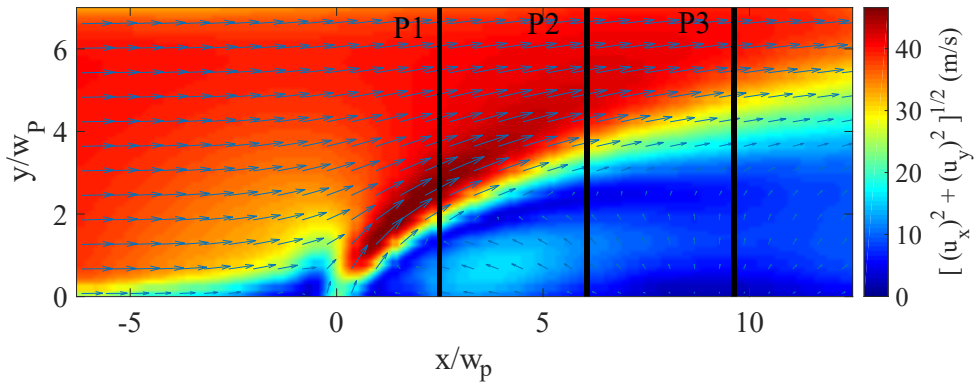

Figure 5.2: PIV velocity field of S010102 and examples of the velocity probes

planar jet. More specifically, the maximum of each profile can be easily localised, which has been marked with 'Max' in Figure 5.3. As discussed earlier, once the planar jet is used for the noise reduction, the bluff body should be situated below the leeward edge, which will enable the local flow speed around the bluff body to be reduced. In other words, the leeward edge can be regarded as the boundary between the low velocity region and the high velocity region. As such, it is directly related to the velocity profile. Therefore, a threshold can be used to separate those regions that are sheltered and not sheltered by the jet. As such, the locus of the threshold in all profiles can be consequently regarded as the leeward edge. In this study, an example of the threshold equal to one quarter of the maximum velocity is adopted. The corresponding locations with a quarter of the maximum speed are also marked in P1, P2 and P3 with "0.25Max", shown in Figure 5.3.

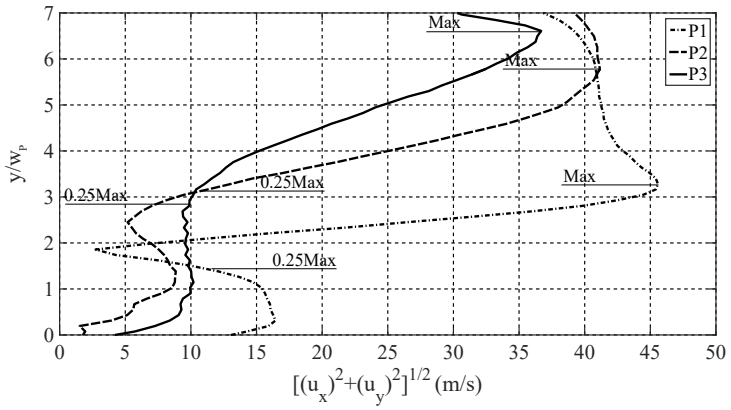

Figure 5.3: Velocity profile of P1, P2 and P3

As previously stated, a number of profiles were extracted from the velocity contour.

Therefore, all points with 0.25 maximum velocity can be localised, illustrated in Figure 5.4. Note that those points with the same x/w_p originate from one probe. It is found that there is more than one point with 0.25 maximum velocity in some probes. These probes are mainly located in the proximity of the jet outlet and the downstream region of this contour window. It suggests that the flow field of these areas is much more complicated than others, which can be possibly attributed to the recirculation. Herein, those points with the highest y/w_p in each probe are simply linked, shown in Figure 5.4. Therefore, a curve can be achieved and this curve is defined as the leeward edge of the planar jet.

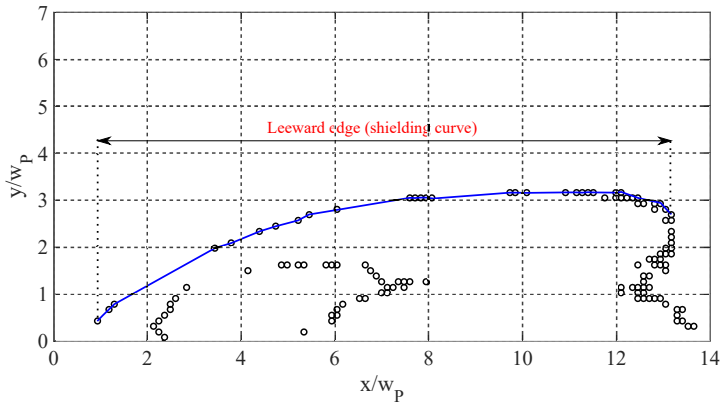

Figure 5.4: Leeward edge definition

Prior to being applied for the engineering use, in general the leeward edge requires a mathematical expression. Due to the parabolic characteristic in the normalised Cartesian coordinate system in Figure 5.4, the second-order polynomial is attempted to fit the leeward edge, written as:

$$\frac{y}{w_p} = f(\frac{x}{w_p}) = p_2(\frac{x}{w_p})^2 + p_1(\frac{x}{w_p})^1 + p_0 \tag{5.1}$$

As shown in Figure 5.5, the scatter illustrates data acquired from the PIV experiment. The fitting has been carried out and the corresponding curves are superimposed on the scattering. Meanwhile, the value of the coefficients in the polynomial is reported in Table 5.2. In the flow range shown, the fitting curves are in good agreement with the experimental data regardless of w_p. One exception is the most downstream point in S010201, which can be eliminated as an outlier point. Then the error range of the fitting is within 5% difference of y/w_p for each point compared to the experimental data. Therefore,

it is concluded that, in the single jet geometry, the leeward edge defined by the on quarter threshold can be well captured by a second order polynomial.

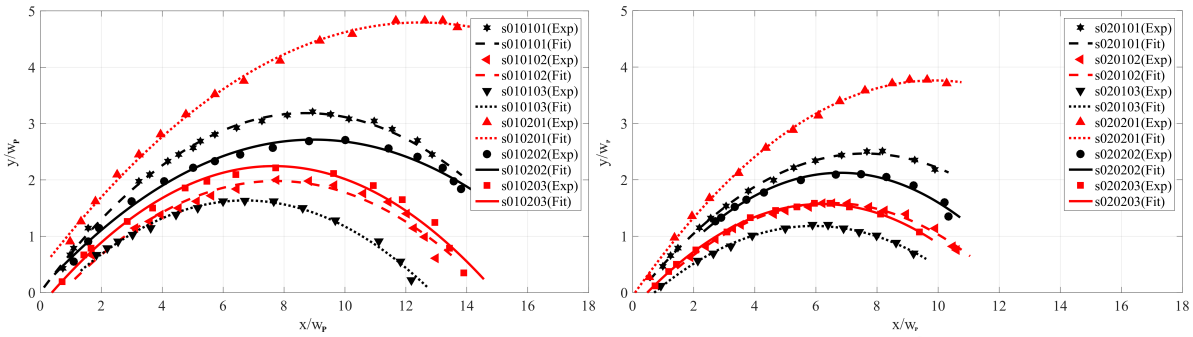

(a) w_p=10mm **(b)** w_p=14mm

Figure 5.5: Fitting of the leeward edge for the single planar jet configuration

In addition, this approach has been also validated to be useful for the dual jets geometry crossflow. To be more specific, the leeward edge of the primary jet in crossflow was also defined with the same process introduced above. Then likewise, a second-order polynomial was fitted to the leeward edge. Comparisons between the raw data and the curves are shown in Figure 5.6. The good agreement confirms the validity of fitting in the dual jets geometry. Therefore, it is concluded that the second order polynomial fitting can be applied to the leeward edge of the primary jet, regardless of the jet number in the crossflow.

Table 5.2: Coefficients of the second order polynomial

Run No.(Single jet)	P_2	P_1	P_0	Run No.(Dual jet)	P_2	P_1	P_0
S010101	-0.041	0.72	0.029				
S010102	-0.041	0.63	-0.456	D0101010101	-0.044	0.85	1.6
S010103	-0.043	0.58	-0.32				
S010201	-0.028	0.71	0.450	D0101010102	-0.036	0.86	0.32
S010202	-0.034	0.61	0.014				
S010203	-0.044	0.67	-0.29	D0101010103	-0.033	0.62	0.65
S020101	-0.044	0.67	-0.11				
S020102	-0.046	0.59	-0.33	D0201010101	-0.095	1.4	0.17
S020103	-0.043	0.51	-0.34				
S020201	-0.039	0.77	-0.06	D0201010102	0.033	0.85	-0.036
S020202	-0.052	0.70	-0.27				
S020203	-0.048	0.60	0.27	D0201010103	-0.035	0.60	0.30

5.1.4 Shielding Curve Increase

As previously discussed, the shielding curve increase plays a crucial role in the dual air curtains geometry for the landing gear noise reduction, which has been schematically illustrated in Figure 4.30. In order to discuss the increase, the corresponding leeward edge of the single jet configuration is also shown in Figure 5.6. It is obvious that shielding curve is dramatically increased when one more jet is introduced upstream to the primary jet.

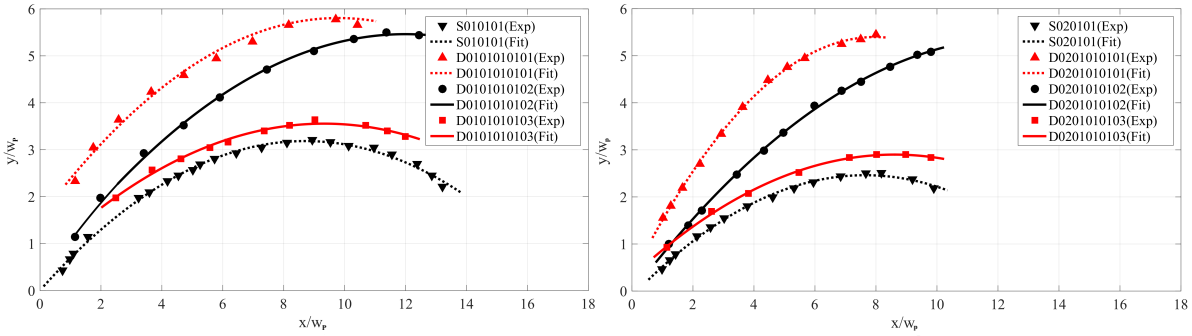

(a) w_p=10mm, w_u=10mm **(b)** w_p=14mm, w_u=10mm

Figure 5.6: Leeward edge fitting of the primary jet in the dual jets geometry

As previously stated, when the jet is given, the bluff body is schemed to be situated below the peak of the leeward edge, which is the optimised position with the highest shielding. The maximum shielding is termed as the shielding height. As such, in order to discuss the shielding increase, the shielding height is compared to the single jet and the configuration of the dual jets. The comparison related to $w_p = 10mm$ is shown in Figure 5.7, in which all cases have the same primary jet speed. Note that the single jet geometry corresponds to the case with the upstream velocity zero. However, the comparison related to $w_p = 14mm$ is not reported because the peak of some dual jets cases has exceeded the frame range.

In Figure 5.7, it is found that the shielding height is positively correlated with the upstream jet speed. It is confirmed that the introduction of the upstream jet can increase the shielding height, which means an improved shielding can be given to the landing gear. Moreover, it is concluded that the leeward definition approach proposed herein can be used to quantitatively analyse the jet shielding increase in the dual jets geometry. For the future research, a semi-empirical model could be derived based on the approach.

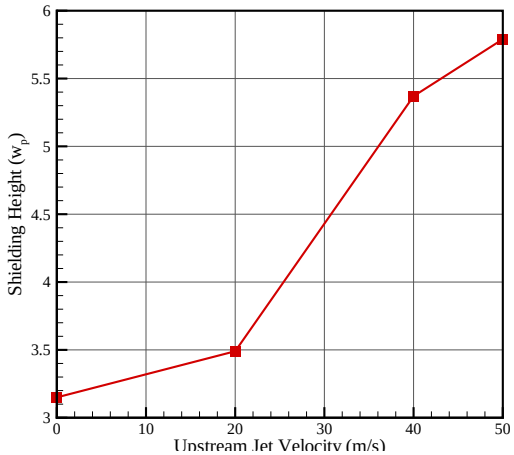

Figure 5.7: Comparison of the shielding height among the single jet and the dual jets configurations

5.1.5 Uncertainty Analysis

Validation of this approach is fully based on the PIV experiment. In addition, due to the limitation of the frame size, the PIV time-mean frame assembly was performed, which has been introduced earlier. However, there is uncertainty that must be addressed and analysed.

First of all, the threshold selection. As previously stated, the leeward edge is defined using a threshold of the maximum speed in a vertical speed profile, which, in this study, is 0.25. Therefore, the arbitrary nature of the threshold selection is one of the main contributors to the uncertainty of this approach.

Secondly, the complexity. It is the frame assembly that allows the approach to capture the full development of the jet. However, the complexity of the PIV frame assembly set-up can increase the acquisition uncertainty of the leeward jet.

Thirdly, the two dimensional representation. This approach is fully dependent on the 2D characteristics of the planar jet in crossflow. However, as a 3D flow region, the two dimensional representation can be a serious issue when the approach is applied for the 3D applications, especially the mass flow that is from the corner of the jet outlet.

As such, in the future studies, in addition to the induction of a semi-empirical model for the prediction of the planar jet, the selection of the threshold, especially its influence on the leeward edge definition needs to be fully investigated. Also, the uncertainty of this

approach on the set-up and the 3D volume representation should be investigated.

5.2 Recirculation

Recirculation is one of the most important characteristics in the planar jet in crossflow, which highly affects the shielding of the air curtain. In this section the recirculation structure of the jet in crossflow is discussed. Figure 5.8 is the time-mean streamlines of PIV test case D0201010101, with dual planar jets. As depicted earlier, one large recirculation structure is induced downstream of the primary jet, hereinafter referred to as the main recirculation. In addition, two more small recirculation structures can be detected upstream of the primary jet. To be more precise, in the zone that is between two jets. As introduced in the Chapter 2, previous research on twin jets in the quiescent flow has termed the area between the two jets as the recirculation zone. When the crossflow is introduced, however, this term can be confused with the main recirculation. Therefore, considering its triangle-like shape, this region is termed as the Delta zone (Δ zone).

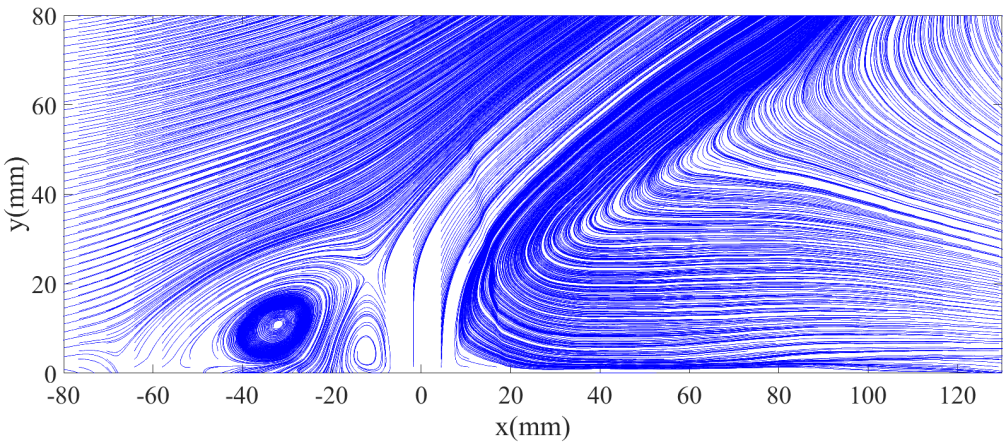

Figure 5.8: Streamlines of D0201010101 in the PIV test matrix

However, it is observed that the streamwise length of the frame, even in the assembly, cannot fully capture the development of the main recirculation. Therefore, those recirculation structures are discussed based on CFD simulations shown in Table 4.2.3 of Section 4.2. There are a few advantages when using the CFD results. First of all and most im-

portantly, those models have been validated using PIV experimental data. Secondly, the computational domain of those models can fully cover the development of the jets, which allows a complete analysis of the flow regime. Thirdly, the ease of the information acquisition from the CFD results process can substantially facilitate analysis. In the remainder of this section, the Delta zone and the main recirculation are discussed.

5.2.1 Recirculation of the Delta Zone

For dual jets in crossflow, the recirculation structures upstream to the primary jet can be detected mainly in the Δ zone. The Δ zone is the area between two jets. Due to the large momentum flux that exists on both sides, fluid in this area is continuously entrained into those two jets and as a result, the pressure gradient is generated, underlying the generation of recirculation. It is obvious that the flow field of this zone is highly dependent on conditions of the jets and crossflow, e.g. $U_{ju}, U_{jp}, U_{\infty}$, etc. In addition, the geometry of the configuration also plays an important role, such as w_u, w_p and d. As Table 4.2.3 shows, in this study the geometry of the configuration was kept constant. Therefore, this study mainly focuses on the effects of the jet speed.

Figure 5.9 illustrates the streamlines of the Δ zone. It is observed that there are two recirculation structures in the zone, which is in agreement with the PIV result in Figure 5.8. Hereinafter, the upstream one is referred to as R1 and the downstream one is referred to as R2. There are some interesting phenomena that can be observed from these two structures.

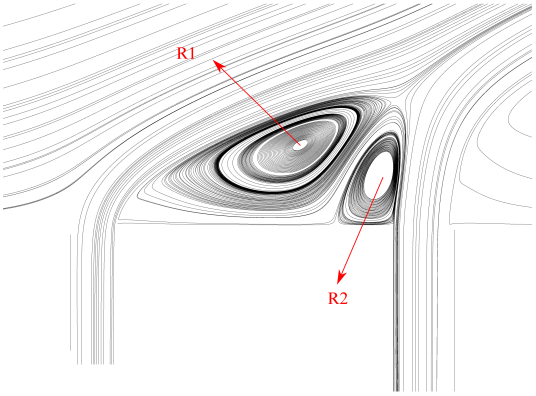

(a) No. 11 ($U_{ju} = 50m/s, U_{jp} = 40m/s$)

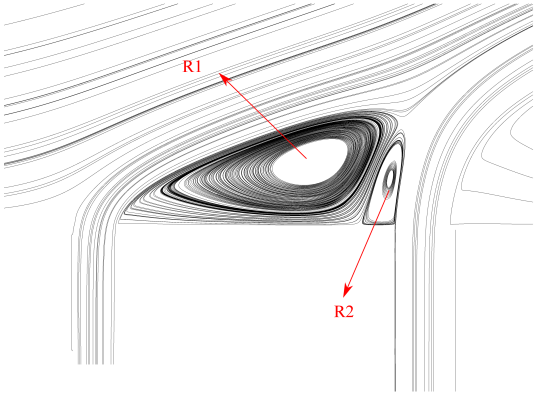

(b) No. 12 ($U_{ju} = 50m/s, U_{jp} = 30m/s$)

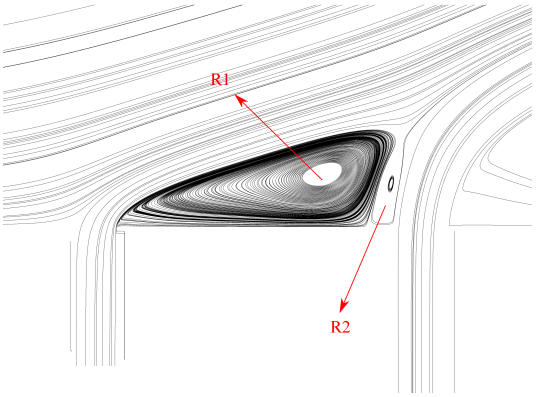

(c) No. 13 ($U_{ju} = 50m/s, U_{jp} = 20m/s$)

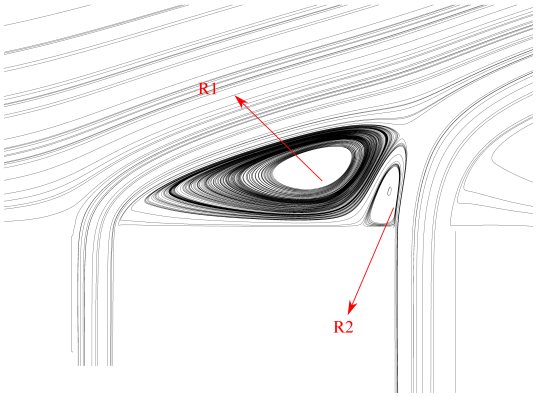

(d) No. 14 ($U_{ju} = 40m/s, U_{jp} = 30m/s$)

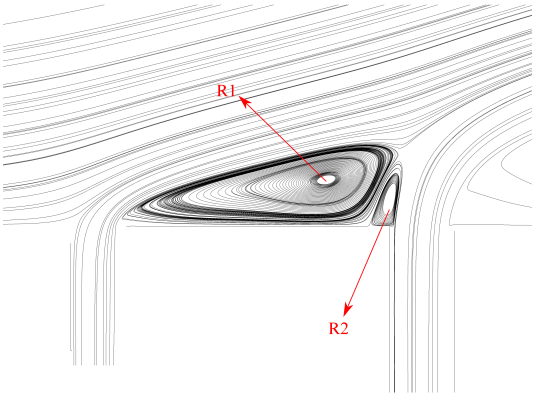

(e) No. 15 ($U_{ju} = 40m/s, U_{jp} = 20m/s$)

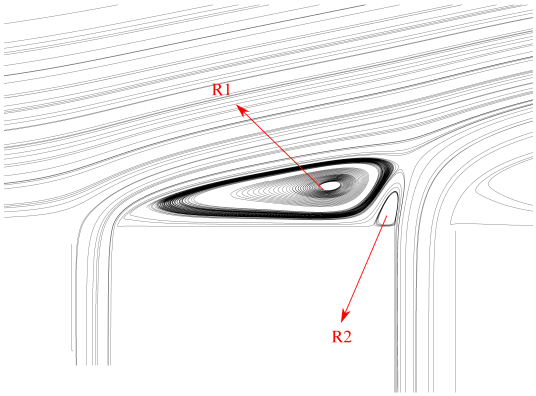

(f) No. 16 ($U_{ju} = 30m/s, U_{jp} = 20m/s$)

Figure 5.9: Δ zone

Firstly, it is observed that R1 is substantially larger than R2 regardless of jet velocities.

If using S_{R1} and S_{R2} to denote the area of R1 and R2, then $S_{R1} > S_{R2}$. However, the quantification of S_{R1} and S_{R2} is still ambiguous. As such, the conclusions are made based on the appearance of the streamlines. It is found that the ratio of S_{R1} and S_{R2} is dependent on U_{jp}/U_{ju}. More specifically, U_{jp} is constant in Cases No. 11, 12 and 13. U_{jp}/U_{ju} varies among $5/4, 5/3$ and $5/2$. As shown in Figure 5.9 (a)-(c), the area ratio, i.e. S_{R1}/S_{R2} appears to be negatively correlated with U_{jp}/U_{ju}. Moreover, the same trend can be also observed in Figure 5.9 (d) and (e), which have same U_{ju} but different U_{jp}. In addition, one more interesting finding is that the total size of S_{R1} and S_{R2}, i.e. area of the Δ Zone, is affected by the sum of U_{jp} and U_{ju}. For example, No. 11 and No. 16 possess the largest and the smallest $U_{jp} + U_{ju}$ respectively. Correspondingly, the size of their Δ Zone is also the largest and the smallest. As reported in Table 4.2.3, $U_{jp} + U_{ju}$ of No. 13 and No. 14 is equal to each other. As shown in Figure 5.9 (c) and (d), the size of the Δ zone is also close. However, this closeness of the zone area existing inside those cases with same $U_{jp} + U_{ju}$ cannot be confirmed yet. Therefore, more dataset is needed.

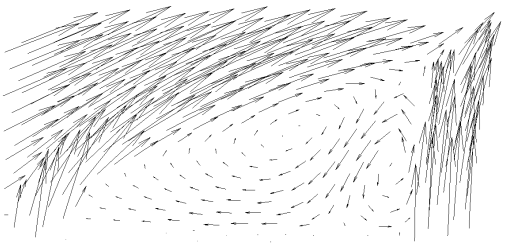

Figure 5.10: Vector field of the flow velocity in the Δ Zone (No.11)

Secondly, the direction of R1 and R2 are found to be opposite. As illustrated in Figure 5.10, the velocity vectors show that the direction of R1 is clockwise and R2 is anti-clockwise. Further to the previous comments, all recirculation structures inside the jet in crossflow is induced by the entrainment. More specifically, fluid below the upstream jet keeps being entrained into the jet, which in turn results in a low pressure area in the upper side of the Δ zone. The fluid in the bottom will continuously ascend to offset the pressure gradient. As such, the flow direction is clockwise, which is R1. By contrast, the downstream fluid in the Δ zone is mostly entrained to the primary jet, which explains the anti-clockwise direction of R2.

5.2.2 Main Recirculation

The main recirculation exists behind the primary jet (or the rear jet in the multiple jets configuration) in crossflow. Since the landing gear or bluff body is situated inside the recirculation, it is one of the flow characteristics that the noise reduction is subject to. Figure 5.11 shows the streamlines in the main recirculation of No. 3, 11, 12 and 13. No. 3 is a single-jet configuration and the rest are with dual jets. However, they all possess equal primary jet velocity.

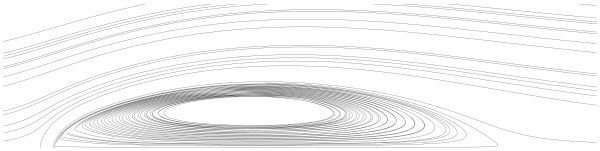

(a) No. 3 (singe jet, $U_\infty = 50m/s, U_{jp} = 50m/s$)

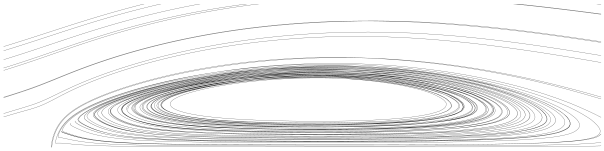

(b) No. 13 (Dual jets, $U_\infty = 50m/s, U_{jp} = 50m/s, U_{ju} = 20m/s$)

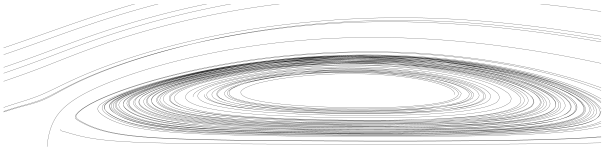

(c) No. 12 (Dual jets, $U_\infty = 50m/s, U_{jp} = 50m/s, U_{ju} = 30m/s$)

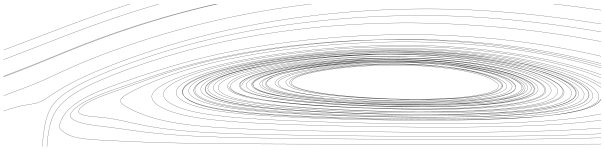

(d) No. 11 (Dual jets, $U_\infty = 50m/s, U_{jp} = 50m/s, U_{ju} = 40m/s$)

Figure 5.11: Main recirculation

In Figure 5.11, it is found that when the upstream jet is introduced, the main recir-

culation traverses downstream, and the translation is positive correlated to the speed of the upstream jet. Also, it can be observed that not only the position but the size of the recirculation varies with the upstream jet speed. To be more specific, the area of the main recirculation is significantly extended with the upstream jet. When the upstream jet speed increases, the area also becomes larger as a result. As discussed in the previous section, the leeward edge gets elevated with the speed of the upstream jet increases. To some extent, the shielding area is equivalent to the area of the main recirculation. As such, it has the same trend with the shielding area.

5.2.3 Impact on the Velocity Field

Recirculation has a substantial impact on the flow field of the dual jets in crossflow. For example, to offset pressure gradient. Moreover, the velocity contour is correlated to the streamlines. Figure 5.12 illustrates the velocity field of No. 11 in the Δ zone and the main recirculation. Overall speaking, the velocity in those zones is significantly reduced due to the shielding from the jets. Inside each structure of the recirculation, the velocity magnitude is much lower in the centre of the recirculation than the outer region. In Figure 5.12 (a), a reversed flow, blowing from the downstream to the upstream, can be detected below the centre of R1. It is this reversed flow that makes the magnitude of the velocity higher in the bottom of this Δ zone. This reversed flow can be also observed in the main recirculation zone. As shown in Figure 5.12 (b), the bottom of the main recirculation possesses higher velocity due to the reversed flow. This also explains why the rods can still be a main noise.

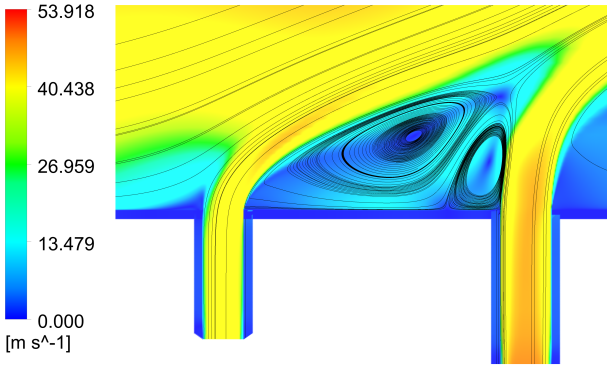

(a) Recirculation zone

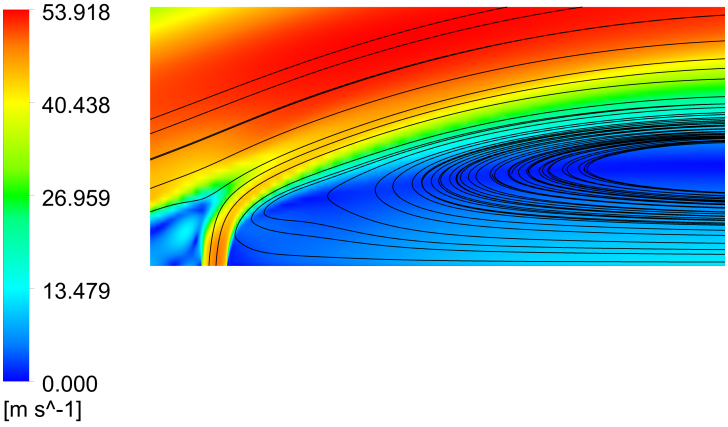

(b) Main recirculation

Figure 5.12: Velocity contour of the flow field with streamlines (No. 11: $U_{ju} = 50m/s$, $U_{jp} = 40m/s$)

5.3 Jets Developments

As previously reviewed in Section 2.2.2.2, significant studies [97, 109, 110] have been conducted on the development of tandem jets in crossflow. A common view has been agreed that those jets will converge, merge and finally combine. As such, the development of the tandem jets, for example, dual jets, can be subdivided as the converging region, merging region and combined region, shown in Figure 5.13. However, there is not a confirmed method to recognise these three regions. Therefore, one approach based on the horizontal velocity profile is proposed in this section.

Research on the tandem jets in quiescent flow, as reviewed in Section 2.2.1.2, used velocity profile to define merging and combination. Likewise, the development of the tandem jets can be subdivided into the converging region, the merging region and the

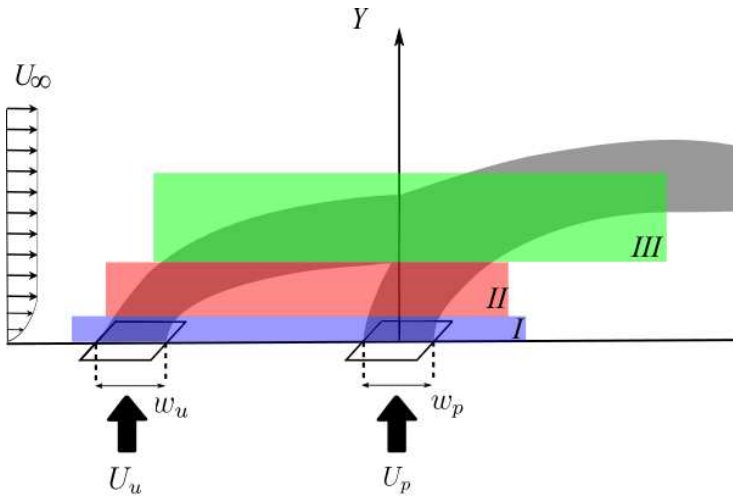

Figure 5.13: Subdivisions of the dual jets in crossflow: I. converging region; II. merging region; III. combined region

combined region. In the spanwise velocity profile, two separate peaks can be found in the converging region, two intersect peaks can be found in the merging region; only one peak can be found in the combined region. When the crossflow is introduced, the development of the jets can be substantially different from in a quiescent environment. In particular, the deflection and the combination of two jets. However, due to the initial moment flux from the jet (M_0), which is normal to the crossflow and can affect the trajectory of the jet, it is believed that in the horizontal velocity profile, one peak can be still observed for each jet prior to the combination.

In order to validate the assumption, a series of horizontal probes were extracted from the velocity contour of each simulation result, shown in Figure 5.14. Height of these lines begin from $y/w_p = 0.5$ to $y/w_p = 5$ and the spacing between is $0.5y/w_p$. The profiles are reported in Figure 5.15, which include Cases 11, 12 and 13. To highlight the peak, the velocity is normalised by U_{max}, i.e. the maximum velocity in each profile. These three cases possess same U_{jp} but different U_{ju}. In Figure 5.15 (a), it is shown that at low y/d, less than 2, two peaks can be easily detected. These two peaks are separate with a gap between, which is marked with red lines. The gap can be characterised by two cusp points on the side. Inside the gap, the speed is extremely low, which corresponds to the Δ zone. However, the width of the gap shrinks when y/d ascends and finally disappears. Obviously, this is due to the converging of two jets. As such, the existence

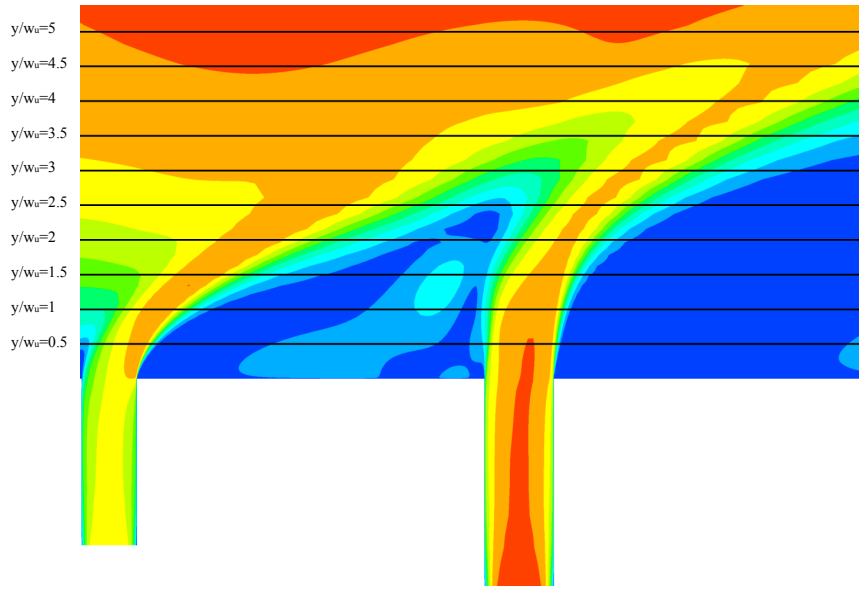

Figure 5.14: Streamwise probes for the streamwise mean velocity profile

of the gap can be used to define the converging region of the dual jet in crossflow. When $y/w_p > 2$, unlike those profiles of the merging region in the dual jets in quiescent flow, the upstream peak becomes indistinct and can be hardly detected. In addition, a saddle with the smooth curve is shown instead of the gap. Likewise, the depth of the saddle decreases with y/w_p ascending. When y/w_p reaches 5, the saddle has completely disappeared. In effect, the variation of the saddle can be explained by the velocity contour. As illustrated in Figure 5.14, the sampling line of $y/w_p = 2.5$ penetrates the Δ zone where the two jets are merging. When $y/w_p = 5$, the sampling line has ascended over the Δ zone, which means two jets have combined. Therefore, the saddle can be a characteristic to distinguish the merging region. In summary, the subdivision of development in the crossflow can be carried out based on the gap and the saddle. More specifically, in the converging region, two clear peaks, separated by a gap, characterised by two cusp points, can be observed in the streamwise velocity profile. In the merging region, only one peak can be observed, with a saddle area upstream. By contrast, in the combined region, no peaks can be observed.

With the subdivision of the tree regions, it is possible to conduct a parametric analysis on the development of two jets. For example, it can be concluded that in No. 11 those sampling probes with $y/w_p = 0.5, 1, 1.5$ and 2 are in the converging region; $y/w_p = 2.5, 3, 3.5, 4$ and 4.5 are inside the merging region and only $y/w_p = 5$ is in the combined

region. Likewise, the distribution of the height in different regions of other cases as well as No. 11 is reported in Figure 5.16 (a). When U_{jp} is fixed, it is found that the combination happens and gets closer to the jet outlet with U_{ju} decreasing. It suggests that the height of the Δ zone also decreases. Furthermore, No.13, No.15 and No.16 are reported in Figure 5.16 (b), which possess same U_{ju} but different U_{jp}. It is observed that the combination also gets closer to the outlet when U_{jp} decreases. Therefore, it is confirmed that the speed of both U_{ju} and U_{jp} has a significant impact on the development of dual jets in crossflow.

In this section, an approach to defining and recognising the sub-regions of the dual jets in the crossflow is proposed and validated. This sub-regions include the converging region, the merging region and the combined regions, which can be characterised by a gap (converging region) and a saddle (merging region) inside the horizontal velocity profiles. With the sub-region definition, it is possible to conduct a parametric analysis on the development of two jets, which is validated through an example.

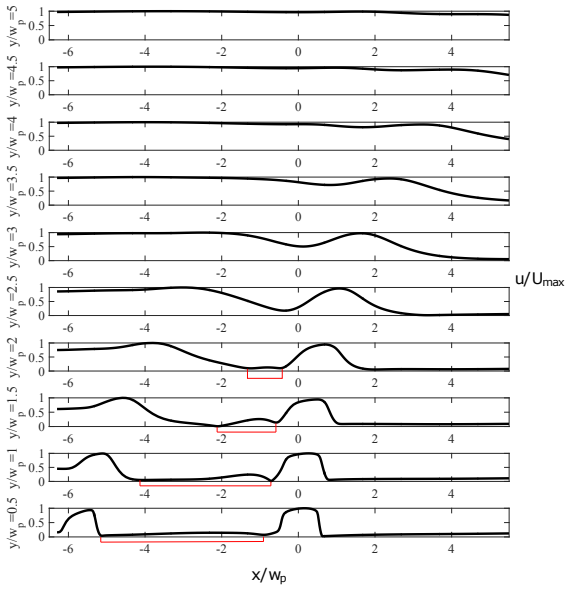

(a) No. 11 ($U_{jp} = 50m/s$, $U_{ju} = 50m/s$, $U_{jp} = 40m/s$)

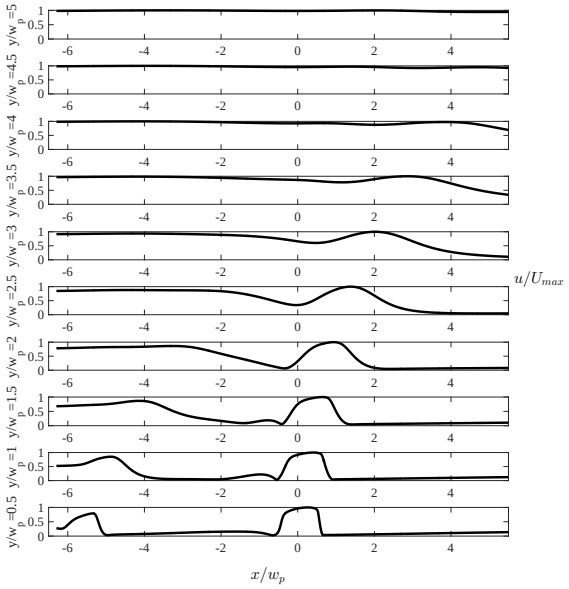

(b) No. 12 ($U_{jp} = 50m/s$, $U_{ju} = 50m/s$, $U_{jp} = 30m/s$)

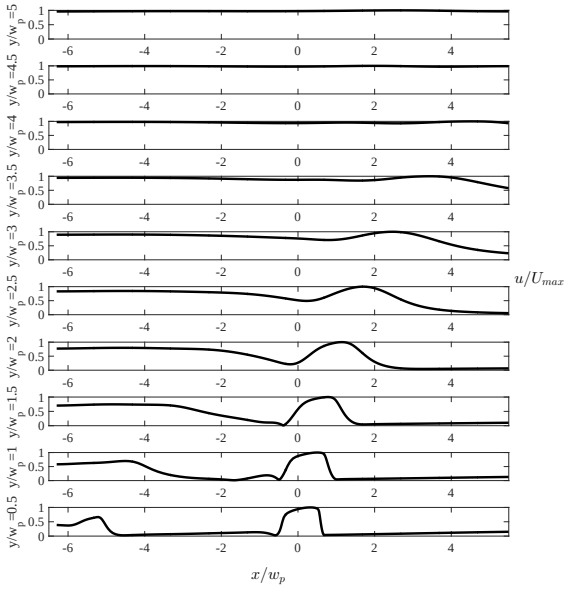

(c) No. 13 ($U_{jp} = 50m/s$, $U_{ju} = 50m/s$, $U_{jp} = 20m/s$)

Figure 5.15: Streamwise velocity profiles of the dual jets in the crossflow at different y/w

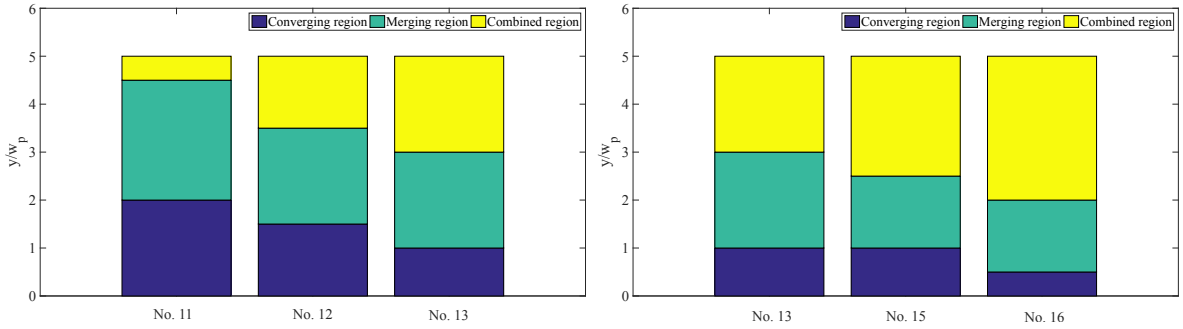

(a) Cases No.11, No.12 and No.13 (U_{jp} is fixed) **(b)** Cases No.13, No.15 and No.16 (U_{ju} is fixed)

Figure 5.16: Subdivisions of the dual jets development in the crossflow

5.4 Summary

In this chapter, the flow regime of the dual jets in the crossflow was discussed. First of all, a novel approach to defining the leeward edge of the primary jet was proposed. Based on the PIV measurement, this approach allows the leeward edge to be mathematically expressed using a second order polynomial. The expression facilitates the establishment of a semi-empirical model for the leeward edge in the future study. Secondly, the recirculation of the flow regime was discussed based on CFD simulations. More specifically, in the Δ zone, two main recirculation structures were detected, termed as R1 and R2. The existence of these two structures was also validated by the PIV experiment. In this section, R1, R2 as well as the main recirculation downstream to the primary jet were characterised. At last, the development of the jet was investigated. The subdivision system that has been widely utilised in the dual jets in the quiescent flow was applied in this section. The development of the dual jets in the crossflow was also subdivided into the converging region, merging region and combined region. Those three regions were characterised using the streamwise velocity profile. Furthermore, the variation of the three regions with the flow initial conditions was discussed.

Chapter 6

Combined Use with Perforated Fairings

The air curtain, as a novel technology proposed for landing gear noise reduction, is expected to not only achieve significant noise reduction, but also avoid disadvantages that other technologies may have, such as impede the inspection, maintenance and brake cooling. Therefore, the solo use of the air curtain technology is believed to be appropriate for landing gear noise reduction. However, discussions on a combined use with other technologies still make sense for reference. As such, in this chapter, investigations on the combined use of the dual jet air curtain with other noise reduction technologies is conducted.

In Section 2.1, the landing gear noise reduction technologies that can be found in publications have been reviewed in detail. It is found that the solid fairing, which possesses the highest technology readiness level, can be a good option for the combinational use due to the ease of set-up. However, it has been observed that high speed flow deflection onto other components and the fairing self-noise are the major disadvantages of these fairing type, which can inhibit the successful application. As such, the perforated fairing , abbreviated as PF in the following, has been proposed. As discussed in Section 2.1.2.1, firstly it is found that the bleeding air through these perforating fairings can further result in better redistribution of the airflow and yield better acoustic performance. Secondly, it is expected to reduce the undesired noise increase from other uncovered component. The solid fairing reduces landing gear noise by deflecting high speed flow. However, the deflected flow may interact with other uncovered components to generate extra noise emission. By contrast, the perforated fairing allows some flow to pass to avoid the extra noise emission. Thirdly, the porosity can reduce the fairing weight so that a less load on the landing gear can be attained.

In this Chapter, the combined use of dual-jet air curtain and PF is discussed for reference.

6.1 Test Programme

In this Chapter, the combined use is discussed and investigated trough ten different geometries.

Likewise, these ten geometries were abbreviated with capital letters. As shown in

Figure 6.1. F, R, AC, ACu and PF are respectively used to denote the crossflow, rods, primary jet, upstream jet and PF. Therefore, these geometries are simply abbreviated as F, F-R, F-AC, F-AC-ACu, F-R-AC, F-R-AC-ACu, F-PF$_u$, F-R-PF$_u$, F-R-AC-ACu-PF$_u$ and F-R-AC-ACu-PF$_d$. More specifically, F is the geometry in which only the crossflow was turned on to characterise the background noise. In F, the outlet of all air curtains was sealed to avoid possible cavity noise. In F-R, the tandem rods were situated inside within the crossflow, in order to characterise the rods noise without any reduction technologies used. F-AC and F-AC-ACu were conducted for characterising the flow regime and jet noise of air curtain within the crossflow. Geometries F-R-AC and F-R-AC-ACu were for evaluating the noise reduction of tandem rods using the single-jet and the dual-jet geometries. Note that in this chapter a_0 and b_0 were achieved using the leeward edge definition discussed above. Also note that in all geometries with dual jets in this chapter, only one configuration of the jet speed was tested, which kept U_{ju} same. The more efficient configuration of the dual jets geometry introduced in the previous Chapter was not tested. This is because the main objective of this Chapter is to investigate whether the introduction of the perforated fairing can improve performance of the total noise reduction. therefore, the improvement attained by the optimization of the dual jets geometry, i.e. reducing the speed of both jets, is not discussed in this Chapter. Geometries that are related to perforated fairings include F-PF$_u$, F-R-PF$_u$, F-R-AC-ACu-PF$_u$ and F-R-AC-ACu-PF$_d$. In F-PF$_u$, only one piece of PF was placed inside the crossflow. This is mainly to characterise its flow regime and noise production of the PF. Then the rods were placed inside behind the fairing. The location was as same as that in the previous geometries. F-R-AC-ACu-PF$_u$ and F-R-AC-ACu-PF$_d$ were conducted as two different geometries with the combined use. In F-R-AC-ACu-PF$_u$ the fairing was placed upstream to the rods, the position is as as same as those geometries mentioned before. While in F-R-AC-ACu-PF$_p$, the perforated fairing was placed downstream to the rods. Explanations and more specifics on this geometry are introduced in the following sections.

In addition, the dimension of both w_u and w_p in this Chapter is $10mm$. U_∞, U_{ju} and U_{jp} were designed to be $50m/s, 50m/s$ and $40m/s$. The real speed measured from the micromanometer is reported in the following Table 6.1.

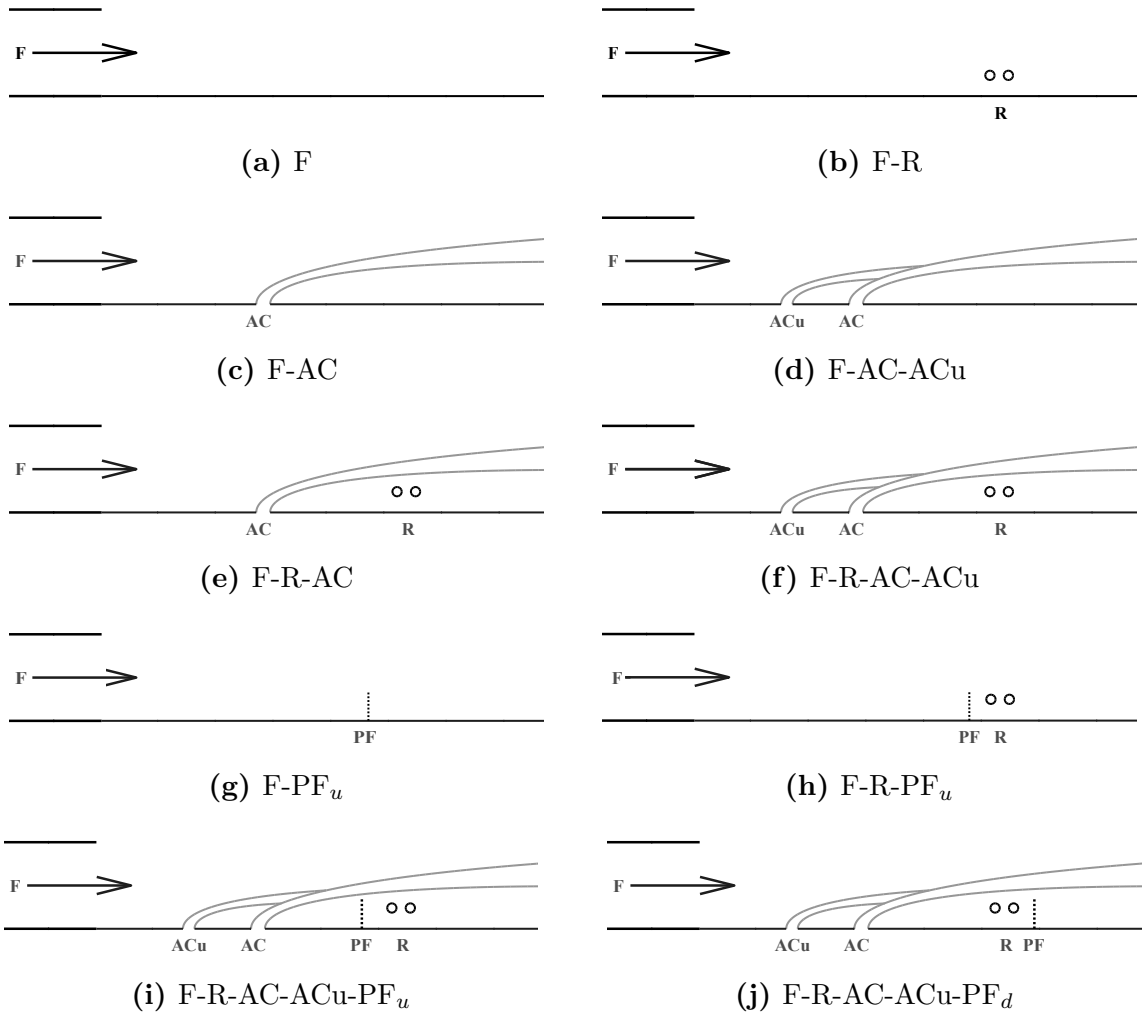

(a) F **(b)** F-R

(c) F-AC **(d)** F-AC-ACu

(e) F-R-AC **(f)** F-R-AC-ACu

(g) F-PF$_u$ **(h)** F-R-PF$_u$

(i) F-R-AC-ACu-PF$_u$ **(j)** F-R-AC-ACu-PF$_d$

Figure 6.1: Geometries of the tests

Table 6.1: Initial conditions of the tests

	U_∞ (m/s)	U_{ju} (m/s)	U_{jp} (m/s)
F	50.12	\	\
F-R	50.23	\	\
F-AC	50.04	\	49.52
F-AC-ACu	49.95	40.95	50.23
F-R-AC	50.04	\	50.05
F-R-AC-ACu	49.87	40.16	50.23
F-PF$_u$	50.15	\	\
F-R-PF$_u$	50.23	\	\
F-R-AC-ACu-PF$_u$	50.42	40.05	50.04
F-R-AC-ACu-PF$_d$	50.23	40.05	50.04

6.2 Optimal Position of the Rods

In Chapter 3, the position of the rods was optimised through the centreline of the jet based on CFD simulations. In this chapter, the optimization is performed using the leeward edge method described in Section 5.1.

As discussed in Section 5.1, the leeward edge of the primary jet can be fitted using a second order polynomial. Therefore, the optimised position is attained by referring to the leeward edge, which makes more sense than the jet centreline. To be more specific, F-AC and F-AC-ACu were tested using PIV. Experimental data and the fitted shielding curves are illustrated in Figure 6.2, along with the corresponding equations. Note that the threshold to define the leeward edge is also 1/4 of the local maximum here. It is clearly observed that the shielding curve is much higher in F-AC-ACu than in F-AC due to the introduction of the upstream jet. As for a_0 and b_0, herein a_0 is made to align with the peak of the shielding curve in F-AC and b_0 is equal to the height of the peak. Therefore, it is found that $(a_0, b_0) = (7.82w_p, 1.62w_p)$. In the meantime, at $x = 7.82w_p$, the height of the shielding curve in the dual jets geometry increases to $3.74w_p$, which is $2.12w_p$ higher than F-AC. Though $x = 7.82w_p$ is not shielding position of F-AC-ACu, the rods were kept at $x = 7.82w_p$ in both F-R-AC and F-R-AC-ACu for comparison. Configuration of the set-up remains to be as same as in Chapter 4, illustrated in Figure 4.3. The top height of the rods was controlled to be lower than $1.62w_p$, which is 16mm.

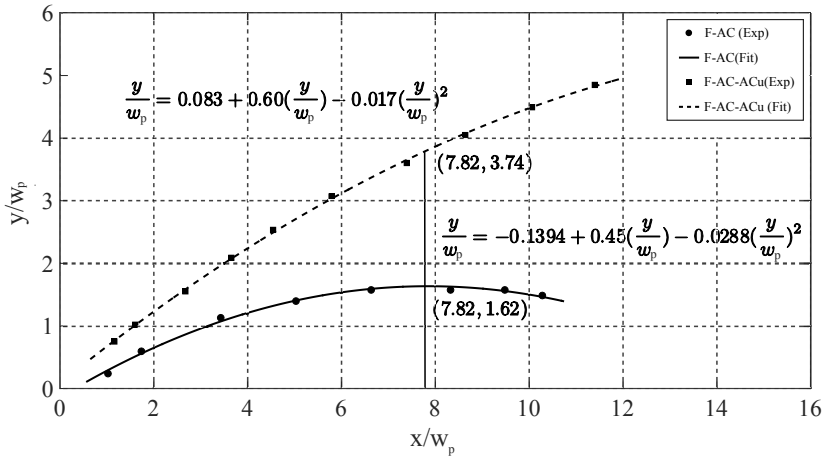

Figure 6.2: Shielding curve of F-AC and F-AC-ACu

It is worth noting that the optimised position of the rods is different from the one

acquired in Chapter 4. First of all, in Chapter 4 the position optimization was refereed to the jet centreline. In this Chapter, it is refereed to the leeward edge, which is more reasonable. Secondly, the dimension used is different, i.e. 8mm for w_u in Chapter 4 and 10mm for w_u in this chapter. At last, these experiment sets in the two chapters were carried out at different time stages. Though the flow has been designed to supply stable conditions, those irresistible factors, e.g. the temperature difference between summer and winter, can make a substantial influence on the measurement. Therefore, results in Chapter 3 and Chapter 5 are not directly comparable.

6.3 Performance of Air Curtain

In this section, the acoustic performance of the air curtain was further evaluated through the measurement using the array.

Figure 6.3 illustrates the averaged one third octave band spectra that are related to the air curtain. As expected, both single and dual jets geometries can be of good use for the flow induced noise reduction. In particular, the peak of SPL in F can be removed, not to mention the obvious overall noise reduction. However, it is found that the SPL of both geometries increase in the last three bands, which should be attributed to the jet noise as discussed earlier. When it comes to the comparison between two geometries, the difference in the low frequency range can be easily observed, which, as discussed before, is mainly a result of the extra noise reduction achieved from the rods. In the last tree bands where F-R-AC and F-R-AC-ACu are more noisy than F-R, it is found that the dual-jet geometry makes slightly more noise than the single-jet.

Figure 6.5 and Figure 6.6 are the noise map attained through beamforming in the frequency domain. In order to illustrate the performance that is related to the frequency, the frequency of interest in the two figures is different, i.e. 7,000Hz and 14,000Hz respectively. When the air curtain is on, to begin with, it is found that the rods are still the main noise source at 7,000Hz in F-R-AC. However, at 14,000Hz the main noise source becomes the air curtain slot. This is in agreement with what has been found in Chapter 3. Then in F-R-AC-ACu, it is observed that the sound pressure level of the rods were further reduced when the dual jets were used. By contrast, the main noise source becomes

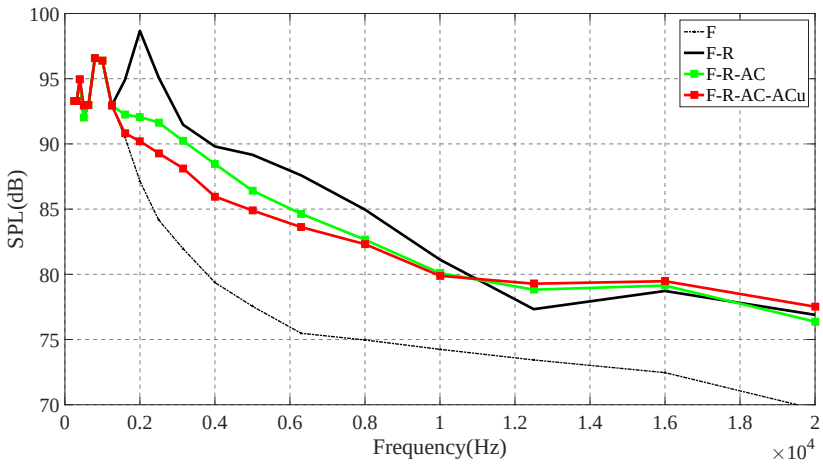

Figure 6.3: One third octave band spectra related to the air curtains

the outlet of the upstream air curtain. Therefore, both spectral analysis and the noise localization confirm the same conclusion that is acquired from Chapter 3. Namely, the total jet noise emission cannot be reduced only by the introduction of the upstream jet. This necessitates keeping the shielding curve approximately same by reducing both jets speed, which has been discussed earlier in Chapter 4.

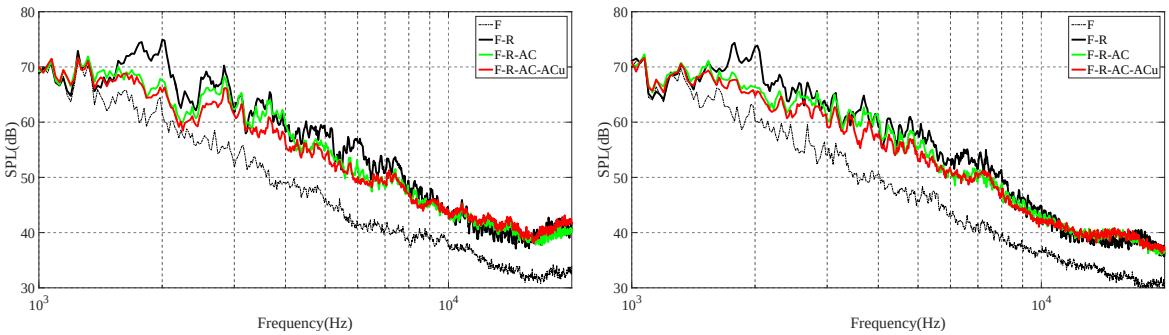

(a) No. 1 **(b)** No. 19

Figure 6.4: Auto-spectra from different microphones in the array

In addition, the auto-spectra from Microphone No. 1 and No. 19 are illustrated in Figure 6.4. As discussed before, the relative height of the two peaks can be found to vary between two microphones due to directivity. They respectively correspond to the vortex shedding behind the upstream rod and the downstream rod. After the air curtain is introduced, in the low frequency range ($f < 10,000Hz$) it is observed that the dual-jet is quieter than the single-jet. By contrast, a reversed trend can be found in the high frequency range. As such, the overall performance is in agreement with the one third

octave band spectra.

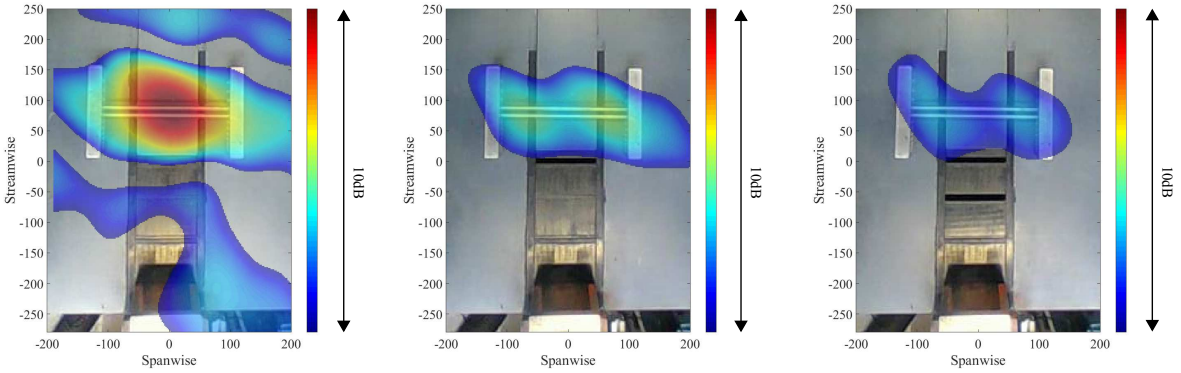

(a) F-R **(b)** F-R-AC **(c)** F-R-AC-ACu

Figure 6.5: Noise map at 7,000Hz

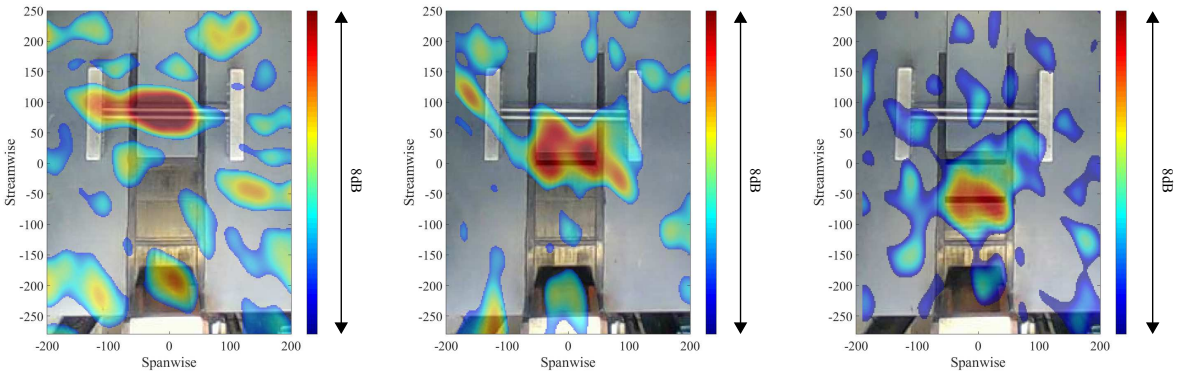

(a) F-PF$_u$ **(b)** F-R-AC-ACu-PF$_u$ **(c)** F-R-AC-ACu-PF$_u$

Figure 6.6: Noise map at 14,000Hz

6.4 Characteristics of PF

As introduced in Section 2.1.2.1, the introduction of PF can bring significant effects on the flow field. Firstly, it can deflect the incoming flow to reduce the downstream flow speed. Secondly, the incoming flow that passes through the holes can be broken up into small vortices. Both of these features are believed to be beneficial for the noise reduction of the landing gear. However, it is found that the characteristics of the flow field, which dominates the noise reduction, are dependent on various factors, e.g. porosity, hole size, etc. Therefore, the flow field of the PF is characterised in this section.

Table 6.2: Specification of PF used in the test campaign

Parameter	Value	Comment
t_p	1	Thickness of the fairing (mm)
d_{or}	2	Diameter of the hole (mm)
p_{or}	3.5	Pitch between holes (mm)
ϕ	60^0	Distribution of the holes
σ	29.61%	Porosity of the perforated material*

To begin with, one sample of a generic PF was tested in this study, the specification of which is reported in Table 6.2. Note that for a metal plate with circular holes and triangular pitch, the porosity (σ) is calculated as: $\sigma = \frac{d_{or}^2 \times 90.69}{{p_{or}}^2}$, where d_{or} and P_{or} are the diameter of the hole and pitch between two holes.

First of all, acoustic measurements were carried out. The measurements were conducted on the geometry of Figure 6.1 (g). The installation of the fairing is described in Figure 6.12 (a). Note that in this test all air curtain slots were sealed to avoid cavity noise. The position and the height of PF are as same as those in Figure 6.1 (h) and (i). To be more specific, the position of the PF was controlled to be 1mm upstream to the upstream rod. The height of the PF was made to be 1mm higher than the top of the rods. By contrast, in Figure 6.1 (j) PF was situated downstream to the rear rod to impair the recirculation flow coming from downstream, in which PF was set to be 1mm far from the rods and 1mm higher than the top of the rods. More specifics of F-R-AC-ACu-PF$_d$ are discussed in the next section.

Figure 6.7 shows the noise map of PF at different frequencies, acquired using frequency domain beamforming. It is clearly shown that a substantial self-noise can be made by the fairing at different frequencies. To be more specific, Figure 6.8 is the one third octave band spectra for F, F-R, F-R-PF and F-PF. When comparing F-PF with F, it is found that the SPL gets much higher in the frequency range that is over 5,000Hz. But it is as quiet as the background noise when the frequency is lower than 5,000Hz. Also, it can be observed that despite that the fairing can make self-noise, it is still much quieter than the rods. In particular, in the frequency range of $f \leq 5,000$, the SPL of F-PF is equal to the background. However, the SPL of the F-R can be up to around 10dB higher than F. In the frequency range of $5,000Hz < f \leq 10,000Hz$, the self-noise of the PF begins to increase but still less than the rods. In the high frequency range over $10,000Hz$, the

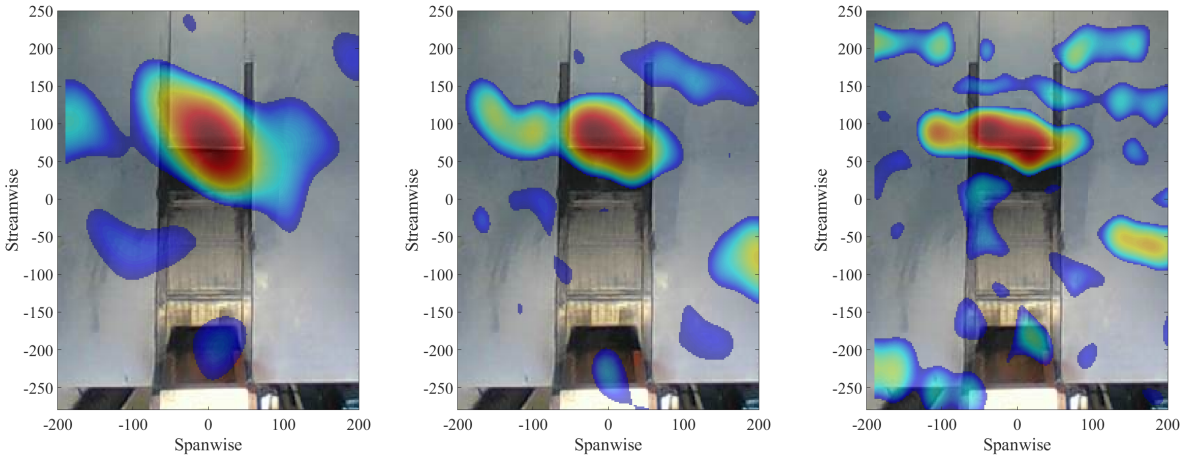

(a) 6,000Hz **(b)** 10,000Hz **(c)** 14,000Hz

Figure 6.7: Noise map of PF at different frequencies

self-noise of the PF becomes worse than the rods.

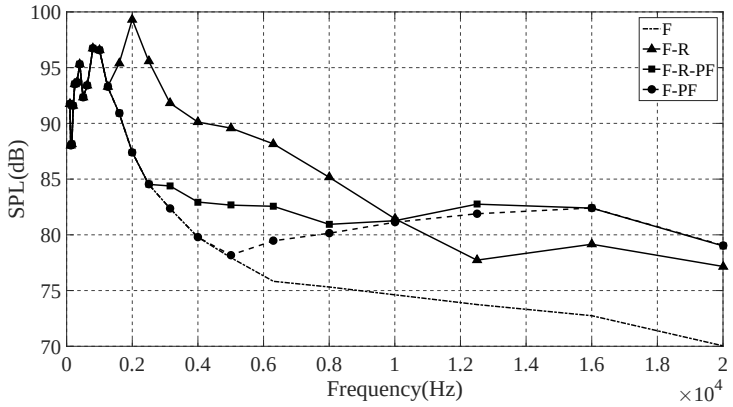

Figure 6.8: One third octave band spectra related to PF

The noise reduction of the rods using PF was also conducted. As introduced earlier, the fairing was installed upstream to the rods, shown in Figure 6.12 (b). From the one third octave band spectra in Figure 6.8, it can be observed that the installation of the fairing well reduces the rods noise. For example, the peak of F-R at 2,000Hz does not exist any more in F-R-PF. To be more specific, it was reduced to the level of the background noise with the fairing. However, in the frequency range of $f \geq 5,000$, SPL of the F-R-PF is found to be higher than without PF. In the meanwhile, it is roughly equal to F-PF. As such, there is no doubt that in this frequency range the self-noise from PF is the dominant source and the rods almost make no noise in this frequency range.

The auto-spectra from microphone No. 1 and No. 19 are used to illustrate more characterises of the noise source as well as directivity. In terms of directivity, not much difference can be detected between the spectra of F-PF and F-R-PF achieved from these two microphones. Therefore, it is suggested that the self-noise of PF can affect both upstream and downstream acoustic fields. In addition, these auto-spectra are in agreement with the one third octave band. To me more specific, when comparing F-PF with F, almost no SPL increase can be detected in the low frequency range. SPL of F-PF exceeds F when $f > 2,500Hz$, and the highest difference is over 10dB, occurring at $f = 1,4160Hz$. In F-R-PF, the rods cause extra noise emission when compared to F-R, especially in the range of $2,350Hz < f < 7,650Hz$. But those tones generated from the rods in F-R, no more exist in F-R-PF and can be reduced to the background noise level. In addition, a slight SPL increase in the frequency range of $10,000Hz < f < 16,000Hz$ can be detected due to the rods. It is known that PF dominates over other noise sources in this frequency range in F-PF. Total noise emission of the rods increased here, which can be possibly attributed to the air blowing through the holes.

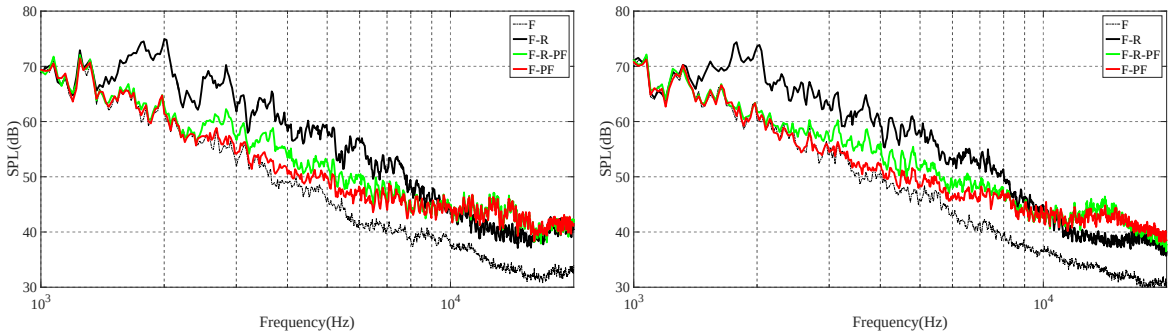

(a) No. 1 **(b)** No. 19

Figure 6.9: Auto-spectra from different microphones in the array related to PF

As such, it is validated that PF can produce substantial self-noise. In order to investigate the mechanism of the noise generation from the fluid mechanics point of view, hot-wire measurements were conducted. In particular, influence from the fairing on the mean velocity and the turbulence intensity of the crossflow was measured, both of which correlates with the noise reduction of the rods and the fairing self-noise generation. Hot-wire traverse was used to control the sampling position, the set-up is shown in Figure 3.8. The measurement plane was parallel to the fairing and 4mm downstream. In the mea-

surement plane, a grid was used to scheme the sampling positions. As shown in Figure 6.10, there are 13 columns of sampling points inside the grid, between each the distance is 5mm. In each column the vertical spacing between two sampling points starts from $1mm$ at the bottom and then alters to $2mm$ when the height is over the plate. This distribution allows a more refined measurement of the flow downstream to the fairing. This grid was used to characterise the PF wake.

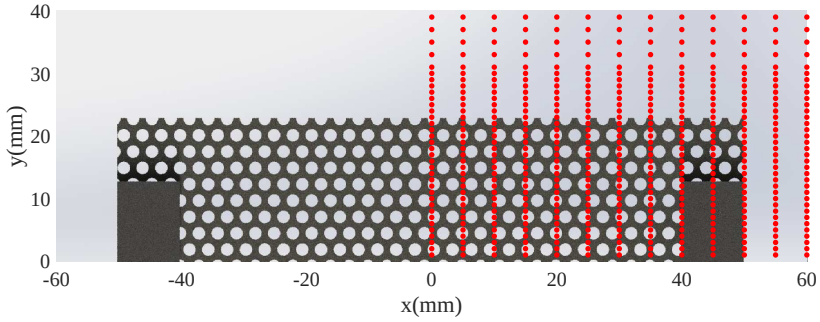

Figure 6.10: Test grid

Figure 6.11 is the results of the measurement, including normalised velocity profile and the turbulence intensity. As the normalised time-mean velocity profile shows in Figure 6.11(a), the speed of flow downstream to the PF, i.e. wake flow is significantly reduced. This to a large extent explains why the PF can reduce the rods noise. The upper edge separates the two regions that are shielded and not shielded by the PF. The rods placed downstream to the fairing are located at the reduced flow speed region of the fairing. The turbulence intensity displayed in Figure 6.11(b) illustrates that turbulence intensity peaks around the upper edge of fairing. Therefore, since the turbulence level is highly correlated to the aerodynamic noise level, it is reasonable to conclude that the fairing self-noise in this case is mainly as a result of edge effects (vortex shedding at edges).

In this section, measurements were carried out to characterise the PF. From the acoustic measurement, it is observed that despite the noise reduction of the rods that can be achieved, using PF can induce self-noise, which mainly concentrates in the high frequency range. Moreover, the aerodynamic measurements carried out by the hot-wire reveal that

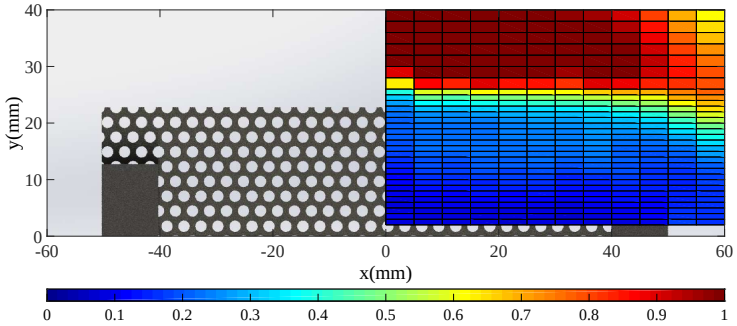

(a) Normalised velocity profile

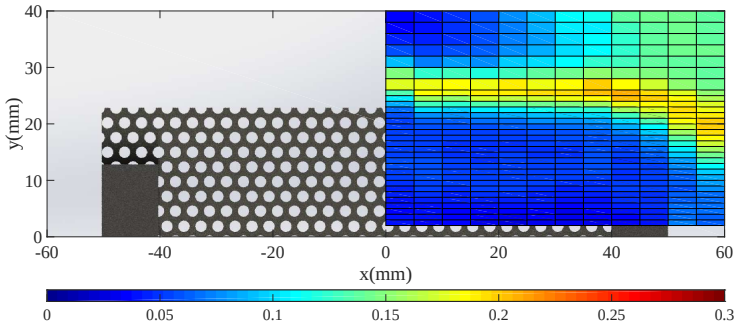

(b) Turbulence Intensity

Figure 6.11: Results of the wake flow measurement of PF

the self-noise is mainly from the edge-blowing. As such, the combined use of the air curtain and the PF is proposed, which will be discussed in the following section.

6.5 Combined Use with PF

As discussed earlier, the use of air curtain can significantly reduce the rods noise, especially the dual jets geometry. However, it is observed that the recirculation introduced by the primary air curtain can result in a local high speed area below the jet, making the rods one of the main noise sources in some frequency range. Also, it is found that the perforated fairing can generate substantial self-noise, which is mainly from the edge blowing of PF by the crossflow. Therefore, a hypothesis is made here that the combined use of the dual air curtains and the PF can improve the noise reduction using one technology alone. This section aims to conduct the discussion on this hypothesis based on experiment.

As shown earlier, there are two geometries of the combined use that were tested in this section, i.e. Figure 6.1 (i) and (j). When the air curtain works, it has been found that the existence of the recirculation can induce flow blowing to the rods from downstream. Therefore, the geometry with the fairing added behind the rods was also tested. The set-up is shown in Figure 6.12 (c) and (d).

As discussed in the last, the edge noise of PF is the key problem that affects the application of fairing. Therefore, in the combined geometries, the perforated fairing should be lower than the shielding curve of the primary jet.

(a) F-PF$_u$

(b) F-R-PF$_u$

(c) F-R-AC-ACu-PF$_u$

(d) F-R-AC-ACu-PF$_d$

Figure 6.12: Test set-up

Figure 6.13 shows the comparison of the acoustic performance among the corresponding cases. In the low frequency range less than 5,000Hz, both configurations with PF, regardless of the set-up, possess lower SPL than F-R-AC-ACu. This noise reduction is up to 3 dB for F-R-AC-ACu-PF$_u$ and 3.5 dB for F-R-AC-ACu-PF$_d$, which confirms that the introduction of PF can further reduce flow-induced noise of the rods. Moreover, in this range, it is found that the reduction achieved as a result of applying PF downstream to the rods exceeds that of the upstream fairing. Therefore, it is concluded that the recircu-

lation is a major factor that affects the subsequent noise emission of the rods. As such, situating the perforated fairing downstream to the rods appears to be more reasonable and beneficial than upstream.

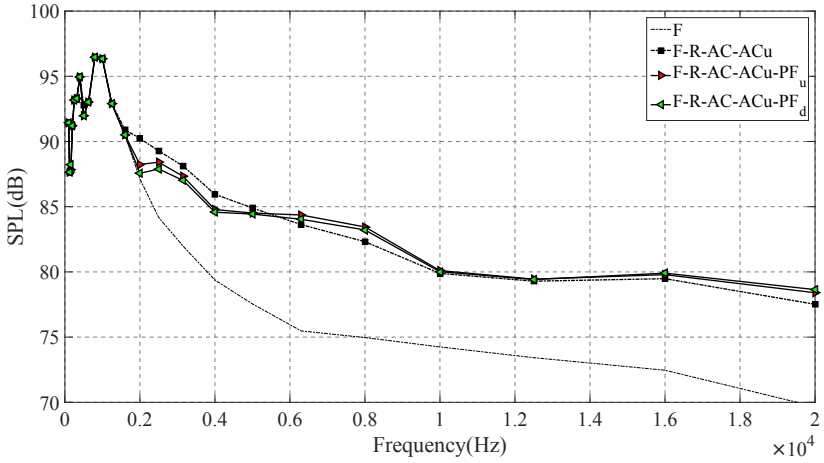

Figure 6.13: One third octave band spectra related to the combined use of air curtains and perforated fairings

One more set of tests were performed to compare the self-noise of the along use of the single-jet, dual-jet and PF. The comparison is illustrated through one-third octave band spectra illustrated in Figure 6.14, which consists of F, F-R, F-AC, F-AC-ACu and F-PF$_u$. It is obvious that among these geometries, F-R is the noisiest in the frequency range below 10,000Hz. By contrast, in the range over 10,000Hz, its SPL shows to be completely higher than F-PF$_u$, which has been discussed in the last section, and lower than the dual jets only in one band. However, the single jet is still quieter than F-R. Among those self-noise sources, to begin with it is found that they are almost as quiet as the background noise in the low frequency range that is below 4,000Hz. When the frequency increases, the fairing possesses the strongest self-noise, followed by the dual jets and then the single jet. There are one distinct point that is worth noting, which is at 5,000Hz. At 5,000Hz, PF is noisier than the dual jets but quieter than the single jet. This can be attributed to the introduction of the upstream jet. Therefore, the increase of SPL in other frequencies necessitates the configuration of reducing the primary jet speed, which has been discussed in the Chapter 5

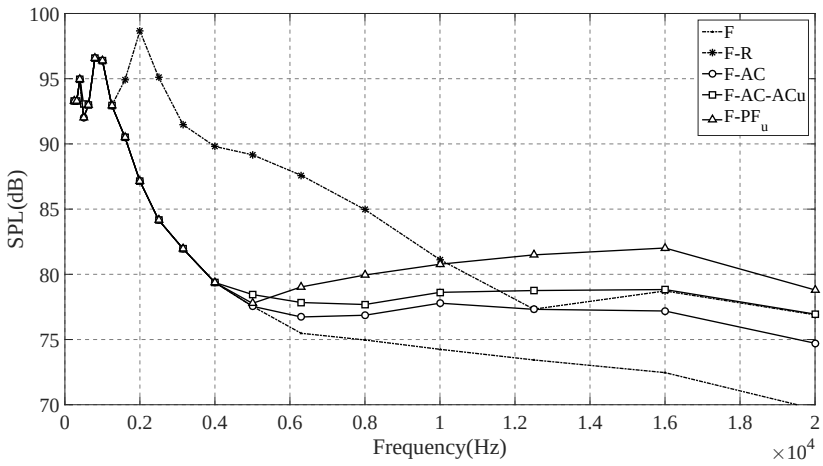

Figure 6.14: One third octave band spectra related to the self-noise of the combined use of air curtains and perforated fairings

6.6 Discussions

This Chapter mainly discussed the possibility of combined use of dual jet air curtains with the perforated fairing. The acoustic performance of the combined configuration with perforated fairing downstream to the rods produced the best result, and was undoubtedly concluded as the best geometry. However, from a realistic and practical implementation perspective, i.e. towards landing gear noise reduction, it is recommended to simply adopt the dual-jet blowing configuration only. This is due to the fact that the additional noise reduction achieved by the introduction of the perforated fairing, when compared to the dual-jet geometry, was minor. Also, the introduction of the fairing can impede the visual inspection, maintenance and proper brake cooling of the landing gear section, not to mention the added structural weight and complexity. Moreover, there exists more potential for noise reduction using the dual-jet configuration by reducing speeds for both jets to achieve the same shielding height. As such, it is recommended to apply the dual-jet air curtain geometry for the reduction of landing gear noise.

Chapter 7

Conclusions and Future Work

7.1 Summary and Conclusions

In this study, a novel geometry with dual air curtains (or planar jets) was proposed and validated to reduce landing gear noise. Previous studies have shown that the single air curtain can be of good use for the flow induced noise reduction. It is designed to be situated upstream to the bluff body, as a generic flow-induced noise source, to deflect the incoming crossflow. As such, the local flow speed that impinges the bluff body can be reduced and so can the aerodynamic noise. However, the self-noise generated from the air curtain itself, as a new subsequent noise source, remains a limiting factor that affects the performance of this technology, which can impede the implementation. Therefore, an extra jet was introduced upstream to the primary jet in the dual air curtains geometry. This novel geometry is based on the hypothesis that the introduction of the upstream jet can enhance the noise reduction achieved using the single jet through suppression of the jet self-noise. To be more specific, the upstream jet, which mainly possesses less speed, can impair interaction between the crossflow and the primary jet to attain less self-noise emission. Despite extra noise emission, the upstream jet is expected to reduce the total noise emission. In the validation process, it was found that an improved configuration of the dual jets can achieve lower noise emission. In particular, the speed of both jets can be managed to be lower than the single jet instead of maintaining the primary jet speed, while achieving the same shielding to the bluff body.

First of all, this thesis begins with an introduction to the background in Chapter 1. The introduction discussed why the aircraft noise is a serious issue and it pointed out the large contribution of the landing gear noise to the total aircraft noise. Also, in this chapter those technologies with high technology readiness level for the landing gear noise reduction were mentioned. More importantly, the necessity of the new technologies proposal was discussed.

Chapter 2 is the literature review. The first section concentrates on a systematic review on the technologies of the landing gear noise reduction, including the air curtain. In the review, there are (perforated) fairings, wheel hub caps, hole covering, mesh, plasma actuator and blowing flow control in the first section. Mechanisms of the noise reduction using these technologies were discussed. To be more specific, influences of each one on the

flow field of the landing gear (or bluff body) and accordingly on its acoustic performance were reviewed in detail. Comments and evaluations on these technologies were given. Then previous studies on the air curtain application were introduced. It reviewed the experimental work carried out in the NLR wind tunnel, which used one single planar jet to shelter the bluff body. It was validated in this study that one single air curtain can be of great use for the flow-induced noise reduction. Moreover, results in this study also revealed that jet self-noise of the air curtain can be a limiting factor that affects the performance of this technology. The second section of this chapter aims to provide a review of studies on the fluid mechanics and aeroacoustics of the jet, including the single jet and the tandem jets, in quiescent flow or in crossflow. The review was conducted because the air curtain, regardless of the jet number, can be simplified as the flow regime of a jet in crossflow. In the first part of this section, the jet in quiescent flow was discussed. An introduction to the fundamental concepts of the jet study was given, including the development of jet, jet half width, entrainment, etc. Also, the theory of the tandem jets and acoustics of the turbulent jet were also involved. The second part mainly focuses on the jet in crossflow. It begins with the development of the jet in crossflow, including MDNF and MDFF regions, and some basic concepts such as the momentum length scale. Then studies on the jet trajectory and edges were reported. In particular, the natural system that was frequently used and the best theoretical model of the planar jet trajectory to date were described. Entrainment and recirculation, which underlie the deflection of the jet, were characterised along with some interesting vortex structure induced by them. Tandem jets in crossflow were also discussed, characteristics of the flow regime possesses similarities to the single jet but more complicated. In addition, information on the acoustics of the jet in the crossflow was also provided despite being limited in scope.

Chapter 3 describes the experimental rig and instrumentation utilised in this study. The rig used in the lab consists of a low speed open-jet wind tunnel, planar jet generator and test platform. The aerodynamic measurements were carried out using different techniques, namely hot-wire anemometry, PIV and flow visualization. All acoustic measurements were conducted through the microphone array. The data were respectively processed with a few algorithms for different purposes, such as spectra analysis and beamforming. In addition, the test conditions, i.e. characteristics of the crossflow and

background noise were addressed.

In the following three chapters, results and conclusions of this comprehensive study were reported. Chapter 4 is the core of this thesis, which is a validation of the dual jets. More specifically, tandem rods were used as the test object being a generic bluff body noise source. Then six different geometries were tested, including the single jet air curtain and dual jets for comparison. Note that in the dual jets geometries, two configurations were tested with different jet speed pairs. Prior to the acoustic measurements, it was found through flow visualization that the best theatrical model to date is not able to predict the jet pattern as accurately as needed. Therefore, a series of CFD simulations were conducted in order to optimise the use of the air curtain application. The simulation model was validated with PIV experiment. Based on simulation results, a new approach for the shielding optimization was proposed and applied. Accordingly, the position of the rods was found for the single jet, and it is worth noting that this position was used in all tests with the rods for the purpose of comparison. The acoustic measurements began with the single jet. It was revealed that the air curtain can be a subsequent main noise source, which was in agreement with previous studies. Moreover, the rods were also found to still produce noise in a different frequency range, which can be attributed to the recirculation induced by the air curtain. In addition, how-wire measurements were carried out in the centre flow between two rods and the wake flow downstream to the rear rod. The results fundamentally explained why the air curtain can reduce noise. The second half of this Chapter focused on the dual jets. First of all, the shielding height increase in the dual jets was described based on the primary jet trajectory. As such, in addition to the initial configuration of dual jets, which maintains the primary jet speed, a new configuration was also tested. As mentioned earlier, the new configuration keeps the shielding approximately same when compared to the corresponding single jet case, by reducing the primary jet speed. The measurement data of both configurations revealed that the dual jets geometry can further enhance the reduction of the rods noise emission. In terms of the jet self-noise, the second configuration is much quieter, even than the single jet geometry. By contrast, total jet self-noise the original configuration in dual jets is noisier than the single jet geometry.

Chapter 5 carried out investigations on the flow regime of dual jets in crossflow. First

of all, a novel method to define the leeward edge of the jet, also referred to the shielding curve, was described. The method aims to avoid the complexity of the natural system definition prior to the edge, and directly works on defining the leeward edge, which is the most important reference to the bluff body position in noise reduction. Based on PIV experiment, the method was tested to be useful for the primary jet in both single jet and dual jets geometries. Moreover, it was found that a second order polynomial can be used to fit the leeward edge. In the flowing sections of the chapter, investigations were carried out based on the CFD simulations. To begin with, the recirculation structures were investigated in this chapter, including those upstream and downstream zones to the primary jet. In the Δ zone upstream to the primary jet, which is the zone between two jets, two recirculation structures were observed. Variation of these two structures with the jet speed were characterised. The main recirculation that is downstream to the primary jet was also discussed. Furthermore, the influence from the recirculation on the velocity contour was analysed. At last part of the chapter, the development of the two tandem jets was characterised using streamwise profiles. To be more specific, likewise to in quiescent flow, the converging region, merging region and combined region were defined. In addition, the turbulence properties in the flow field were also investigated.

Chapter 6 provides a comparative study on the possibility of the combined use of dual jets with other technologies. The perforated fairing was the example in this study. Likewise, the rods position was optimised using the leeward edge definition described above. Then different geometries were tested, including the use of the dual jets air curtain, the use of the perforated fairings and the combined use. For the combined use, two geometries were compared: one with the fairings upstream to the rods and the other downstream. The downstream one was proposed to shield the recirculation flow coming from the downstream of the rods. Acoustic performance of each geometry was evaluated based on measurement. In particular, the self-noise of the perforated fairing was characterised using the microphone array and the wake flow downstream using hot-wire. Despite the reduction of the rods noise, it was observed that the vortex shedding of the fairing edge can induce significant noise in the high frequency range. When the dual jets were introduced in the combined geometry, more noise reduction was achieved, especially when the fairing was situated downstream of the rods. However, despite this slight improvement

in noise reduction, the geometry with only dual air curtains is still recommended from an implementation point of view.

7.2 Future Work

Work in this study is not the end of the research on the air curtain technology. On the contrary, more work is needed due to the low technology readiness level of the dual air curtains for the landing gear noise reduction. Therefore, future work is expected to be but not limited to:

- Air curtain nozzle shape optimization. Previous studies confirmed that shape of the jet nozzle is directly related to the jet noise emission. Therefore, more jet noise suppression can be achieved through using an optimised nozzle shape.
- Shielding increase quantification. It is concluded that shielding from the air curtain to the bluff body dominates performance of the noise reduction and introduction of the upstream jet can increase shielding of the primary jet. In order to ultimately design the dual jet rig for landing gear, a quantification of the shielding increase is needed, which is foreseen to be of benefit in the implementation.
- Jet noise in crossflow. To date, little information can be found on the jet noise in crossflow except that it is higher than the jet in the quiescent flow. As such, a more complete characterization of this aeroacoustic sources is required.

Appendix A

Octave bands and One-Third Octave Bands

Table A.1: Range of the Octave bands and One-Third Octave Bands

Octave Bands			1/3 Octave bands		
Lower Limit (Hz)	Centre (Hz)	Upper Limit (Hz)	Lower Limit (Hz)	Centre (Hz)	Upper Limit (Hz)
			14.1	16	17.8
11	16	22	17.8	20	22.4
			22.4	25	28.2
			28.2	31.5	35.5
22	31.5	44	35.5	40	44.7
			44.7	50	56.2
			56.2	63	70.8
44	63	88	70.8	80	89.1
			89.1	100	112
			112	125	141
88	125	177	141	160	178
			178	200	224
			224	250	282
177	250	355	282	315	355
			355	400	447
			447	500	562
355	500	710	562	630	708
			708	800	891
			891	1,000	1,122
710	1,000	1,420	1,122	1,250	1,413
			1,413	1,600	1,778
			1,778	2,000	2,239
1,420	2,000	2,840	2,239	2,500	2,818
			2,818	3,150	3,548
			3,548	4,000	4,467
2,840	4,000	5,680	4,467	5,000	5,623
			5,623	6,300	7,079
			7,079	8,000	8,913
5,680	8,000	11,360	8,913	10,000	11,220
			11,220	12,500	14,130
11,360	16,000	22,720	14,130	16,000	17,780
			17,780	20,000	22,390

Bibliography

[1] U. Rosenhall, K. Pedersen, and A. Svanborg, "Presbycusis and Noise-Induced Hearing Loss," *Ear and Hearing*, vol. 11, no. 4, pp. 257–263, 1990. doi: 10.1097/00003446-199008000-00002

[2] K. D. Kryter, *The Handbook of Hearing and the Effects of Noise: Physiology, Psychology, and Public Health*, 1994, Academic Press.

[3] P. W. Alberti, "Noise Induced Hearing Loss," *BMJ: British Medical Journal*, vol. 304, no. 6826, p. 522, 1992. doi: 10.1136/bmj.304.6826.522

[4] E. Directive, "Directive 2002/49/EC of the European Parliament and of the Council relating to the Assessment and Management of Environmental Noise," *Official Journal of the European Communities*, vol. 189, no. 12, pp. 12–26, June, 2002.

[5] R. Astley, A. Agarwal, P. Joseph, R. Self, M. Smith, R. Sugimoto, and B. Tester, "Predicting and Reducing Aircraft Noise," in *14th International Congress on Sound and Vibration*, Cairns, Australia, 09-12 July 2007, p. 34.

[6] M. J. T. Smith, *Aircraft Noise*, 1989, Cambridge University Press.

[7] P. Argüelles, M. Bischoff, P. Busquin, B. Droste, S. R. Evans, W. Kröll, J. Lagardere, A. Lina, J. Lumsden, and D. Ranque, "European Aeronautics: A vision for 2020," The European Commission, Tech. Rep., January 2001.

[8] Y. Li, X. Wang, and D. Zhang, "Control Strategies for Aircraft Airframe Noise Reduction," *Chinese Journal of Aeronautics*, vol. 26, no. 2, pp. 249–260, 2013. doi: 10.1016/j.cja.2013.02.001

[9] W. Dobrzynski, "Almost 40 Years of Airframe Noise Research: What Did We Achieve?" *Journal of Aircraft*, vol. 47, no. 2, pp. 353–367, 2010. doi: 10.2514/1.44457

[10] L. Leylekian, M. Lebrun, and P. Lempereur, "An Overview of Aircraft Noise Reduction Technologies," Tech. Rep. 6, 2014, aerospaceLab.

[11] D. G. Crighton, "Airframe Noise," in *Aeroacoustics of Flight Vehicles: Theory and Practice. Volume 1: Noise Sources*, vol. 1, 1991, pp. 391–447.

[12] J.-F. Piet, N. Molin, and C. Sandu, "Aircraft Landing Gear Provided with at Least One Noise Reducing Means," May 2012, US Patent US20100108805 A1.

[13] N. Molin, J.-F. Piet, L. C. Chow, M. Smith, W. Dobrzynski, and C. Seror, "Prediction of Low Noise Aircraft Landing Gears and Comparison with Test Results (AIAA 2006-2623)," in *12th AIAA/CEAS Aeroacoustics Conference*, Cambridge, Massachusetts, 2006. doi: 10.2514/6.2006-2623

[14] W. M. Dobrzynski, B. Schöning, L. C. Chow, C. Wood, M. Smith, and C. Seror, "Design and Testing of Low Noise Landing Gears," *International Journal of Aeroacoustics*, vol. 5, no. 3, pp. 233–262, 2006. doi: 10.1260/1475-472X.5.3.233

[15] T. Sijpkes and J. Wickerhoff, "Aeroplane Provided with Boise-reducing Means, as well as a Landing Gear and Blowing Means," June 2004, US Patent US20040104301 A1.

[16] L. Guyonnaud, C. Solliec, M. D. Virel, and C. Rey, "Design of Air Curtains Used for Area Confinement in Tunnels," *Experiments in Fluids*, vol. 28, pp. 377–384, 2000. doi: 10.1007/s003480050397

[17] N. Luo, A. Li, R. Gao, Z. Tian, W. Zhang, S. Mei, L. Feng, and P. Ma, "An Experiment and Simulation of Smoke Confinement and Exhaust Efficiency Utilizing a Modified Opposite Double-Jet Air Curtain ," *Safety Science*, vol. 55, no. 0, pp. 17 – 25, 2013. doi: 10.1016/j.ssci.2012.12.002

[18] R. F. Huang and C. I. Chou, "Flow and Performance of an Air-curtain Biological Safety cabinet," *Annals of Occupational Hygiene*, vol. 53, no. 4, pp. 425–440, 2009. doi: 10.1093/annhyg/mep020

[19] S. Oerlemans and A. d. Bruin, "Reduction of Landing Gear Noise Using an Air Curtain (AIAA 2009-3156)," in *15th AIAA/CEAS Aeroacoustics Conference*, Miami, Florida, 2009. doi: 10.2514/6.2009-3156

[20] K. Boorsma, "Aeroacoustic Control of Landing Gear Noise Using Perforated Fairings," Ph.D. dissertation, University of Southampton, June 2008.

[21] H. H. Heller and W. M. Dobrzynski, "Sound Radiation from Aircraft Wheel-WelVLanding-Gear Configurations," *Journal of Aircraft*, vol. 14, no. 8, pp. 768–774, 1977. doi: 10.2514/3.58851

[22] W. Humphreys and T. Brooks, "Noise Spectra and Directivity for a Scale-model Landing Gear," *International Journal of Aeroacoustics*, vol. 8, no. 5, pp. 409–443, 2009. doi: 10.1260/147547209788549316

[23] W. Dobrzynski, L. Chow, P. Guion, and D. Shiells, "A European Study on Landing Gear Airframe Noise Sources (AIAA 2000-1971)," in *6th Aeroacoustics Conference and Exhibit*, Lahaina, USA, 2000. doi: 10.2514/6.2000-1971

[24] L. Chow and C. Wood, "Landing Gear Noise Reduction," Feb. 2009, US Patent US7484688 B2.

[25] J. Piet, L. Chow, F. Laporte, and H. Remy, "Flight Test Investigation of High-lift Devices and Landing Gear Modifications to Achieve Airframe Noise Reduction," in *ECCOMAS 2004 Conference*, Jyvaeskylae, Finland, 2004.

[26] Y. Li, X. Wang, and D. Zhang, "Control Strategies for Aircraft Airframe Noise Reduction," *Chinese Journal of Aeronautics*, vol. 26, no. 2, pp. 249–260, 2013. doi: 10.1016/j.cja.2013.02.001

[27] W. Dobrzynski, L. Chow, P. Guion, and D. Shiells, "Research into Landing Gear

Airframe Noise Reduction (AIAA 2002-2409)," in *8th AIAA/CEAS Aeroacoustics Conference*, Breckenridge, Colorado, USA, 2002. doi: 10.2514/6.2002-2409

[28] A. Abeysinghe, J. Whitmire, D. Nesthus, J. Moe, C. Vista, and G. Stuczynski, "QTD 2 (Quiet Technology Demonstrator) Main Landing Gear Noise Reduction Fairing Design and Analysis (AIAA 2007-3456)," in *13th AIAA/CEAS Aeroacoustics Conference*, Rome, Italy, 2007. doi: 10.2514/6.2007-3456

[29] P. A. Ravetta, R. A. Burdisso, and W. F. Ng, "Wind Tunnel Aeroacoustic Measurements of a 26%-scale 777 Main Landing Gear Model (AIAA 2004-2885)," in *10th AIAA/CEAS Aeroacoustics Conference*, Manchester, UK, 2004. doi: 10.2514/6.2004-2885

[30] Y. Li, M. Smith, and X. Zhang, "Measurement and Control of Aircraft Landing Gear Broadband Noise," *Aerospace Science and Technology*, vol. 23, no. 1, pp. 213–223, 2012. doi: 10.1016/j.ast.2011.07.009

[31] K. Boorsma, X. Zhang, and N. Molin, "Landing Gear Noise Control Using Perforated Fairings," *Acta Mechanica Sinica*, vol. 26, no. 2, pp. 159–174, 2010. doi: 10.1007/s10409-009-0304-0

[32] L. Chow, D. Foot, and C. Wood, "Aircraft Noise Reduction Apparatus," Sep 2003, US Patent US6619587 B1.

[33] P. Eret, J. Kennedy, and G. J. Bennett, "Effect of Noise Reducing Components on Nose Landing Gear Stability for a Mid-size Aircraft Coupled with Vortex Shedding and Freeplay," *Journal of Sound and Vibration*, vol. 354, pp. 91–103, 2015. doi: 10.1016/j.jsv.2015.06.022

[34] S. Oerlemans, C. Sandu, N. Molin, and J.-F. Piet, "Reduction of Landing Gear Noise Using Meshes (AIAA 2010-3972)," in *16th AIAA/CEAS Aeroacoustics Conference*, Stockholm, Sweden, 2010. doi: 10.2514/6.2010-3972

[35] P. N. Okolo, K. Zhao, J. Kennedy, and G. J. Bennett, "Mesh Screen Application for Noise Reduction of Landing Gear Strut (AIAA 2016-2845)," in *22nd AIAA/CEAS Aeroacoustics Conference*, Lyon, France, 2016. doi: 10.2514/6.2016-2845

[36] E. Moreau, "Airflow Control by Non-thermal Plasma Actuators," *Journal of Physics D: Applied Physics*, vol. 40, no. 3, p. 605, 2007. doi: 10.1088/0022-3727/40/3/S01

[37] Y. Li, X. Zhang, and X. Huang, "The use of plasma actuators for bluff body broadband noise control," *Experiments in Fluids*, vol. 49, no. 2, pp. 367–377, 2010. doi: 10.1007/s00348-009-0806-3

[38] X. Huang, X. Zhang, and Y. Li, "Broadband Flow-Induced Sound Control Using Plasma Actuators," *Journal of Sound and Vibration*, vol. 329, no. 13, pp. 2477–2489, 2010. doi: 10.1016/j.jsv.2010.01.018

[39] F. O. Thomas, A. Kozlov, and T. C. Corke, "Plasma Actuators for Cylinder Flow Control and Noise Reduction," *AIAA Journal*, vol. 46, no. 8, pp. 1921–1931, 2008. doi: 10.2514/1.27821

[40] D. Angland, X. Zhang, and M. Goodyer, "Use of Blowing Flow Control to Reduce Bluff Body Interaction Noise," *AIAA Journal*, vol. 50, no. 8, pp. 1670–1684, 2012. doi: 10.2514/1.J051074

[41] M. Aubert, O. Stalnov, D. Angland, and X. Zhang, "Numerical Investigation of Active Flow Control using Steady Blowing for Landing Gear Noise Reduction (AIAA 2014-2893)," in *20th AIAA/CEAS Aeroacoustics Conference 2014*, Atlanta, GA, USA, 2014. doi: 10.2514/6.2014-2893

[42] H. Haniu and B. Ramaprian, "Studies on Two-Dimensional Curved Nonbuoyant Jets in Cross flow," *Journal of Fluids Engineering*, vol. 111, no. 1, pp. 78–86, 1989. doi: 10.1115/1.3243603

[43] B. Cushman, *Environmental Fluid Mechanics*, 2006, John Wiley & Sons, Incorporated.

[44] N. Rajaratnam, *Turbulent Jets*, 1976, vol. 5, Elsevier.

[45] S. Sivakumar, R. Sangras, and V. Raghavan, "Characteristics of Turbulent Round Jets in its Potential-Core Region," *World Academy of Science, Engineering and Technology*, vol. 61, pp. 526–532, 2012. doi: 10.1.1.309.9595

[46] E. Förthmann, "Turbulent Jet Expansion," National Advisory Committee for Aeronautics, Tech. Rep., 1934.

[47] J. S. Turner, *Buoyancy Effects in Fluids*, 1973, Cambridge University Press.

[48] E. List and J. Imberger, "Turbulent Entrainment in Buoyant Jets and Plumes," *Journal of the Hydraulics Fivision-ASCE*, vol. 101, no. NHY 5, pp. 617–620, 1975.

[49] A. Roshko, "Structure of Turbulent Shear Flows: A New Look," *AIAA Journal*, vol. 14, no. 10, pp. 1349–1357, 1976.

[50] P. E. Dimotakis, "Two-Dimensional Shear-Layer Entrainment," *AIAA Journal*, vol. 24, no. 11, pp. 1791–1796, 1986. doi: 10.2514/3.9525

[51] S. Chhabra, T. N. Shipman, and A. K. Prasad, "The Entrainment Behavior of a Turbulent Axisymmetric Jet in a Viscous Host Fluid," *Experiments in Fluids*, vol. 38, no. 1, pp. 70–79, 2005. doi: 10.1007/s00348-004-0888-x

[52] B. Morton, G. Taylor, and J. Turner, "Turbulent Gravitational Convection from Maintained and Instantaneous Sources," in *Proceedings of the Royal Society of London A: Mathematical, Physical and Engineering Sciences*, vol. 234, no. 1196. The Royal Society, 1956, pp. 1–23.

[53] J. Turner, "Turbulent Entrainment: the Development of the Entrainment Assumption, and its Application to Geophysical Flows," *Journal of Fluid Mechanics*, vol. 173, pp. 431–471, 1986. doi: 10.1017/S0022112086001222

[54] A. M. Falcone and J. C. Cataldo, "Entrainment Velocity in an Axisymmetric Turbulent Jet," *Journal of Fluids Engineering*, vol. 125, no. 4, pp. 620–627, 2003. doi: 10.1115/1.1595674

[55] A. Bejan, *Convection Heat Transfer*. John Wiley & Sons, 2013.

[56] N. E. Kotsovinos, "A Note on the Spreading Rate and Virtual Origin of a Plane Turbulent Jet," *Journal of Fluid Mechanics*, vol. 77, no. 02, pp. 305–311, 1976. doi: 10.1017/S0022112076002127

[57] M. L. Albertson, Y. Dai, R. Jensen, and H. Rouse, "Diffusion of Submerged Jets," *Transactions of the American Society of Civil Engineers*, vol. 115, no. 1, pp. 639–664, 1950.

[58] J. FLORA, JR and V. Goldschmidt, "Virtual Origins of a Free Plane Turbulent Jet," *AIAA Journal*, vol. 7, no. 12, pp. 2344–2346, 1969. doi: 10.2514/3.5543

[59] V. Goldschmidt and S. Eskinazi, "Two-phase Turbulent Flow in a Plane Jet," *Journal of Applied Mechanics*, vol. 33, no. 4, pp. 735–747, 1966. doi: 10.1115/1.3625176

[60] G. Heskestad, "Hot-wire Measurements in a Plane Turbulent Jet," *Journal of Applied Mechanics*, vol. 32, no. 4, pp. 721–734, 1965. doi: 10.1115/1.3627309

[61] P. Jenkins and V. Goldschmidt, "Mean Temperature and Velocity in a Plane Turbulent Jet," *Journal of Fluids Engineering*, vol. 95, no. 4, pp. 581–584, 1973. doi: 10.1115/1.3447073

[62] N. Kotsovinos, "A Study of the Entrainment and Turbulence in a Plane Turbulent Jet," Tech. Rep., 1975, California Institute of Technology, Rep. KH R-32, WM Keck Laboratory of Hydrology and Water Resources, Pasadena, California.

[63] W. Mih and J. Hoopes, "Mean and Turbulent Velocities for Plane jet," *Journal of Hydraulic Engineering*, vol. 98, no. 7, pp. 1275–1294, 1972.

[64] D. R. Miller and E. W. Comings, "Static Pressure Distribution in the Free Turbulent Jet," *Journal of Fluid Mechanics*, vol. 3, no. 1, pp. 1–16, 1957. doi: 10.1017/S0022112057000440

[65] H. Nkaguchi, "Jet along a Curved Wall," Tech. Rep., 1961, University of Tokyo.

[66] D. R. Miller and E. W. Comings, "Force-momentum Fields in a Dual-jet Flow," *Journal of Fluid Mechanics*, vol. 7, no. 02, pp. 237–256, 1960. doi: 10.1017/S0022112060001468

[67] E. Tanaka, "The Interference of Two-Dimensional Parallel Jets: 2nd Report, Experiments on the Combined Flow of Dual Jet," *Bulletin of JSME*, vol. 17, no. 109, pp. 920–927, 1974. doi: 10.1299/jsme1958.17.920

[68] Y. Lin and M. Sheu, "Interaction of Parallel Turbulent Plane Jets," *AIAA Journal*, vol. 29, no. 9, pp. 1372–1373, 1991. doi: 10.2514/3.10749

[69] A. Nasr and J. Lai, "Two Parallel Plane Jets: Mean Flow and Effects of Acoustic Excitation," *Experiments in Fluids*, vol. 22, no. 3, pp. 251–260, 1997. doi: 10.1007/s003480050044

[70] E. A. Anderson and R. E. Spall, "Experimental and Numerical Investigation of Two-dimensional Parallel Jets," *Journal of Fluids Engineering*, vol. 123, no. 2, pp. 401–406, 2001. doi: 10.1115/1.1363701

[71] N. Fujisawa, K. Nakamura, and K. Srinivas, "Interaction of Two Parallel Plane Jets of Different Velocities," *Journal of Visualization*, vol. 7, no. 2, pp. 135–142, 2004. doi: 10.1007/BF03181586

[72] Z. qin Yin, H. jun Zhang, and J. zhong Lin, "Experimental study on the Flow Field Characteristics in the Mixing Region of Twin Jets," *Journal of Hydrodynamics, Ser. B*, vol. 19, no. 3, pp. 309 – 313, 2007. doi: 10.1016/S1001-6058(07)60063-8

[73] A. Karimpour, N. Kaye, and A. Khan, "CFD Study of Merging Turbulent Plane Jets," *Journal of Hydraulic Engineering*, vol. 137, no. 3, pp. 381–385, 2011. doi: 10.1061/(ASCE)HY.1943-7900.0000308

[74] Z. Baratian-Ghorghi, J. R. SMITH *et al.*, "The Merging of Two Unequal Axisymmetric Parallel Turbulent Jets," *Journal of Hydrodynamics, Ser. B*, vol. 24, no. 2, pp. 257–262, 2012. doi: 10.1016/S1001-6058(11)60242-4

[75] M. Lighthill, "On Sound Generated Aerodynamically. I. General Theory," in *Proceedings of the Royal Society of London A: Mathematical, Physical and Engineering Sciences*, vol. 211, no. 1107. The Royal Society, 1952. doi: 10.1098/rspa.1952.0060 pp. 564–587.

[76] M. J. Lighthill, "On Sound Generated Aerodynamically. II. Turbulence as a Source of Sound," in *Proceedings of the Royal Society of London A: Mathematical, Physical and Engineering Sciences*, vol. 222, no. 1148. The Royal Society, 1954. doi: 10.1098/rspa.1954.0049 pp. 1–32.

[77] C. K. Tam, "Jet Noise: Since 1952," *Theoretical and Computational Fluid Dynamics*, vol. 10, no. 1-4, pp. 393–405, 1998. doi: 10.1007/s001620050072

[78] M. J. Lighthill, "Jet Noise," *AIAA Journal*, vol. 1, no. 7, pp. 1507–1517, 1963. doi: 10.2514/3.1848

[79] G. Lilley, "Jet Noise Classical Theory and Experiments," *Aeroacoustics of flight vehicles: theory and practice*, vol. 1, pp. 211–289, 1991.

[80] R. Hoch, J. Duponchel, B. Cocking, and W. Bryce, "Studies of the Influence of Density on Jet Noise," *Journal of Sound and Vibration*, vol. 28, no. 4, pp. 649–668, 1973. doi: 10.1016/S0022-460X(73)80141-5

[81] H. Tanna, P. Dean, and M. Fisher, "The Influence of Temperature on Shock-free Supersonic Jet Noise," *Journal of Sound and Vibration*, vol. 39, no. 4, pp. 429–460, 1975. doi: 10.1016/S0022-460X(75)80026-5

[82] H. Tanna, "An Experimental Study of Jet Noise Part I: Turbulent Mixing Noise," *Journal of Sound and Vibration*, vol. 50, no. 3, pp. 405–428, 1977. doi: 10.1016/0022-460X(77)90493-X

[83] M. Fisher, P. Lush, and M. H. Bourne, "Jet Noise," *Journal of Sound and Vibration*, vol. 28, no. 3, pp. 563–585, 1973. doi: 10.1016/S0022-460X(73)80040-9

[84] S. E. Munro and K. Ahuja, "Development of a Prediction Scheme for High Aspect-ratio Jet Noise (AIAA 2003-3255)," in *9th AIAA/CEAS Aeroacoustics Conference*, Hilton Head, South Carolina, USA, 2003. doi: 10.2514/6.2003-3255

[85] S. Munro and K. K. Ahuja, "Aeroacoustics of a High Aspect-ratio Jet (AIAA 2003-3323)," in *9th AIAA/CEAS Aeroacoustics Conference*, Hilton Head, South Carolina, USA, 2003. doi: 10.2514/6.2003-3323

[86] K. Viswanathan, "Mechanisms of Jet Noise Generation: Classical Theories and Recent Developments," *International Journal of Aeroacoustics*, vol. 8, no. 4, pp. 355–407, 2009. doi: 10.1260/147547209787548949

[87] S. C. Crow and F. Champagne, "Orderly Structure in Jet Surbulence," *Journal of Fluid Mechanics*, vol. 48, no. 03, pp. 547–591, 1971. doi: 10.1017/S0022112071001745

[88] G. L. Brown and A. Roshko, "On Density Effects and Large Structure in Turbulent Mixing Layers," *Journal of Fluid Mechanics*, vol. 64, no. 04, pp. 775–816, 1974. doi: 10.1017/S002211207400190X

[89] P. Bradshaw, D. H. Ferriss, and R. F. Johnson, "Turbulence in the Noise-producing Region of a Circular Jet," *Journal of Fluid Mechanics*, vol. 19, p. 591624, Mar 1963. doi: 10.1017/S0022112064000945

[90] S. C. Crow and F. H. Champagne, "Orderly Structure in Jet Turbulence," *Journal of Fluid Mechanics*, vol. 48, no. 3, p. 547591, Mar 1971. doi: 10.1017/S0022112071001745

[91] W. Olsen and A. Karchmer, "Lip Noise Generated by Flow Separation from Nozzle Surfaces (1976-3)," in *14th Aerospace Sciences Meeting*, Washington, D.C., USA, 1976. doi: 10.2514/6.1976-3

[92] F. Leppington, "Scattering of Quadrupole Sources Bear the End of a Rigid Semi-infinite Circular Pipe," *Aeronautical Research Council*, vol. 1195, p. 5, 1972.

[93] J. Ffowcs Williams and C. Gordon, "Noise of Highly Turbulent Jets at Low Exhaust Speeds," *AIAA Journal*, vol. 3, no. 4, pp. 791–793, 1965. doi: 10.2514/3.2994

[94] S. J. Wright, "Effects of Ambient Crossflows and Density Stratification on the Characteristic Behavior of Round Turbulent Buoyant Jets," Tech. Rep., 1977, PhD thesis, California Institute of Technology.

[95] J. Keffer and W. Baines, "The Round Turbulent Jet in a Crosswind," *Journal of Fluid Mechanics*, vol. 15, no. 04, pp. 481–496, 1963. doi: 10.1017/S0022112063000409

[96] J. Andreopoulos and W. Rodi, "Experimental Investigation of Jets in a

Crossflow," *Journal of Fluid Mechanics*, vol. 138, pp. 93–127, 1984. doi: 10.1017/S0022112084000057

[97] D. Yu, M. Ali, and J. H. Lee, "Multiple Tandem Jets in Crossflow," *Journal of Hydraulic Engineering*, vol. 132, no. 9, pp. 971–982, 2006. doi: 10.1061/(ASCE)0733-9429(2006)132:9(971)

[98] K. Mahesh, "The Interaction of Jets with Crossflow," *Annual Review of Fluid Mechanics*, vol. 45, pp. 379–407, 2013. doi: 10.1146/annurev-fluid-120710-101115

[99] Y. Kamotani and I. Greber, "Experiments on a Turbulent Jet in a Crossflow," *AIAA Journal*, vol. 10, no. 11, pp. 1425–1429, 1972. doi: 10.2514/3.50386

[100] S. Smith and M. Mungal, "Mixing, Structure and Scaling of the Jet in Crossflow," *Journal of Fluid Mechanics*, vol. 357, pp. 83–122, 1998. doi: 10.1017/S0022112097007891

[101] H. Squire, "Jet Flow and Its Effects on Aircraft," *Aircraft Engineering and Aerospace Technology*, vol. 22, no. 3, pp. 62–67, 1950. doi: 10.1108/eb031870

[102] S. Muppidi and K. Mahesh, "Passive Scalar Mixing in Jets in Crossflow (AIAA 2006-1098)," in *44th AIAA Aerospace Sciences Meeting and Exhibit, Reno, Nevada*, Reno, Nevada, USA, 2006. doi: 10.2514/6.2006-1098 pp. 2006–1098.

[103] B. Ramaprian and M. Chandrasekhara, "LDA Measurements in Plane Turbulent Jets," *Journal of Fluids Engineering*, vol. 107, no. 2, pp. 264–271, 1985. doi: 10.1115/1.3242472

[104] R. Camussi, G. Guj, and A. Stella, "Experimental Study of a Jet in a Crossflow at Very Low Reynolds Number," *Journal of Fluid Mechanics*, vol. 454, pp. 113–144, 2002. doi: 10.1017/S0022112001007005

[105] W. Jones and M. Wille, "Large-eddy Simulation of a Plane Jet in a Crossflow," *International Journal of Heat and Fluid Flow*, vol. 17, no. 3, pp. 296–306, 1996. doi: 10.1016/0142-727X(96)00045-8

[106] D. Crabb, D. Durao, and J. Whitelaw, "A Round Jet Normal to a Crossflow," *Journal of Fluids Engineering*, vol. 103, no. 1, pp. 142–153, 1981. doi: 10.1115/1.3240764

[107] K. Ahmed, D. Forliti, J. Moody, and R. Yamanaka, "Flowfield Characteristics of a Confined Transverse Slot Jet," *AIAA Journal*, vol. 46, no. 1, pp. 94–103, 2008. doi: 10.2514/1.29799

[108] R. F. Huang and R. H. Hsieh, "Sectional Flow Structures in Near Wake of Elevated Jets in a Crossflow," *AIAA Journal*, vol. 41, no. 8, pp. 1490–1499, 2003. doi: 10.2514/2.2099

[109] M. S. Ali, "Mixing of a Non-buoyant Multiple Jet Group in Crossflow," Master's thesis, University of Hong Kong, 2003.

[110] Y. Kamotani and I. Greber, "Experiments on Confined Turbulent Jets in Crossflow," Tech. Rep., 1974, NASA technical report.

[111] M. Schwendemann, "A Wind Tunnel Investigation of Stratified Jets and Closely Spaced Jets Exhausting into a Crossflow," Tech. Rep., 1973, Northrop Aircraft Division, Hawthorne, CA, Rept. NOR.

[112] H. Ziegler and P. Wooler, "Analysis of Stratified and Closely Spaced Jets Exhausting into a Crossflow," National Aeronautics and space Administration, Washington, DC, Tech. Rep., 1973.

[113] K. Isaac and J. Schetz, "Analysis of Multiple Jets in a Crossflow."

[114] J. F. Campbell and J. A. Schetz, "Flow Properties of Submerged Heated Effluents in a Waterway," *AIAA Journal*, vol. 11, no. 2, pp. 223–230, 1973. doi: 10.2514/3.50452

[115] J. Schetz, A. Jakubowski, and K. Aoyagi, "Jet Trajectories and Surface Pressures Induced on a Body of Revolution with Various Dual Jet Configurations," *Journal of Aircraft*, vol. 20, no. 11, pp. 975–982, 1983. doi: 10.2514/3.48201

[116] K. Isaac and A. Jakubowski, "Experimental Study of the Interaction of Multiple Jets with a Crossflow," *AIAA Journal*, vol. 23, no. 11, pp. 1679–1683, 1985. doi: 10.2514/3.9151

[117] E. J. Gutmark, I. M. Ibrahim, and S. Murugappan, "Dynamics of Single and Twin Circular Jets in crossflow," *Experiments in Fluids*, vol. 50, no. 3, pp. 653–663, 2011. doi: 10.1007/s00348-010-0965-2

[118] T. New and B. Zang, "On the Trajectory Scaling of Tandem Twin Jets in Crossflow in Close Proximity," *Experiments in Fluids*, vol. 56, no. 11, pp. 1–12, 2015. doi: 10.1007/s00348-015-2070-z

[119] Furness Controls, "Low Pressure Microprocessor Micromanometer," Accessed:2016-12-04, http://www.deltastrumenti.com/misura/Furness_FP/FCO510_2.pdf.

[120] H. H. Bruun, "Hot-wire Anemometry: Principles and Signal Analysis," *Measurement Science and Technology*, vol. 7, no. 10, 1996. doi: 10.1088/0957-0233/7/10/024

[121] F. E. Jrgensen, "How to Measure Turbulence with Hot-Wire Anemometers: A Practical Guide," Tech. Rep., Dantec Dynamics.

[122] P. Bearman, "Corrections for the Effect of Ambient Temperature Drift on Hot-wire Measurements in Incompressible Flow," *DISA information*, vol. 11, no. 1, pp. 25–30, 1971.

[123] C. Brossard, J. C. Monnier, P. BARRICAU, F. X. Vandernoot, Y. Le Sant, F. Champagnat, and G. Le Besnerais, "Principles and Applications of Particle Image Velocimetry," no. 1, pp. p. 1–11.

[124] "FLowMaster-Advanced PIV / PTV Systems for Quantitative Flow Field Analysis," June 2012, La Vision User Manuel.

[125] J. K. Sveen, "An Introduction to MatPIV v. 1.6. 1," Tech. Rep., 2004, Matematisk Institutt, Universitetet i Oslo.

[126] S. Wereley and C. Meinhart, "Second-order Accurate Particle Image Velocimetry," *Experiments in Fluids*, vol. 31, no. 3, pp. 258–268, 2001. doi: 10.1007/s003480100281

[127] C. E. Willert and M. Gharib, "Digital Particle Image Velocimetry," *Experiments in Fluids*, vol. 10, no. 4, pp. 181–193, 1991. doi: 10.1007/BF00190388

[128] M. Raffel, C. E. Willert, S. Wereley, and J. Kompenhans, *Particle Image Velocimetry: A Practical Guide*, 2nd ed., 2013, Springer.

[129] D. Dabiri, "Cross-correlation Digital Particle Image VelocimetryA Review," Tech. Rep., 2006, turbulencia. ABCM, Curitiba.

[130] "NI PXI-1033 User Manual," Tech. Rep., May 2012, National Instruments.

[131] G. J. Bennett, "Noise Source Identification for Ducted Fans," Ph.D. dissertation, Trinity College Dublin, University of Dublin, 2006.

[132] P. Stoica and R. L. Moses, *Introduction to Spectral Analysis*, 2005, vol. 452, Prentice hall Upper Saddle River.

[133] G. Strang, "Wavelets," *American Scientist*, vol. 82, no. 3, pp. 250–255, 1994.

[134] M. P. Norton and D. G. Karczub, *Fundamentals of Noise and Vibration Analysis for Engineers*, 2003, Cambridge University Press.

[135] J. Christensen and J. Hald, "Technical Review Beamforming," Tech. Rep., 2004, Bruel & Kjaer.

[136] A. Meyer and D. Dbler, "Noise Source Localization within a Car Interior Using 3D-Microphone Arrays," in *1st Berlin Beamforming Conference*, Berlin, Germany, 2006.

[137] D. Robert, "Advanced Time-Domain Beamforming Techniques (AIAA 2004-2955)," in *10th AIAA/CEAS Aeroacoustics Conference*, Manchester, UK, 2004. doi: 10.2514/6.2004-2955

[138] O. Jaeckel, "Strengths and Weaknesses of Calculating Beamforming in the Time Domain," in *1st Berlin Beamforming Conference*, Berlin, Germany, 2006.

[139] P. Sijtsma, "Experimental Techniques for Identification and Characterisation of Noise Sources," *Advances in Aeroacoustics and Applications, VKI Lecture Series*, vol. 5, pp. 15–19, 2004.

[140] H. S. Ribner, "Reflection, Transmission, and Amplification of Sound by a Moving Medium," *The Journal of the Acoustical Society of America*, vol. 29, no. 4, pp. 435–441, 1957. doi: 10.1121/1.1908918

[141] J. W. Miles, "On the Reflection of Sound at an Interface of Relative Motion," *The Journal of the Acoustical Society of America*, vol. 29, no. 2, pp. 226–228, 1957. doi: 10.1121/1.1908836

[142] R. Amiet, "Refraction of Sound by a Shear Layer," *Journal of Sound and Vibration*, vol. 58, no. 4, pp. 467–482, 1978. doi: 10.1016/0022-460X(78)90353-X

[143] K. Ahuja, B. Tester, and H. Tanna, "Calculation of Far Field Jet Noise Spectra from Near Field Measurements with True Source Location," *Journal of Sound and Vibration*, vol. 116, no. 3, pp. 415 – 426, 1987. doi: 10.1016/S0022-460X(87)81374-3

[144] C. Bahr, N. Zawodny, T. Yardibi, F. Liu, D. Wetzel, B. Bertolucci, and L. Cattafesta, "Shear Layer Correction Validation using a Non-intrusive Acoustic Point Source (AIAA 2010-3735)," in *16th AIAA/CEAS Aeroacoustics Conference*, Stockholm, Sweden, 2010. doi: 10.2514/6.2010-3735

[145] R. H. Schlinker and R. K. Amiet, "Refraction and Scattering of Sound by A Shear Layer (AIAA 1980-973)," in *6th AIAA Aeroacoustics Conference*, Hartford, CT, USA, 1980. doi: 10.2514/6.1980-973

[146] M.Zdravkovich, "Flow Induced Oscillations of Two Interfering Circular Cylinders," *Journal of Sound and Vibration*, vol. 101, no. 4, pp. 511–521, 1985. doi: 10.1016/S0022-460X(85)80068-7

[147] M. Zdravkovich, "The Effects of Interference between Circular Cylinders in Cross-flow," *Journal of Fluids and structures*, vol. 1, no. 2, pp. 239–261, 1987. doi: 10.1016/S0889-9746(87)90355-0

[148] Y. Dai, T. Kobayashi, and N. Taniguchi, "Large Eddy Simulation of Plane Turbulent Jet Flow Using a New Outflow Velocity Boundary Condition," *JSME International Journal Series B Fluids and Thermal Engineering*, vol. 37, no. 2, pp. 242–253, 1994. doi: 10.1299/jsmeb.37.242

[149] C. Le Ribault, S. Sarkar, and S. Stanley, "Large Eddy Simulation of a Plane Jet," *Physics of Fluids*, vol. 11, no. 10, pp. 3069–3083, 1999. doi: 10.1063/1.870165

[150] S. Stanley, S. Sarkar, and J. Mellado, "A Study of the Flow-field Evolution and Mixing in a Planar Turbulent Jet Using Direct Numerical Simulation," *Journal of Fluid Mechanics*, vol. 450, pp. 377–407, 2002. doi: 10.1017/S0022112001006644

[151] Y. Liu, P. Tucker, and R. M. Kerr, "Linear and Nonlinear Model Large-eddy Simulations of a Plane Jet," *Computers and Fluids*, vol. 37, no. 4, pp. 439–449, 2008. doi: 10.1016/j.compfluid.2007.02.005

[152] D. Benmouhoub and A. Mataoui, "Inclined Plane Jet Impinging a Moving Heated Wall," *Fluid Dynamics and Materials Processing*, vol. 10, no. 2, pp. 241–260, 2014. doi: 10.3970/fdmp.2014.010.241

[153] S. Alimohammadi, T. Persoons, D. B. Murray, M. S. Tehrani, B. Farhanieh, and J. Koehler, "A Validated Numerical-Experimental Design Methodology for a Movable Supersonic Ejector Compressor for Waste-Heat Recovery," *Journal of Thermal Science and Engineering Applications*, vol. 6, no. 2, p. 021001, 2014. doi: 10.1115/1.4025090

[154] S. Alimohammadi, D. B. Murray, and T. Persoons, "Experimental Validation of a CFD Methodology for Transitional Flow Heat Transfer Characteristics of a Steady Impinging Jet," *Journal of Heat Transfer*, vol. 9, no. 136, 2014. doi: 10.1115/1.4027840

[155] R. J. Adrian, "Twenty Years of Particle Image Velocimetry," vol. 39, no. 2, pp. 159–169. doi: 10.1007/s00348-005-0991-7

[156] F. Moisy, "PIVMat Toolbox for Matlab," *Laboratory FAST, University Paris-Sud*, 2016. [Online]. Available: http://www.fast.u-psud.fr/pivmat/